CONTROLLED ENGINEERING of RARE-EARTH DOPED CORE-SHELL NANOCRYSTALS

By

Deming Liu

Department of Physics and Astronomy

Supervisors:

Prof. Dayong Jin, Prof. Ewa M. Goldys

MACQUARIE University
SYDNEY·AUSTRALIA

This thesis is presented for the degree of Doctor of Philosophy

February 2016

I certify that the work in this thesis has not previously been submitted for a degree nor has it been submitted as part of requirements for a degree to any other university or institution other than Macquarie University.

I also certify that the thesis is an original piece of research and it has been written by me. Any help and assistance that I have received in my research work and the preparation of the thesis itself have been appropriately acknowledged.

In addition, I certify that all information sources and literature used are indicated in the thesis.

The research presented in this thesis was approved by Macquarie University Ethics Review Committee, reference number: 5201100617 LAB on 11 Aug 2011.

Deming Liu 26-Feb-2016

Acknowledgements

First I would like to thank my principal supervisor Prof. Dayong Jin who has always been motivating and supportive to me. He teaches me not only academic research skills but also personal skills during my last 3.5-year Ph.D candidature period. Like a veteran coach, guiding his athletes, he trains us every day and leads us to win the final game. Jin is the soul of our team. His passion on the science research always impacts me to firmly believe what we do and will win in the end. I learnt a lot from Prof. Jin's self-motivated and optimistic attitude to life, and aspiring, energetic and collaborative research style, although I still cannot apply all of these skills to myself by now. I really appreciate his sincere help and thoughtful suggestions not only on my PhD program but also my research career development. I also thank Jin for patiently teaching me on academic writing in a way that make my writings easily understandable by general audience.

I also would like to thank my supervisor Prof. Ewa Goldys for helping me formulating my PhD research structure and her professional advice on my project. She gave me a lot of thoughtful comments on my publications and thesis draft.

Next, I would like to thank my colleagues, in particular, Dr. Xiaoxue (Helen) Xu, Dr. Jiangbo (Tim) Zhao, Dr. Lixin Zhang, and Dr. Yiqing Lu, for significant contributions to my projects and publications. I also thank Dr. Jie Lu and Xianlin Zheng, Yujia Liu and other peers within our research group. I had a wonderful teamwork experience with them. Many colleagues at Macquarie University, including Wei, Run, Wan, Zack, Sandya, and others, gave me many valuable advice through my research projects. I also want to thank our international collaborators, Yuhai Zhang, Xian Qin, Du Yi, and Xiaogang Liu, and other members in their respective labs. Their expertise and contributions added great values to my research projects. I sincerely appreciate the generous help from all these nice people.

I acknowledge the financial support I received from Macquarie University and China Scholarship Council (CSC) to offer me many opportunities to expand my research experiences.

Finally, I would like to thank my beloved family. I thank my parents, Likun Jiao and Xilin Liu, and my parents in law, Wenxue Jin and Yuhua Xin, and other relatives, who have

been backing me up over years. My wife Puyu has been sacrificing so much to support me. I am really grateful for the love and joy she brings to my life.

List of Publications

Research paper:

[1] **Liu, Deming**, Xiaoxue Xu, Yi Du, Xian Qin, Yuhai Zhang, Chenshuo Ma, Shihui Wen, Wei Ren1,5, Ewa M. Goldys, James A Piper, Shixue Dou, Xiaogang Liu, Dayong Jin, Three-dimensional controlled growth of monodisperse sub-50 nm heterogeneous nanocrystals, ***Nature Communications***.7 (2016) DOI: 10.1038/ncomms10254

[2] **Liu, Deming**, Xiaoxue Xu, Fan Wang, Jiajia Zhou, Chao Mi, Lixin Zhang, Yiqing Lu, Chenshuo Ma, Ewa Goldys, Jun Lin, and Dayong Jin, "Emission stability and reversibility of upconversion nanocrystals", ***Journal of Materials Chemistry C.***(2016), DOI: 10.1039/C6TC02990F

[3] Lu, Yiqing, Jiangbo Zhao, Run Zhang, Yujia Liu, **Deming Liu**, Ewa M. Goldys, Xusan Yang, Peng Xi, Anwar Sunna, Jie Lu, Yu Shi, Robert C. Leif, Yujing Huo, Jian Shen, James A. Piper, J. Paul Robinson and Dayong Jin. "Tunable lifetime multiplexing using luminescent nanocrystals." ***Nature Photonics*** 8, no. 1 (2014): 32-36.

[4] Zheng, Xianlin, Yiqing Lu, Jiangbo Zhao, Yuhai Zhang, Wei Ren, **Deming Liu**, Jie Lu, James A. Piper, Robert C. Leif, Xiaogang Liu and and Dayong Jin. "High-precision pinpointing of luminescent targets in encoder-assisted scanning microscopy allows high-speed quantitative analysis." ***Analytical chemistry***, 88 (2), (2016):1312–1319

[5] Lu, Jie, Yinghui Chen, **Deming Liu**, Wei Ren, Yiqing Lu, Yu Shi, James Piper, Ian Paulsen, and Dayong Jin. "One-step protein conjugation to upconversion nanoparticles." ***Analytical chemistry*** 87, no. 20 (2015): 10406-10413.

[6] Clement, Sandhya, Wei Deng, Krystyna Drozdowicz-Tomsia, **Deming Liu**, Cameron Zachreson, and Ewa M. Goldys. "Bright, water-soluble CeF3 photo-, cathodo-, and X-ray luminescent nanoparticles." ***Journal of Nanoparticle Research*** 17, no. 1 (2015): 1-9.

[7] Ismail, Wan Zakiah Wan, **Deming Liu**, Sandhya Clement, David W. Coutts, Ewa M. Goldys, and Judith M. Dawes. "Spectral and coherence signatures of threshold in random lasers." ***Journal of Optics*** 16, no. 10 (2014): 105008.

[8] Liu, Yujia, Yiqing Lu, Xianlin Zheng, Xavier Vidal, Jiangbo Zhao, **Deming Liu**, Chenshuo Ma,James A. Piper, Peng Xi, Dayong Jin. "Photon-avalanche-induced population inversion allows stimulated emission in single upconversion nanocrystal" (Submitted)

([1] - [5] are closely related to my PhD program)

Conference paper:

[1] **Liu, Deming**, Lixin Zhang, Run Zhang, Ewa Goldys and Dayong Jin, " Shape Control and Shell Growth of Upconversion SuperDots", International Conference of on Nanoscience and Nanotechnology (ICONN), 2014 (Oral)

[2] **Liu, Deming**, Lixin Zhang, Run Zhang, Yiqing Lu, Ewa Goldys and Dayong Jin, "Luminescence Properties of Core-shell Upconversion SuperDots", International Conference of on Nanoscience and Nanotechnology (ICONN), 2014 (Poster)

[3] **Liu, Deming**, Lixin Zhang, Ewa Goldys and Dayong Jin, "$NaYF_4$:Yb,Er@$NaYF_4$ Inert Shell Luminescence Enhancement: The Role of Inert Shell Thickness" The 10th Asia-Pacific Conference on Near-field Optics (APNFO10), 2015 (poster)

[4] Zhang, Lixin, Xianlin Zheng, **Deming Liu**, Yujia Liu, and Dayong Jin. "Biophotonics and Nanophotonics Powered by Upconversion SuperDots". Australian and New Zealand Conference on Optics and Photonics, Western Australia, 2013. (Oral)

[5] Zhang, Lixin, **Deming Liu**, Jiangbo Zhao, Yiqing. Lu, Judith M. Dawes, Ewa Goldys and Dayong Jin "Characterization of Single Upconversion Nanocrystals by a purpose-built nanophotonic platform", 2012 MQ BioFocus Research Centre Conference, Sydney, Australisa. (Poster)

[6] Zhang, Lixin, **Deming Liu**, Jiangbo Zhao, Yiqing. Lu, Judith M. Dawes, Ewa Goldys James Piper Tanya Monro and Dayong Jin "Comprehensive Characterization of Single Upconversion Nanocrystals by Time-resolved 3-D Spectrometry", 20th Australian Institute of Physics Congress 2012.(Poster)

CONTROLLED ENGINEERING of RARE-EARTH DOPED CORE-SHELL NANOCRYSTALS

Abstract:

Controlled engineering of rare-earth doped core-shell nanocrystals to improve the original physical and chemical properties, and to integrate multiple functionalities in one particle with desirable size and shape, promises a huge potential in enabling new nanotechnologies, such as ultra-sensitive bio-sensing, multi-modal biomedical imaging, targeted delivery and release of drugs, high efficiency hybrid catalyst, green energy harvesting, lightening, and 3D volumetric displays.

This thesis focuses on exploring the epitaxial shell growth of nanocrystals as an efficient method for controlled synthesis of rare-earth doped core-shell nanocrystals. I demonstrate that wet-chemical synthesis can be developed as a very promising approach towards the high-yield, low-cost and mass production of a library of new types of heterogeneous nanocrystal in the solution phase. Particularly, I find that much more freedom and flexibility of control shell growth of nanocrystal can be achieved in wet chemical synthesis.

This thesis starts with a comprehensive review of controlled growth of nanomaterials with particular focus on the recent development of rare-earth doped (core-shell) nanomaterials. The thesis has two major parallel projects to investigate techniques to enable the unidirectional synthesis with uniform shells (chapter 2) and directional controlled growth of heterogeneous shells (chapters 3 and 4) respectively.

Chapter 2 reports a simple technique for homogeneous shell growth by adjusting the amount of oleylamine. I extend this technique to study the upconversion emission stability and reversibility at different pH and temperature conditions. By controlled synthesis of the homogeneous core-shell nanocrystals via adjusting the ratio of oleic acid and oleylamine, I find that the intact shells at controlled thickness are useful in fully protecting the core nanocrystal from quenching by the surface ligands and solvent. I demonstrate the passivation effect by the intact shells will not only enhance the luminescence intensity but also improve the emission stability against temperature and pH variations for biomedical applications.

In Chapters 3 and 4, I systemically study the reaction mechanisms of the epitaxial shell growth of rare earth fluoride nanocrystal in wet chemical synthesis. I find that oleate anions (OA^-), as the dissociated form of oleic acid molecules (OAH), have variable, dynamic

roles in mediating the growth of alkaline rare-earth fluoride ($AREF_4$) nanocrystals. I demonstrate that the control over the ratio of OA^- to OAH can be used to directionally inhibit, promote, or etch the crystallographic facets of the nanoparticles. This control enables selective grafting of shells with complex morphologies grown over nanocrystal cores, thus allowing for access to a diverse library of monodisperse sub-50 nm nanoparticles. With such programmable additive and subtractive engineering, the heterogeneous nanocrystals in 3D shapes can be designed and scaled from the bottom-up. Our findings may lead to a new class of multifunctional nanomaterials and provide the first bases for developing previously unforeseen applications of nanoparticles with complex programmable shapes and surface properties.

The results reported in this thesis suggest that using epitaxial shell growth of nanocrystals via wet chemical route, some other heterogeneous nanocrystals may be synthesized based on semiconductor, noble metal and metal oxide nanocrystals, (e.g. Pd@Pt, $Au@Fe_3O_4$, Au@CdS, et. al.) The interesting synthesis mechanisms that direct the epitaxial shell growth of nanocrystals and the combinatory factors that jointly determine the growth direction are the key to unlock a new horizon of nanomaterials science.

The major results (result chapters 2-4) reported here have formed two first-authored manuscripts: 1) "*Emission Stability and Reversibility of Upconversion Nanocrystals*", has published on *Journal of Materials Chemistry C*. 2) "*Three-dimensional controlled growth of monodisperse sub-50 nm heterogeneous nanocrystals*", as a research article including a 61-page supplementary information section, has been published on the prestigious journal *Nature Communications* in 2016; and

Key Words: nanocrystals, core-shell, heterogeneous structure, nanocrystal engineering, $NaYF_4$, rare earth fluorides, lanthanides, upconversion, morphology control, epitaxial shell growth.

Contents

List of Acronyms (in alphabetic order)

CVD	chemical vapor deposition
DFT	density functional theory
EDS	energy-dispersive X-ray spectroscopy
GGA	generalized gradient approximation
NIR	near infrared ray
ODE	1-octadecene
OA	oleic acid
OA^-	oleate anions
OAH	oleic acid molecular
OM	oleylamine
RE	rare earth elements
STEM	scanning transition electron microscopy
TFA	trifluoroacetate
TEM	transition electron microscopy
UV	ultraviolet
UC	upconversion
UCNPs	upconversion nanoparticles
XPS	X-ray photoelectron spectroscopy
XRD	X-ray powder diffraction

Aim and Outline

Thesis aim

The controlled synthesis of heterogeneous structured nanocrystals and hybrid nanomaterials becomes the next grand challenge aiming to integrate many different functionalities and positively enhance each properties within one nanoscale platform. Directional growth controls in epitaxial growth of desirable shells, however does remain a challenge via the wet chemical synthesis route. This thesis thus aims to probe the key mechanisms in shaping both homogeneous and new heterogeneous core-shell nanomaterials and then use this understanding to further develop a robust engineering protocol for scalable and reproducible fabrications of monodisperse multifunctional luminescent nanocrystals. The results of this thesis will indicate that unidirectional, directional growth and etching controls based on rare-earth doped $NaREF_4$ nanocrystals is achievable by the approach of surfactant molecular anisotropic passivating of the nanocrystal different surfaces.

Thesis outline

This thesis consists of one introduction chapter, three result chapters to explore the controlled growth of rare-earth doped (core-shell) nanocrystals, and a conclusion chapter. Result Chapter 2 in the format of a manuscript has been submitted to *ACS Sensors*. Chapter 3 and 4 were developed in parallel to Chapter 2, and the key results were eventually summarized into a major paper recently published in *Nature communications* (the main text article attached to the end of this introduction chapter).

Chapter 2 reports a technique I developed to synthesize $NaYF_4$ nanocrystals with homogeneous shells. I used this technique to synthesize a series of samples with incremental thickness of inert shells to protect the core nanocrystals, and therefore we used these samples to quantitatively study the role of different thickness of shells on enhancing the luminescence intensity, stabilizing their emissions against varied pH and temperature aqueous solution.

In Chapter 3, we systemically studied the impact surfactants on the shell growth of $NaREF_4$ nanocrystals and demonstrated precise engineering of three-dimensional heterogeneous $NaREF_4$ nanocrystals. By adjusting the ratio of oleic acid ions (OA^-) to oleic acid molecules (OAH), we found that the shell growth direction can be well controlled either along longitudinal direction or transversal direction to form nano-rods or nano-plates.

Chapter 4 demonstrated the combinational approaches, including homogeneous shell growth, longitudinal shell growth, transversal shell growth and migration growth, can be further tailored for a highly controlled programmable synthesis of a library of 3D core-shell heterogeneous $NaREF_4$ nanocrystals with distinct shapes.

Finally, Chapter 5 summarizes the key research outcomes of my thesis and discusses the future prospects of core-shell nanocrystal engineering.

Chapter 1: Introduction

The last decade has witnessed major advances made in the control of nanoscale synthesis, characterizations, and nanotechnology, which has led to a range of new nanomaterials engineered with many new properties arising from their homogeneous or heterogeneous composition. This considerable investment in the development of engineered nanomaterials has led to a greater control over their synthesis and their application to biomedical, green energy harvesting, high speed communications, optoelectronics devices, smart phones and environmental pollution controls.

Since the luminescent, magnetic and catalytic properties are highly dependent on the morphology and surface conditions, the scalable, reproducible, controlled synthesis of nanocrystals with desirable size, shape, surface and composites is the key to the optimized performance of these materials. A trial-and-error approach is frequently used to produce nanoparticles with spherical, rod-like or other shapes by varying dopant concentrations and/or constituent materials, reaction time and temperature. This random sampling of a typically vast, multidimensional parameter space, provides the impetus for a rational approach and as well the proper understanding of the underpinning growth mechanisms of the material being developed. These two aspects are the key to efficiently directing the large effort required for the controlled synthesis of future homogeneous and heterogeneous nanocrystals.

In particular, the last decade as seen many successes in the epitaxial shell growth of core-shell heterogeneous nanocrystals with complex nanostructures and multifunctional properties. Epitaxial growth is the formation of a crystal on the face of another crystal substrate. These composite crystal structures are usually well defined and thus have properties that are superior. Already there have been demonstrations of this in the core-shell and in some common heterogeneous structures, such as rods and nanoscale dumbbells in materials such as noble metals, semiconductors and iron oxide nanocrystals. Directional growth controls in epitaxial growth of desirable shells, however does remain a challenge via the wet chemical synthesis route.

This thesis thus aims to probe the key mechanisms in shaping both homogeneous and new heterogeneous core-shell nanomaterials and then use this understanding to further develop a robust engineering protocol for scalable and reproducible fabrications of monodisperse multifunctional luminescent nanocrystals. The results of this thesis will indicate that unidirectional, directional growth and etching controls based on rare-earth doped $NaREF_4$

nanocrystals is achievable by the approach of surfactant molecular anisotropic passivating of the nanocrystal different surfaces.

The structure used to organize the contents of the thesis are illustrated in a flow chart given below. This introductory chapter starts by introducing recent work in advancement in the field of controlled nanocrystal engineering, followed by reviewing the major mechanisms that direct this controlled nanocrystal synthesis. It then provides examples of the many advantages of using rare-earth doped fluorides nanocrystals, which then provides the basis for the formation of the objectives for studying epitaxial shell growth control that were undertaken in the course of this thesis. Finally, this chapter provides a description of the current progress on the field of core-shell nanocrystal synthesis and the known limitations of the current techniques that it uses.

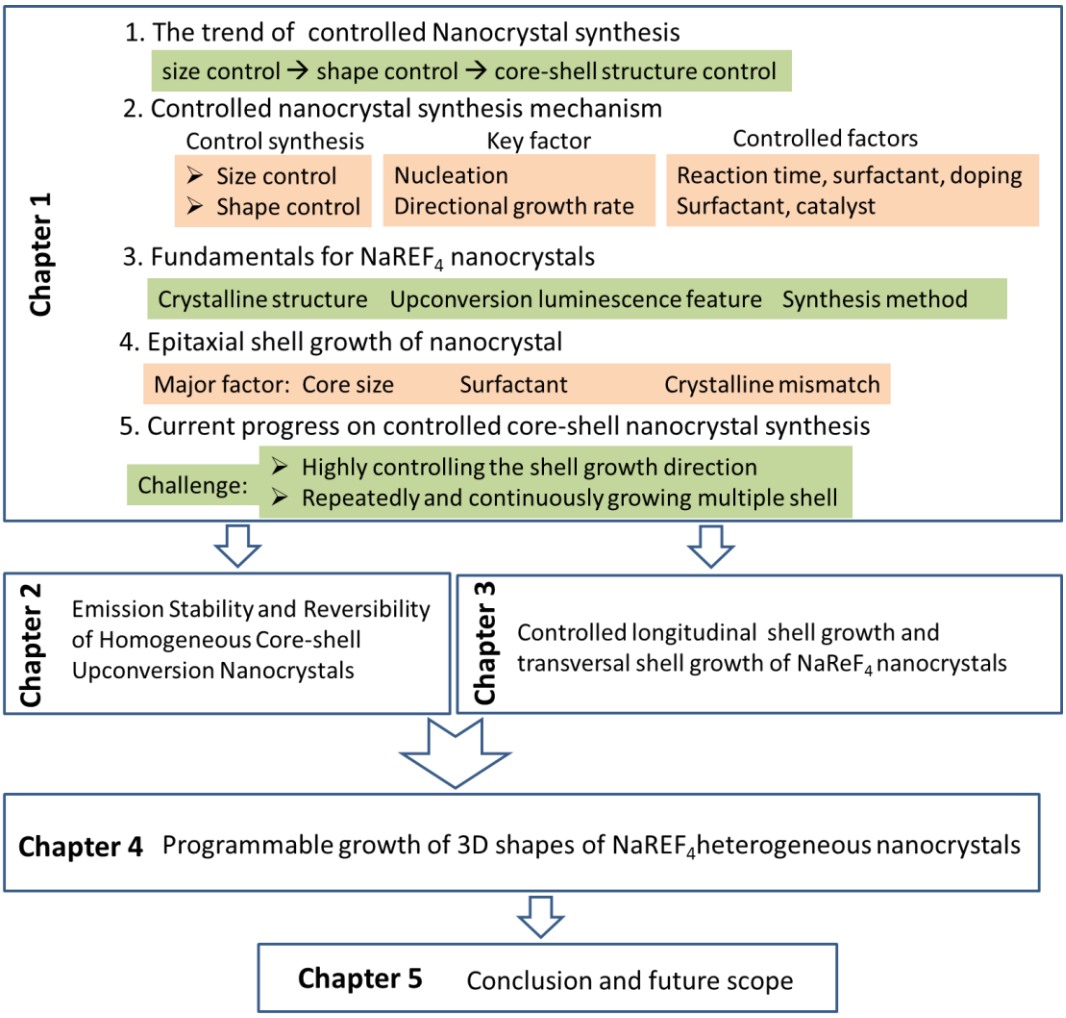

Flow chart outlines the logic structure of this thesis

1.1 The trend of controlled nanocrystal synthesis

1.1.1 Nanocrystal engineering by wet chemical synthesis

Nanocrystal engineering in wet chemical synthesis route is to design and synthesize of nanocrystals with desired size, shape, surface and compositions based on the understanding and exploitation of the nucleation and growth process.[1] There are more and more interesting size-dependent and shape-dependent properties being discovered from the monodisperse nanomaterials. The trend in searching reproducible protocols towards the controlled nanocrystal synthesis becomes obvious, pursued by both fundamental understanding of the nucleation and growth process and demands from a broad range of applications that critically requires the high quality and reliable nanomaterials with outstanding physical and chemical properties.[2]

Many successes have been made in recent years with a range of novel nanocrystals being widely applied in different application areas including bioimaging [3-7], bio-sensing [8-10], catalysis [8-10], photonics [11, 12], electronics [13-18] and photovoltaics [19-25]. Due to the attribute of large amount of investigations made on controlled nanocrystal synthesis, there are many matured protocols available to guide controlled synthesis of uniform core-shell nanoparticles or rods-like non-spherical nanocrystals.

The controlled synthesis of heterogeneous structured nanocrystals and hybrid nanomaterials becomes the next grand challenge aiming to integrate many different functionalities and positively enhance each properties within one nanoscale platform. For example, the hybrid nanocrystals are in high demands to realize multi-modality sensing, imaging, diagnostics, and localized targeted therapies of diseases, following the new concept of “theranostics” for the synergistic diagnosis and therapy of diseases [26-29]. To realize such degree of controls, the epitaxial growth of new materials along a desirable direction remains highly challenging in materials science. This requires thorough investigations on the anisotropic crystalline facets, their interactions with the growth environments, and systematic experimental designs and characterizations. There remain a lot of new synthesis methods to be discovered before the fully controlled synthesis of a range of new heterogeneous and hybrid nanocrystals become possible. The deeper explorations of new mechanisms, methods and materials properties around the anisotropic nanocrystals via epitaxial growth of foreign shell materials will further advance the field of nanocrystal engineering and broadly the development of nanoscience and nanotechnology.

1.1.2 Size-dependent properties of nanocrystals

Many size-dependent phenomena have been discovered in a wide range of nanocrystals including noble metal [30-32], semiconductor [33-35], metal oxide [36] and rare earth fluorides [37-39]. The size dependent effect is first primarily caused by the fast increased surface-area-to-volume ratio. [40, 41] When the size of crystals decreases from buck to nanoscale, the largely increased exposure of surface increases exponentially to introduce more interactions between the nanocrystal surface and its surrounding environments, which makes the physical and chemical properties of nanocrystal more size sensitive [42-46]. The properties, such as luminescence intensity, luminescence lifetime, electrics, magnetics and catalysis, can be highly influenced by the size change in nanoscale. The size-dependent effect to some nanocrystals introduces many advantages.

- The fine tunable luminescence from blue emission to red emission in quantum dots can be simply achieved by increasing the semiconductor nanocrystals' size;
- The reactivity and catalytic property in metal alloys can be enhanced by reducing the metal nanocrystals' size;
- The colors of noble metal colloids can be fine-tuned as a result of different absorption and scattering of light by adjusting the noble metal nanocrystals size;
- Changeable superparamagnetic property in the iron oxide magnetic nanocrystals can be also controlled when the size is below 20 nm.

We illustrate below these interesting size-dependent phenomena by focusing on luminescence and magnetic materials.

Size-dependent properties of quantum dots and doped luminescent nanocrystals

When the size of semiconductor nanocrystals is down to several nanometers, they exhibit a strong quantum size effect. When the size of semiconductor nanocrystals is smaller than the Bohr exciton radius in at least one dimension, the crystal will never maintain its continuous band structure and the densities of electronic states of the nanocrystal will no longer be continuous. Illustrated in Figure 1.1.1, the bandgaps of semiconductor quantum dots can be fine-tuned simply by controlling their size and shape, without changing chemical compositions. The adjustable band structures via accurately controlled growth of different size nanocrystals also induce novel and tunable electrical and optical properties, leading to many new technology applications, such as light emitting devices[47-49], displays[50], biological probes[51, 52], solar cells[53-55], etc.

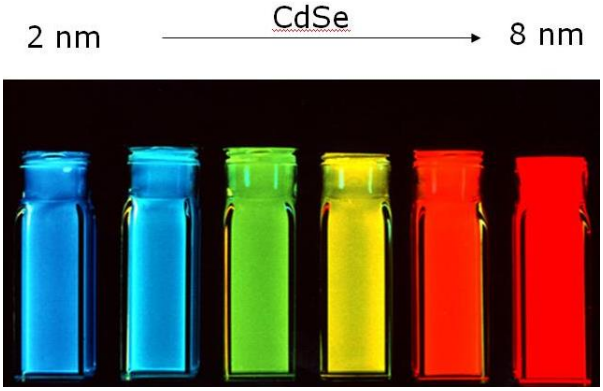

Figure 1.1.1 Size –dependent emission property of fluorescence CdSe quantum dots. The smaller dots emit higher energy shorter wavelength emissions. Reprint from the reference [56]

Different from semiconductor quantum dots, the size of a range of doped luminescent nanoparticles does not determine its emission properties as the host material is normally an insulator, but as mentioned above the decrease in size causes increase in surface to volume ratio and the size of doped nanoparticles will influence its intrinsic emissions. For example, upconversion nanocrystals (UCNPs) also display a size-dependent luminescent property due to the increased activities of surface phonons that quenches the luminescence emissions. Generally, the emission intensity and their luminescence lifetimes of UCNPs drop when the size decreases. Figure 1.1.2 illustrates that decreasing size of $NaYF_4$: Yb^{3+},Er^{3+} nanocrystals from 45 nm to 6 nm will shorten the luminescence lifetimes and increase the red-to-green luminescence intensity ratio [10].

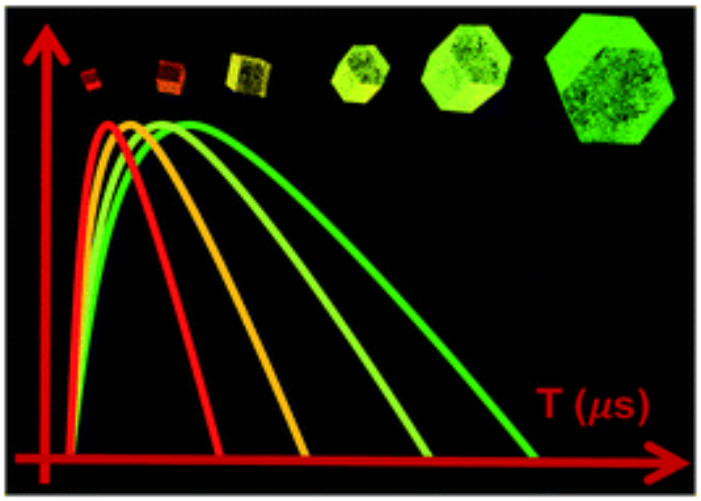

Figure 1.1.2 Size –dependent luminescence property of luminescence $NaYF_4$: Yb^{3+},Er^{3+} nanocrystals. The smaller nanocrystals have shorter luminescent lifetime and emit more red emissions than green. Reprint from reference [10].

Size-dependent properties of superparamagnetic nanocrystals and Gd^{3+} doped nanocrystals

Superparamagnetism phenomenon appears in the ferromagnetic or ferrimagnetic nanocrystals when their sizes are smaller than 20 nm. (Figure 1.1.3) Within this size range, magnetization can randomly flip direction under the influence of temperature and their overall magnetization appears to be in average zero. In this superparamagnetic state, an external magnetic field is able to magnetize the nanoparticles, similarly to a paramagnet. Superparamagnetic nanocrystals are not subject to strong magnetic interactions in dispersion, which is why they are very promising for a range of biomedical applications, such as imaging contrast agents in Magnetic Resonance Imaging (MRI), magnetic separation of cells and biomolecules, targeted drug delivery, and magnetic hyperthermia.

Moreover, there are other size-dependent magnetic properties observed in magnetic nanocrystals. With the size reduce, the saturation magnetization of magnetic nanocrystals will drop quickly. [57] (Figure 1.1.3) Chen and his co-workers also reported the saturation magnetization of iron oxide magnetic nanocrystals decreased with decreasing size in proportion to the specific surface area of the nanocrystals[58]. To achieve superparamagnetic nanocrystals with high saturation magnetization, their size were often controlled in the range of 11nm to 20 nm. [59, 60]

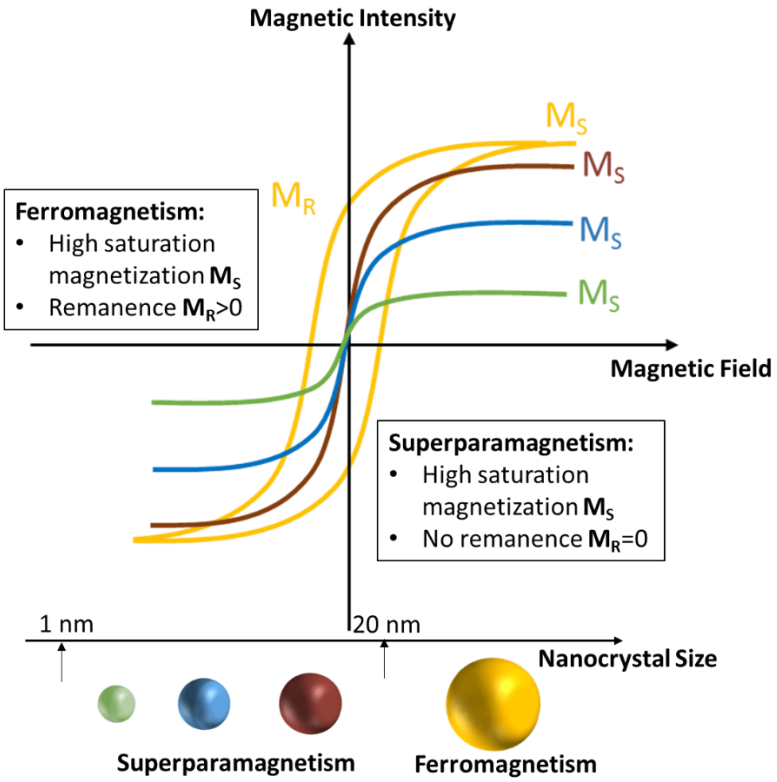

Figure 1.1.3 Scheme of size-dependent superparamagnetism of ferromagnetism nanocrystals. The Hysteresis loops of different sized superparamagnetic and ferromagnetic nanocrystals.

Furthermore, paramagnetic Gd^{3+} doped upconversion nanocrystals are another kind of attractive optical-magnetic imaging contrast agents. With the advanced synthesis techniques available and the booming area of upconversion nanotechnology, this kind of nanoparticles becomes a highly promising nanoplatform with multi-functionality for multi-modality imaging, diagnostics and targeted delivery of nanomedicine, the concept of "theronostics". Compared with traditional gadolinium chelates (complex) that are commonly used as the MRI contrast agents, doping Gd^{3+} ions into the crystalline lattice of $NaREF_4$ not only results in an extremely high Gd^{3+} payload (over 10^4, depending on $NaGdF_4$ thickness) but also facilitates a rigid binding of the lanthanide ions. This kind of nanoparticles may reduce the potential risk of toxic ion-leaching in vivo, and provide super resolution to achieve MR cellular imaging.

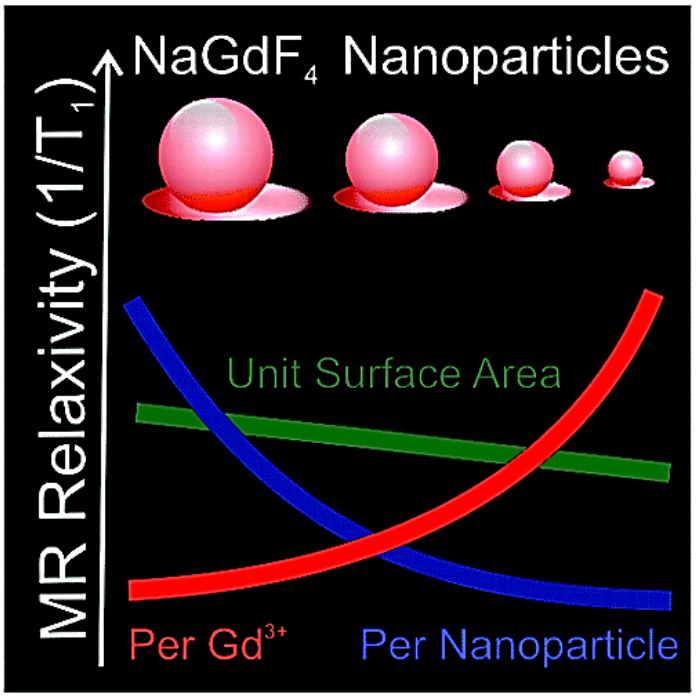

Figure 1.1.4 Size dependent magnetic property: scheme of the MR relaxivity of $NaGdF_4$ change with the size decrease. Size reducing results in the decrease of unit surface area and MR relaxivity of single nanoparticle, but promotes the increase of the MR relaxivity of each Gd^{3+} increased. Reprint from the reference [58].

The size of Gd^{3+} doped UCNPs also highly influences their magnetic performance. In 2011, Shi and his coworkers demonstrated that only Gd^{3+} ions on the surface within the ultrathin $NaGdF_4$ layer are responsible for shortening the T_1-relaxation time of water protons and an optimal $NaGdF_4$ thickness of 1 nm has been suggested for achieving a balanced

performance of both UCL and MR modalities [61], which suggest that the smaller size of $NaGdF_4$ with larger surface area will enhance MRI signal by shortening the T_1 relaxation time of water proton. In the same year, Johnson and his coworkers presented that the water proton T_1 relaxation rate with $NaGdF_4$ nanocrystals can be effective shortened by reducing the size from 8.0 nm to 2.5 nm, with the smallest 2.5-nm nanocrystals showing higher relaxivities, compared to clinical Gd^{3+} complexes [62] (see Figure 1.1.4).

Tuning the nanocrystals' size will lead to positively or negatively influences on their physical properties. The Gd^{3+} doped UCNPs here serve as a good example: although the smaller one can has the better T_1 relaxation, their weak luminescence will limit their overall performance. Therefore controlling nanocrystals' size in a suitable range is necessary to balance these properties towards a better performance. The luminescence intensity of UCNPs will be quenched by increasing the surface to volume ratio, while the magnetic properties of UCNPs prefer smaller sizes. This suggests design of core-shell nanoparticles with consideration of the morphology, size and composition of ions as an essential requirement for the controlled nanomaterials engineering.

1.1.3 Shape-dependent properties of nanocrystals

At nanoscale, the shape of nanocrystals formed follows the rule of the minimum surface energy during its growth phase. This however is not the only determinate. The shape of certain nanocrystals can be varied with changes to its crystalline structure and synthesis condition. Different shapes of nanocrystals cause difference to the distribution of the charge present on its and differences in its surface-to-volume ratio, and therefore these changes can affect the performance of nanocrystals. For example, catalyst materials prefer a high surface-to-volume ratio. If the particles are star and flower-like shapes in shape, this can led to improvements in performance [63-66]. Luminescence materials prefer low surface-to-volume ratio, and so spherical or cubic shaped particles normally deliver a higher intensity [67]. The shape is also an important factor for magnetic nanocrystals. Qing Song and his coworkers reported synthesizing a library of high-quality and monodisperse spinel cobalt ferrite, $CoFe_2O_4$, nanocrystals with highly controllable spherical or cubic shapes. They observed that the shape of the nanocrystals was a dominating factor for its coercivity because of the effect of surface anisotropy [68]. The shape also affects the localized surface plasmon property in noble metal nanocrystals [69]. Figure 1.1.5 shows that the light scattering peaks and dark-field scattering colors are also tunable when the shape of the gold nanocrystals was changed. The plasmon bands of Ag nanocrystals were able to span the visible spectrum and into the infrared region by changes to the shape of Ag nanocrystals via an etching method [70].

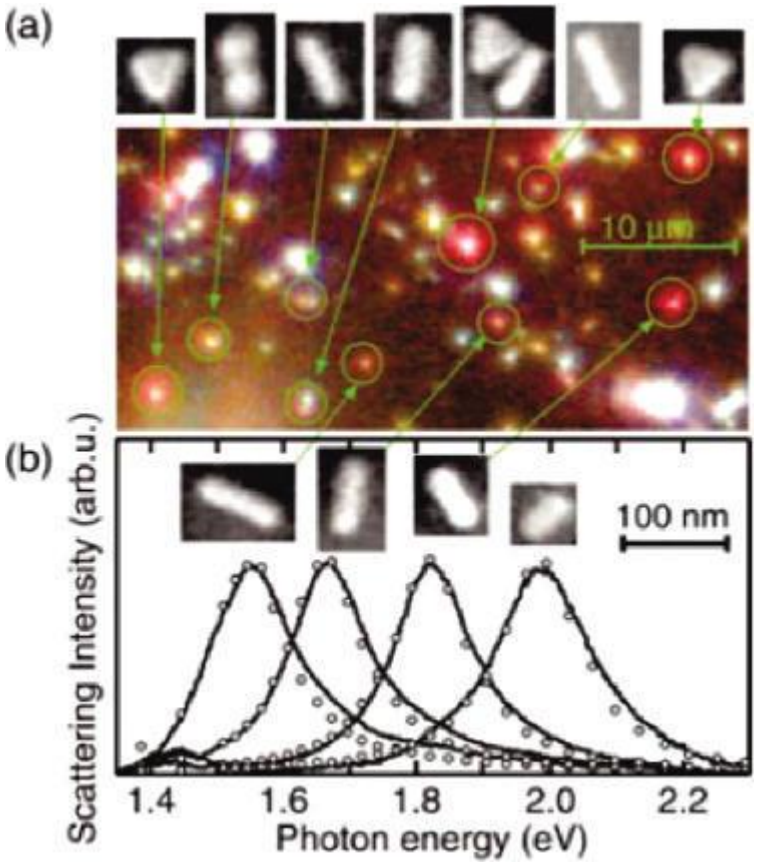

Figure 1.1.5 (a) Dark-field microscopy image and corresponding SEM images and (b) light scattering spectra of Au nanocrystals of different shapes. The scattering peaks do red-shift with increasing the aspect ratio Reprinted from the reference [69]

These examples above show the significant role of nanocrystal engineering the shape of the crystals is necessary for the optimization of their performance. Compared to the techniques needed to engineer precise size controls, the controlled synthesis of desirable shapes of nanocrystals requires a higher level of understanding of the growth mechanisms and fine-tuning of growth protocols and is the main focus of this thesis.

1.1.4 Multifunctional properties of Core-shell nanocrystals

Beyond the controls over the size and shape of nanocrystals, controlled synthesis of core-shell nanoscale architectures has become the current research focus for the engineering of nanomaterials. The ability to manipulate the compositions of colloidal nanocrystals by epitaxial growth of closely lattice matched material(s) has been widely exploited to fabricate core–shell and hetero-generous structures that are tailored for particular nanomaterial applications [71]. This allows integration and optimization of many advanced physical or

chemical properties into one single unit on a multifunctional nanocrystals platform (shown in Figure 1.1.6). The most popular integrations reported so far include the above-mentioned optical and magnetic properties of rare-earth doped $NaGdF_4$ upconversion nanocrystals, the thermal and magnetic properties of Fe_3O_4 nanocrystals, the catalytic and optical properties of novel metal nanocrystals, and the thermal and plasmonic properties of noble metal nanocrystals.

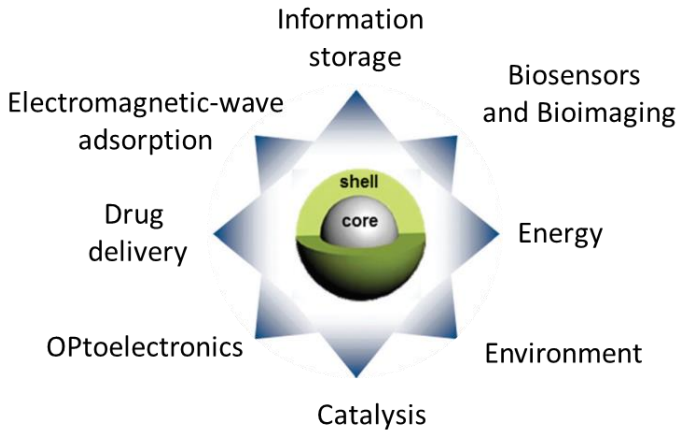

Figure 1.1.6 Applications of core-shell nanocrystals in various areas of modern technology. Reprint from reference [72].

Ideally, these attractive multifunctional particles and the selection of their properties should be able to be synthesized just by selecting different materials and combining them together, but there are two outstanding obstacles to this: (1) the interactions between different compositions can introduce a negative effect on each other with the introduction of either counteracting the expected outcome of the other, and (2) the synthesis routes for different materials are often not compatible and therefore the controlled synthesis becomes highly challenging. As an example, the emission enhancement effect of a gold nanocrystal to a luminescent nanocrystal is highly dependent on the distance between them, iron oxide magnetic nanocrystals are known to quench the luminescence and fluorescence nanocrystals, and the energy transfer effects within the luminescence materials are highly dependent on the positions and distance of sensitizers, bridge spacer and photon activators. A possible solution to this conundrum is to precisely control the growth of one nanocrystals structure onto the desired position of the substrate host material and it is this key solution to maximizing the positive interactions and minimizing the negative effects that is one of the prime objectives of this thesis: To maximize the positive interaction and minimize the negative interaction, controlling the combination structure of the compositions is essential.

To achieve such a level of control, both of the core-shell and heterogeneous structures there is a lot of research that focuses on compatible integration of two or more functions in one single nanostructure. While the core-shell structure can be used to spatially isolate the core luminescent materials from the surrounding (e.g., solvents and surface ligands) to minimize quenching and significantly enhance their luminescent intensity, the heterogeneous structure is useful to spatially separate each the composites within each particle and to reduce the negative interactions of these different materials. Furthermore, the size and shape of each part of materials will also influence the overall property when building the sophisticated system of core-shell or heterogeneous nanostructures, which is another important factor to be taken into the consideration when to design and optimize the multifunctional nanocrystals.

1.1.5 Brief conclusion

The size, shape and composition of nanocrystals can highly effect their physical and chemical properties and the eventual desired performance of nanocrystals. The ability of precisely controlling the growth of nanocrystals according to the desirable designs is the key technical challenge for optimizing nanocrystals' properties so that they can be tailored to meet the specific requirements of a particular application. The size and shape control of different kinds of nanocrystal is necessary and the basis of effective nanocrystals engineering, while the composition control of core-shell and heterogeneous structured nanocrystals via epitaxial shell growth is the current focus of research in the field of nanocrystals engineering.

1.2 Current controlled nanocrystal synthesis mechanism

Understanding the formation mechanisms during the nanocrystals growth is the key to realize the high levels of controls over the size, shape and composition of nanocrystals. In wet chemical synthesis system, the formation process of nanocrystal generally includes two steps: homogeneous nucleation and heterogeneous crystal growth. Controlling the nucleation rate and reaction time are the key factors to control the size of nanocrystals, while differentiating the directional growth rates on different facets of the nanocrystals is essential to achieve the final shape of nanocrystals, as shown in Figure 1.2.1. In this section, we will introduce homogeneous nucleation and crystal growth, the two key processes, and to identify opportunities to realize nanocrystal morphology controls.

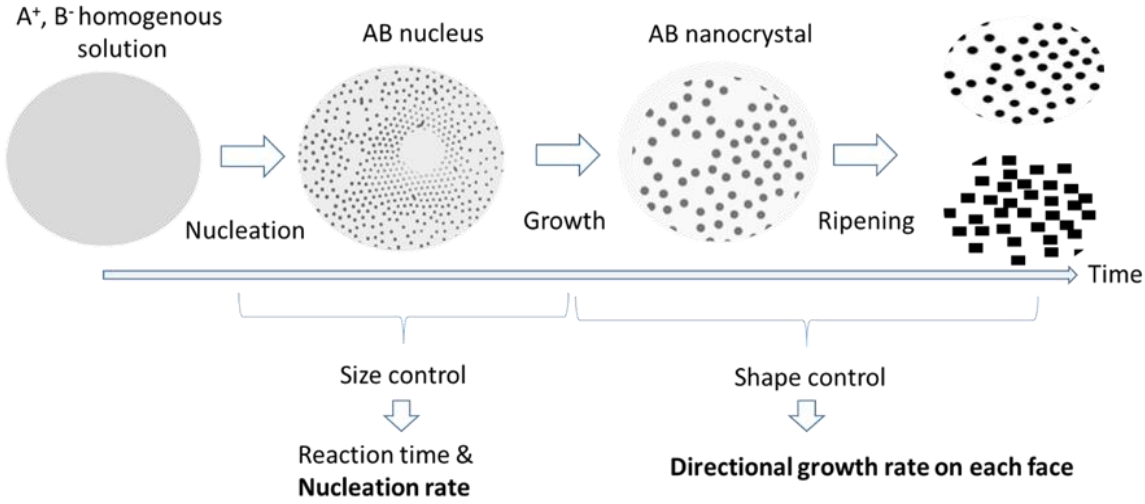

Figure 1.2.1 Scheme of controlled nanocrystal synthesis process in a wet chemical synthesis system.

1.2.1 Homogeneous nucleation

Nucleation is the process whereby nuclei (seeds) act as templates for crystal growth. Primary nucleation or Homogeneous nucleation, defined by Mullin [73], describes the case of nucleation without the presence of other crystalline matters, broadly suitable for interpreting the nucleation process for many chemical syntheses. The homogeneous nucleation of nanocrystal synthesis is a similar process with salt precipitation in principle. When the concentration of a solute in a solvent exceeds its equilibrium solubility, a new solid phase appears and the overall Gibbs free energy of a supersaturated solution gets reduced. The process of nanocrystals nucleation is more complicated than the salt precipitation process involving interactions between the mixture of solvent, surfactant and precursor molecule at a certain temperature range. To study the mechanism, certain conditions are applied to build a model based on the thermodynamics and statistical physics, but all follow the same principle as the case of salt

precipitation from a supersaturated solution: the high overall Gibbs free energy from a solution with solute exceeding the solubility would be reduced by segregating solute from the solution, before maintaining an equilibrium concentration in the solution. The reduction of overall Gibbs free energy is the driving force for both nucleation and growth of nanocrystals. When the temperature is fixed, the change of Gibbs free energy per unit volume of the solid phase, $\Delta G_{v,}$ is dependent on the concentration of the solute:

$$\Delta G_v = - kT/\Omega \ln(C/C_o) \quad (1.1)$$

Where C is the concentration of the solute, C is the equilibrium concentration or solubility, Ω is the atomic volume. With $C \leq C_o$, ΔG_v is zero or positive, and no nucleation would occur. With $C > C_o$, ΔG_v is negative and nucleation occurs spontaneously.

Assuming a spherical nucleus with a radius of r is formed, the change of Gibbs free energy or volume energy, $\Delta\mu_v$, can be described by:

$$\Delta\mu_v = (4/3)\pi r^3 \Delta G_v \quad (1.2)$$

However, this energy reduction is counter balanced by the introduction of surface energy, which accompanied with the formation of new solid phase (nucleation). This results in an increase in the surface energy, $\Delta\mu_s$, of the system:

$$\Delta\mu_s = 4\pi r^2 \gamma \quad (1.3)$$

Where γ is the surface energy per unit area. The total change of chemical potential for the formation of the nucleus, ΔG, is given by:

$$\Delta G = \Delta\mu_s + \Delta\mu_v = 4\pi r^2 \gamma + (4/3)\pi r^3 \Delta G_v \quad (1.4)$$

From the figure 1.2.2, we can easily see that the newly formed nucleus is stable only when its radius exceeds a critical size, r*. A nucleus smaller than r* will dissolve into the solution to reduce the overall free energy, whereas a nucleus larger than r* is stable and continues to grow bigger. At the critical size $r = r^*$, $d\Delta G/dr = 0$ and the critical size, r*, and critical energy, ΔG^*, are defined by:

$$r^* = -2\gamma/\Delta G_v \quad (1.5)$$

$$\Delta G^* = 16\pi\gamma/3(\Delta G_v)^2 \quad (1.6)$$

ΔG* is the energy barrier that a nucleation process must overcome and r* represents the minimum size of a stable spherical nucleus.

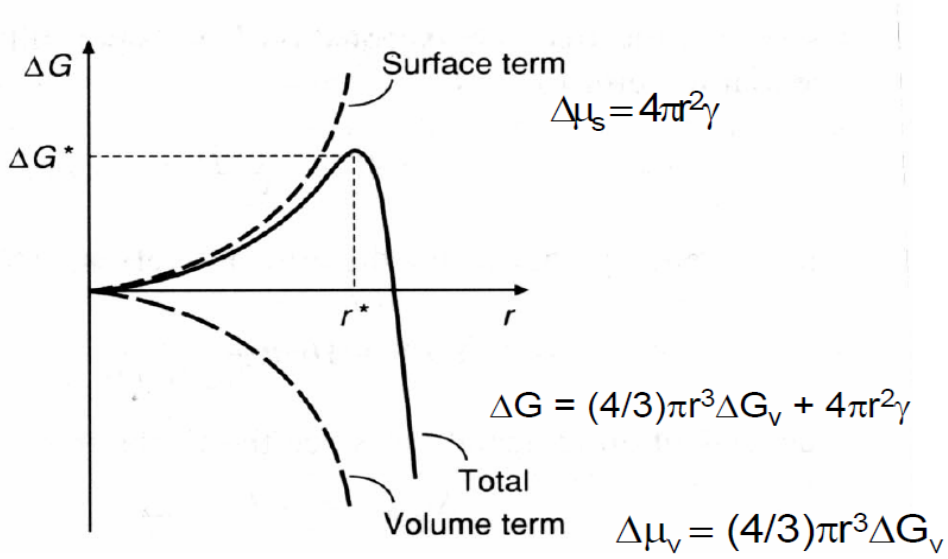

Figure 1.2.2 schematically shows the change of volume free energy, $\Delta\mu_v$, surface free energy, $\Delta\mu_s$, and total free energy, ΔG, as functions of nucleus' radius. Reprint from reference [74].

In the synthesis of nanocrystals by nucleation from supersaturation solution, the size of nanocrystals can be controlled via adjusting the number of nuclei or nucleation rates. The more nuclei or the faster nucleation rate, the size of nanocrystals will be smaller. From the Figure 1.2.2 and equations1.4-1.6, we can summarize that this critical size r* represents the limit how small nanocrystals can be synthesized. Smaller r*, and lower ΔG* lead to the higher rate of nucleation and the smaller size of nanocrystals. To reduce free energy and the critical size, one needs to reduce the surface energy of the new phase, γ, and increase the change of Gibbs free energy, ΔGv. Equation 1.1 indicates that ΔGv can be significantly increased by increasing concentration C, for a given system. ΔGv can also be changed by temperature that influences surface energy. Surface energy of the solid nucleus will change more significantly near the roughening temperature. Other possibilities to control the nanocrystal's size include: (1) use of different solvent, (2) additives in solution, and (3) applying dopants into solid phase, when other requirements are not compromised.

1.2.2 Nanocrystal growth process

Following the nucleation process, the subsequent growth process of the nuclei is essential to the size distribution and final shape of nanocrystals. The nuclei growth process combines several major steps, including generation of growth species, diffusion of the growth, surface growth through irreversible incorporation of growth species onto the solid surface [74].

These steps can be further grouped into two processes: (1) the monomer's diffusion to the surface and (2) the surface reaction. Supplying the growth species to the nanocrystal surface is termed as diffusion that includes the generation, diffusion, and adsorption of growth species onto the growth surface, whereas incorporation of growth species adsorbed on the growth surface into solid structure belongs to growth process. The diffusion of monomers is closely related to the size distribution of nanocrystals, while the anisotropic surface reactions determine the shape of the nanocrystals.

Growth controlled by diffusion

When the concentration of growth species reduces below the minimum concentration for nucleation, nucleation stops, whereas the growth continues. If the growth process is controlled by the diffusion of growth species from the bulk solution to the particle surface, the growth rate is given by:

$$\delta r/\delta t = D(C-Cs)\ \Omega /r \qquad (1.7)$$

Where D is the diffusion coefficient of the growth species, r is the radius of spherical nucleus, C is the bulk concentration, Cs is the concentration on the surface of solid nanocrystals, and Ω is the molar volume of the nuclei. By solving this differential equation and assuming the initial size of nucleus, r_o, and the change of bulk concentration negligible, we have:

$$r^2 = 2\ D(C-Cs)\ \Omega\ t + r_o^2 \qquad (1.8)$$

or

$$r^2 = kDt + r_o^2 \qquad (1.9)$$

where $kD = 2D(C-Cs)Vm$. For two nanocrystals with initial radius difference, δr_o, the radius difference, δr, decreases as time increases or nanocrystals grow bigger, according to:

$$\delta r = r_o\ \delta r_o/r \qquad (1.10)$$

Combining with equation 1.9, we have:

$$\delta r = r_o\ \delta r_o\ /(kDt + r_o^2)1/2 \qquad (1.11)$$

Both equations 1.10 and 1.11 indicate that the radius difference decreases with an increase of nuclear radius and prolonged growth time. The diffusion-controlled growth promotes the formation of uniformly size nanocrystals.

Growth controlled by surface process

When the diffusion of growth species from the bulk to the growth surface is sufficiently rapid, i.e., the concentration on the surface is the same as that in the bulk and the crystal growth rate is controlled by the surface process. There are two mechanisms for the surface processes: mononuclear growth and poly-nuclear growth. For the mononuclear growth, the growth proceeds in a layer-by-layer process; the growth species are incorporated into one layer and proceeds to another layer after the growth of the previous layer is completed.

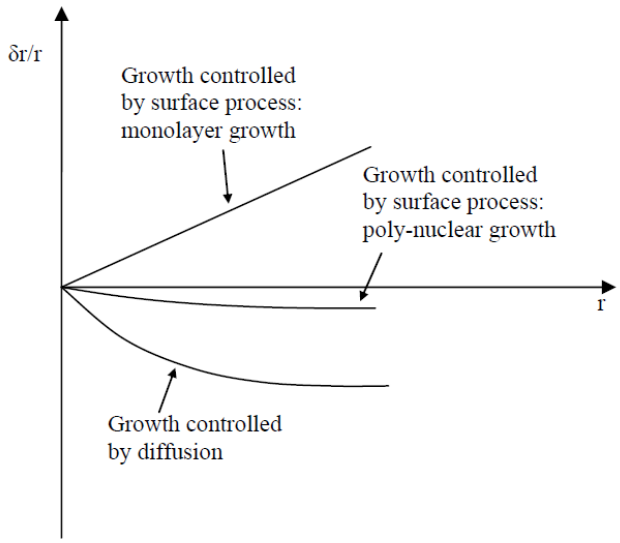

Figure 1.2.3 Description of growth controlled by surface processes

There is a sufficient time for the growth species to diffuse on the surface. The growth rate is thus proportional to the surface area:

$$\delta r/\delta t = k_m(C)\, r^2 \qquad (1.12)$$

Where $k_m(C)$ is a proportionality constant, dependent on the concentration of growth species. The growth rate is given by solving the above equation:

$$1/r = 1/r_o - k_m t \qquad (1.13)$$

The radius difference increases with an increasing radius of the nuclei:

$$\delta r = r^2 \delta r_o / r_o^2 \qquad (1.14)$$

Substituting equation 1.13 into 1.14 yields:

$$\delta r = \delta r_o /(1 - k_m r_o t)^2 \qquad (1.15)$$

Where $k_m t r_o < 1$. This boundary condition is derived from equation 1.13, and means that the radius if the nucleus is not infinite large, i.e., $r < \infty$. Equation 1.15 shows that the radius difference increases with a prolonged growth time. Obviously, this growth mechanism does not favor the synthesis of monosized nanocrystals.

During poly-nuclear growth, which occurs when the surface concentration is very high, surface process is so fast that second layer growth proceeds before the first layer growth is complete. The growth rate of nanocrystals is independent of particle size or time, i.e., the growth rate is constant:

$$\delta r/\delta t = k_p \tag{1.16}$$

Where k_p is a constant only dependent on temperature. Hence the nanocrystals grow linearly with time:

$$r = k_p t + r_o \tag{1.17}$$

The relative radius difference remains constant regardless the growth time and the absolute particle size:

$$\delta r = \delta r_o \tag{1.18}$$

It is worth noting that the relative radius difference would inversely proportional to the particle radius and the growth time, though the absolute radius difference keeps as the same. As nanocrystals grow bigger, the radius difference become smaller; therefore, we can conclude that this growth mechanism also favors the synthesis of monosized nanocrystals. Figure 1.2.3 schematically illustrates the radius difference as functions of crystal size and growth time for the three mechanisms of subsequent crystal growth discussed above. It is obvious that a diffusion controlled growth mechanism is required for the synthesis of monosized nanocrystals by the homogeneous nucleation. Williams suggested that the growth of nanocrystals included the three mechanisms. Monolayer growth mechanism may dominate, when the nuclei are small, while poly-nuclear growth may become predominant when the nuclei size is increased. The diffusion process is predominant for the growth of relatively larger nanocrystals, when there are no other procedures or measures applied to prevent certain growth mechanisms. When favorable growth conditions are established, some growth mechanisms can become predominant. For instances, when the supply of growth species is very slow due the low concentration of precursors or a slow chemical reaction, the growth rate of nuclei would most likely be predominant by the diffusion-controlled process. For the formation of monosized nanocrystals, diffusion-limited growth is required. There are several options to build the diffusion-limited growth. For example, keeping

the concentration of growth species extremely low, diffusion distance would be very large, which may result in diffusion becoming the limiting step. Also, increasing the viscosity of solution is another option. Using surfactants as a barrier layer on the surface of a growing crystal is yet another approach. Controlled the concentration of precursors is another method to control the growth process. Controlling the concentration of by-product, reactant, and catalyst is another method to adjust the reaction rate, when growth species are generated through chemical reactions.

1.2.3 Brief conclusion

The nanostructure of nanocrystals is determined by the reaction parameters through the processes from nucleation to growth. The key to the size control of nanocrystals lies in the nucleation rate and growth time of nanocrystals. The other factors, including surfactants, precursor concentration and temperature, will influence the nucleation rate and can be used to adjust the nanocrystals size. The key to the shape control of nanocrystals lies in the differential growth rates along the desired directions compared with the other directions on different crystal facets. This suggests that the factors, including surfactant, precursor concentration ratio, reaction temperature and catalyst, may play different roles in the crystal formation on different crystal facets, and therefore can be used to control the shape of nanocrystals. Many pioneering works frequently reported the control synthesis of nanocrystals through the control over the surfactant[75-77], precursor concentration[78], temperature[68, 79] and catalyst[78]. The following section focuses on the literature review on many reported experimental results towards the controlled synthesis of a variety of nanocrystals, which provides insightful guidance to the works presented by this thesis.

1.3 Fundamentals for $NaREF_4$ nanocrystals

$NaREF_4$ (RE = rare earth elements) series of nanocrystals, with unique luminescent, paramagnetic and piezoelectric properties have drawn many attentions due to their broad applications in biomedical assays, solid-state lasers, three-dimensional volumetric displays, green energy harvesting and near infrared biomedical imaging using low intensity laser illumination. Particularly, $NaREF_4$ nanocrystals (e.g. $NaYF_4$, $NaGdF_4$ or $NaLuF_4$ as host), once doped with rare earth ions to form a network of photon sensitizers (e.g. Yb^{3+} or Nd^{3+} ions) and emission activators (e.g. Tm^{3+}, Er^{3+} or Ho^{3+} ions), will emit upconversion luminescence, an unique capability to covert low energy infrared light into higher energy emissions in visible and UV range. The last decade has witnessed a major development in demonstrating the upconversion nanoparticles (UCNPs) as a new generation of phosphor probes for bio-imaging and bio-sensing applications, since exciting UCNPs at longer wavelength light in NIR region will permit better penetration of light into the deep tissue, and detection of the anti-stocks' emission at shorter-wavelength can easily avoid auto-fluorescence background. UCNPs are also photo-stabile without photo-bleaching and photo-blinking issues and low-toxic suitable long-term in vivo imaging applications. These potential applications have attracted many research efforts made on controlled synthesis of monodisperse $NaREF_4$ nanocrystals for the past decade.

In this section, we will introduce the basic crystallography knowledge of $NaREF_4$ family nanocrystals, and summarize the current synthesis methods to realize the size and shape controls.

1.3.1 Rare earth elements

The rare-earth elements are a group of 17 metal elementals which comprise the lanthanide series of elements (lanthanum (La) - lutetium (Lu)), in addition to scandium (Sc) and yttrium (Y), which show similar physical and chemical properties to the lanthanides. As shown in Table 1.3.1, except Sc^{3+}, the ionic radius of other RE^{3+} ions are similar in size, in the small range from 0.861 Å to 1.045 Å. This leads to rare earth compounds usually owning similar crystalline structure and chemical properties. Due to this reason, lanthanides ions can be easily doped into rare earth family compounds with generating fewer amounts of internal defects.

Table 1.3.1 Number of 4f electrons and unpaired 4f electrons and ionic radius for the RE^{3+} ion

Rare-earth element	Number of 4f electrons	Number of unpaired 4f electrons	Ionic radius for the R3+ ion (Å)
La	0	0	1.045
Ce	1	1	1.01
Pr	2	2	0.997
Nd	3	3	0.983
Pm	4	4	0.97
Sm	5	5	0.958
Eu	6	6	0.947
Gd	7	7	0.938
Tb	8	6	0.923
Dy	9	5	0.912
Ho	10	4	0.901
Er	11	3	0.890
Tm	12	2	0.880
Yb	13	1	0.868
Lu	14	0	0.861
Sc	0	0	0.745
Y	0	0	0.900

1.3.2 Cubic and hexagonal phase crystal structure of $NaREF_4$

In crystallography, crystalline structure is a unique arrangement of atoms, ions or molecules in a crystalline liquid or solid [81]. Varied crystal structure with different crystal fields will bring significant differences in the chemical and physical property of nanocrystals. Therefore, understanding the different crystal structures is necessary for systemically studying their synthesis mechanism and their properties.

$NaREF_4$ series of nanocrystals have two major types of crystalline structures: cubic phase (α) and hexagonal phase (β). The cation distributions in the two crystalline structures are totally different. In α-$NaREF_4$, Na^+ and RE^{3+} cations are randomly distributed in the cationic sub-lattice, while β-$NaREF_4$ has three cation sites: a one-fold site occupied by RE^{3+}, a one-fold site 50% occupied by Na^+ and 50% by RE^{3+}, and the other two-fold sites are occupied randomly by Na^+ and vacancies.[82] Figure 1.3.1 shows the unit cells of α-$NaREF_4$ and β-$NaREF_4$ crystals. β-$NaREF_4$ is in an anisotropic crystal structure, in which (100) $(1\bar{1}0)$ (010) and (001) faces have lower surface energy than other facets. Therefore, hexagonal prism

and hexagonal disk are the typical shapes of β-$NaREF_4$ nanocrystals (size above 40 nm), while α-$NaREF_4$ nanocrystals are usually in cube and sphere isotropic crystal structure. Their difference in crystal structures results in different performance in upconversion luminescence, for example, the lanthanides doped β-$NaYF_4$ UCNPs generally are ten times higher than the α-$NaYF_4$ UCNPs.

However, synthesizing pure mono-dispersed β-$NaYF_4$ nanocrystals is usually more difficult, because α-$NaYF_4$ nanocrystals, with a lower forming energy than β-$NaYF_4$ nanocrystals, will nucleate earlier as a temporary product. To transfer the α-$NaYF_4$ nanocrystals to β-$NaYF_4$ nanocrystals, α-$NaYF_4$ nanocrystals have to overcome an energy barrier. Usually methods, including increasing reaction temperature, growing reaction pressure, and extending reaction time, have been used to transfer the crystal phase from α-$NaYF_4$ to β-$NaYF_4$, but these methods will result in side effects, such as particle aggregation, increase in the crystal size from sub 10 nm to tens of nanometers. Therefore, many efforts have been made by identifying an appropriate reaction temperature, introducing doping larger radius rare-earth ions (e.g. Gd^{3+}, Sm^{3+}, Eu^{3+}) [83], applying co-surfactants (e.g. oleylamine and oleic acid) [84, 85], and post heat treatment [86], for synthesizing pure mono-disperse β-$NaYF_4$ nanocrystals.

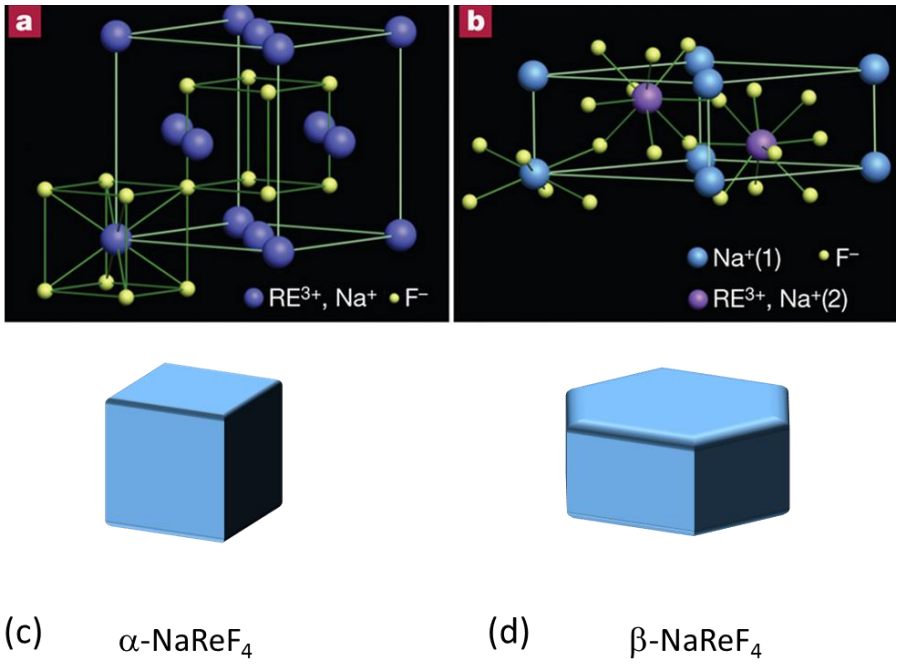

Figure 1.3.1 Schematics of the unit cells and typical shapes of cubic phase $NaREF_4$ (a and c) and hexagonal phase $NaREF_4$ (b and d). Reprinted from Reference [83].

1.3.3 $NaREF_4$ nanocrystal synthesis methods

To obtain mono-disperse β-$NaREF_4$ nanocrystals, several wet chemical synthesis methods have been developed, as summarized in Table 1.3.2. that includes a brief description, advantages and disadvantages for each popular method towards the morphology control.

Amongst these methods, thermal decomposition method and high-temperature co-precipitation method show their outstanding features to achieve morphology control of nanocrystals with good crystallinity. Both methods require high boiling point organic solvent (e.g. 1-octadecene) and surfactant (e.g. oleic acid, oleylamine), high reaction temperature (280 °C - 330 °C) in nitrogen or argon flow environment. The main difference between the two methods is their precursors used.

Table 1.3.2 Table of major nanocrystal synthesis methods and their features for size and shape control.

Method	Thermal co-precipitation	Thermal decomposition	Solvo-/hydrothermal	Microemulsion
Description of the method	Rare earth Oleate or Rare earth inorganic salt as, NH_4F and NaOH as precursors, nucleation at relative high temperature in a high boling-point organic solvent (e.g. 1-octadecene, oleic acid and oleylamine)	Organometallic compounds(Re(e.g. $CF_3COO)_3$, $NaCF_3COO$) as the precursors, decomposed at relatively high temperature in a high boiling-point organic solvent.	Applying high pressure generated by using low boiling point solvent as the reaction medium in a closed system	Nucleation was confined in the interface of two phase. The growth is automatically stopped as the size increasing
Advantages	• Well controlled on size and shape • Good crystallinity (no need annealing)	• Well controlled on size and shape • Good crystallinity (no need annealing)	• Easy operate. • Good crystallinity • Synthesize some crystal cannot be synthesized by other wet chemical synthesis method.	• Well controlled on size
Drawbacks	• Small amount synthesis (~100 mg)	• toxic reactants • HF may released during the reaction • Small amount synthesis	• Big size • Hard to do tunable controlled synthesis due to complex synthesis mechanism	• Only for small size nanocrystal • Poor crystallinity, further heating treatment needed.
Size control	Very good (monodisperse nanocrystals with tunable size from 10 nm to 80 nm)	Very good (monodisperse nanocrystals with tunable size from 10 nm to 80 nm)	Good	Good
Shape control	Very good (sphere, hexagonal prism)	Very good (sphere, hexagonal prism)	Not good	not good
If applicable for shell growth	Yes	Yes	Not sure	Not sure

Single source precursors are often used in the typical thermal decomposition method. In 2005, Yan and his coworkers[87] reported the synthesis of LaF_3 nanodisks by using $Re(CF_3COO)_3$ as precursors in the thermal decomposition method. $Re(CF_3COO)_3$ as precursors can provide both of rare earth source and fluoride source for decomposition. This strategy has been developed into a universally applicable method for the synthesis of monodispersed UCNPs, including $NaREF_4$, as well as, $LiReF_4$, $KReF_4$, and $BaReF_5$.

Since rare-earth trifluoroacetate and sodium trifluoroacetate are highly air-sensitive, highly toxic and even releasing highly corrosive HF, therefore highly hazardous to the user and environment, other precursors have been investigated to replace $Re(CF_3COO)_3$ precursors. Chen and his coworkers synthesized β-$NaREF_4$ UCNPs with low toxic precursors, NaF and Re oleate as precursors [88]. They control the morphology of UCNPs by simply regulating the ratio of NaF to Re oleate, but this method often require some extra amount of NaF that causes impurity for the final product.

The co-precipitation method has the advantage in using the user friendly precursors and at relatively lower temperature range (typically 290 ^oC – 310 ^oC). Zhang and his coworkers pioneered this method to synthesize mono-dispersed β-$NaYF_4$:Yb,Er/Tm UCNPs [89]. In this method, a methanol solution containing NaOH and NH_4F is added into a homogeneous solution of $ReCl_3$, oleic acid, and 1-octadecene. The advantage of this method lies in that a stoichiometric amount of fluoride reagents is already injected into the reaction solution at room temperature, so that negligible amount of the HF gas and fluorinate species can be generated at room temperatures. The method also provides an opportunity to tune the size and shape of $NaREF_4$ nanocrystals adjusting the amount ratio of Na^+/F^-, RE^{3+}/Na^+, RE^{3+}/F^- separately.

1.3.4 Size control of $NaREF_4$ nanocrystals

In this section, we will introduce the current techniques for controlling the size and shape of $NaREF_4$ nanocrystals in thermal decomposition method and co-precipitation method.

In 1.2.1 section, we illustrated that the size of nanocrystals is dependent on the nuclei amount and crystal growth rate, while the nuclei amount and crystal growth rate can be influenced by reaction parameters, including reaction temperature, surfactant concentration, reagent concentration, dopants concentration and reaction time.

Size control by reaction temperature and reaction time

Reaction temperature and time have been firstly investigated for tuning the size of nanocrystals. Yan's group has systemically studied the nucleation and growth process of both of α-$NaYF_4$ and β-$NaYF_4$ nanocrystals in thermal decomposition method.[90] They reported that mono-disperse α-$NaYF_4$:Yb,Er nanopolyhedra at different sizes (5-14 nm) were readily obtained via only prolonging the reaction time. Although β-$NaYF_4$:Yb,Er nanocrystals with tunable sizes in a broad range from 20 to 300 nm can be also obtained by increasing the temperature to at 330 °C, which restricts or enhances the Ostwald-ripening process, it is difficult to precisely control the size and their mono-disparity because the size of the nanocrystals will increase abruptly at high temperature. Song's group also comprehensively studied the size control of $NaLuF_4$ nanocrystals via adjusting the reaction temperature and demonstrated mono-dispersed $NaLuF_4$ nanocrystals from 17 nm to 246 nm by tuning the temperature from 300 °C to 320 °C. [91] Gao's group systemically studied several reaction factors, including temperature, F^- source concentration, and Na^+ concentration, the concentration ratio of Na^+/RE^{3+} and F^-/RE^{3+}, and found that temperature can tune the size of $NaGdF_4$ from 5 nm to 20 nm when increasing the temperature from 270 °C to 320 °C. [92] (Figure 1.3.2)

As we can see, smaller sized $NaGdF_4$ nanocrystals than $NaYF_4$, $NaLuF_4$ nanocrystals were obtained by controlling the temperature, because $NaGdF_4$ nanocrystals need relatively lower nucleation temperature. It is still quite difficult to obtain sub -10 nm $NaYF_4$ and $NaLuF_4$ nanocrystals only decreasing the temperature, because lower reaction temperature may cause the formation of the impure of α-$NaYF_4$.

.

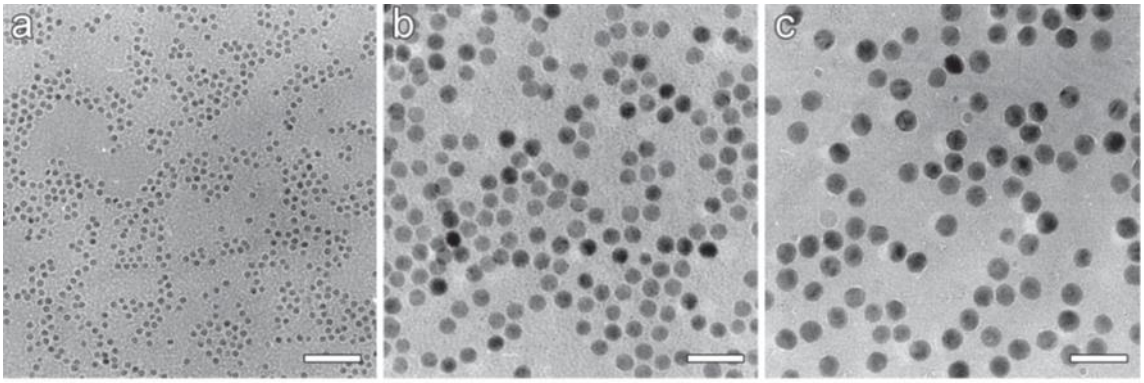

Figure 1.3.2 TEM images of $NaGdF_4$ nanocrystals synthesized under different reaction temperature and reaction time. 5.4 nm, 15.1 nm, and 19.8 nm $NaGdF_4$ nanocrystals prepared by reaction time of 45 min at 270 °C (a), 60 min at 300 °C (b), 60 min at 320 °C (c). Reprint from reference [92] (scale bar: 50 nm)

Size control by surfactants

Surfactants play a significant role in controlling nanocrystal's size. By adjusting surfactant concentration, nanocrystals' size can be fine-tuned. For example, Liu and his coworkers reported that the size of β-$NaYF_4$ can be fine-tuned from 50 nm to 30 nm via just increasing OA concentration.[93] They believe that before forming the nanocrystal structure the RE^{3+} ions should already be coordinated by the carboxylic groups of OA and subsequently absorbed onto the growing nanocrystals. This led to a delayed growth rate of the nanocrystals, and thereby with increasing the amount of OA smaller nanocrystals were formed.[93]

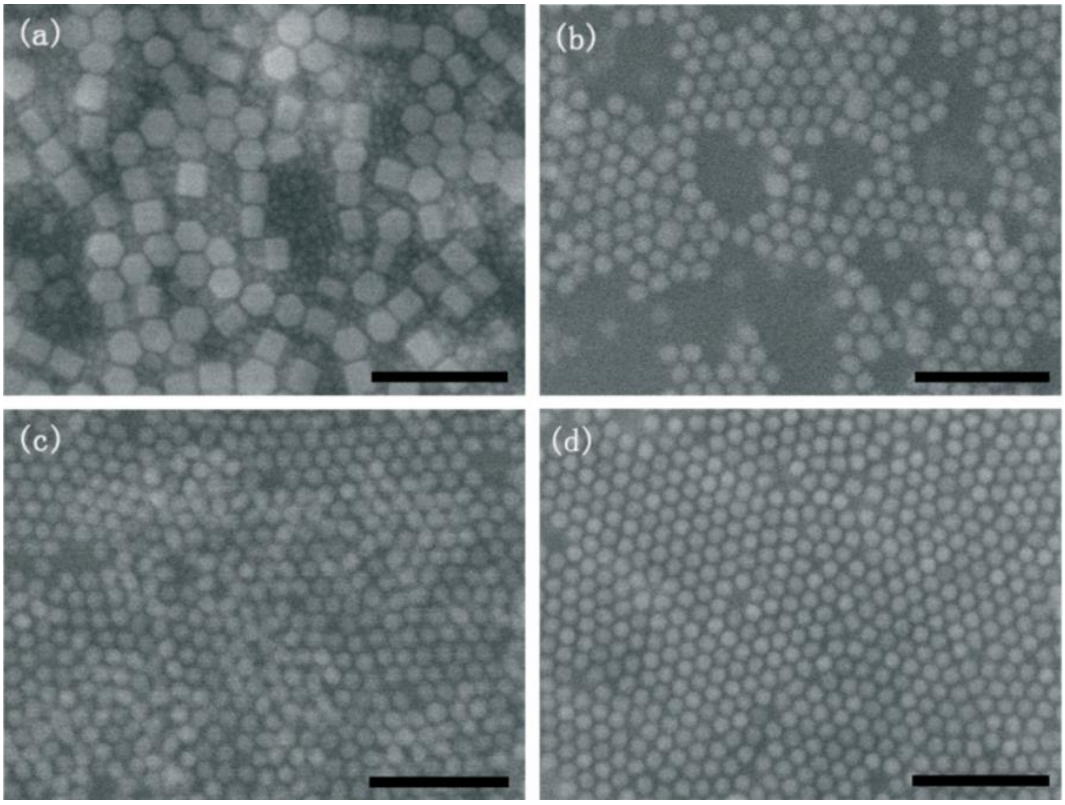

Figure 1.3.3 Effect of added NaF amount. SEM images of $NaYF_4$:Yb/Er nanocrystals obtained at different NaF concentrations at 300 °C for 1 h: (a) 4 mmol, (b) 6 mmol, (c) 8 mmol and (d) 12 mmol. All scale bars are 200 nm. Reprint from reference [93].

Different types of surfactants also affect the size of β-$NaREF_4$. For example, Cohen's group found that using oleylamine and oleic acid as co-surfactants is essential for synthesizing sub-10 nm β-$NaREF_4$ nanocrystals.[85] By adjusting the ratio of oleic acid to oleylamine, the size of β-$NaYF_4$ nanocrystals can tuned from 4.5 nm to 15 nm. They also found that in the presence of oleylamine reaction temperature and reaction time had little effect to the size of nanocrystals.

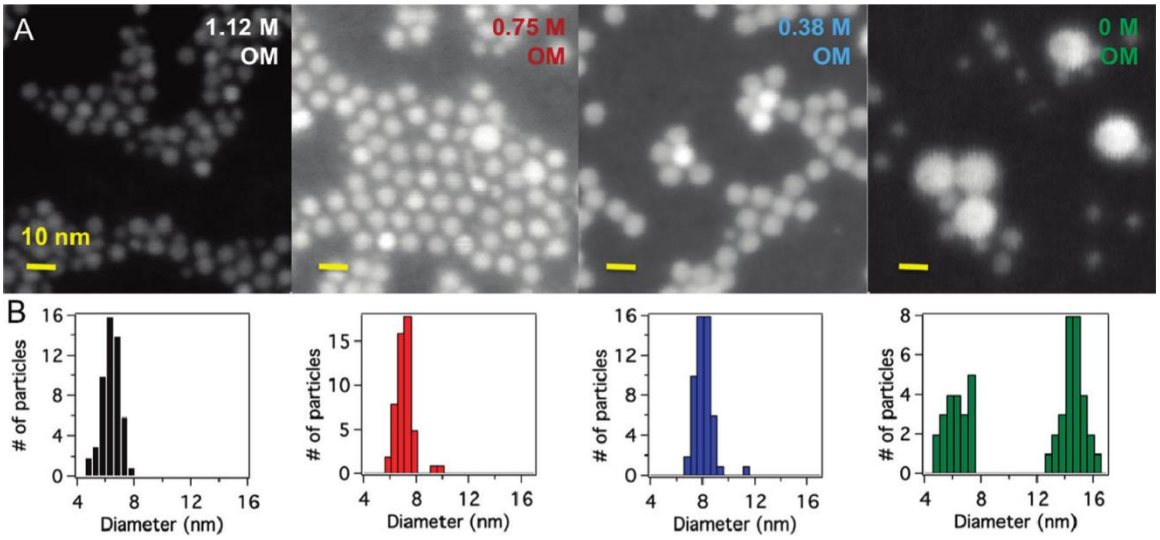

Figure 1.3.4 Scanning transmission electron microscopy (STEM) images of representative β-$NaYF_4$ nanocrystal samples at different oleylamine concentrations of 1.12, 0.75, 0.38, and 0 M. (Each scale bars: 10 nm). Reprint from reference [85].

1.3.5 Brief conclusion

$NaREF_4$ series of nanocrystals has similar crystalline structure and small differences in unit cell parameters due to the similar ionic radius of rare earth ions. Monodispersed β-$NaYF_4$ nanocrystals can be synthesized by both thermal decomposition and co-precipitation methods. Reaction temperature and reaction time are useful for controlling the size from 30 nm to 200 nm, while for synthesizing sub 10 nm b-$NaYF_4$ nanocrystals co-surfactants of oleylamine and oleic acid are necessary.

1.4 Epitaxial shell growth of nanocrystals

Since different sized monodispersed nanocrystals can be synthesized by different control techniques, new research starts to challenge the controls over the shape and structure of nanocrystals. Core-shell and heterogeneous structured nanocrystals by epitaxial shell growth strategy show superiority in luminescence enhancement [94-97], catalytic capability improvement [98] and integration of multifunctional properties [99-102]. Nowadays, wet chemical synthesis techniques to produce monodispersed nanocrystals are getting matured, controlled synthesis of 3-D structured nanocrystals starts to attract an increasing amount of interests. The key is to control the shell growth process by understanding the shell growth mechanism.

In this section, we will introduce some basic knowledge on epitaxial shell growth of nanocrystals and review some current results towards control synthesis of core-shell and heterogeneous nanocrystals.

1.4.1 Basics on core-shell nanocrystals

Synthesizing core-shell nanocrystals via epitaxial shell growth strategy has been found as a good method to improve the luminescence property and generate multi-functional nanoparticles. For example, the emission efficiency of rare earth doped $NaYF_4$ upconversion nanocrystals can be enhanced by tens to hundreds of times by a 5 nm –10 nm insert shells.[103-107] Also, epitaxial growth of Fe_3O_4 shells onto upconversion nanocrystals can generate bifunctional magnetic-luminescent probes for bioimaging application [108]. The core-shell structured nanocrystals also have shown advantages in the catalyst and 3D display areas. For example, $NaREF_4$ core-shell nanocrystals with selective doped Tm^{3+}, Ho^{3+}, Ce^{3+}, Yb^{3+} and Nd^{3+} in multiple shell layers show fine-tuned luminescence under near infrared excitation, which is useful for volumetric three-dimensional full-colour displays.

Different applications require different design of core-shell structures. For the purpose of luminescence enhancement, centrosymmetric core-shell structure is ideal (Figure 1.4.1a), because uniform shell can minimize the quenching by the surface defects. Uniform core-shell structure of CdS/ZnS quantum dots is preferred to prevent

the release of toxic ions, Cd^{2+} from CdS host. To produce multifunctional nanoparticles, anisotropic structures or heterogeneous structures are better with lager surface area and smaller interaction area at the interface of different materials as the building units. For example, iron oxide/$NaYF_4$ magnetic luminescence probes require smaller interface between iron oxide and $NaYF_4$ because iron oxide will quench the luminescence.

Epitaxial growth of uniform core-shell structures requires smaller mismatch between core and shell materials and careful control on the shell growth rate along each crystal direction. In most cases, the core-shell structures with non-centrosymmetric anisotropic structures or heterogeneous anisotropic structures are formed due to the relatively bigger mismatch between core and shell materials (Figure 1.4.1 b and c). To meet different requirements by applications, it is essential to realize controlled synthesis according to the design of any desired structure of nanocrystals.

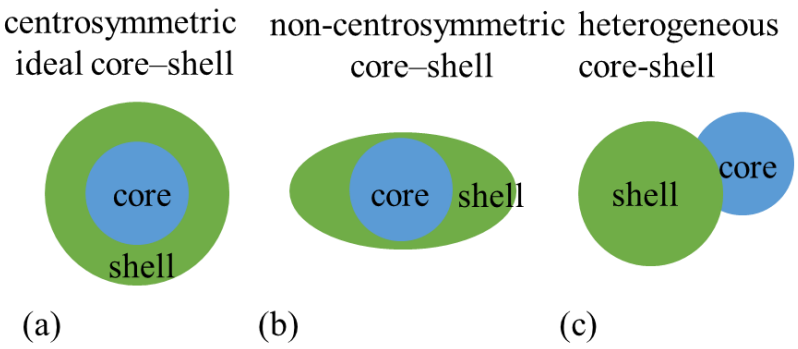

Figure 1.4.1 Schemes of (a) centrosymmetric ideal core–shell structures, (b) non-centrosymmetric core–shell anisotropic structures and (c) heterogeneous anisotropic structure.

1.4.2 Major reaction factors influence the shell growth

In a typical epitaxial shell growth process (see Figure 1.4.2), core nanocrystals are prepared first as the substance to anchor new crystal layers. When the core and shell are made of the same materials, the epitaxial shell growth is relatively easier as long as the temperature rises above a threshold temperature close to the nucleation temperature of the nanocrystals.

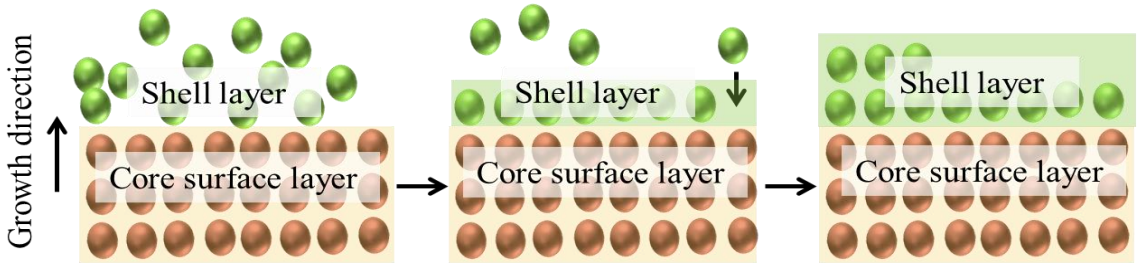

Figure1.4.2 Scheme of epitaxial shell growth process in wet chemical synthesis system.

To obtain uniform core-shell nanocrystals, some reaction factors need to be carefully controlled.

Using a proper concentration of shell precursors is important to prevent the formation of new nanocrystals. The threshold temperature for shell growth reaction is close to the nucleation temperature, and thereby shell growth process is always accompanied by the nucleation of new crystals from the shell precursors. Moreover, the shell growth rate is much lower than the nuclei growth rate, often resulting in the fast consumption of shell precursors. The thermodynamics process at presence of core-shell nanocrystals, newly formed nanocrystals and the concentration of shell precursors in suspension will decide the final structure of core-shell nanocrystals.

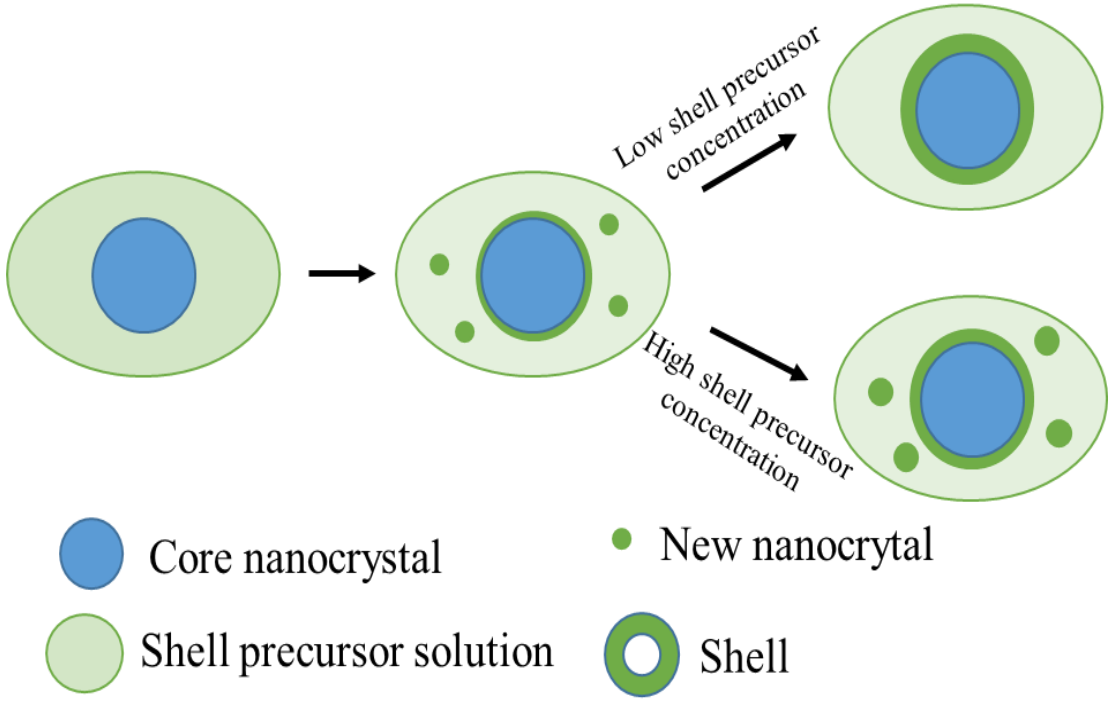

Figure 1.4.3 Scheme of the effect of shell precursor concentration on the shell growth.

In the case of low shell precursor concentration, the newly formed nanocrystals don't have sufficient precursors to grow any bigger, and as the smaller nanocrystals are unstable in the unsaturated reaction solution they will dissolve gradually and become shell sources again that will be eventually consumed by the process of shell growth. At high concentrations of shell precursors, the newly formed nanocrystals will keep growing bigger and become stable in the reaction solution. Therefore, it is very important to applying a suitable amount of the shell precursors for synthesizing uniform core-shell nanocrystals.

Core nanocrystal size. To avoid synthesis impurity, the size of the core nanocrystal should not be too small, otherwise the core nanocrystals and new form nuclei are in the competition for the fixed amount of shell precursors. Applying relatively lower reaction temperature and lower concentration of shell precursor would be helpful for the shell growth of smaller sized core nanocrystals.

Crystalline mismatch. To synthesize core-shell nanocrystals by two different materials, the crystalline mismatch between core and shell materials is a key factor

towards epitaxial shell growth. According to the degrees of crystalline mismatch, crystal materials can be grouped. Materials with similar crystalline structure, but slight different in unit parameters, such as quantum dots materials including ZnS, CdS, CdSe, CsTe, magnetic materials including Fe_2O_3, Co_2O_3, Ni_2O_3, Mn_2O_3, noble metal materials including Ag, Au, Pt., can be grouped for synthesis of heterogeneous core-shell nanocrystals. When the crystalline mismatches between two materials are too large it is too hard for them to grow core-shell structures. In some cases, the crystalline of core and shell materials can only be matched on a certain facet, it is still possible for the shell to be grown onto the facet with smaller mismatch of the core nanocrystals. In this condition, heterogeneous structured nanocrystals can be formed. For example, Fe_3O_4/Au [109], Fe_2O_3/CdS [110, 111], PbS/Au[112] heterodimers nanocrystals were demonstrated due to their match facets existed in core and shell materials.

Surfactants: Surfactants are molecules composed of a polar head group and one or more hydrocarbon chains with hydrophobic character.[71] Surfactant has a significant impact on the shell growth direction in the epitaxial shell growth process. Surfactants have been widely applied for controlled synthesis of nanocrystals towards a certain size and shape. They can specifically bind with metal ions on the crystal surface, and reduce the crystal surface energy and finally slow down the crystal growth rate. In process of shell growth, surfactants play a similar role but more specific on a certain facet and thereby influence the shell growth direction. Because of the anisotropic crystalline structure, crystal facets are different in polarity that determines different binding strength of surfactant molecules onto different crystal facets. Surfactants can passivate further growth of shells to the crystal surface and slow down the directional growth rate. This will result in the shell growth along a preferred growth direction. Rod-like or disk-like shaped core-shell nanocrystals are often synthesized. Although there are many efforts investigating on how the shell growth prefer one direction over the other, it remain challenging to find a clear answer on the surfactants working mechanism.

1.4.3 Brief conclusion

Epitaxial shell growth of nanocrystals is a major method for synthesizing core-shell nanocrystals in wet chemical synthesis route. To well control the core-shell

structure, it is essential to fully understand the impact of crystalline mismatch between core and shell materials and the role that surfactants play in influencing the shell growth direction.

1.5 Current progress on controlled synthesis of core-shell nanocrystals

In this section, we first outline the major methods used for synthesizing core-shell nanocrystals, with particular focus on synthesis methods in the most popular OA-ODE synthesis system, including the thermal decomposition and high-temperature co-precipitation methods. We illustrate here core shell structures made of most popular nanomaterials, including rare earth fluorides, semiconductor quantum dots, iron oxides and noble metal nanocrystals, and we group them by the type of core-shell structures, including homogenous core-shell structure and heterogeneous structure, to facilitate our discussions.

1.5.1 Homogeneous core-shell structure

Homogeneous core-shell structures, made of the same material, are found useful to achieve luminescence enhancement of luminescent nanocrystals, especially for rare earth doped $NaREF_4$ upconversion nanocrystals. The methods for core–shell synthesis include the heat-up method and the hot-injection method. Both methods are widely used for synthesizing different kinds of core-shell nanocrystals. In the heat-up method, the core nanocrystals are pre-synthesized and then mixed with shell precursors and high boiling solvents separately subsequently followed by increasing the temperature higher enough to allow shell growth. In the hot-injection method, shell precursors are dissolved in high boiling solvents first and injected directly into the hot reaction mixture to allow the shell to be grown onto the core.

Heat-up method

The heat-up method is generally referred to as seed-mediated shell growth, where the pre-synthesized core nanocrystals act as seeds for the shell growth. The idea of separating the core and shell growth processes was first reported in 2007 by Yan et al.[113] and refined in 2008 by Zhang et al. [114]. In both studies, the $NaYF_4$ core nanocrystals were synthesized first and washed out from the reaction media. The prepared core nanocrystals were transferred to a fresh reaction pot to mediate the growth of the shell layer following an identical protocol for the core synthesis.

One prominent advantage of the heat-up strategy is that the pre-synthesized core nanocrystals can be used as a standard starting material to serve in a batch of succeeding coating processes. Furthermore, the strategy also allows for arbitrary combinations of dissimilar synthetic approaches for flexible core–shell fabrication. For example, the core nanocrystals can be synthesized in water by hydrothermal method, while the shell coating can be carried out in OA–ODE through the oleate route [115].

The heat-up method has been considered to be the most commonly used method for the fabrication of core-shell nanocrystals, but it does not provide the uniform shell growth. The control on the thickness of core-shell nanocrystals has been an important research topic due to the importance to achieve luminescence enhancement that highly depends on the shell thickness. As discussed above, generally the uniform concentric shell is preferred for luminescence enhancement purpose. The shell thickness can be calculated by the average difference between the diameters of core-only and core-shell nanocrystals. It has been difficult to grow thicker uniform shell though shell below 5 nm can be readily well controlled by adjusting the mass ratio of shell precursor to core nanocrystals [116]. A precise control over the thin shell thickness was demonstrated by Wang and Liu et al. by heating the $NaGdF_4$:Yb/Er nanocrystals in OA–ODE solution at varying amount of precursors for $NaGdF_4$ shell.[116] By quantifying the shell precursor concentrations based on the spherical concentric shell model, they synthesized a series of $NaYF_4$:Yb/Er@$NaGdF_4$ core–shell nanocrystals with a thin shell thickness corresponding between one and ten Gd atomic layers. When growing nanocrystals with relative thinker shells above 5 nm, the core-shell structure becomes anisotropic [117, 118] and the size distribution becomes slightly wider. The possible reason for this is that the different binding strength of surfactants to different crystal facets, making shell growth preferable along a favorite direction. The anisotropic growth trend cannot be observed when growing thin shell due to the tiny shell thickness difference.

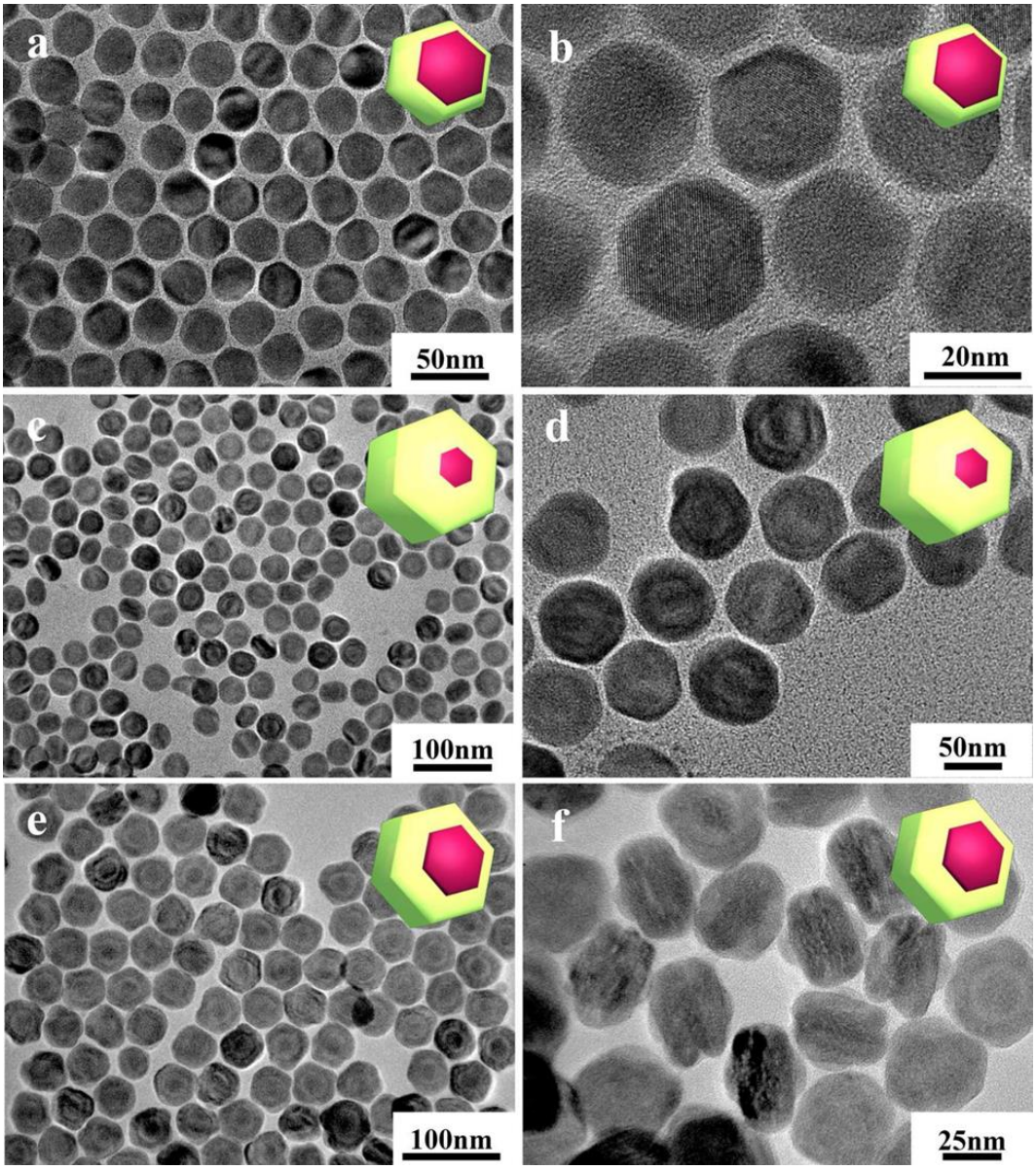

Figure 1.5.1 Transversal shell growth trend. TEM images of $NaYF_4$ nanocrystals with different $NaGdF_4$ shells at different magnifications (a, b) 4nm $NaGdF_4$ shell. (c, d) 8 nm $NaGdF_4$ shell. (e, f) 10 nm $NaGdF_4$ shell. Reprint from the reference [117].

The trend for anisotropic shell growth can be observed by using two different materials with the crystalline mismatch between core and shell materials. Zhang and Lee discovered a phenomenon of the prevalence of anisotropic shell growth in upconversion $NaREF_4$ systems [117], in which the shell prefer to growth transversally. $NaGdF_4$ or $NaYbF_4$ shell is only grown around the lateral faces of the core $NaYF_4$ nanocrystals (Figure 1.5.1). They explained this anisotropy was caused by the

combination of several factors: the selective adsorption of oleic acid on specific faces of the core NCs due to the crystal structure of the latter, the etching action of the oleic acid capping agent, and the lattice mismatch between core and shell components. They concluded that the specific adsorption of oleic acid on NCs faces was the major cause of anisotropic growth. It was postulated that oleic acid adsorbed preferentially on the {001} faces, thereby slowing the growth in the [001] direction [117].

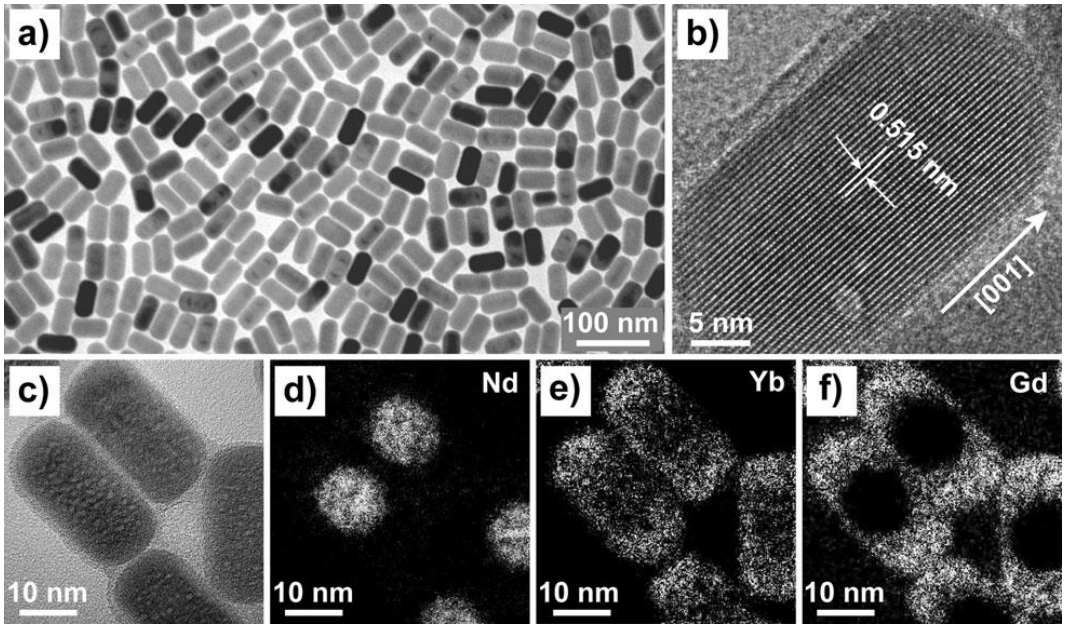

Figure 1.5.2 longitudinal shell growth trend. Typical TEM image of the as-synthesized $NaYbF_4/Na(Yb,Gd)F_4/NaGdF_4$ core–shell–shell nanocrystals. (b) High-resolution TEM image of a nanocrystal. (c) TEM image of randomly selected nanocrystals for compositional analysis. (d–f) Element maps of Nd, Yb, and Gd in the nanocrystals shown in (c). Reprint from reference [119].

However, the anisotropic shell growth trend is not always same. Wang and his co-worker found another anisotropic shell growth trend, in which $NaGdF_4$ shell was grown along the [001] direction, the longitudinal direction of $NaYbF_4$ core nanocrystals. The final core-shell nanocrystal was in a rod-like shape (Figure 1.5.2) [119]. Some similar longitudinal trend results in shell growth have also been reported by other groups [120, 121]. But why the $NaREF_4$ core nanocrystal shows two different favorite growth directions? Unfortunately, the answer is unknown. The current explanation for the different shell anisotropic growth phenomenon is the same, which is surfactant molecule's selective adhering on the crystal surface, but more comprehensive studies

are needed to understand the role of surfactants in the shell growth process to reveal the secrets of epitaxial shell growth of nanocrystals.

Hot-injection method

To grow uniform homogenous shells, hot injection method originally used for controlled synthesis of core–shell semiconductor nanocrystals [122-125] was adapted to synthesize $NaYF_4$:Yb/Er-$NaYF_4$ core–shell nanocrystals in 2007 by Yi and Chow [119]. Hot-injection method was first used in the thermal decomposition synthesis, in which trifluoroacetate precursors are first heated at 340 °C in OM solution for 30 min to grow the $NaYF_4$:Yb/Er core nanocrystals and subsequently an OM solution comprising of shell precursors are injected into the reaction solution for the epitaxial growth of a $NaYF_4$ homogeneous shell.

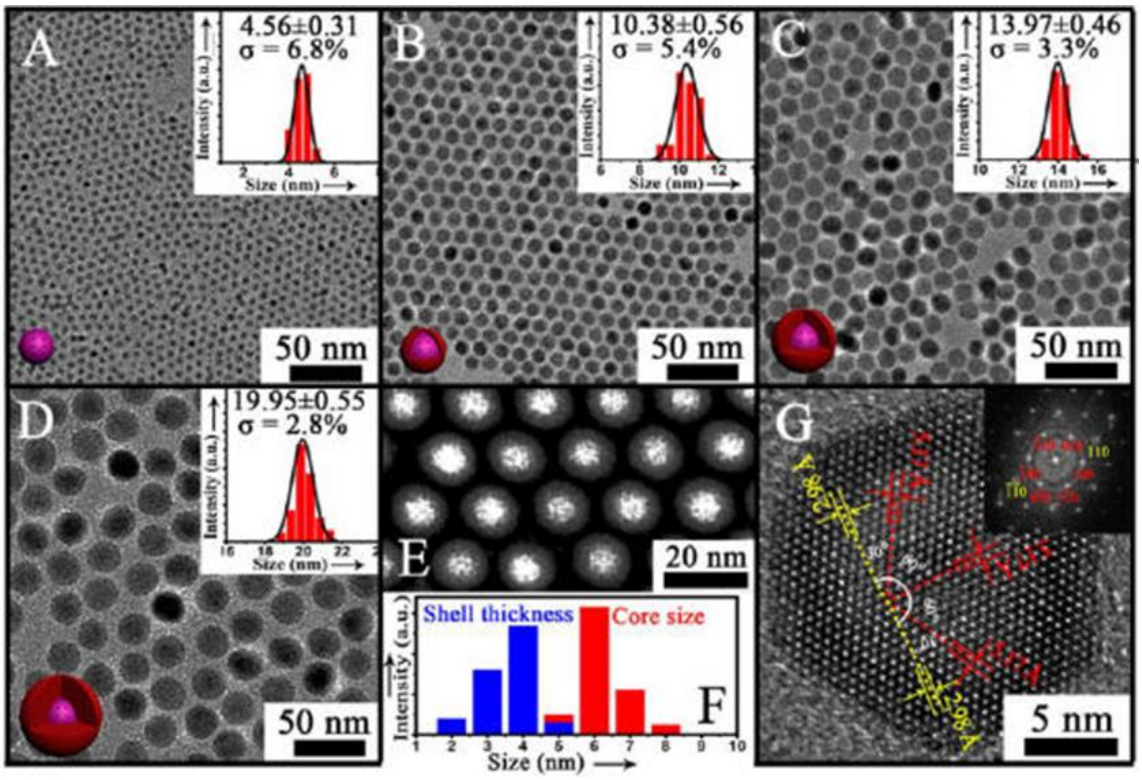

Figure 1.5.3 TEM images and size distribution of β-$NaGdF_4$:Yb,Er core NPs and β-$NaGdF_4$:Yb,Er/$NaYF_4$ core/shell NPs with different shell thickness by using the SLBL method. Reprint reference from [126].

Due to the high toxicity of trifluoroacetate precursors, different low-toxic shell precursors were investigated to synthesize homogenous shells. Zhao and Zhang's group developed an one-pot successive layer-by-layer (SLBL) strategy to fabricate the core/shell upconversion nanocrystals by using high boiling-point rare earth oleate (rare-earth chlorides dissolved in oleic acid at 140 °C) and Na-TFA-OA (sodium trifluoroacetate dissolved in oleic acid at room temperature) as shell precursor solutions [126]. The homogeneous core-shell structure was confirmed by STEM images (Figure 1.5.3). By simply tuning the amounts of shell precursors, the shell thickness of obtained nanocrystals with narrow size distribution ($\sigma < 10\%$) can be well controlled from 0.36 nm to more than 8 nm.

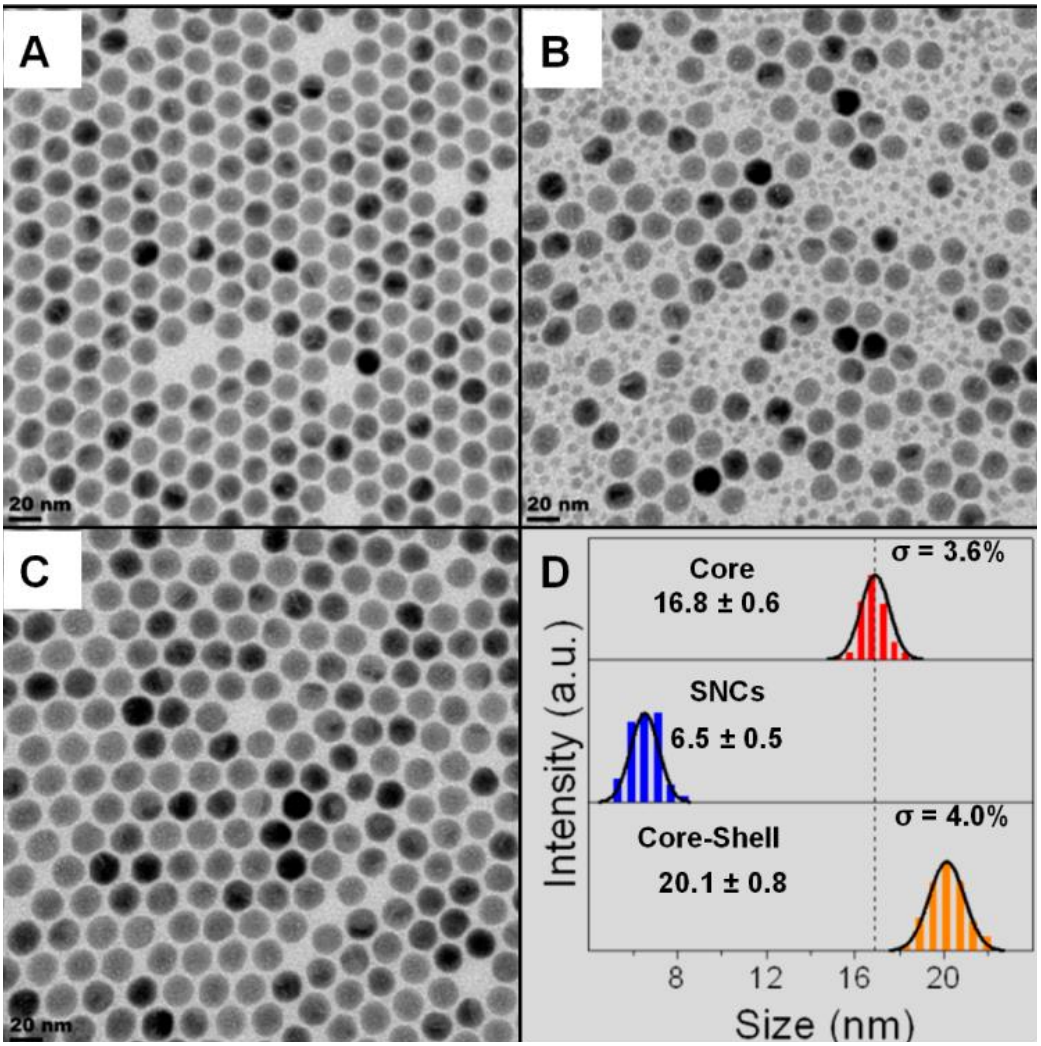

Figure 1.5.4 TEM images of core nanocrystals (A), just after injecting a-$NaYF_4$ (B), core-shell nanocrystals (C), and size distribution of β-$NaYF_4$ core, a-$NaYF_4$ shell precursor, and core-shell nanocrystals. (D), Reprint from reference [103].

Zhang's group applied a similar method to grow multiple shells in one pot synthesis, based on the continuous injection of different shell precursors at very low dosages. [127] This method also avoids the formation of impure nanocrystals, which case often happens in heating-up method. Moreover, van Veggel's group demonstrated that small α-$NaYF_4$ nanocrystals can be used as shell precursors. [103] Due to the lower chemical stability of small α-$NaYF_4$ nanocrystals than β-$NaYF_4$ in OA-ODE reaction system, α-$NaYF_4$ nanocrystals will be quickly dissolved to supply the epitaxial growth of shells onto the core of β-$NaYF_4$ nanocrystals (see Figure 1.5.4). The shell thickness can also be well controlled by adjusting the ratio of shell precursors and core nanocrystals. Another advantage of this method is that synthesis based on α-$NaYF_4$ shell precursors are non-toxic. On the other side of the coin, to grow thicker shells will need a large amount of α-$NaYF_4$ shell precursors and it is time consuming to synthesize α-$NaYF_4$ nanocrystals.

1.5.2 Heterogeneous core-shell structures

Heterogeneous core-shell structured nanocrystals are generally made of different composition and structures. Heterogeneous core-shell nanocrystals make it possible to integrate two or more distinct properties into one nanoparticle, which field has attracted increasing amount of research interests for biomedical and green energy applications. Controlling the shell growth of heterogeneous core-shell nanocrystal is much difficult than for the case of homogeneous core-shell nanocrystals due to crystalline lattice mismatch between the core and the shell materials. Here we introduce two ways for controlling the heterogeneous shell growth, switching solvent polarity (Figure 1.5.5) and using intermediate step to bridge the crystalline mismatch between the core and shell nanocrystals materials.

Heterogeneous core-shell nanocrystals, made of two metals (e.g., Ag–Au), metals and semiconductors (e.g., Au/CdSe), metals and insulators (e.g., Co/Fe_3O_4), and

different semiconductors or insulators (e.g., CdSe/ZnS or ZnS/Fe_3O_4), have been recently demonstrated. These heterodimer nanocrystals were formed by fusing the two nanocrystals at a matched facet following the process of nucleation and growth of the second component on the preformed core nanocrystals. Several heterodimer nanocrystals have been synthesized, such as Au/Fe_3O_4, Ag/Fe_3O_4, Au/CdSe [128], Au/CdS, Au/PdS, FePt/CdS nanocrystals.

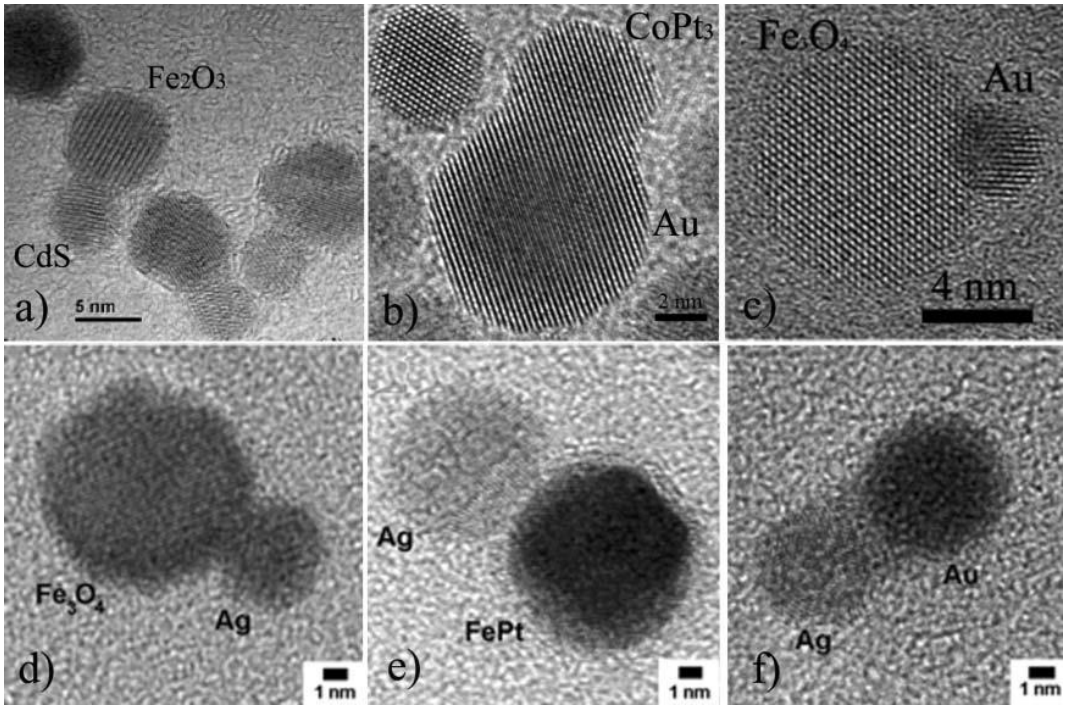

Figure 1.5.5. High resolution TEM images of different types of heterodimer nanocrystals: (a) Fe_2O_3/CdS; (b) $CoPt_3$/Au; (c) Fe_3O_4/Au; (d) Fe_3O_4–Ag; (e) FePt/Ag; (f) Au–Ag Reprint from the reference of [71].

Epitaxial growth of heterodimers follows the similar procedures to that of core-shell nanocrystals, while many experimental parameters, including the precursor ratio, solution concentration and heating profile will affect the final morphologies of heterodimers. A convenient route to control core/shell vs. heterodimer structure formation is to control the polarity of the solvent. Sun's group reported that dumbbell-like Au/Fe_3O_4 heterogeneous core-shell nanocrystals were synthesized by decomposition of $Fe(CO)_5$ onto the surface of Au nanocrystals followed by oxidation in 1-octadecene solvent, in which (111) plane of Fe_3O_4 matched with (111) plane of gold nanocrystals. They found that the heterogeneous structure of Au/Fe_3O_4 changed from

heterodimer to core-shell just by switching the solvent from nonpolar hydrocarbon to slightly polarized diphenyl ether. Once Fe_3O_4 nanocrystals starts to nucleate on Au facet, the free electrons from the Au will compensate for the charge induced by the polarized plane at the interface. As the Au nanocrystal has only a very limited source of electrons, this compensation makes all other facets of the Au nanocrystal electron deficient and unsuitable for multi-nucleation, leading to only the dumbbell structure. If the polarity of the solvent used for the synthesis is increased, the Au nanocrystals could compensate for the apparent electron density loss with charges from the solvent, allowing nucleation on multiple facets. Similar results were found in Au/PbS [129], CdS/FePt [130-132], Ag/Fe_3O_4 nanocrystals [133-137].

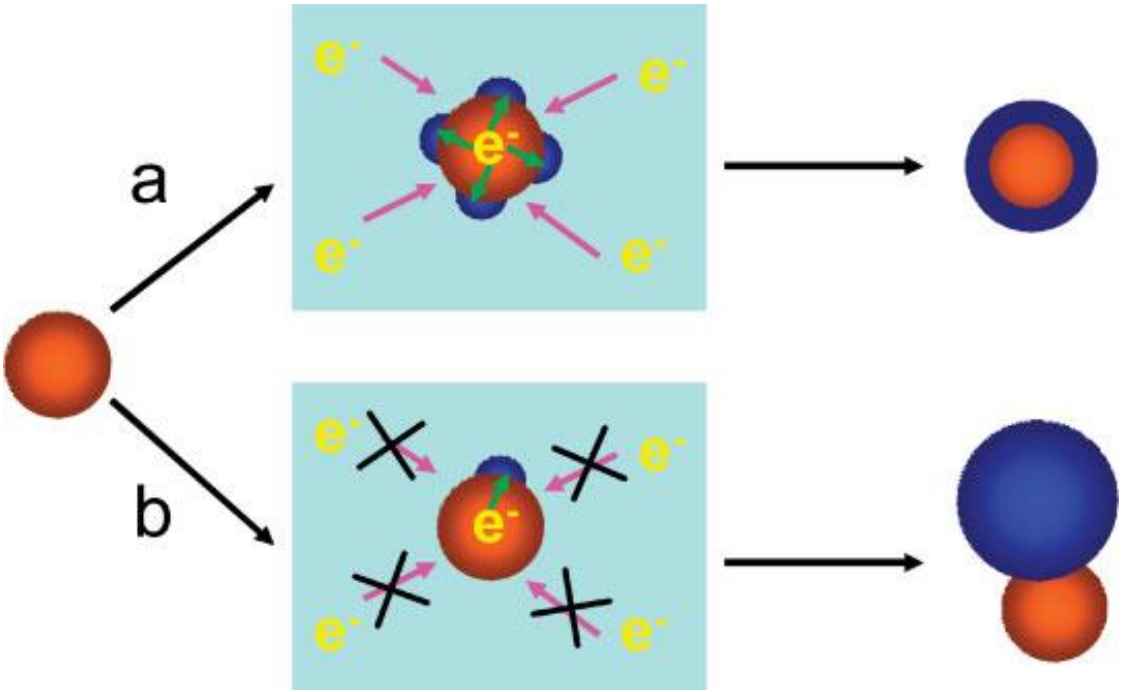

Figure 1.5.6 Schematic diagram showing the mechanism of formation of core/shell nanocrystals in a polar solvent (top) and heterodimers in a nonpolar solvent (bottom). Reprint from reference [138].

The formation of a heterogeneous structure often depends on the crystal lattice mismatch between the core and shell nanocrystals. To efficiently decrease the difficulty of shell growth with relative big crystalline mismatches to the core, some intermediate steps can be applied to bridge the epitaxial shell growth process, instead of directly growing the desired shells onto the core nanocrystals.

For example, the big crystalline mismatch between Au core and CdSe shell makes it difficult to directly synthesize Au/CdSe core-shell nanocrystals. Zhang and his co-workers invented a new method to grow semiconductor shell onto gold core nanocrystal [139]. In this method, Gold nanocrystals were coated with Ag shell firstly, then Ag shell was reacted with selenide precursor to form Ag_2S (Ag_2Se) shell, followed by the reaction with Cd^{2+} and TBP^{+} catalyst to form the final Au/CdSe core-shell nanocrystals.

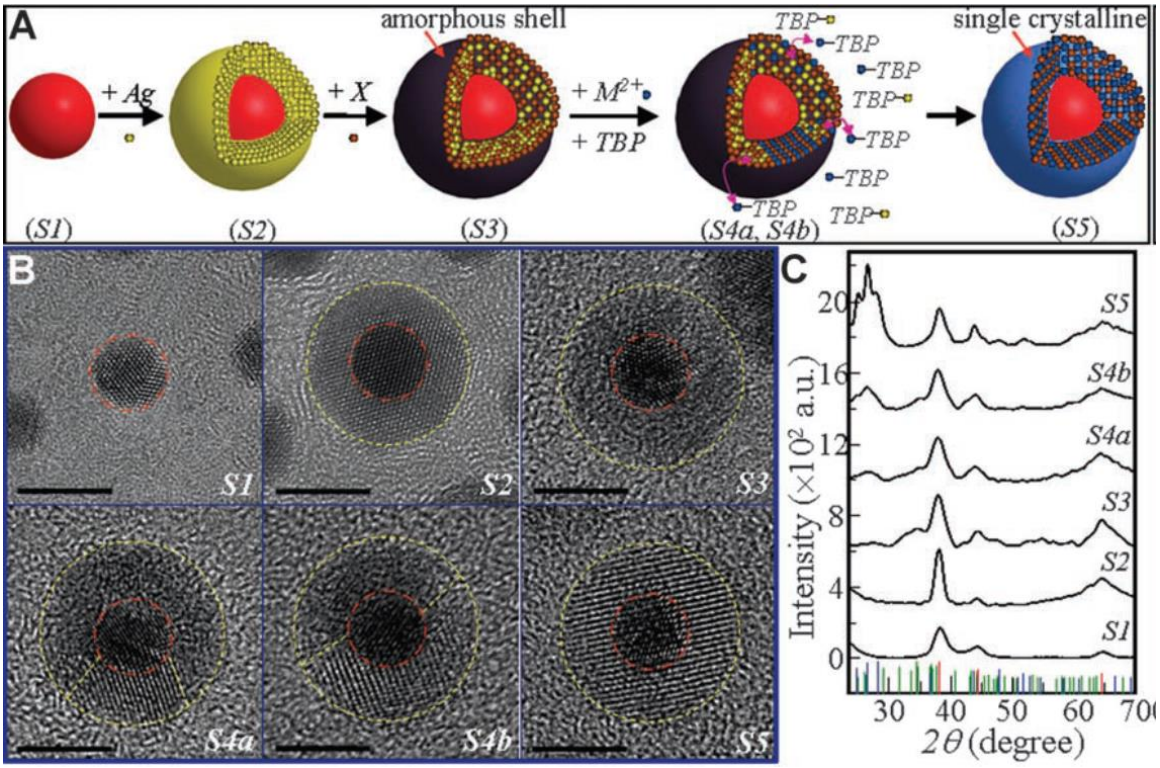

Figure 1.5.7 Scheme of synthesizing heterogeneous core-shell nanocrystals with large lattice mismatch (A), their TEM images (B) and XRD (C) spectrum at different steps. Reprinted from reference [139].

In addition, Guardia and his co-workers reported a Au_2Cd/CdSe heterogeneous core-shell structure made of a Au_2Cd alloy core surrounded by a CdSe shell synthesized via a one-pot approach (See Figure 1.5.7). The concept they exploited was to start with gold nanocrystals as the seeds that were later converted into AuCd alloy nanocrystals as an intermediate bridging material. Then, once a Se precursor was injected in the solution containing the AuCd nanocrystals, a CdSe shell will be formed [140]. The

Figure 1.5.7 (b) shows the big crystalline mismatch between the Au_2Cd core and CdSe shell.

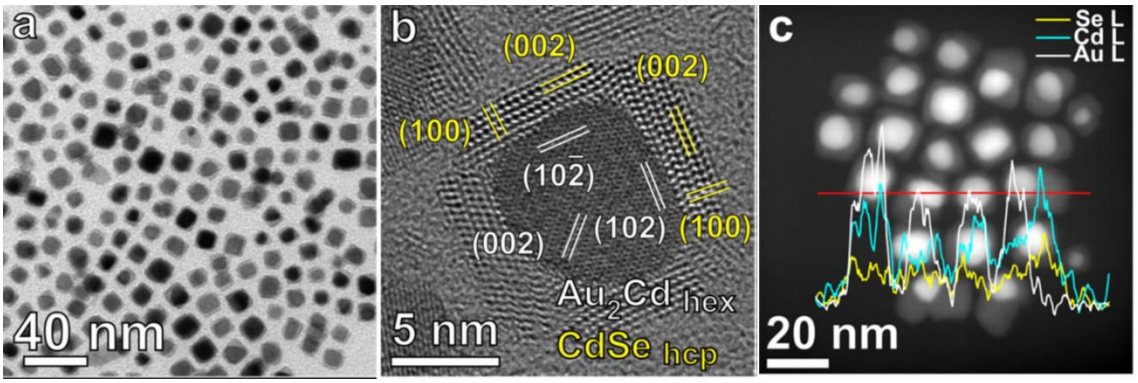

Figure 1.5.8 (a) TEM image of Au_2Cd/CdSe core/shell nanocrystals. (b) HRTEM image of a single Au_2Cd/CdSe core/shell NC exhibiting the characteristic (102) and (002) lattice planes of hexagonal Au_2Cd, (c) HAADF STEM image and EDX spectrum of a group of Au_2Cd/CdSe core/shell NCs. Reprinted form the reference [140].

Rare-earth fluorides based heterogeneous structures

Rare-earth fluorides series of nanocrystals have the same crystalline phase structure and similar unit parameters, which reduced the difficulty of shell growth between the different rare-earth fluorides nanocrystals. The reported $NaREF_4$ heterogeneous core-shell nanocrystals include $NaYF_4$/$NaGdF_4$ [118, 141-144], $NaYF_4$/$NaLuF_4$ [145-147], $NaYF_4$/$NaNdF_4$ [127, 148], $NaLuF_4$/$NaGdF_4$ [149], and so on. For these heterogeneous core-shell nanocrystals, the crystal lattice mismatch rates between core and shell are low below 10%. (See Table 1.5.1) Their core-shell structures can be well characterized by TEM and STEM. In addition to $NaREF_4$ heterogeneous core-shell nanocrystals, $LiReF_4$ heterogeneous core-shell nanocrystals also have been synthesized. Moreover, $LiReF_4$ and CaF_2 nanocrystals can also be grown into core-shell structures. Zhai and his co-workers synthesized $LiLuF_4$/$LiGdF_4$ core-shell nanocrystals [150], and Prorok and his coworkers have successfully synthesized α-$NaYF_4$/CaF_2 heterogeneous core-shell nanocrystals [151]. These rare-earth heterogeneous core-shell nanocrystals results demonstrated that rare-earth fluorides were ideal engineering

objects with choices among tens of different crystals for building the pairs of core and shell heterogeneous materials.

Table 1.5.1 $NaREF_4$ crystalline unit cell parameters

Crystal Host	a&b (Å)	c (Å)
NaLaF4	6.178	3.828
NaCeF4	6.150	3.781
NaNdF4	6.100	3.711
NaEuF4	6.059	3.625
NaSmF4	6.051	3.640
NaGdF4	6.020	3.601
NaTbF4	6.008	3.580
NaPrF4	5.991	3.537
NaDyF4	5.985	3.554
NaYF4	5.960	3.530
NaErF4	5.959	3.514
NaTmF4	5.953	3.494
NaYbF4	5.925	3.471
NaLuF4	5.901	3.453

1.5.3 Brief conclusion

Core-shell structured nanocrystals have been synthesized via the seeds-mediating epitaxial shell growth strategy. Heating-up method and hot injection method are widely used for synthesizing homogeneous core-shell nanocrystals. The crystalline mismatch rate between core and shell materials highly impacts on the morphology and structure of final epitaxial shell growth of heterogeneous nanocrystals. Heterodimer structured heterogeneous nanocrystals have been demonstrated. To control the core-shell and heterodimer structure formation, two methods, switching solvent polarity and using an intermediate step to bridge the crystalline mismatch between the core and shell

materials, are used. Comparing with other heterogeneous nanocrystal materials, rare-earth fluorides series of nanocrystals have the advantage to achieve different homogenous and heterogeneous core-shell structures by engineering different crystal materials with the same crystal structure and small crystalline mismatch.

1.6 Reference

[1] L. Polavarapu, S. Mourdikoudis, I. Pastoriza-Santos, J. Pérez-Juste, CrystEngComm, 17 (2015) 3727-3762.
[2] M. Zielinski, S. Winter, R. Kolkowski, C. Nogues, D. Oron, J. Zyss, D. Chauvat, Opt Express, 19 (2011) 6657-6670.
[3] H. Chen, X.S. Zhai, D. Li, L.L. Wang, D. Zhao, W.P. Qin, J Alloy Compd, 511 (2012) 70-73.
[4] X.J. Li, Z.Y. Hou, P.A. Ma, X. Zhang, C.X. Li, Z.Y. Cheng, Y.L. Dai, J.S. Lian, J. Lin, Rsc Adv, 3 (2013) 8517-8526.
[5] Q. Liu, Y. Sun, T.S. Yang, W. Feng, C.G. Li, F.Y. Li, J Am Chem Soc, 133 (2011) 17122-17125.
[6] X. Wang, Y.J. Li, Z.G. Song, Z.Y. Yin, J.B. Qiu, Z.W. Yang, D.C. Zhou, Y. Yang, Z.Y. Zhao, C. Li, N. Yang, Q. Wang, J Nanosci Nanotechno, 14 (2014) 3910-3913.
[7] S.J. Zeng, Z.G. Yi, W. Lu, C. Qian, H.B. Wang, L. Rao, T.M. Zeng, H.R. Liu, H.J. Liu, B. Fei, J.H. Hao, Adv Funct Mater, 24 (2014) 4051-4059.
[8] E.P. Schartner, D. Jin, H. Ebendorff-Heidepriem, J.A. Piper, T.M. Monro, Third Asia Pacific Optical Sensors Conference, 8351 (2012).
[9] Y.L. Wang, N.M. Estakhri, A. Johnson, H.Y. Li, L.X. Xu, Z.Y. Zhang, A. Alu, Q.Q. Wang, C.K. Shih, Sci Rep-Uk, 5 (2015).
[10] J.B. Zhao, Z.D. Lu, Y.D. Yin, C. Mcrae, J.A. Piper, J.M. Dawes, D.Y. Jin, E.M. Goldys, Nanoscale, 5 (2013) 944-952.
[11] J.Q. Grim, L. Manna, I. Moreels, Chemical Society Reviews, 44 (2015) 5897-5914.
[12] T. Zheng, L.D. Sun, J.C. Zhou, W. Feng, C. Zhang, C.H. Yan, Chem Commun, 49 (2013) 5799-5801.
[13] M. Aslam, N.K. Chaki, J. Sharma, K. Vijayamohanan, Curr Appl Phys, 3 (2003) 115-127.
[14] M.R. Langille, M.L. Personick, C.A. Mirkin, Angew Chem Int Edit, 52 (2013) 13910-13940.
[15] M.G. Panthani, B.A. Korgel, Annu Rev Chem Biomol, 3 (2012) 287-311.
[16] A.I. Savchuk, P.N. Gorley, V.V. Khomyak, A.G. Voloshchuk, V.I. Fediv, S.V. Bilichuk, I.D. Stolyarchuk, A. Perrone, Mat Sci Eng C-Bio S, 23 (2003) 753-756.
[17] V. Singh, Y.X. Yu, Q.C. Sun, B. Korgel, P. Nagpal, Nanoscale, 6 (2014) 14643-14647.
[18] K.A. Stancheva, Oxid Commun, 35 (2012) 662-673.
[19] S.A. McDonald, G. Konstantatos, S.G. Zhang, P.W. Cyr, E.J.D. Klem, L. Levina, E.H. Sargent, Nat Mater, 4 (2005) 138-142.
[20] Z.J. Ning, D. Zhitomirsky, V. Adinolfi, B. Sutherland, J.X. Xu, O. Voznyy, P. Maraghechi, X.Z. Lan, S. Hoogland, Y. Ren, E.H. Sargent, Adv Mater, 25 (2013) 1719-1723.
[21] I. Sevonkaev, V. Privman, D. Goia, J Solid State Electr, 17 (2013) 279-297.
[22] C.J. Stolle, T.B. Harvey, B.A. Korgel, Curr Opin Chem Eng, 2 (2013) 160-167.
[23] S.M. Thon, E.H. Sargent, Thin Film Solar Technology Iii, 8110 (2011).
[24] Z.Y. Yang, A. Janmohamed, X.Z. Lan, F.P.G. de Arquer, O. Voznyy, E. Yassitepe, G.H. Kim, Z.J. Ning, X.W. Gong, R. Comin, E.H. Sargent, Nano Lett, 15 (2015) 7539-7543.
[25] D. Zhitomirsky, M. Furukawa, J. Tang, P. Stadler, S. Hoogland, O. Voznyy, H. Liu, E.H. Sargent, Adv Mater, 24 (2012) 6181-6185.
[26] B. Liu, C.X. Li, P.A. Ma, Y.Y. Chen, Y.X. Zhang, Z.Y. Hou, S.S. Huang, J. Lin, Nanoscale, 7 (2015) 1839-1848.
[27] R. Zhao, C.P. Hollis, H. Zhang, L. Sun, R.A. Gemeinhart, T. Li, Mol Pharm, 8 (2011) 1985-1991.
[28] W.C. Chan, Bio-applications of Nanoparticles, Springer Science & Business Media, 2009.
[29] W. Wu, J. Shen, P. Banerjee, S. Zhou, Biomaterials, 32 (2011) 598-609.

[30] R. Negishi, T. Hasegawa, H. Tanaka, K. Terabe, H. Ozawa, T. Ogawa, M. Aono, Surf Sci, 601 (2007) 3907-3911.
[31] A. Safaei, M.A. Shandiz, Physica E, 41 (2009) 359-364.
[32] C. Kilic, Solid State Commun, 150 (2010) 2333-2336.
[33] J. Jasieniak, M. Califano, S.E. Watkins, Acs Nano, 5 (2011) 5888-5902.
[34] C.C. Yang, Q. Jiang, Sol St Phen, 121-123 (2007) 1069-1072.
[35] C.C. Yang, S. Li, J Phys Chem B, 112 (2008) 14193-14197.
[36] Y.P. He, Y.M. Miao, C.R. Li, S.Q. Wang, L. Cao, S.S. Xie, G.Z. Yang, B.S. Zou, C. Burda, Phys Rev B, 71 (2005).
[37] N.C. Dyck, F.C.J.M. van Veggel, G.P. Demopoulos, Acs Appl Mater Inter, 5 (2013) 11661-11667.
[38] S.W. Hao, W. Shao, H.L. Qiu, Y.F. Shang, R.W. Fan, X.Y. Guo, L.L. Zhao, G.Y. Chen, C.H. Yang, Rsc Adv, 4 (2014) 56302-56306.
[39] X.J. Xue, S. Uechi, R.N. Tiwari, Z.C. Duan, M.S. Liao, M. Yoshimura, T. Suzuki, Y. Ohishi, Opt Mater Express, 3 (2013).
[40] F. Wang, J.A. Wang, X.G. Liu, Angew Chem Int Edit, 49 (2010) 7456-7460.
[41] H. Liang, M. Upmanyu, H. Huang, Phys Rev B, 71 (2005) 241403.
[42] J.C. Angus, I. Greber, K. Kash, J Electrostat, 71 (2013) 1055-1060.
[43] S. Chakraborty, S. Bhowmick, J.Q. Ma, H.W. Tan, N. Das, Inorg Chem Front, 2 (2015) 290-297.
[44] Y. Chalopin, H. Dammak, M. Hayoun, M. Besbes, J.J. Greffet, Appl Phys Lett, 100 (2012).
[45] V. Kumar, K. Saxena, A.K. Shukla, Micro Nano Lett, 8 (2013) 311-314.
[46] D. Sahu, G.M. Kannan, R. Vijayaraghavan, J Toxicol Env Heal A, 77 (2014) 177-191.
[47] S. Coe-Sullivan, W. Liu, P. Allen, J.S. Steckel, ECS J Solid State Sci and Techno, 2 (2013) R3026-R3030.
[48] X. Dai, Z. Zhang, Y. Jin, Y. Niu, H. Cao, X. Liang, L. Chen, J. Wang, X. Peng, Nature, 515 (2014) 96-99.
[49] G.J. Supran, K.W. Song, G.W. Hwang, R.E. Correa, J. Scherer, E.A. Dauler, Y. Shirasaki, M.G. Bawendi, V. Bulović, Adv Mater, 27 (2015) 1437-1442.
[50] K. Bourzac, Nature, 493 (2013) 283.
[51] X. Michalet, F. Pinaud, L. Bentolila, J. Tsay, S. Doose, J. Li, G. Sundaresan, A. Wu, S. Gambhir, S. Weiss, Science, 307 (2005) 538-544.
[52] H. Mattoussi, G. Palui, H.B. Na, Adv Drug Deliver Rev, 64 (2012) 138-166.
[53] A.J. Nozik, M.C. Beard, J.M. Luther, M. Law, R.J. Ellingson, J.C. Johnson, Chem Rev, 110 (2010) 6873-6890.
[54] S. Rühle, M. Shalom, A. Zaban, ChemPhysChem, 11 (2010) 2290-2304.
[55] K. Zhao, Z. Pan, I. Mora-Seró, E. Cánovas, H. Wang, Y. Song, X. Gong, J. Wang, M. Bonn, J. Bisquert, J Am Chem Soc, 137 (2015) 5602-5609.
[56] M. Bawendi.
[57] S. Ayyappan, J. Philip, B. Raj, Mater Chemy Physcs, 115 (2009) 712-717.
[58] J.P. Chen, C.M. Sorensen, K.J. Klabunde, G.C. Hadjipanayis, E. Devlin, A. Kostikas, Phys Rev B, 54 (1996) 9288-9296.
[59] S. Sun, H. Zeng, J Am Chem Soc, 124 (2002) 8204-8205.
[60] S. Sun, H. Zeng, D.B. Robinson, S. Raoux, P.M. Rice, S.X. Wang, G. Li, J Am Chem Soc, 126 (2004) 273-279.
[61] F. Chen, W.B. Bu, S.J. Zhang, X.H. Liu, J.N. Liu, H.Y. Xing, Q.F. Xiao, L.P. Zhou, W.J. Peng, L.Z. Wang, J.L. Shi, Adv Funct Mater, 21 (2011) 4285-4294.
[62] N.J. Johnson, W. Oakden, G.J. Stanisz, R. Scott Prosser, F.C. van Veggel, Chem Mater, 23 (2011) 3714-3722.
[63] Y.J. Kang, J.B. Pyo, X.C. Ye, R.E. Diaz, T.R. Gordon, E.A. Stach, C.B. Murray, Acs Nano, 7 (2013) 645-653.
[64] O.J. Hildreth, W. Lin, C.P. Wong, Acs Nano, 3 (2009) 4033-4042.
[65] K.C. Wang, W. Huang, Y.F. Zhou, D.Y. Yan, Chem J Chinese U, 28 (2007) 1365-1370.

[66] Y.L. Qin, X.B. Zhang, J. Wang, L.M. Wang, J Mater Chem, 22 (2012) 14861-14863.
[67] M.B. Mohamed, C. Burda, M.A. El-Sayed, Nano Lett, 1 (2001) 589-593.
[68] Q. Song, Z.J. Zhang, J Am Chem Soc, 126 (2004) 6164-6168.
[69] M.E. Stewart, C.R. Anderton, L.B. Thompson, J. Maria, S.K. Gray, J.A. Rogers, R.G. Nuzzo, Chem Rev, 108 (2008) 494-521.
[70] M.J. Mulvihill, X.Y. Ling, J. Henzie, P.D. Yang, J Am Chem Soc, 132 (2010) 268-274.
[71] P.D. Cozzoli, T. Pellegrino, L. Manna, Chem Soc Rev, 35 (2006) 1195-1208.
[72] M.B. Gawande, A. Goswami, T. Asefa, H.Z. Guo, A.V. Biradar, D.L. Peng, R. Zboril, R.S. Varma, Chem Soc Rev, 44 (2015) 7540-7590.
[73] N.T.K. Thanh, N. Maclean, S. Mahiddine, Chem Rev, 114 (2014) 7610-7630.
[74] S.L. Brock, J Am Chem Soc, 126 (2004) 14679-14679.
[75] L. Manna, E.C. Scher, A.P. Alivisatos, J Am Chem Soc, 122 (2000) 12700-12706.
[76] N. Zhao, L.M. Qi, Adv Mater, 18 (2006) 359-+.
[77] H. Na, K. Woo, K. Lim, H.S. Jang, Nanoscale, 5 (2013) 4242-4251.
[78] Z.B. Zhuang, Q. Peng, Y.D. Li, Chem Soc Rev, 40 (2011) 5492-5513.
[79] Y.N. Xia, Y.J. Xiong, B. Lim, S.E. Skrabalak, Angew Chem Int Edit, 48 (2009) 60-103.
[80] H.X. Mai, Y.W. Zhang, R. Si, Z.G. Yan, L.D. Sun, L.P. You, C.H. Yan, J Am Chem Soc, 128 (2006) 6426-6436.
[81] H.E.H. J.R. Hook, Solid State Phys (2nd Edition),, 2010.
[82] R. Thoma, H. Insley, G. Hebert, Inorg Chem, 5 (1966) 1222-1229.
[83] F. Wang, Y. Han, C.S. Lim, Y. Lu, J. Wang, J. Xu, H. Chen, C. Zhang, M. Hong, X. Liu, Nature, 463 (2010) 1061-1065.
[84] Q. Liu, Y. Sun, T. Yang, W. Feng, C. Li, F. Li, J Am Chem Soc, 133 (2011) 17122-17125.
[85] A.D. Ostrowski, E.M. Chan, D.J. Gargas, E.M. Katz, G. Han, P.J. Schuck, D.J. Milliron, B.E. Cohen, ACS nano, 6 (2012) 2686-2692.
[86] Z.L. Wang, J. Hao, H.L. Chan, W.T. Wong, K.L. Wong, Small, 8 (2012) 1863-1868.
[87] Y.-W. Zhang, X. Sun, R. Si, L.-P. You, C.-H. Yan, J Am Chem Soc, 127 (2005) 3260-3261.
[88] C. Liu, H. Wang, X. Zhang, D. Chen, J Mater Chem, 19 (2009) 489-496.
[89] Z. Li, Y. Zhang, Nanotechnology, 19 (2008) 345606.
[90] H.-X. Mai, Y.-W. Zhang, L.-D. Sun, C.-H. Yan, The J Phy Chem C, 111 (2007) 13730-13739.
[91] J. Wang, H. Song, W. Xu, B. Dong, S. Xu, B. Chen, W. Yu, S. Zhang, Nanoscale, 5 (2013) 3412-3420.
[92] C. Liu, Z. Gao, J. Zeng, Y. Hou, F. Fang, Y. Li, R. Qiao, L. Shen, H. Lei, W. Yang, ACS nano, 7 (2013) 7227-7240.
[93] X.D. Liu, X. Zhang, G. Tian, W.Y. Yin, L. Yan, L.F. Ruan, Z.Y. Yang, D.B. Xiao, Z.J. Gu, Crystengcomm, 16 (2014) 5650-5661.
[94] N.J.J. Johnson, F.C.J.M. van Veggel, Nano Res, 6 (2013) 547-561.
[95] Y. Wu, W. Wu, X.M. Zou, L. Xu, J.C. Li, Mater Lett, 84 (2012) 147-150.
[96] H.L. Zhu, D.T. Zuo, J Phys Chem C, 113 (2009) 10402-10406.
[97] G.K. Das, L. Sudheendra, I.M. Kennedy, Proc Spie, 8956 (2014).
[98] G.J. Zhou, Y.M. Xu, Y.Z. Fu, Y. Yang, Y.C. Zhang, Int J Electrochem Sc, 9 (2014) 3990-3999.
[99] R. Buonsanti, M. Casavola, G. Caputo, P.D. Cozzoli, Recent Pat Nanotech, 1 (2007) 224-232.
[100] M. Casavola, R. Buonsanti, G. Caputo, P.D. Cozzoli, Eur J Inorg Chem, (2008) 837-854.
[101] H. Guo, Z.Q. Li, H.S. Qian, Y. Hu, I.N. Muhammad, Nanotechnology, 21 (2010).
[102] T.J. Zhou, M.H. Lu, Z.H. Zhang, H. Gong, W.S. Chin, B. Liu, Adv Mater, 22 (2010) 403-+.
[103] N.J.J. Johnson, A. Korinek, C.H. Dong, F.C.J.M. van Veggel, J Am Chem Soc, 134 (2012) 11068-11071.

[104] A.F. Khan, R. Yadav, P.K. Mukhopadhya, S. Singh, C. Dwivedi, V. Dutta, S. Chawla, J Nanopart Res, 13 (2011) 6837-6846.
[105] X.M. Li, F. Zhang, D.Y. Zhao, Nano Today, 8 (2013) 643-676.
[106] W. Shao, G.Y. Chen, T.Y. Ohulchanskyy, A. Kuzmin, J. Damasco, H.L. Qiu, C.H. Yang, H. Agren, P.N. Prasad, Adv Opt Mater, 3 (2015) 575-582.
[107] D.M. Yang, P.A. Ma, Z.Y. Hou, Z.Y. Cheng, C.X. Li, J. Lin, Chem Soc Rev, 44 (2015) 1416-1448.
[108] A. Xia, Y. Gao, J. Zhou, C.Y. Li, T.S. Yang, D.M. Wu, L.M. Wu, F.Y. Li, Biomaterials, 32 (2011) 7200-7208.
[109] W.L. Shi, H. Zeng, Y. Sahoo, T.Y. Ohulchanskyy, Y. Ding, Z.L. Wang, M. Swihart, P.N. Prasad, Nano Lett, 6 (2006) 875-881.
[110] K.W. Kwon, M. Shim, J Am Chem Soc, 127 (2005) 10269-10275.
[111] H.W. Gu, R.K. Zheng, X.X. Zhang, B. Xu, J Am Chem Soc, 126 (2004) 5664-5665.
[112] Z. Hens, D. Vanmaekelbergh, E.J.A.J. Stoffels, H. van Kempen, Phys Rev Lett, 88 (2002).
[113] H.X. Mai, Y.W. Zhang, L.D. Sun, C.H. Yan, J Phys Chem C, 111 (2007) 13721-13729.
[114] H.S. Qian, Y. Zhang, Langmuir, 24 (2008) 12123-12125.
[115] F. Wang, R.R. Deng, J. Wang, Q.X. Wang, Y. Han, H.M. Zhu, X.Y. Chen, X.G. Liu, Nat Mater, 10 (2011) 968-973.
[116] F. Wang, R.R. Deng, X.G. Liu, Nat Protoc, 9 (2014) 1634-1644.
[117] C. Zhang, J.Y. Lee, Acs Nano, 7 (2013) 4393-4402.
[118] K.A. Abel, J.C. Boyer, C.M. Andrei, F.C.J.M. van Veggel, J Phys Chem Lett, 2 (2011) 185-189.
[119] H. Wen, H. Zhu, X. Chen, T.F. Hung, B. Wang, G. Zhu, S.F. Yu, F. Wang, Angew Chem Int Edit, 125 (2013) 13661-13665.
[120] J. Pichaandi, J.C. Boyer, K.R. Delaney, F.C.J.M. van Veggel, J Phys Chem C, 115 (2011) 19054-19064.
[121] L. Chen, X.M. Li, D.K. Shen, L. Zhou, D. Zhu, C.H. Fan, F. Zhang, Anal Chem, 87 (2015) 5745-5752.
[122] O.G.R. Valencia, J.L.C. Espinola, M.C. Tellez, J Phys Conf Ser, 619 (2015).
[123] R.K. Capek, K. Lambert, D. Dorfs, P.F. Smet, D. Poelman, A. Eychmuller, Z. Hens, Chem Mater, 21 (2009) 1743-1749.
[124] B.C. Fitzmorris, J.K. Cooper, J. Edberg, S. Gul, J.H. Guo, J.Z. Zhang, J Phys Chem C, 116 (2012) 25065-25073.
[125] Q.Q. Dai, D.M. Li, J.J. Chang, Y.L. Song, S.H. Kan, H.Y. Chen, B. Zou, W.P. Xu, S.P. Xu, B.B. Liu, G.T. Zou, Nanotechnology, 18 (2007).
[126] X.M. Li, D.K. Shen, J.P. Yang, C. Yao, R.C. Che, F. Zhang, D.Y. Zhao, Chem Mater, 25 (2013) 106-112.
[127] R. Wang, X.M. Li, L. Zhou, F. Zhang, Angew Chem Int Edit, 53 (2014) 12086-12090.
[128] K.K. Haldar, N. Pradhan, A. Patra, Small, 9 (2013) 3424-3432.
[129] J.S. Lee, E.V. Shevchenko, D.V. Talapin, J Am Chem Soc, 130 (2008) 9673-+.
[130] S.L. He, H.W. Zhang, S. Delikanli, Y.L. Qin, M.T. Swihart, H. Zeng, J Phys Chem C, 113 (2009) 87-90.
[131] J.S. Son, J.S. Lee, E.V. Shevchenko, D.V. Talapin, J Phys Chem Lett, 4 (2013) 1918-1923.
[132] M. Zanella, A. Falqui, S. Kudera, L. Manna, M.F. Casula, W.J. Parak, J Mater Chem, 18 (2008) 4311-4317.
[133] J. Jiang, H.W. Gu, H.L. Shao, E. Devlin, G.C. Papaefthymiou, J.Y. Ying, Adv Mater, 20 (2008) 4403-4407.
[134] M.E.F. Brollo, R. Lopez-Ruiz, D. Muraca, S.J.A. Figueroa, K.R. Pirota, M. Knobel, Sci Rep-Uk, 4 (2014).
[135] J.M. Huang, Y.H. Sun, S.S. Huang, K. Yu, Q. Zhao, F. Peng, H. Yu, H.J. Wang, J. Yang, J Mater Chem, 21 (2011) 17930-17937.
[136] Y.W. Mao, P.W. Yi, Z.W. Deng, J.P. Ge, Crystengcomm, 15 (2013) 3575-3581.

[137] D. Muraca, O.F. Odio, E. Reguera, K.R. Pirota, Ieee T Magn, 49 (2013) 4606-4609.
[138] H. Zeng, S.H. Sun, Adv Funct Mater, 18 (2008) 391-400.
[139] J.T. Zhang, Y. Tang, K. Lee, O.Y. Min, Science, 327 (2010) 1634-1638.
[140] P. Guardia, K. Korobchevskaya, A. Casu, A. Genovese, L. Manna, A. Comin, Acs Nano, 7 (2013) 1045-1053.
[141] D. Wawrzynczyk, M. Nyk, A. Bednarkiewicz, W. Strek, M. Samoc, J Lumin, 133 (2013) 138-144.
[142] K.A. Abel, J.C. Boyer, F.C.J.M. van Veggel, J Am Chem Soc, 131 (2009) 14644-+.
[143] K.A. Abel, J.C. Boyer, F.C.J.M. van Veggel, J Am Chem Soc, 132 (2010) 5533-5533.
[144] X.M. Li, R. Wang, F. Zhang, L. Zhou, D.K. Shen, C. Yao, D.Y. Zhao, Sci Rep-Uk, 3 (2013).
[145] D.A. Hirsh, N.J.J. Johnson, F.C.J.M. van Veggel, R.W. Schurko, Chem Mater, 27 (2015) 6495-6507.
[146] H. Chen, Y.B. Lang, Y.L. Zhang, D. Zhao, G.S. Qin, C.F. Wu, K.Z. Zheng, W.P. Qin, J Mater Chem C, 3 (2015) 6314-6321.
[147] Q. Liu, W. Feng, T.S. Yang, T. Yi, F.Y. Li, Nat Protoc, 8 (2013) 2033-2044.
[148] H.Y. Peng, B.B. Ding, Y.C. Ma, S.Q. Sun, W. Tao, Y.C. Guo, H.C. Guo, X.Z. Yang, H.S. Qian, Appl Surf Sci, 357 (2015) 2408-2414.
[149] Y. Sun, X.J. Zhu, J.J. Peng, F.Y. Li, Acs Nano, 7 (2013) 11290-11300.
[150] X.S. Zhai, P.P. Lei, P. Zhang, Z. Wang, S.Y. Song, X. Xu, X.L. Liu, J. Feng, H.J. Zhang, Biomaterials, 65 (2015) 115-123.
[151] K. Prorok, A. Bednarkiewicz, B. Cichy, A. Gnach, M. Misiak, M. Sobczyk, W. Strek, Nanoscale, 6 (2014) 1855-1864.

Chapter 2 Emission Stability and Reversibility of Homogeneous Core-shell Upconversion Nanocrystals

Uniform core-shell growth as part of controlled engineering of core-shell nanocrystals, is significant for synthesizing bright UCNP nanocrystals. In the chapter 2, I mainly focus on the study of controlled growth of homogeneous core-shell nanocrystals. I aim to investigate a simple method for the homogeneous core-shell nanocrystal synthesis via adjusting the ratio of oleic acid and oleylamine.

Coating UNCP nanocrystal with an inert shell is an efficient way to enhance their luminescence. However, highly controlled uniform inert shell growth is still difficult for UCNPs. I found that oleic acid and oleylamine as co-surfactants with a right balance can result in homogeneous core-shell $NaYF_4$ nanocrystals. The intact shells at controlled thickness is useful in fully protecting the core nanocrystal from queening by the surface ligands and solvent. I found the passivation effect by the intact shells will not only enhance the luminescence intensity but also improve the emission stability against temperature and pH variations for more robust performance in biomedical applications.

This chapter was initially developed to study controlled synthesis of core-shell upconversion nanocrystals. One of the technique challenges was to realize coating of uniform shells onto an upconversion nanocrystal core. I found a simple robust technique for homogeneous shell growth by adjusting the amount of oleylamine (see supplementary Figure 1). The field has progressed so quickly and several research groups have reported the uniform centrosymmetric core-shell structures during my PhD candidature. This makes my preliminary results not publishable. After several discussions with my supervisor, we decided on extending my growth technique to study the upconversion emission stability and reversibility at different pH and temperature conditions. This work adds new values by providing new characterization results for advanced design of the upconversion nanocrystals based

temperature sensors or probes for pH responsive applications, which were now summarized as a manuscript accepted by *Journal of Materials Chemistry C*.

2.1 Contribution to Paper 1

	D.L	X.X	F.W	J.Z	C.M	L.Z	C.M	Y.L	E.G	J.L	D.J
Experiment Design	•										
Sample Preparation	•				•						
Data Collection	•		•			•	•				
Analysis	•	•		•				•			
Manuscript	•	•							•	•	•

This project has been primarily carried out by myself on my second year of PhD, which reflects my independence in conducting research from concept development, experimental design, sample preparations, data collections and analysis, to the final stage of publication preparation.

2.2 Paper 1

Liu D., Xu X., Wang F., Zhou J., Mi C., Zhang L., Lu Y., Ma C., Ewa G., Lin J. and Jin, D., Emission stability and reversibility of upconversion nanocrystals. *Journal of Materials Chemistry C*.(2016), advance online publication 5th September 2016, doi: 10.1039/C6TC02990F

Journal of Materials Chemistry C

PAPER

View Article Online
View Journal

Cite this: DOI: 10.1039/c6tc02990f

Emission stability and reversibility of upconversion nanocrystals†

Deming Liu,[abc] Xiaoxue Xu,*[abc] Fan Wang,[abc] Jiajia Zhou,[cd] Chao Mi,[bc] Lixin Zhang,[a] Yiqing Lu,[a] Chenshuo Ma,[a] Ewa Goldys,[a] Jun Lin[ce] and Dayong Jin*[abc]

Received 15th July 2016,
Accepted 2nd September 2016

DOI: 10.1039/c6tc02990f

www.rsc.org/MaterialsC

Rare-earth doped upconversion nanocrystals have emerged as a novel class of luminescent probes for biomedical applications. The knowledge about their optical stability in aqueous solution under different pH and temperature conditions has not been comprehensively explored. Here we conduct a systematic investigation and report the emission stability and reversibility of typical $NaYF_4$:Yb^{3+},Er^{3+} nanocrystals and their core–shell nanostructures in aqueous solution at different temperatures and with different pH values. These nanocrystals show reversible luminescence response to temperature changes, while low pH permanently quenches their luminescence. With the addition of inert shells, with thicknesses ranging from 1.5 nm to 8 nm, the emission stability and reversibility change significantly. Thicker inert shells not only lead to a significant enhancement in the emission intensity but also stabilize its optical responses which become less affected by temperature variations and pH conditions. This study suggests that upconversion nanocrystal-based sensitive temperature and pH sensors do not generally benefit from the core–shell structure usually recommended for enhanced upconversion luminescence.

Introduction

Lanthanide-doped upconversion nanoparticles (UCNPs) that absorb near infrared excitation and exhibit anti-Stokes emission in visible and ultra-violet regions have attracted significant interest in the last decade.[1,2] They offer key advantages in bioimaging and luminescence detection including low detection background, tunable emission spectrum[3] and decay lifetime,[4,5] the absence of photo-bleaching and blinking,[6,7] deep penetration of the excitation light,[8] and low toxicity with excellent chemical and biological compatibility.[9,10] They are widely regarded as ideal luminescent probes for a range of biomedical applications, such as ultrasensitive biomolecular assays,[11–14] multimodal biomedical imaging,[15–21] and photodynamic therapies.[22,23]

Several groups reported that UCNPs can serve as accurate nanoscale sensors for intracellular monitoring of temperature[24] or pH.[25] They can also be applied as photoresponsive carriers for controlled delivery and release of drugs *in vivo*,[26–31] where high temperature and/or lower pH conditions trigger drug release. The ratio-metric green emissions of Er^{3+} doped UCNPs are sensitive to cellular temperature with a resolution of 0.5 °C in the biological range of 25 °C to 45 °C.[32] The red emission of the Er^{3+} UCNPs was found to be responsive to pH variations and to increase at low pH.[32] Li and co-workers recently reported a hybrid design of carbon@ inert shell @UCNPs for real-time monitoring of the localized temperature increase during photodynamic therapy.[33] We demonstrated a drug release sensing scheme by using the luminescence intensity of UCNPs. In this scheme we monitored the drug release process in the low pH environment (around pH = 5), as the drug on the surface of UCNPs was designed to quench the luminescence increase upon drug release.[34]

The understanding of luminescence responses to the varied temperature and pH environment[35–37] require more detailed consideration of the stability and reversibility of UCNP luminescence under different pH and temperature conditions. The literature reports on the subject remain scattered. Wei *et al.* reported the stable emission of the UC nanocrystals with different surface ligands, but it was only tested at neutral pH in aqueous solutions.[38] Li *et al.* reported the thermal stability of UCNPs and an anomalous relationship between temperature and the upconversion luminescence.[39,40] Xu *et al.* reported that

[a] *Advanced Cytometry Labs, ARC Centre of Excellence for Nanoscale BioPhotonics, Macquarie University, Sydney, NSW, 2109, Australia. E-mail: xiaoxue.xu@mq.edu.au, dayong.jin@uts.edu.au*
[b] *Institute for Biomedical Materials and Devices, Faculty of Science, University of Technology Sydney, NSW, 2007, Australia*
[c] *Australian Research Council Research Hub for Integrated Device for End-user Analysis at Low-levels (IDEAL), Faculty of Science, University of Technology Sydney, NSW, 2007, Australia*
[d] *College of Optical Science and Engineering, State Key Laboratory of Modern Optical Instrumentation, Zhejiang University, Hangzhou, 310027, P. R. China*
[e] *State Key Laboratory of Rare Earth Resource Utilization, Changchun Institute of Applied Chemistry, Chinese Academy of Sciences, Changchun, 130022, P. R. China*
† Electronic supplementary information (ESI) available. See DOI: 10.1039/c6tc02990f

α-NaYb(Mn)F_4:Er^{3+}@$NaYF_4$ UCNPs can be applied as luminescent nano-thermometers over a wide temperature range. But these tests were done only for the dry powder.

Coating inert shells onto the core UCNPs is a well-established and effective solution to minimize the surface quenching effect and therefore to enhance the upconversion luminescence by a factor of several to hundreds, depending on the core size and shell thickness.[41–44] However, the role of the inert shells in influencing the stability and reversibility of luminescence at varied pH and temperature in aqueous solution has not yet been investigated.

In this work, we systematically investigated and compared the luminescence response of Er^{3+} doped UCNPs to different pH and temperature values in aqueous solution for both core-only and core–shell UCNPs. Using a modified hot-injection method, we prepared a systematic series of UCNPs by epitaxial growth of the homogeneous $NaYF_4$:Yb^{3+},Er^{3+} UCNPs with different shell thicknesses from 1.5 to 8 nm. To characterize these nanoparticles in aqueous solution, we removed the surface organic ligand of oleic acids and transfer the hydrophilic UCNPs into the aqueous phase using an acid-based ligand removal method reported by Capobianco *et al.*[45] We chose this approach to reduce the influence of surface ligands[38] on UCNP upconversion luminescence. Our results show that the luminescence intensity of UCNPs decreases in either an acid or an alkali pH environment. In an acidic environment this luminescence decrease is not reversible. Conversely, higher temperature significantly reduces the luminescence intensity in a reversible way. The inert shell also reduces the sensitivity and resolution of the ratiometric response of green emissions (524 nm/545 nm) of Er^{3+} doped UCNPs for temperature sensing below 60 °C. This work compliments the current knowledge underpinning the rapid development of upconversion nanosensors for emerging biomedical applications and further suggests that new careful designs are necessary to accurately sense temperature and pH in specific applications.

Materials and methods

Yttrium chloride hexahydrate (YCl_3·$6H_2O$, 99.99%), ytterbium chloride hexahydrate ($YbCl_3$·$6H_2O$, 99.998%), erbium chloride hexahydrate ($ErCl_3$·$6H_2O$, 99.9%), sodium hydroxide (NaOH, 98%), ammonium fluoride (NH_4F, 99.99%), oleic acid (OA, 90%), 1-octadecene (ODE, 90%) and hydrochloric acid (HCl, 37%) were purchased from Sigma-Aldrich. Oleylamine (OM, 90%) was purchased from Pfaltz & Bauer. All reagents were used as received without further purification.

Synthesis of β-$NaYF_4$:Yb^{3+},Er^{3+} cores

A modified synthesis method was adopted to prepare β-$NaYF_4$:20%Yb^{3+},2%Er^{3+} as core UCNPs. In a typical procedure, 1 mL of $LnCl_3$ in methanol (1.0 mmol, Ln = Y, Yb, Er) was mixed with OA (6 mL) and ODE (15 mL) in a 100 mL three-neck round-bottom flask. The mixture solution was degassed under Ar flow during the heating up to 150 °C followed by 30 min isothermal reaction to form a clear solution, and then cooled down to room temperature. 10 mL of methanol containing NH_4F (4 mmol) and NaOH (2.5 mmol) was added to the flask and then stirred for 60 min. The solution was slowly heated up to 110 °C and kept at 110 °C for 30 min to completely remove the methanol and any residual water. Then the reaction solution was quickly heated up to 310 °C and kept isothermally for 1 h, before being cooled down to room temperature. Ethanol was added to precipitate the nanocrystals, which were washed 4 times with cyclohexane, ethanol and methanol. The obtained pure $NaYF_4$:Yb^{3+},Er^{3+} nanocrystals were re-dispersed in 10 mL of cyclohexane for coating the inert shell.

Synthesis of α-$NaYF_4$ shell precursors

A modified literature method[46] was used, with all the preparation and pre-treatment steps similar to that in the $NaYF_4$:Yb^{3+},Er^{3+} core synthesis method. The only two differences were that the lanthanide precursor was changed to be 1 mmol YCl_3 and the reaction temperature became 290 °C (instead of 310 °C). After the reaction, the nanoparticles were washed and re-dispersed in cyclohexane. The obtained pure α-$NaYF_4$ seeds in cyclohexane solution was mixed with 10 mL of ODE in one 100 mL three-neck flask. Then, the mixture was kept at 110 °C for 30 min under Ar flow. After the mixture was cooled to room temperature, α-$NaYF_4$ ODE solution as the precursor of the inert shell was obtained.

Synthesis of β-$NaYF_4$:Yb^{3+},Er^{3+}@$NaYF_4$ core–shell nanocrystals

A modified hot-injection method[46] was used for growing undoped shells onto the core nanocrystals. 1 mL (0.2 mmol Ln^{3+}) the obtained $NaYF_4$:Yb^{3+},Er^{3+} core cyclohexane stock solution was mixed with OA (5 mL), OM (1 mL) and ODE (8 mL) in a 100 mL three-neck flask. The mixture was degassed under Ar flow and kept at 110 °C for 30 min to completely remove cyclohexane as well as any residual water. After that, it was quickly heated to 305 °C and the pure α-$NaYF_4$ seeds in ODE solution were injected using a syringe (injection rate: 0.05 mmol α-$NaYF_4$ seed solution every 10 min; for total amounts of injected α-$NaYF_4$ seeds for shells of different thicknesses refer to Table S1, ESI†). After the reaction, the precipitate was washed and stored in cyclohexane.

Characterization

Standard transmission electron microscope (TEM) measurements were performed using a Philips CM10 TEM equipped with an Olympus Sis Megaview G2 Digital Camera. The samples were prepared for TEM analysis by placing a drop of a dilute suspension of nanocrystals onto formvar-coated copper grids (300 meshes) and were allowed to dry in a desiccator at room temperature before use. Powder X-ray diffraction (XRD) patterns were obtained on a PANalytical X'Pert Pro MPD X-ray diffractometer using Cu Ka1 radiation (40 kV, 40 mA, λ = 0.15418 nm). The XRD samples were prepared by repeatedly drying drops of nanocrystal dispersions in cyclohexane cast on a zero-background silicon wafer. The temperature-dependent and pH dependent upconversion luminescence spectra of colloidal

solutions in quartz cuvettes with 10 mm path length were acquired using a Fluorolog-Tau3 spectrofluorometer (JobinYvon-Horiba) equipped with an external 980 nm CW diode laser with a pump power of 200 mW. UCNPs in the aqueous dispersion were tuned to the same number concentration. Temperature control is *via* a homemade water bath equipment. The pH values of UCNPs dispersed in aqueous solution were adjusted using Milli-Q water and the PBS solutions with pH 3 and 12 respectively. The luminescence lifetimes were measured using a purpose-built high-throughput 3-dimensional time-resolved spectrometer,[47] with pulsed 980 nm laser excitation (100 mW) at a repetition rate of 50 Hz.

Results and discussion

Fig. 1 illustrates our design of the experiments to systematically study the luminescence response of core–shell UCNPs in aqueous solution in varying pH and temperature environments. Homogeneous core–shell structures were synthesized on the $NaYF_4$:Yb^{3+},Er^{3+} core UCNPs by controlling the amount of OM in a hot injection method (Fig. S1, ESI†). The shell thickness of homogeneous core–shell UCNPs was controlled by adjusting the amount of shell precursors. (Table S1, ESI†). Fig. S2 (ESI†) showed that the 24 nm β-$NaYF_4$:Yb^{3+},Er^{3+} core was sequentially coated with a series of $NaYF_4$ shells of different thicknesses. These samples were treated with a diluted acid solution to remove the surface ligands so that the as-prepared UCNPs became hydrophilic and were transferred into aqueous solution (Fig. 1a). Such ligand-free UCNPs will avoid the test influence from surface ligands. Fig. 1b–k shows the morphology characterization of the as-prepared hydrophilic core and core–shell UCNP samples. $NaYF_4$:Yb^{3+},Er^{3+} core UCNPs displayed uniform spherical shape, with an average size of 24.1 nm (Fig. 1b and g) and a narrow size distribution. The core–shell nanocrystals were also spherical, with average sizes of 27.2 nm, 28.9 nm, 33.2 nm and 40.2 nm, respectively, and have narrow size distribution (Fig. 1c–f). Their average shell thickness was calculated by comparing the average diameters of core and core–shell nanocrystals[48] from Fig. 1(g–k).

Fig. 2(a) illustrates the major four emissions' energy transfer processes between energy levels of Yb^{3+} and Er^{3+} under 980 nm light excitation. The three-dimensional time resolved luminescence spectrum of UCNPs was obtained by high-throughput time-resolved luminescence spectroscopy that simultaneously provides the emission spectrum and the lifetime decay curve, as shown in Fig. 2(b). The luminescence enhancement and increased lifetimes due to coating of the UCNPs with the inert

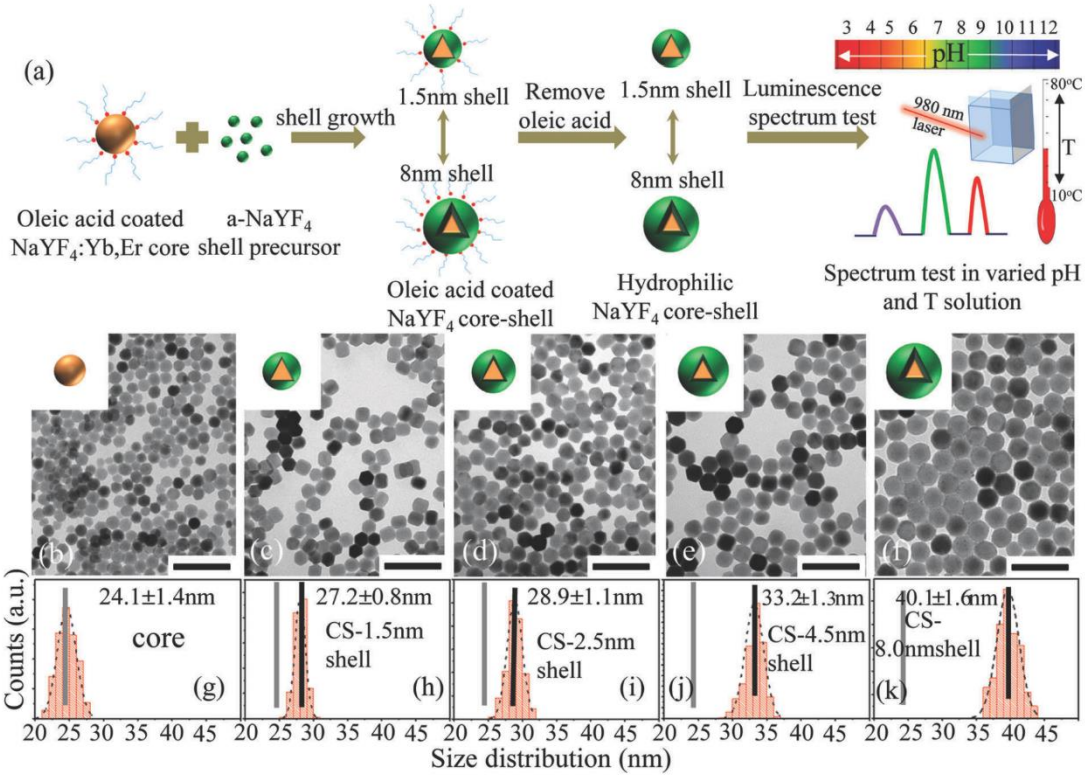

Fig. 1 Synthesis and testing of the core and core–shell UCNPs' luminescence response to varying pH and temperature environments (a), TEM images and size distribution charts of core-only (b, g) and core–shell UCNPs with 1.5 nm (c, h), 2.5 nm (d, i), 4.5 nm (e, j) and 8.0 nm (f, k) homogeneous $NaYF_4$ shells. (Scale bar: 50 nm).

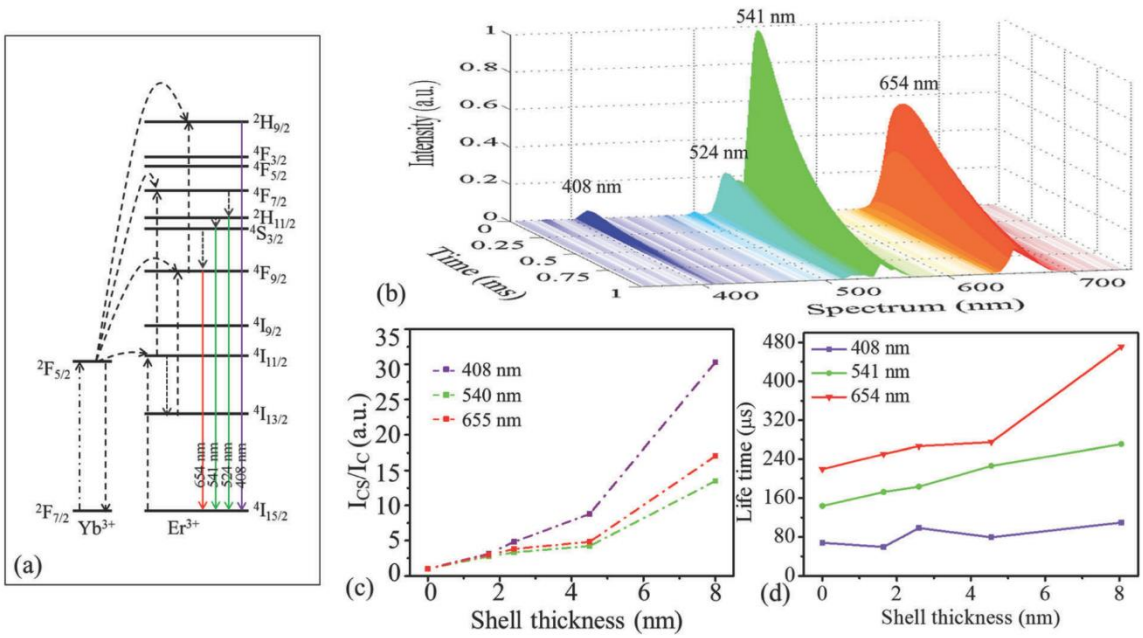

Fig. 2 (a) Schematic illustration of the transition energy levels of $NaYF_4:Yb^{3+},Er^{3+}$ nanocrystals. Arrows indicate: – · ➔ NIR excitation, – – ➔ energ transfers, ---➔ multiphonon nonradiative relaxation, ⟶, ⟶, ⟶ and upconversion emissions. (b) Typical real-time resolved emissio spectrum of $NaYF_4:Yb^{3+},Er^{3+}$ UCNPs. Intensity enhancement factors (c) and luminescence decay lifetimes (d) for emissions at 408 nm, 540 nm an 655 nm were plotted as functions of shell thickness.

shells (as shown in Fig. S3 and S4, ESI†) was consistent with other reports in the literature.[43,46,49–51] Fig. 2(c) shows that the enhancement of emissions increased with increased thickness of the shells, while enhancement factors at varied emission positions were also different. The emission peaks at 408 nm, 540 nm, and 655 nm were only enhanced by about 3 times by coating a 1.5 nm inert $NaYF_4$ shell, and the enhancement factors of 30, 12 and 15 were achieved for these peaks when a 8 nm shell was coated. Similar exceptional enhancement of violet emissions was also observed for the $NaYF_4:Yb^{3+},Tm^{3+}$@ CaF_2 core–shell nanocrystals.[52] This suggested that higher order energy transfer processes benefited more from the inert shell protection. The luminescence lifetime data, shown in Fig. 2(d), further confirmed that the uniform shells were coated onto the core UCNPs. The luminescence lifetimes from the three emission bands (violet, green and red) increased with thicker shells. Both these strongly enhanced emission intensities and significantly longer lifetimes confirmed the successful growth of a series of homogeneous core–shell UCNPs.

Fig. 3 and Fig. S5 (ESI†) show the impact of the shell on the luminescence stability and reversibility against pH changes. The luminescence spectra of core-only and core–shell UCNPs were tested in aqueous solution under varying pH values. Fig. S5 (ESI†) shows that the acidic solution had a strong quenching effect on the UCNPs' luminescence and the inert shells were able to alleviate the quenching to some degree. Both the green and red emissions displayed similar emission quenching trends with the pH decrease (Fig. 3(a)). The green emission from the core UCNPs decreased to 28% of its initial intensity with the pH decreasing from 7 to 3, while the green emission from the core–shell UCNPs onl decreased to about 65% of its original intensity. The alkalin conditions have been found to have less influence on th emissions. The emission from the core UCNPs was reduce only by 20% with the pH increasing from 7 to 12, while th emission from core–shell UCNPs only experienced a sligh decrease under alkaline conditions. These data showed tha the inert shells help in improving the luminescence stabilit against pH changes.

Fig. 3(b) shows the luminescence reversibility of luminescenc of the core and core–shell UCNPs when repeatedly varying the pH conditions between pH = 4 and pH = 7. The quenching effect b the acidic aqueous solution was not reversible regardless of th presence of thick inert shells. Once the pH of the samples wa decreased to pH = 4 for less than ten minutes, irreversibl luminescence quenching occurred. Luminescence in thes samples did not recover even by bringing the pH back to 7 The irreversible luminescence quenching of the UNCPs in th acidic environment suggested that the crystal surface may experi ence chemical damage under low pH conditions. To prove this we carefully compared the TEM images of ligand free UCNP before (Fig. 3(c)) and after (Fig. 3(d)) treatment with the pH = acid solution for 1 hour. Interestingly, we observed an obviou decrease in size from 24 nm to 21 nm and a rough surfac morphology, showing that the nanocrystals were chemicall etched. This chemical damage from weak acid was also foun in other rare earth fluoride nanocrystals, such as $NaEuF_4$[53] an $Lu_6O_5F_8$.[54] We attributed this to the dissociation of Ln–F bond of the $NaYF_4$ nanocrystals in the solution with low pH ($\leq$3).

View Article Online
Journal of Materials Chemistry C Paper

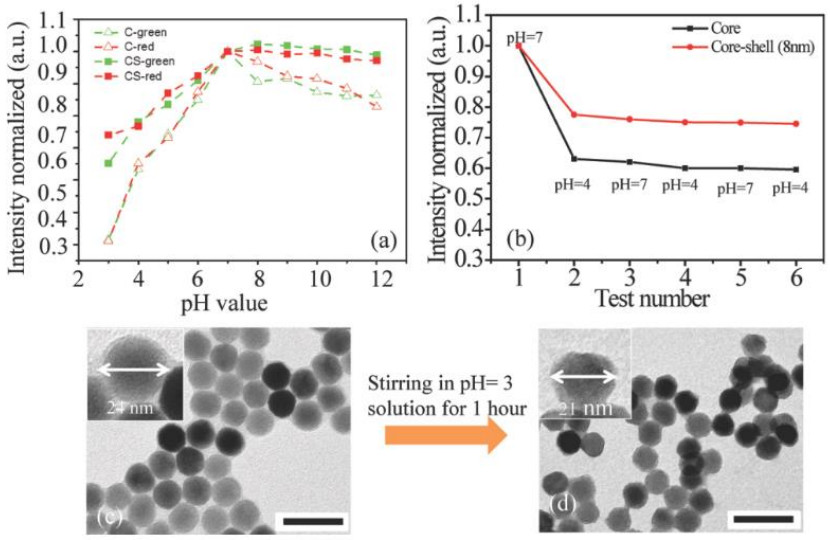

Fig. 3 (a) Luminescence responses of the $NaYF_4$:Yb^{3+},Er^{3+}core UCNPs and $NaYF_4$:Yb^{3+},Er^{3+}@$NaYF_4$ core–shell UCNPs in the green (524 nm and 545 nm) and red emission bands. The data were normalized at pH = 7 and plotted as a function of pH values of the solution. (b) The reversibility test for the 655 nm emissions of the core and core–shell UCNPs by switching the pH values between pH = 4 and pH = 7. TEM images of ligand free UCNPs before (c) and after (d) stirring in pH = 3 solution for 1 hour. The inset TEM images in (c) and (d) show the size changes of UCNPs before and after the treatment. (Scale bar is 50 nm).

We further measured the spectra of $NaYF_4$:Yb^{3+},Er^{3+} core-only and core–shell UCNPs in Milli-Q water at various temperatures from 10 °C to 80 °C (shown in Fig. 4 and Fig. S6, ESI†). Fig. S6a and b (ESI†) shows the luminescence intensities of both core-only and core–shell nanocrystals decreased at a higher temperature with the core UCNPs being more strongly affected. The green emission of the core-only UCNPs decreased quickly to 78% of its original intensity even when the temperature was increased only from 10 °C to 30 °C. With a further temperature increase from 30 °C to 80 °C, the green emission decreased to nearly half of its original intensity at 10 °C. The shell protection again was found to alleviate the temperature-induced quenching, with the green emission from the core–shell UCNPs decreasing by only 27% at 80 °C. The quenching of the red emission was similar to the green emission, when it occurred at lower temperatures from 10 °C to 40 °C. However, the red emission has slightly higher stability than the green emission in the higher temperature range from 40 °C to 80 °C. We think that the reason for red emission receiving a lower quenching effect than the green emission at the higher temperature range is due to an increase of population transition from $^4S_{3/2}$ to $^4F_{9/2}$. According to Xiaogang Liu group's investigation[55] on the relationship between relative emission intensity and nanocrystal surface defects that the higher energy level excited state would receive multiphonon nonradioactive relaxation from surface quenchers. The relative low energy level of $^4F_{9/2}$ would receive some population from the higher energy levels (*e.g.* $^4S_{3/2}$), and therefore the red emission presents relatively higher stability than the green emission at a higher temperature.

Fig. 4(b) demonstrates the reversibility of the luminescence emission against temperature, and it shows that the emission

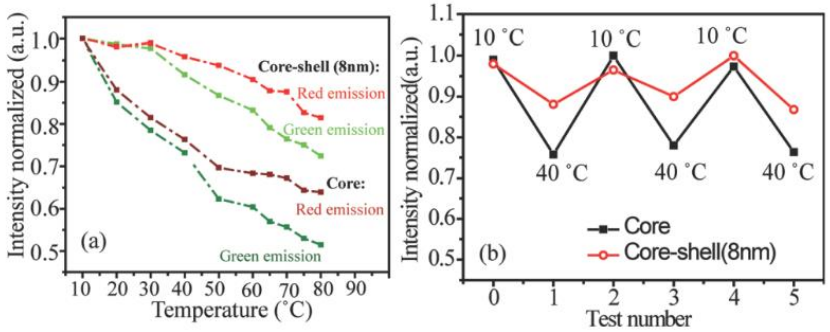

Fig. 4 (a) The intensity response at green and red bands for the core and core–shell UCNPs as a function of temperature. The data were normalized at 10 °C; (b) green emission intensity response as a function of temperature repeatedly switched between 10 °C and 40 °C.

View Article Online

Paper Journal of Materials Chemistry C

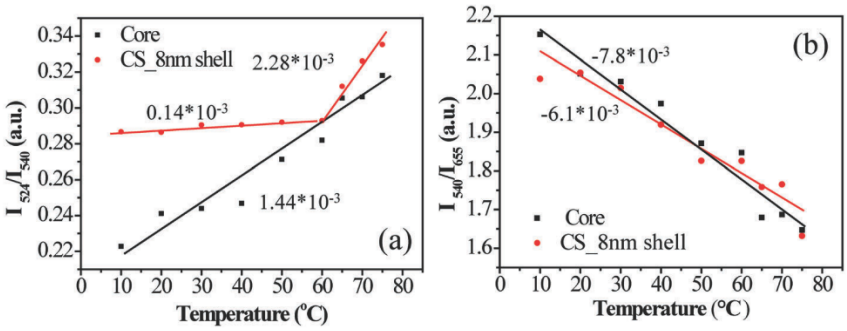

Fig. 5 Emission intensity ratio (a) of 524 nm/540 nm from core and core–shell UCNPs and (b) emission intensity ratio of 540 nm/655 nm from core and core–shell UCNPs as a function of temperature.

intensities of both the core-only and core–shell nanocrystals followed the temperature change between 10 °C and 40 °C, and these changes were fully reversible. The degree of intensity variations for the core–shell nanocrystals was lower than that of the core nanocrystals. These results suggested that the core–shell structure of $NaYF_4$:Yb^{3+},Er^{3+}/$NaYF_4$ has a less pronounced response to temperature variations, especially in the range from 10 °C to 40 °C, relevant for *in vivo* biomedical applications. The observed improvement in emission stability by coating the passivation shell suggested that the inert shell can effectively reduce the quenching effect from the vibrational energies and optical traps arising from the particle surface. The water molecule is known as a surface oscillator that significantly quenches the luminescence of lanthanide dopant ions, because of the high energy (*ca.* 3500 cm^{-1}) of the stretching vibration. As the temperature increases, the water molecular on the crystal surface could be more intensely vibrating, which may affect the Ln–F bond on the crystal surface and create more phonons. By coating the inert shell structure, forming a gap between the emitters and the quenchers can effectively reduce the quenching effect caused by a temperature increase.

The ratiometric emissions (I_{524}/I_{540}) from the $NaYF_4$:Yb^{3+},Er^{3+} UCNPs have been broadly used in nanoscale thermometry[56] because the population distributions on $^2H_{11/2}$ and $^4S_{3/2}$ are dominated by Boltzmann's thermal distribution and elevated temperature leads to rapid population of the $^2H_{11/2}$ state.[57] Fig. 5 shows the intensity ratios of 524 nm to 540 nm (I_{524}/I_{540}) and 540 nm to 655 nm (I_{540}/I_{655}) emissions for the core-only and core–shell nanocrystals. The ratio of I_{524}/I_{540} in Fig. 5(a) for the core nanocrystals shows a linear increase with temperature in the range from 10 °C to 80 °C, which is consistent with previously reported results.[57,58] The ratio of I_{524}/I_{540} of core–shell nanocrystals is slightly higher than that of core-only nanocrystals at 10 °C, which suggests that the inert shell effectively saved some population on $^2H_{11/2}$ from nonradioactive relaxation. As the temperature was increased from 10 °C to 60 °C, the ratio of I_{524}/I_{540} of core–shell nanocrystals slightly increases; however, the ratio increases quickly when the temperature was increased from 60 °C to 75 °C. This anomalous temperature-dependent phenomenon was also found and reported by other groups for small sized upconversion nanocrystals.[59] The population distribution changes on $^2H_{11/2}$ and $^4S_{3/2}$ could be caused by surface defects and surface molecular quenchers (*e.g.* water molecular vibration) and temperature. Higher temperature helps to increase the population distribution on $^2H_{11/2}$. On the other hand, stronger surface quenchers would decrease the population on $^2H_{11/2}$ compared to that on $^4S_{3/2}$ because the higher level excited state of $^2H_{11/2}$ could receive more quenching effects.[55] At elevated temperatures, not only the thermal factor of nanocrystals would become larger but also the surface quenching effect would be stronger. The slow increase rate of I_{524}/I_{540} of core–shell nanocrystals in the low temperature range is due to the competition of the two different effects. Due to the inert shell which effectively blocks the quenching effect at high temperatures, the fast increasing rate of I_{524}/I_{540} can attribute to the sole thermal factor. These data suggested that the core–shell UCNPs may not be sensitive for temperature measurements in the temperature range from 10 °C to 60 °C.

Fig. 5(b) further shows that the ratios of I_{540}/I_{655} emissions for the core and core–shell nanocrystals linearly decreased with temperature between 10 °C to 80 °C, which was consistent with the results reported by other authors.[57] Higher temperature increases the comparative influence of the non-radiative relaxation channels, from $^4I_{11/2}$ to $^4I_{13/2}$ and from $^4S_{3/2}$, $^2H_{11/2}$ to $^4F_{9/2}$, leading to an increase of the ratio of I_{540}/I_{655} emission.

Conclusion

In summary, we demonstrated here that oleic acid and oleylamine as co-surfactants with a right balance can be used to synthesize homogeneous core–shell $NaYF_4$ nanocrystals. The intact shells with controlled thickness were useful in fully protecting the core nanocrystal from quenching by the surface ligands and solvent. This passivation effect by the intact shells enhanced the luminescence intensities particularly for violet emissions by a factor of up to 30 times. Our key finding reported here is that coating UCNPs with the inert shells improved the luminescent emission stability and reversibility of UCNPs against quenching caused by increased temperature or decreased pH. Moreover, we found that the upconversion emissions at different temperatures for both core-only and core–shell UCNPs were fully recoverable, but

once the UCNPs experienced lower pH conditions (<pH = 7) their luminescence was observed to be permanently quenched suggesting that the acidic environment could chemically damage the surface of the nanocrystals. Furthermore, by a careful characterization, we found that the ratiometric emissions from the core–shell UCNPs were less sensitive to the response to the temperature changes in the range from 10 °C to 60 °C. This work suggests that the luminescence stability and reversibility properties of UCNPs and their core–shell design should be taken into consideration for nanoscale bio-sensing applications in various temperature and pH conditions.

Acknowledgements

We thank D. Birch and Nicole in the Microscope Unit at Macquarie University for their help with TEM characterization. This project is primarily supported by the Australian Research Council (ARC) Future Fellowship Scheme (FT 130100517; D. Jin), Macquarie University Research Fellowship Scheme (X. Xu) and China Scholarship Council CSC scholarships (No. 201206170136, D. Liu). D. Jin and E. Goldys acknowledge partial support from the ARC Centre of Excellence for Nanoscale Biophotonics CE14010003.

References

1 B. Zhou, B. Y. Shi, D. Y. Jin and X. G. Liu, *Nat. Nanotechnol.*, 2015, **10**, 924–936.
2 D. Liu, X. Xu, Y. Du, X. Qin, Y. Zhang, C. Ma, S. Wen, W. Ren, E. M. Goldys, J. A. Piper, S. Dou, X. Liu and D. Jin, *Nat. Commun.*, 2016, **7**, 10254, DOI: 10.1038/ncomms10254.
3 F. Wang and X. Liu, *J. Am. Chem. Soc.*, 2008, **130**, 5642–5643.
4 Y. Lu, J. Zhao, R. Zhang, Y. Liu, D. Liu, E. M. Goldys, X. Yang, P. Xi, A. Sunna and J. Lu, *Nat. Photonics*, 2014, **8**, 32–36.
5 J. B. Zhao, Z. D. Lu, Y. D. Yin, C. Mcrae, J. A. Piper, J. M. Dawes, D. Y. Jin and E. M. Goldys, *Nanoscale*, 2013, **5**, 944–952.
6 J. Shen, L. Zhao and G. Han, *Adv. Drug Delivery Rev.*, 2013, **65**, 744–755.
7 S. Wu, G. Han, D. J. Milliron, S. Aloni, V. Altoe, D. V. Talapin, B. E. Cohen and P. J. Schuck, *Proc. Natl. Acad. Sci. U. S. A.*, 2009, **106**, 10917–10921.
8 D. Lu, S. K. Cho, S. Ahn, L. Brun, C. J. Summers and W. Park, *ACS Nano*, 2014, **8**, 7780–7792.
9 A. Gnach, T. Lipinski, A. Bednarkiewicz, J. Rybka and J. A. Capobianco, *Chem. Soc. Rev.*, 2015, **44**, 1561–1584.
10 D. E. Achatz, R. Ali and O. S. Wolfbeis, *Top. Curr. Chem.*, Springer, 2010, pp. 29–50.
11 D. E. Achatz, R. Ali and O. S. Wolfbeis, *Top. Curr. Chem.*, 2011, vol. 300, pp. 29–50.
12 Q. Liu, J. J. Peng, L. N. Sun and F. Y. Li, *ACS Nano*, 2011, **5**, 8040–8048.
13 R. Arppe, T. Näreoja, S. Nylund, L. Mattsson, S. Koho, J. M. Rosenholm, T. Soukka and M. Schäferling, *Nanoscale*, 2014, **6**, 6837–6843.
14 K. L. Wong, G. L. Law, Y. Y. Yang and W. T. Wong, *Adv. Mater.*, 2006, **18**, 1051–1054.
15 L. Cheng, C. Wang and Z. Liu, *Nanoscale*, 2013, **5**, 23–37.
16 W. Zheng, S. Y. Zhou, Z. Chen, P. Hu, Y. S. Liu, D. T. Tu, H. M. Zhu, R. F. Li, M. D. Huang and X. Y. Chen, *Angew. Chem., Int. Ed.*, 2013, **52**, 6671–6676.
17 Q. Liu, W. Feng, T. S. Yang, T. Yi and F. Y. Li, *Nat. Protoc.*, 2013, **8**, 2033–2044.
18 P. Huang, W. Zheng, S. Zhou, D. Tu, Z. Chen, H. Zhu, R. Li, E. Ma, M. Huang and X. Chen, *Angew. Chem., Int. Ed.*, 2014, **53**, 1252–1257.
19 Y. Min, J. Li, F. Liu, E. K. Yeow and B. Xing, *Angew. Chem., Int. Ed.*, 2014, **53**, 1012–1016.
20 Y. Yang, Q. Shao, R. Deng, C. Wang, X. Teng, K. Cheng, Z. Cheng, L. Huang, Z. Liu and X. Liu, *Angew. Chem., Int. Ed.*, 2012, **51**, 3125–3129.
21 X. Wu, Y. Zhang, K. Takle, O. Bilsel, Z. Li, H. Lee, Z. Zhang, D. Li, W. Fan and C. Duan, *ACS Nano*, 2016, **10**, 1060–1066.
22 D. M. Yang, P. A. Ma, Z. Y. Hou, Z. Y. Cheng, C. X. Li and J. Lin, *Chem. Soc. Rev.*, 2015, **44**, 1416–1448.
23 Y. M. Yang, *Microchim. Acta*, 2014, **181**, 263–294.
24 F. Vetrone, R. Naccache, A. Zamarron, A. Juarranz de la Fuente, F. Sanz-Rodríguez, L. Martinez Maestro, E. Martín Rodriguez, D. Jaque, J. García Solé and J. A. Capobianco, *ACS Nano*, 2010, **4**, 3254–3258.
25 R. J. Meier, J. M. Simbürger, T. Soukka and M. Schäferling, *Anal. Chem.*, 2014, **86**, 5535–5540.
26 Y. L. Dai, P. A. Ma, Z. Y. Cheng, X. J. Kang, X. Zhang, Z. Y. Hou, C. X. Li, D. M. Yang, X. F. Zhai and J. Lin, *ACS Nano*, 2012, **6**, 3327–3338.
27 Z. Y. Hou, C. X. Li, P. A. Ma, Z. Y. Cheng, X. J. Li, X. Zhang, Y. L. Dai, D. M. Yang, H. Z. Lian and J. Lin, *Adv. Funct. Mater.*, 2012, **22**, 2713–2722.
28 X. Zhang, P. P. Yang, Y. L. Dai, P. A. Ma, X. J. Li, Z. Y. Cheng, Z. Y. Hou, X. J. Kang, C. X. Li and J. Lin, *Adv. Funct. Mater.*, 2013, **23**, 4067–4078.
29 Y. L. Dai, D. M. Yang, P. A. Ma, X. J. Kang, X. Zhang, C. X. Li, Z. Y. Hou, Z. Y. Cheng and J. Lin, *Biomaterials*, 2012, **33**, 8704–8713.
30 P. Zhao, J. Zhang, Y. H. Zhu, X. L. Yang, X. Jiang, Y. Yuan, C. S. Liu and C. Z. Li, *J. Mater. Chem. B*, 2014, **2**, 8372–8377.
31 Y. Zhang, L. Huang, Z. Li, G. Ma, Y. Zhou and G. Han, *ACS Nano*, 2016, **10**, 3881–3885.
32 N. Bogdan, F. Vetrone, G. A. Ozin and J. A. Capobianco, *Nano Lett.*, 2011, **11**, 835–840.
33 W. F. Xingjun Zhu, J. Chang, Y.-W. Tan, J. Li, M. Chen, Y. Sun and F. Li, *Nat. Commun.*, 2016, **7**, 10.
34 Y. Dai, P. a. Ma, Z. Cheng, X. Kang, X. Zhang, Z. Hou, C. Li, D. Yang, X. Zhai and J. Lin, *ACS Nano*, 2012, **6**, 3327–3338.
35 E. E. Lees, T.-L. Nguyen, A. H. Clayton and P. Mulvaney, *ACS Nano*, 2009, **3**, 1121–1128.
36 S. Wang, J. Feng, S. Song and H. Zhang, *CrystEngComm*, 2013, **15**, 7142–7151.

37 P. Sharma, S. Brown, G. Walter, S. Santra and B. Moudgil, *Adv. Colloid Interface Sci.*, 2006, **123**, 471–485.
38 Y. C. Wei, Q. Chen, B. Y. Wu, A. G. Zhou and D. Xing, *Nanoscale*, 2012, **4**, 3901–3909.
39 D. D. Li, Q. Y. Shao, Y. Dong and J. Q. Jiang, *Mater. Lett.*, 2013, **110**, 233–236.
40 D. Li, Q. Shao, Y. Dong and J. Jiang, *J. Phys. Chem. C*, 2014, **118**, 22807–22813.
41 B. Zhou, B. Shi, D. Jin and X. Liu, *Nat. Nanotechnol.*, 2015, **10**, 924–936.
42 J. C. Boyer and F. C. J. M. van Veggel, *Nanoscale*, 2010, **2**, 1417–1419.
43 D. Q. Chen and P. Huang, *Dalton Trans.*, 2014, **43**, 11299–11304.
44 Y. F. Wang, L. D. Sun, J. W. Xiao, W. Feng, J. C. Zhou, J. Shen and C. H. Yan, *Chem. – Eur. J.*, 2012, **18**, 5558–5564.
45 N. Bogdan, E. M. Rodríguez, F. Sanz-Rodríguez, M. C. I. de la Cruz, Á. Juarranz, D. Jaque, J. G. Solé and J. A. Capobianco, *Nanoscale*, 2012, **4**, 3647–3650.
46 N. J. J. Johnson, A. Korinek, C. H. Dong and F. C. J. M. van Veggel, *J. Am. Chem. Soc.*, 2012, **134**, 11068–11071.
47 L. X. Zhang, A. Mckay and D. Y. Jin, *RSC Adv.*, 2013, **3**, 8670–8673.
48 N. J. Johnson and F. C. van Veggel, *Nano Res.*, 2013, **6**, 547–561.
49 L. P. Qian, D. Yuan, G. S. Yi and G. M. Chow, *J. Mater. Res.*, 2009, **24**, 3559–3568.
50 Q. Tian, K. Tao and K. Sun, *Micro Nano Lett.*, 2013, **8**, 731–734.
51 L. X. Liu, F. Qin, H. Zhao, T. Q. Lv, Z. G. Zhang and W. W. Cao, *Opt. Lett.*, 2013, **38**, 2101–2103.
52 J. Shen, G. Y. Chen, T. Y. Ohulchanskyy, S. J. Kesseli, S. Buchholz, Z. P. Li, P. N. Prasad and G. Han, *Small*, 2013, **9**, 3213–3217.
53 S. Zhou, W. Zheng, Z. Chen, D. Tu, Y. Liu, E. Ma, R. Li, H. Zhu, M. Huang and X. Chen, *Angew. Chem.*, 2014, **126**, 12706–12710.
54 J. Xu, S. Zhou, D. Tu, W. Zheng, P. Huang, R. Li, Z. Chen, M. Huang and X. Chen, *Chem. Sci.*, 2016, **7**, 2572–2578.
55 F. Wang, J. Wang and X. Liu, *Angew. Chem.*, 2010, **122**, 7618–7622.
56 L. H. Fischer, G. S. Harms and O. S. Wolfbeis, *Angew. Chem., Int. Ed.*, 2011, **50**, 4546–4551.
57 W. Yu, W. Xu, H. Song and S. Zhang, *Dalton Trans.*, 2014, **43**, 6139–6147.
58 Y. Tian, B. Tian, P. Huang, L. Wang and B. Chen, *RSC Adv.*, 2015, **5**, 14123–14128.
59 J. Xi, M. Ding, J. Dai, Y. Pan, D. Chen and Z. Ji, *J. Mater. Sci.: Mater. Electron.*, 2016, **27**, 8254–8270.

Supporting Information

Table S1 Table of expected shell thickness and measured shell. (The expected shell thickness was calculated based on the size of core nanocrystal, the amount of core and the amount of shell precursor; the measured shell thickness was calculated by comparing the size difference between the core and core-shell nanocrystals.)

Sample	Core – shell with 1.7 nm shell	Core – shell with 2.5 nm shell	Core – shell with 4.5 nm shell	Core – shell with 8.0 nm shell
Amount of $NaYF_4$:Yb,Er core (mmol)	0.2	0.2	0.2	0.2
Amount of α-$NaYF_4$ seeds as shell precursor (mmol)	0.1	0.2	0.4	0.8
Average size of $NaYF_4$:Yb,Er cores (nm)	24.1	24.1	24.1	24.1
Expected average size of the core-shell $NaYF_4$:Yb,Er@ $NaYF_4$ (nm)	27.4	30.5	34.9	41.2
Measured average size of the core-shell $NaYF_4$:Yb,Er@$NaYF_4$ (nm)	27.1	28.9	33.2	40.1
Expected average thickness of the shell (nm)	1.65	3.15	5.35	8.10
Measured average thickness of the shell (nm)	1.5	2.5	4.5	8.0

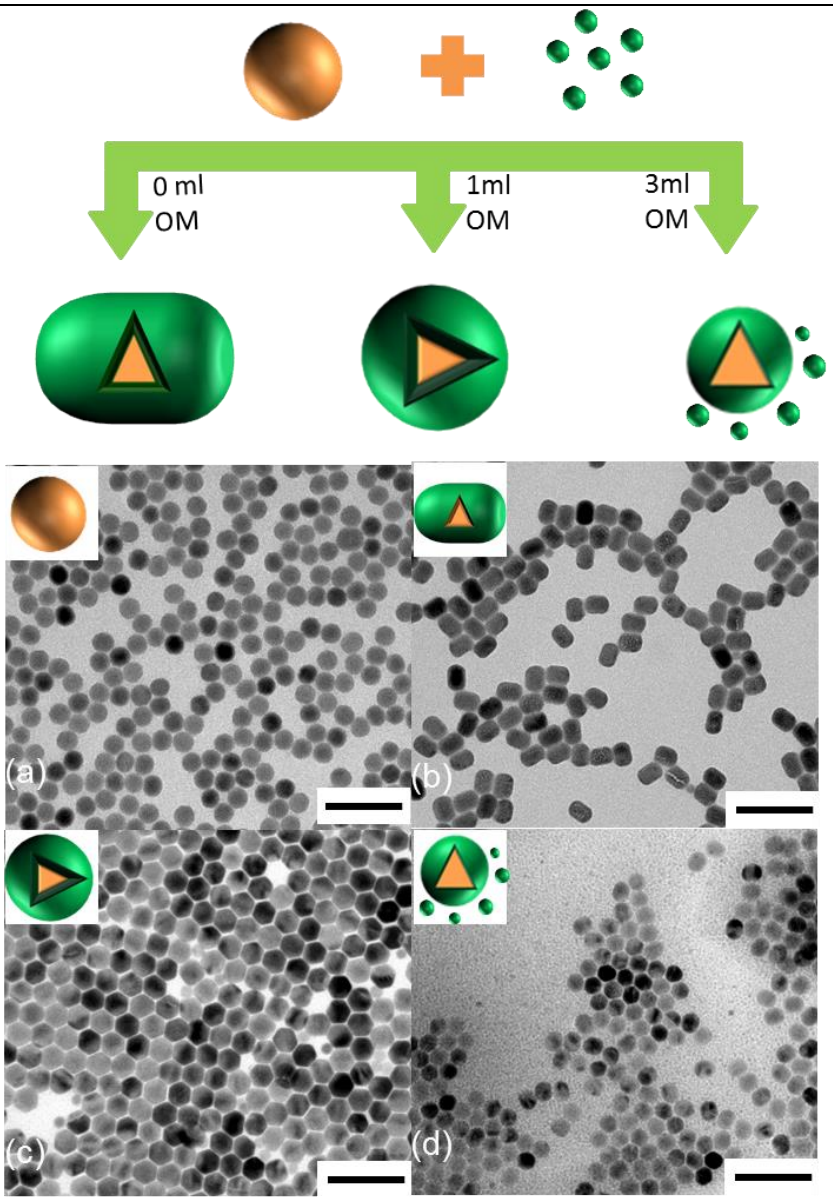

Figure S1 Schematic graph to show the controlled growth of homogeneous shells by adjusting the amount of oleylamine (OM). TEM images of core (a) and core-shell UCNPs synthesized with 0 ml, 1ml and 3ml OM, at the same reaction temperature, reaction time, and the same amounts of 5 mL OA and 8 mL ODE.

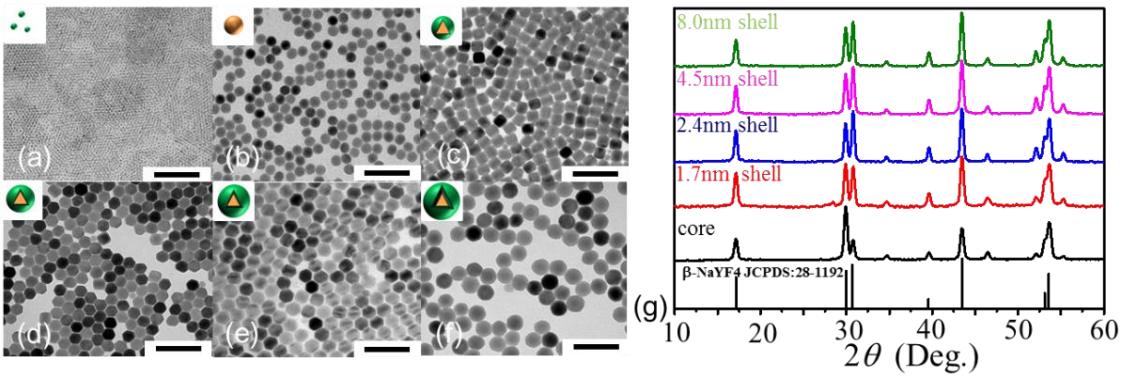

Figure S2 Materials characterization. TEM images of a-$NaYF_4$ shell precursor (a), $NaYF_4$: Er,Yb core (b), and $NaYF_4$: Er,Yb@$NaYF_4$ core-shell UCNPs with different shell thickness, 1.5 nm (c), 2 nm (d), 2.5 (e) and 4.0 nm (f); XRD spectra of core and core-shell UCNPs (g) (Scale bar: 50 nm)

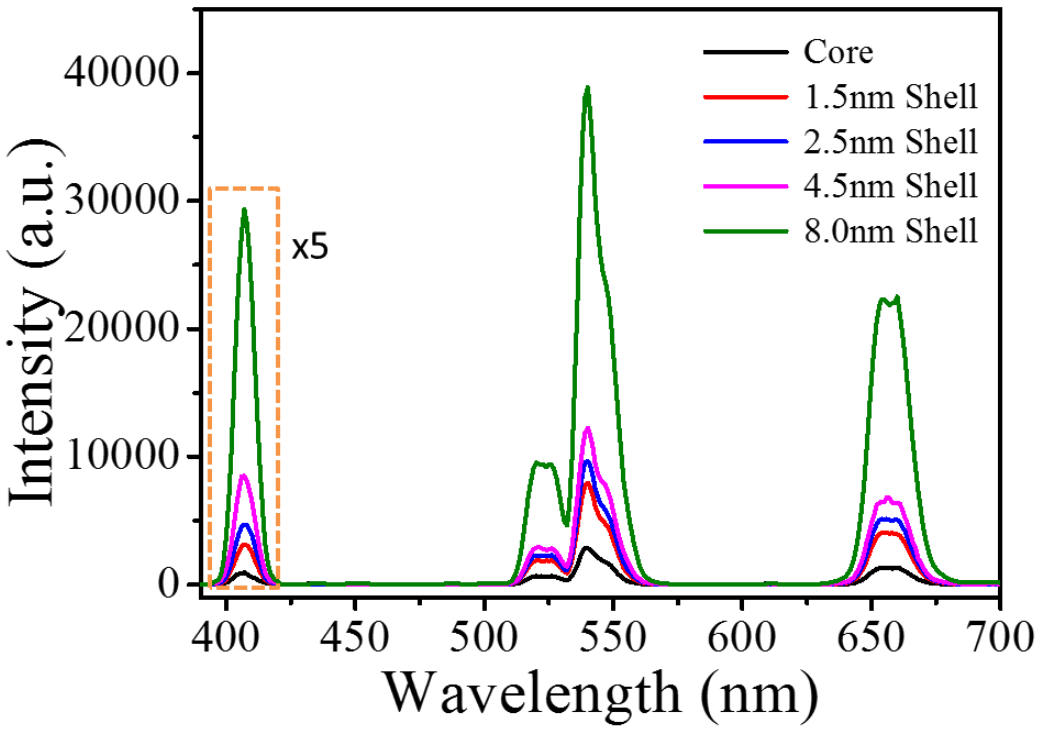

Figure S3 Luminescence spectra to qualify the enhancement by different thickness of shells. Luminescence spectrum of core-only and core-shell UCNPs under 200 mW 980 nm laser. The violet emission band was amplified by 5 times.

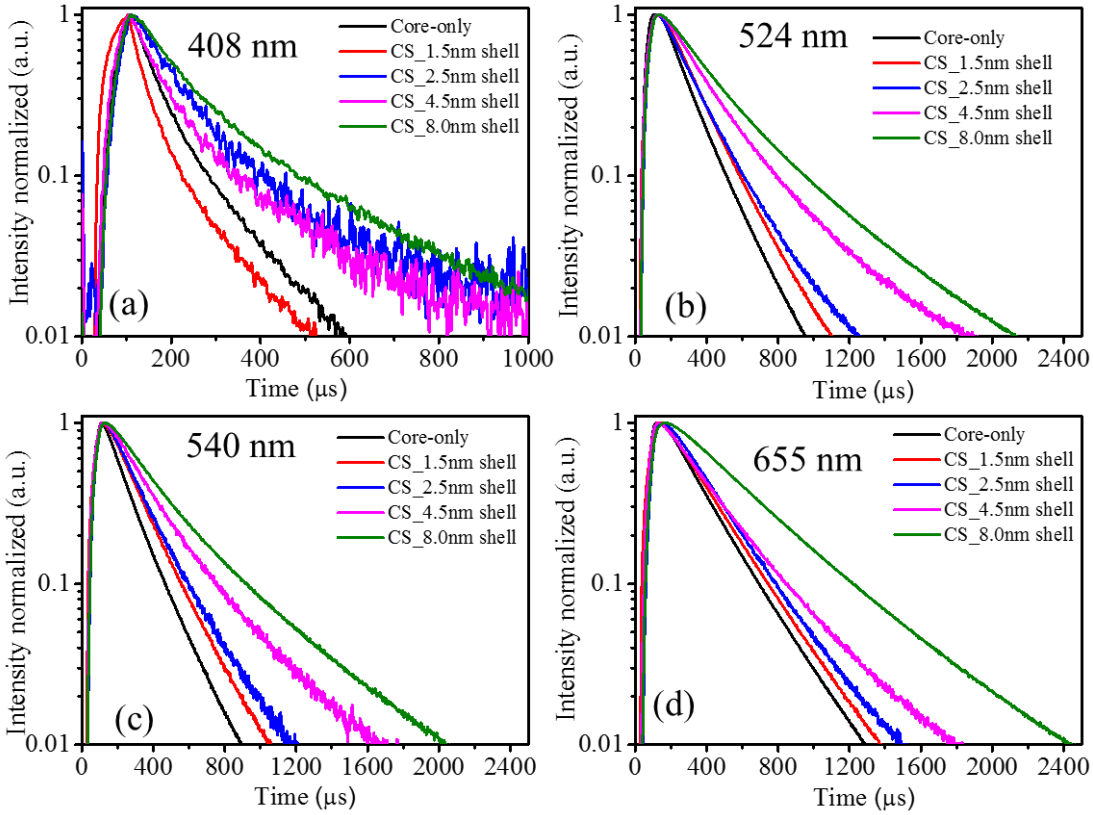

Figure S4 Luminescence decay lifetimes from core and core-shell UCNP samples with different thickness of shells at emissions of 408nm (a), 524 nm (b), 540 nm (c) and 655 nm (d).

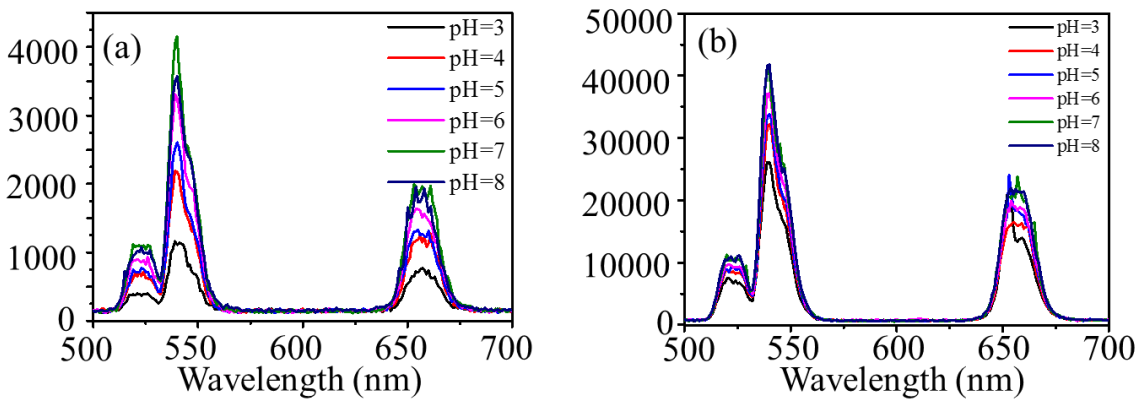

Figure S5 Emission spectra of core-only (a) and core-shell UCNP samples (b) to study the shell impact on the luminescence stability in different pH solution.

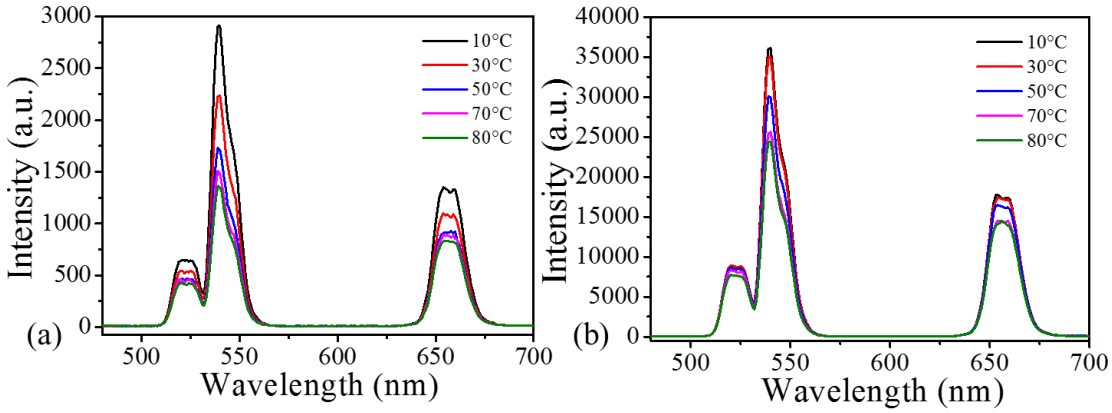

Figure S6 spectra of core-only sample (a) and core-shell samples (b) to study the shell impact on the luminescence stability under varied temperature.

2.3 Remarks

Homogeneous core-shell UCNPs with fine-tuned thickness inert shells have been successfully synthesized via a modified hot injection method. The shapes of core-shell UCNPs were tuned from rod-like to sphere by increasing the amount of OM from 0 mL to 1 mL, which suggests the shell growth control can be made via adjusting surfactants concentration. We will systemically study the influences of surfactants concentration to the shell growth process.

Chapter 3 Longitudinal Growth and Transversal Growth of $NaREF_4$ Nanocrystals

In addition of controlled growth of homogeneous core-shell nanocrystals, highly controlled anisotropic shell growth of core-shell nanocrystals is a much challenging work. To allow design complicated heterogeneous structured nanocrystals, we need to invent a method which allow us to do longitudinal shell growth and transversal shell growth. In Chapter 2, the ratio of oleic acid and oleylamine was used to controlled growth of homogeneous core-shell nanocrystals, which suggest that surfactants are useful tool for control shell growth direction.

In this chapter, we aim to reveal the surfactant's impact on the shell growth of nanocrystals. We comprehensively designed a series of experiments to study the role of the surfactants in affecting the shell growth direction of anisotropic $NaREF_4$ nanocrystals in the typical OA-ODE synthesis system. We first hypothesized that there were two types of surfactants working in the shell growth process: 1) the Oleic acid molecule (OAH), has low polarity, prefers to bind onto the crystalline plane with low polarity; 2) Oleate anion (OA^-), has high polarity, and prefers to bind onto the crystalline planes with high polarity. Base on this hypothesis, we conducted computational simulations (see Appendix A, primarily carried out by our collaborators Dr. Xian Qin and Prof. Xiaogang Liu in Singapore) to calculate the binding energy of OAH and OA^- on (001) and (100) planes via first principle theory. The computing results showed that OA^- and OA preferred to bind to different planes (see Table 2.1.1). OA^- had stronger binding energy onto (100) planes than (001) planes, while OAH had stronger binding energy onto (001) planes than (100) planes, as shown in the Figure 3.1. To prove our hypothesis is correct, we designed a series of experiments to control the shell growth directions by adjusting the ratio of OA^-/OAH. We separately studied the impact from the other experimental parameters, such as temperature, reaction time, reagent concentrations, shell materials and so on. The experimental results directly proved our hypothesis that shell growth along [001] direction with high ratio of OA^-/OAH, while the shell growth along [100] directions under low ratio of OA^-/OAH. According to this new mechanism, we successfully demonstrated a technique to tune the shell growth direction between longitudinal and transversal by adjusting the ratio of OA-/OAH. Furthermore, $NaYF_4$/$NaGdF_4$ nano-rods, nano-dumbbells, and bamboo-like multiple section $NaYF_4$/$NaGdF_4$ nanorods. We characterized these heterogeneous core-shell nanocrystals by TEM, STEM, EDS and XRD.

Table 3.1.1. Binding energy of OA^- and OAH to (001) and (100) planes

	(001) planes (meV)	(100) planes (meV)
OA^-	-21.8	-35.4
OAH	-9.4	-4.6

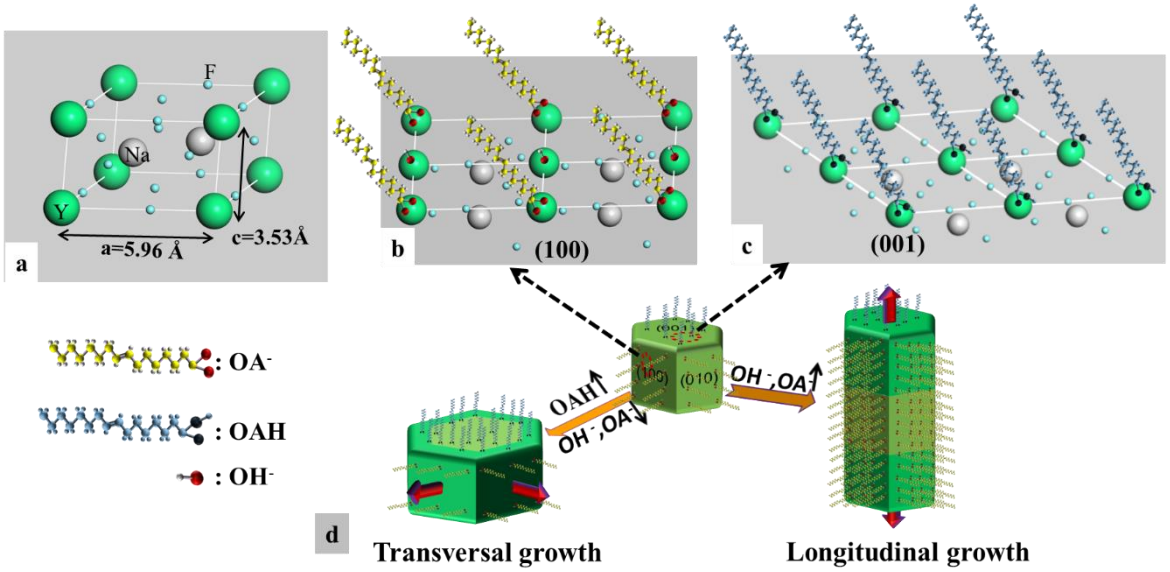

Figure 3.1.1 Scheme of Crystalline unit cell of b-$NaYF_4$ nanocrystals, the surfactants attached on different crystal face and hypothesis of controlling shell growth direction by adjusting the ratio of OA-/OAH

3.1 Materials and Equipment

3.1.1 Chemical Materials

Reagents: $YCl_3.6H_2O$ (99.99%), $YbCl_3.6H_2O$ (99.99%), $GdCl_3.6H_2O$ (99.99%), $NdCl_3.6H_2O$ (99.99%), $TbCl_3.6H_2O$ (99.99%), $LuCl_3.6H_2O$ (99.99%), NH_4F (99%), $ErCl_3.6H_2O$ (99.99%), KOH (99%), NaOH (99%), 1-octadecene (ODE) (90%), NaF (99%), Ethanol (100%), Methanal (99%) and oleic acid (OA) (90%) were purchased from Sigma-Aldrich. Unless otherwise noted, all materials were used as starting materials and without further purification.

3.1.2 Equipment

Heating mental, temperature controller (working range 0 to 400 ºC), magnetic stirrer, thermometer (range to 20 to 350 ºC), ultrasonic, centrifuge, argon (scientific grade).

3.1.3 Transmission Electron Microscopy Characterization

Standard transmission electron microscope (TEM) measurements were performed using a Philips CM10 TEM with Olympus Sis Megaview G2 Digital Camera. The samples were prepared for TEM analysis by placing a drop of a dilute suspension of nanocrystals onto formvar-coated copper grids (300 meshes) and were allowed to dry in a desiccator at room temperature before using.

High resolution transmission electron microscope (TEM) measurements were performed with an aberration-corrected analytical transmission electron microscopy (TEM, JEOL ARM-200F) operated at 80 kV. High-angle annular dark-field (HAADF) scanning transmission electron microscope (STEM) images and their corresponding element mapping images were collected with the same TEM equipped with a Centurio SSD energy-dispersive X-ray spectroscopy (EDS) detector set at 77 K.

3.2 Hydrothermal synthesis of micron-sized $NaYF_4$ crystals

There are two popular methods used to synthesize fluoride nanocrystals: the hydrothermal method and the co-precipitation method. In this work, micro-sized $NaYF_4$ crystals were synthesized with the hydrothermal route and different ratios of OA^-/OAH were used to validate the selective roles of oleate anions in the formation of $NaYF_4$ crystals with different aspect ratio.

Methods:

The β-$NaYF_4$ disks were synthesized via a slightly modified hydrothermal reaction. In a typical experiment, NaOH (0.15 g; 3.75 mmol) was first dissolved into 1.5 mL of double distilled water, followed by the addition of 2.5 mL of oleic acid (7.5 mmol) and 2.5 mL of ethanol while undergoing vigorous stirring. Thereafter, an aqueous solution of NaF (0.5 M; 2 mL) was added to form a turbid mixture. Subsequently, a 1.2 mL aqueous solution of YCl_3 (Yb^{3+}/Tm^{3+} = 10/0.5 mol%; 0.2 M) was added and the solution was stirring for 20 min. The resulting mixture was then transferred into a 14 mL Teflon-lined autoclave and heated to 220 ^oC and the temperature maintained for 12 h. After cooling down to room temperature, the reaction product was isolated by centrifugation and washed with ethanol. In this work, different amount of NaOH were added to adjust the ratio of OA^-/OAH by its reaction with OAH to form OA^-.

Results and Discussions:

As shown in the Figure 3.1.1, the aspect ratio of the disks were readily tuned in this method by varying the amount of NaOH (3.75, 5, 6.25, and 7.5 mmol) added in the reaction mixture. The aspect ratio was used as a general metric for the evaluation of crystal growth along either axis. For example, the aspect ratio of 0.2 suggested that the epitaxy rate along *a* axis was five times faster than that along the *c* axis when 3.75 mmol NaOH was added to the reaction system; when 7.5 mmol of NaOH was added, the epitaxy rates along *a* and *c* axis were almost the same; the resulting aspect ratio was 0.95.

Brief conclusion:

In this work, the crystals formed from the hydrothermal method shows that the direction of growth was corresponded closely to the ratio of OA^-/OAH used in the initial reaction solution. It was found that a high concentration of OA^- encouraged epitaxial growth in the longitudinal direction of the crystal. It was found that changes to the shape of the $NaYF_4$ crystals closely matched the change in the OA^-/OAH ratio of the reaction mix

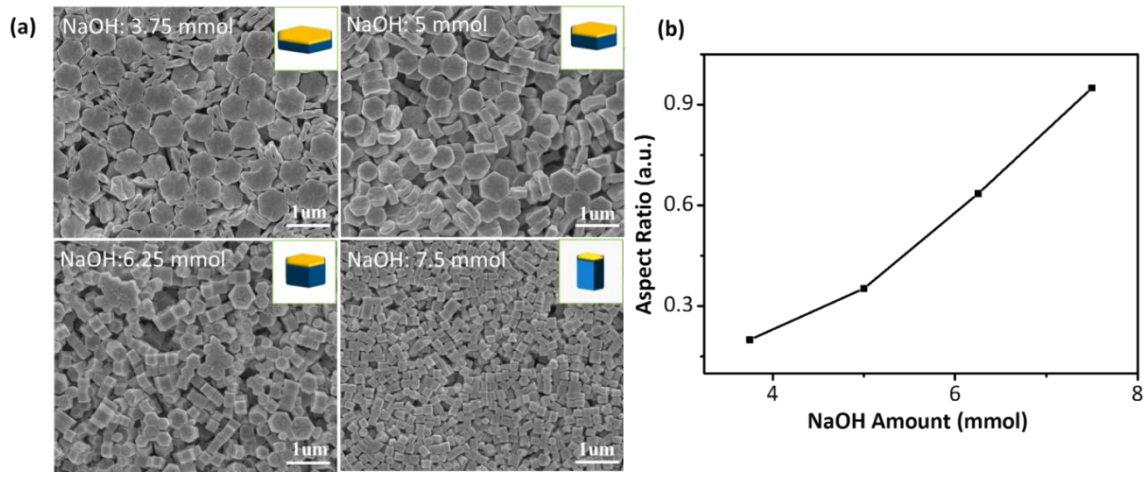

Figure 3.2.1. (a) SEM images of the $NaYF_4$ disks and rods synthesized under hydrothermal conditions and with different amounts of NaOH (Scale bars: 1 μm). (b) The observed aspect ratio of $NaYF_4$ crystals is graphed against the amount of NaOH used in the reaction mix

3.3 Longitudinal epitaxial-growth of $NaYF_4$ nanocrystals via the co-precipitation route

The co-precipitation method for the epitaxial growth of rare-earth doped core-shell nanostructured crystals was widely reported elsewhere.[1-8] However, the mechanism of crystal growth remains not clearly understood.[9] In the main text of this work, it was revealed that the oleic acid in the co-precipitation method plays a dual role in directing the epitaxial growth of $NaYF_4$ nanocrystal and in forming a variety of nanostructures, such as nanorods, nanodisks, hour-glass shaped nanocrystals, top-spin shaped nanocrystals, and flower-shaped nanocrystals. The details of this synthesis which involved changes to the ratio of oleate anion and oleic acid (OA^-/OAH ratios) added, the reaction temperature of the synthesis, and the concentration of the reagents are summarized below for (1) the anisotropic epitaxial-growth of crystals in their longitudinal and transversal directions and also for (2) their migration growth.

We first established the conditions for controlling the epitaxial growth of $NaYF_4$ purely along [001] direction (longitudinal), and in parallel we then controlled the epitaxial shell growth along [100] [010] directions (transverse) by adjusting the ratio of OA^-/OAH. The synthesis detail, result and discussion for each morphologically different crystals are described in the following sections.

3.3.1 Longitudinal epitaxial-growth of homogeneous $NaYF_4$ nanocrystals

Method for growth of $NaYF_4$ nanocrystal cores

In a typical procedure, 4 mL of methanol solution of YCl_3 (2.0 mmol) was magnetically mixed with OA (38 mmol) and ODE (93 mmol) in a 100 mL three-neck round-bottom flask. The mixture was then degassed under the Ar flow and then heated to 150 ˚C for 30 min to form a clear solution, before cooling to room temperature. 15 mL of methanol solution containing NH_4F (8 mmol) and NaOH (5 mmol) was added to the solution of YCl_3 in ODE and stirred for 60 min. The mixture solution was slowly heated to 110 ˚C and kept at 110 ˚C for 30 minutes to completely remove methanol and any residual water. The mixture solution was then quickly heated to the reaction temperature of 300 ˚C and aged for 1 hour. After the solution was left to cool down to room temperature, ethanol was added to precipitate the nanocrystals. The product was washed with cyclohexane, ethanol and methanol for at least 4 times, before the final $NaYF_4$ nanocrystals were re-dispersed in 10 mL cyclohexane in preparation for their further use.

Method for longitudinal growth to form $NaYF_4$ nanorods

0.2 mmol of YCl_3 in 1 ml methanol solution was magnetically mixed with OA (9.5mmol) and ODE (25mmol) in a 50 mL three-neck round-bottom flask. The mixture was degassed under Ar flow and heated to 150 ˚C for 30 min to form a clear solution, and then cooled to room temperature. 5 mL of methanol solution containing NH_4F (0.8 mmol) and NaOH (0.5 mmol) was added and stirred for 60 minutes. The solution was slowly heated to 110 ˚C and kept at 110 ˚C for 30 minutes to completely remove methanol and residual water. The solution was then injected with 0.2 mmol $NaYF_4$ of nanocrystals in cyclohexane and the mixture kept at 110 ˚C for another 10 min to evaporate the cyclohexane. Then, the reaction mixture was quickly heated to 310 ˚C and aged for 1 hour.

Method for characterization of rare earth ions on the nanocrystal surface

Rare earth doped fluoride nanocrystals were usually synthesized by reacting lanthanide precursors in organic media in the presence of capping ligands to increase their size and shape uniformity. These nanocrystals are often heavily aggregated in aqueous solutions owing to the hydrophobic nature of the capping ligands; surfactants are typically introduced during the reaction to keep the crystals colloidally stable as they grow in reaction solvent. To test the amount of rare earth ions on their surfaces, we first remove surface capping ligands including both Oleic Acid and Oleate ions from $NaYF_4$ nanocrystals with a well followed procedure which is based on acid treatment [2]. The as-prepared ligands-capped nanocrystals are first dispersed in a 2 mL HCl solution (0.1 M) and ultrasonicated for 30 min,

followed by their centrifugation at 14,500 rpm for 10 min and their purification by adding an acidic ethanol solution (at a pH of 4; prepared by adding 0.1 M HCl aqueous solution to the absolute ethanol). The resulting products of ligand-free nanocrystals are further washed with ethanol and deionized water three times, before they are re-dispersed in deionized water.

Results and Discussions:

Morphology observation and size calculations

The TEM characterization (Figures 2.3.1) for the sample nanocrystals obtained from the above experiment confirmed that the epitaxial growth of shells onto the core was initiated by the formation of α-$NaYF_4$ nanocrystals at the beginning of the epitaxial growth, before these transformed into the stable β-$NaYF_4$ nanocrystals.

The size of α-$NaYF_4$ nanocrystals increased for the first 20 minutes, and decreased for the following 20 minutes until being completely consumed and epitaxial grown onto the β-$NaYF_4$ cores which then transformed into the β-$NaYF_4$ nanorods after 50 minutes of the start of the reaction. At the same time, the length of β-$NaYF_4$ cores gradually grows up for the whole reaction process longitudinally from 25 nm to 35 nm with the width of β-$NaYF_4$ nanocrystals remaining at the similar values about 25-27 nm (Figure 3.3.2).

Figure 3.3.3 further illustrates that mono-disperse nanorods with high aspect ratio (>2) can be step-by-step synthesized by the secondary epitaxial growth in a high concentration of oleate ions when reacted at high temperature by the co-precipitation method.

The surface properties:

Due to the fact that oleate and oleic acid are very similar in chemical structure, standard measurements, such as X-ray photoelectron spectroscopy (XPS), unfortunately could not differentiate OA from OA- ions on the surface of nanocrystal. But there is indirect evidence supporting the existence of OA^-; the hydrophobic nanocrystals become hydrophilic in water after treatment with diluted HCl solution and after ultrasonication. This indicates that the strongly binding oleate ions (OA^-) reacts with H^+ to form OAH at a lower binding energy, and is removeable by the ultrasonic treatment.

After both OAH molecules and OA^- Oleate ions have been removed from the crystal facets, the zeta potential of ligand free $NaYF_4$ nanocrystals in MQ water was about +20 mV, which suggests that the naked nanocrystals are highly positively charged by their exposed rare earth ions on their surface. (Figure 3.3.4)

Brief conclusion:

At high concentration of oleate ions (OA^-), the deposition and epitaxial growth of the shells have a preference for the bottom and top surfaces (001) of the crystal particles.

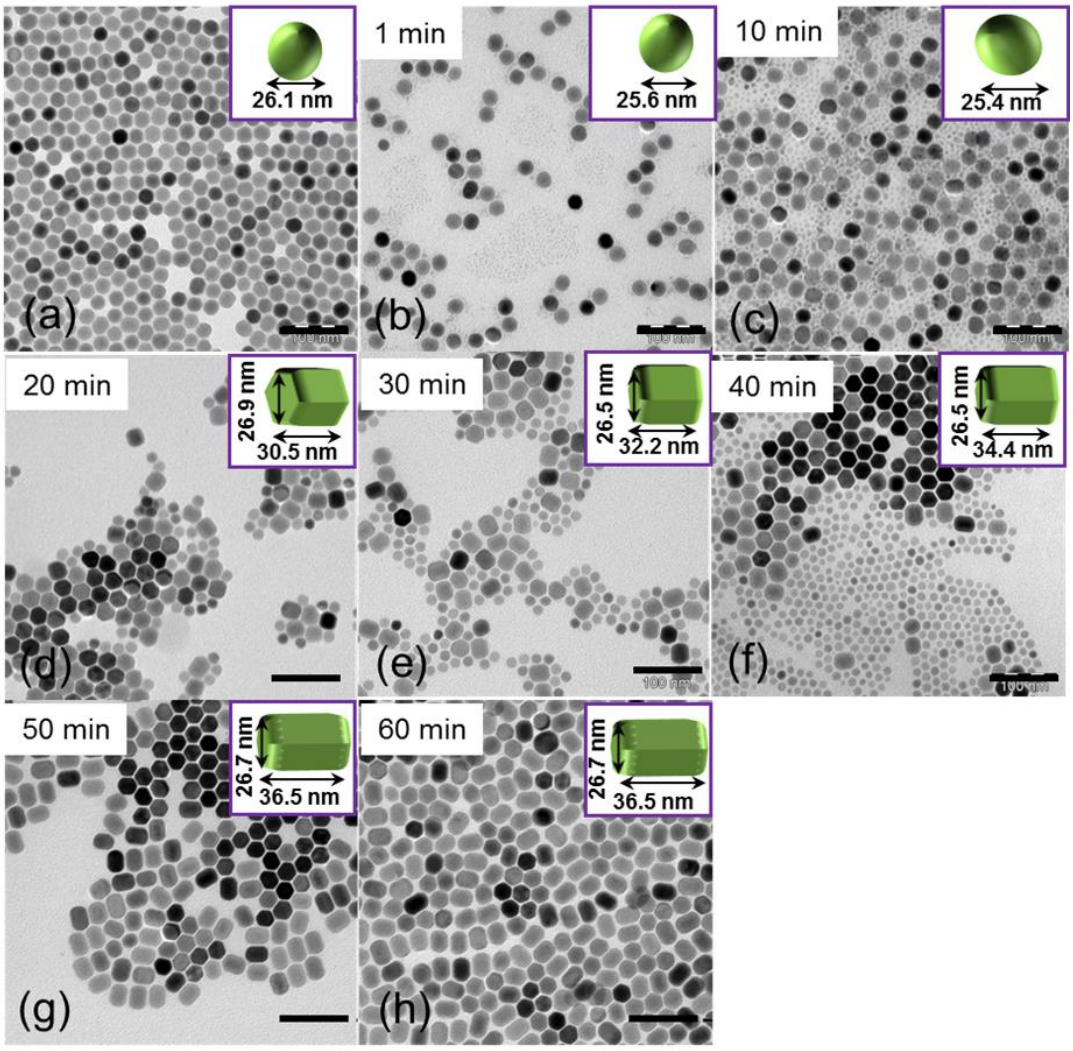

Figure 3.3.1. Real-time monitoring of the epitaxial growth process of crystals from their $NaYF_4$ nanocrystal cores to their longitudinally form as $NaYF_4$ nanorods. TEM images of the $NaYF_4$ core (a) and their products after step-by-step sampling at after 1 minute (b), 10 minutes (c), 20 minutes (d), 30 minutes (e), 40 minutes (f), 50 minutes (g) and 60 minutes (h) of reaction time (Scale bars: 100 nm).

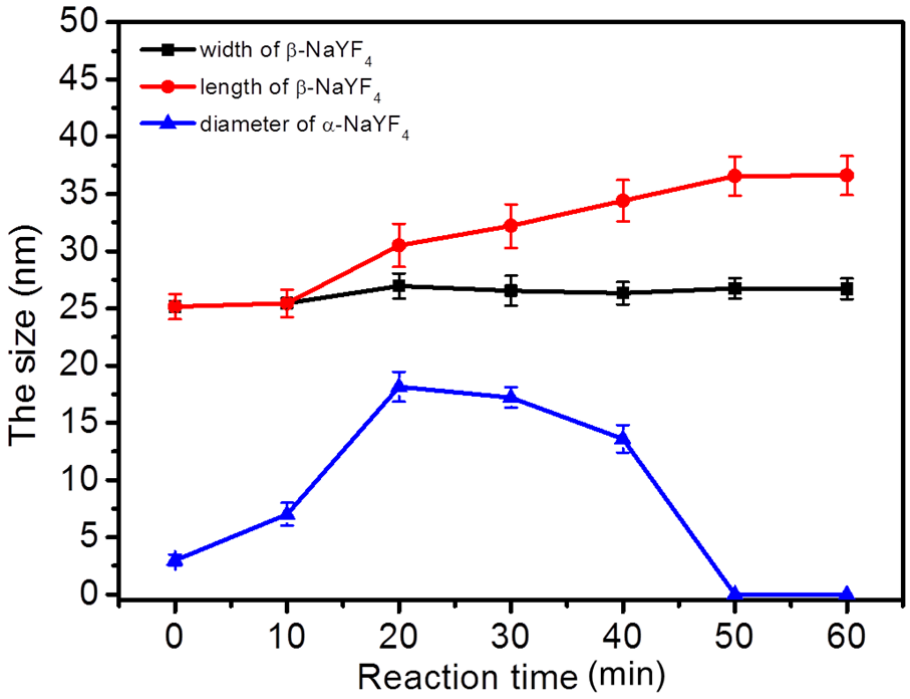

Figure 3.3.2. Chart graph shows the size evolution of both α phase $NaYF_4$ nanocrystals in diameter and β-$NaYF_4$ nanorods in their width and length as function of their reaction time from 0 minutes to 60 minutes.

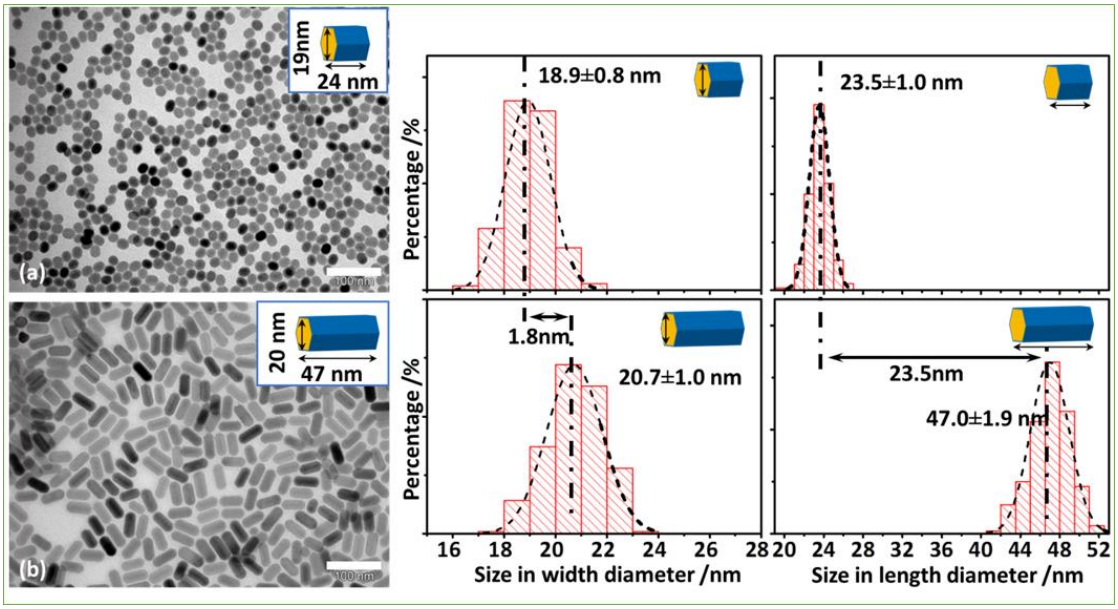

Figure 3.3.3. TEM images and size distributions of the $NaYF_4$ core nanocrystals (a) and the $NaYF_4$ nanocrystals after their epitaxial growth in the longitudinal direction (b). The size of the $NaYF_4$ visibly increases in the longitudinal direction after the secondary growth of $NaYF_4$ shell from 24 nm to 47 nm. This was accompanied by a slight increase (1.8 nm) in their transversal dimension. (Scale bar is 100 nm)

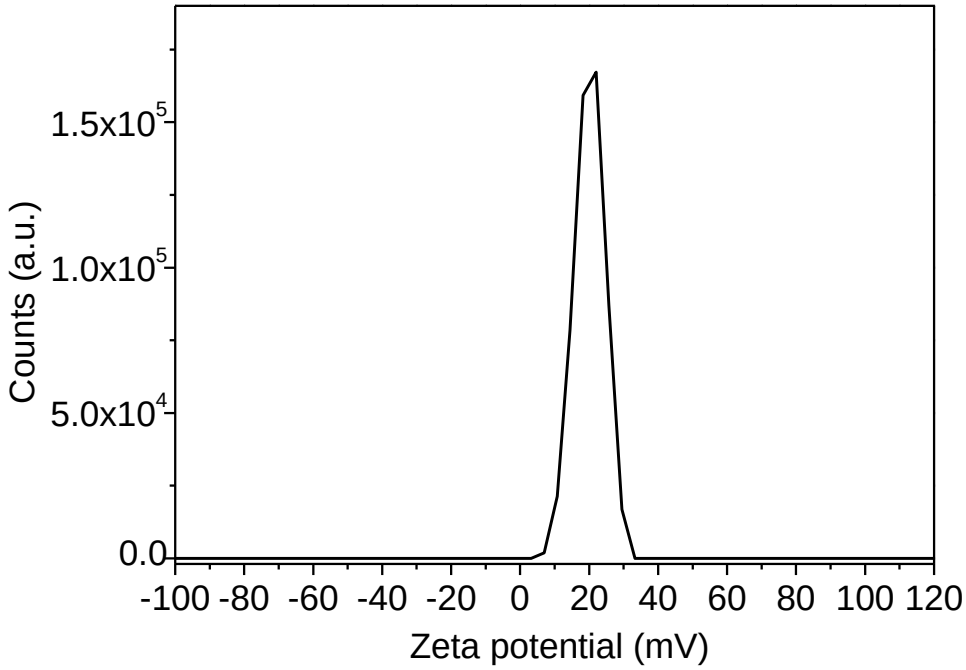

Figure 3.3.4. Zeta potential graph of ligand-free $NaYF_4$ nanocrystals.

3.3.2 Investigation of the reaction temperature effect on the epitaxial shell growth

Methods:

The purpose for this experiment was to assess the role of different reaction temperature in the directional epitaxial growth of shells onto the core. We adopted the same synthesis method used in section 2.4.1, except step-wise varying the reaction temperature at 290 ˚C, 300 ˚C, 310 ˚C, 320 ˚C.

Results and discussion:

As shown in the Figure 3.3.5, within the wide range of the reaction temperature (290 to 320 ˚C), the epitaxial growth occurred in the longitudinal direction with high ratio of OA^- /OAH. We noted that the synthesis has accompanied with the newly formed nanocrystals at 290 ˚C, which suggested the shell growth speed at 290 ˚C was too low to complete the shell growth within 1 hour. At elevated temperature from 290 ˚C to 300 ˚C and to 310 ˚C, the shell growth speed was increased with longer nanorods formed. With an obvious trend in the longitudinal growth direction, however, the higher temperature at 320 ˚C resulted in aggregated nanorods. These results indicated that the reaction temperature will only influence the speed of the directional epitaxial growth, but with optimum temperature (310 ˚C) to produce the crystal with high degree of mono dispersity.

These results by investigating the temperature effect on the growth direction have further provided additional evidence to support our discovered mechanism ruled by the binding energy difference between OA^- and OAH onto (001) and (100) planes. Since the low temperature does not provide sufficient thermal vibration, both of the surfaces are well passivated by OA^- and OAH surfactants causing the slow growth speed, though there is relatively better passivation to the (100) planes by more available OA^- surfactants due to the high ratio of OA^-/OAH. Increasing the temperature to 300 ˚C and 310 ˚C will increase the thermal agitation that first unlock (unbind) the OAH off the (001) plane to encourage the longitudinal growth.

The interesting result of aggregated nanorods shown in Figure 3.3.5(e) has further suggested that the higher-temperature induced thermal agitation at 320 ˚C could even affect the stability of strong binding OA^- on the (100) planes which caused the aggregation.

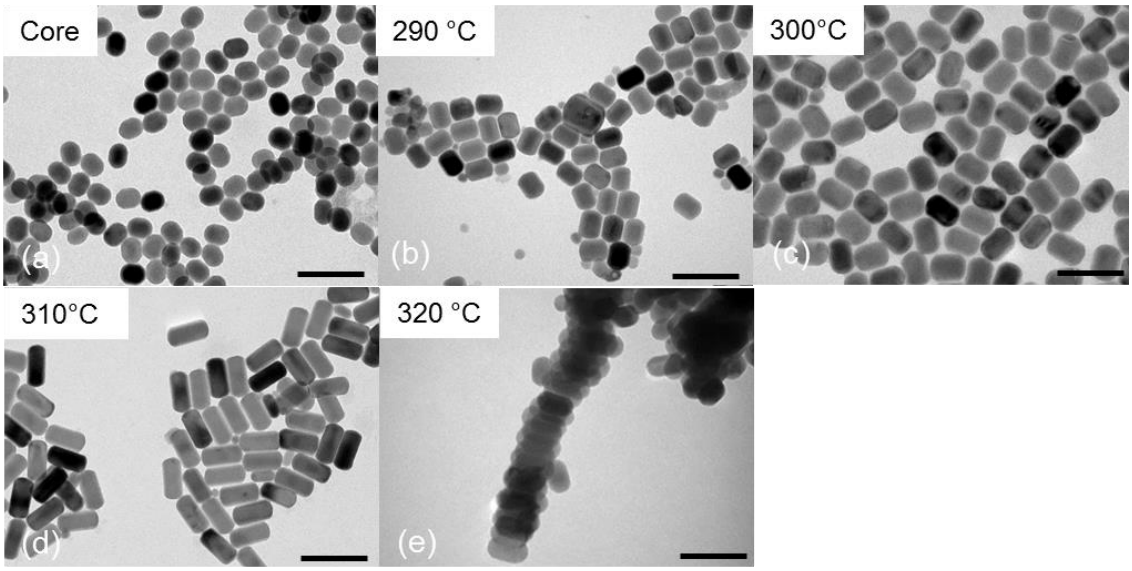

Figure 3.3.5, TEM images of $NaYF_4$ core nanocrystals (a) and related core-shell nanocrystals synthesized under the temperature of 290 ˚C (b), 300 ˚C (c), 310 ˚C (d) and 320 ˚C (e). Note, all of reaction time were kept for 1 hour. (Scale bar: 100 nm)

Brief conclusion:

The reaction temperature does not alter the direction of epitaxial growth, but affect the growth speed. At lower reaction temperature (290 ^{o}C), both OA^- and OAH surfactants are stable to passivate the crystal surfaces, which slows down the epitaxial growth speed; at higher temperature (300 and 310 ^{o}C), the OAH surfactants become unstable on the (001) planes so that the end surfaces are first unlocked to allow the obvious longitudinal shell growth; at further increased temperature (320 ^{o}C), both surfactants become unstable causing aggregation with low stability of the nanorods.

3.3.3 The role of OA concentration to shell growth

Method:

The purpose for this experiment was to assess the role of OA (sum of OA^- and OAH) concentration in the directional epitaxial growth of shells onto the core. We adopted the same synthesis method used in section 2.3.1, except step-wise varying the OA concentrations from 1.70 mmol/mL, 1.42 mmol/mL, 1.14 mmol/mL, and to 0.85 mmol/mL.

To keep other reagent concentrations as same as that used in the previous experiments, the same total reaction solvent volume, four group of different amount of OA and ODE were applied separately, as shown in Table 2.4.1.

Table 3.4.1. *The different amounts of OA and ODE used in experiments*

OA concentration (mmol/mL)	The amount of OA (mmol)	The amount of ODE (mmol)
1.70	19	15.6
1.42	25.8	18.6
1.14	12.7	21.8
0.85	9.5	25

Results and discussion:

As shown in the Figure 3.3.6, decreasing the OA concentration from 1.70 mmol/mL to 0.85 mmol/mL, the epitaxial shell growth direction has changed from being homogenous to longitudinal. This result has further supported our mechanism that the ratio of OA^-/OAH determines the epitaxial shell growth direction, as the high concentration of OA, that equals to high concentration of OAH, can well passivate the (001) planes and the decrease in OA concentration, that equivalently increases the ratio of OA^-/OAH, will first reduce the passivation effect on the ends surfaces ((001) planes) to encourage the epitaxial shell growth along the longitudinal growth direction.

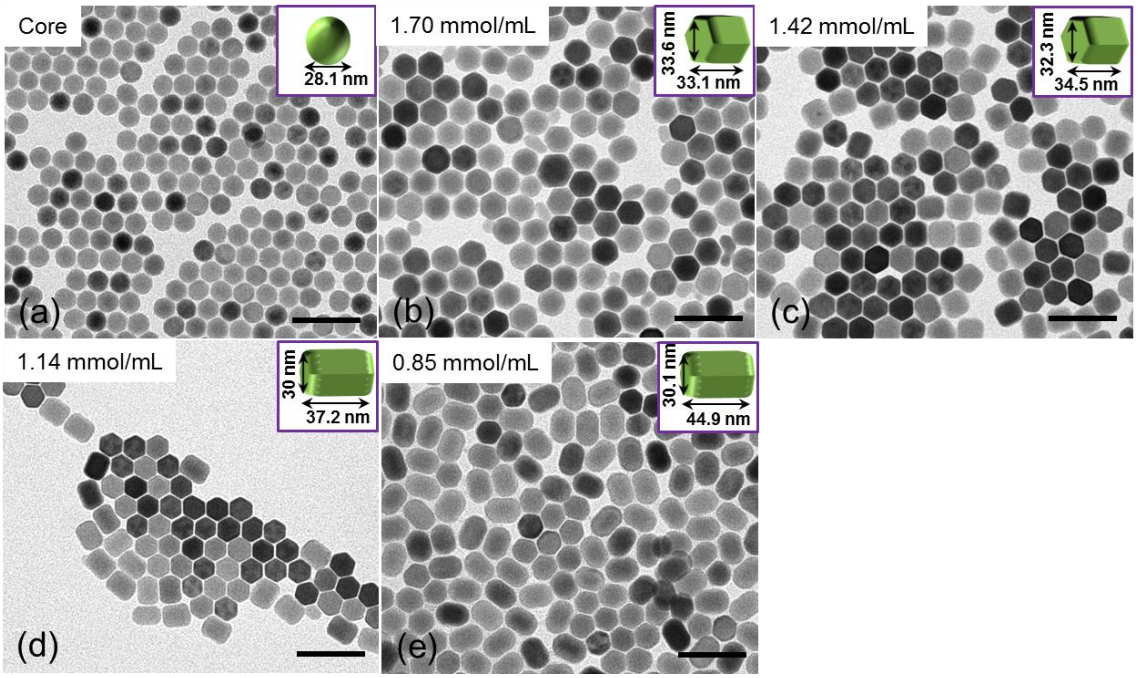

Figure 3.3.6, TEM images of $NaYF_4$ core only nanocrystals (a) and related core-shell nanocrystals synthesized under OA (including OA^- and OAH) concentration of 1.70 mmol/mL (b), 1.42 mmol/mL (c), 1.14 mmol/mL (d), 0.85 mmol/mL (e). Note, other reaction conditions were kept the same in the longitudinal growth process. (Scale bar: 100 nm)

Brief conclusion:

The OAH molecule concentration primarily determines the growth activity on the (001) plane, and the OA^- is mainly responsible to passivate the (100) planes, the balance between OAH and OA^-, the ratio of OA^-/OAH, will determine the epitaxial shell growth direction.

3.3.4 The role of F^- concentration to shell growth

Method:

The purpose for this experiment is to assess the role of varied F^- concentration in the directional epitaxial growth of shells onto the core. We adopted the same synthesis method used in section 2.3.1, except step-wise increasing the amount of NH_4F from 0.4 mmol to 0.6 mmol, and to 0.8 mmol, with the F^- concentration calculated as 36.4 μmol/mL to 54.5 μmol/mL, and to 72.8 μmol/mL.

Results and discussion:

As shown in Figure 3.3.7, by increasing the concentration of F^- from 36.4 μmol/mL to 54.5 μmol/mL, and to 72.8 μmol/mL, the nanocrystals grew only along the longitudinal direction, but with the obvious trend showing that higher concentration of F^- leads to longer nanocrystals.

The observation of epitaxial shell growth only along the longitudinal direction is consistent to the longitudinal growth condition at the fixed ratio of OA^-/OAH; Varying the F^- concentration will only affect the speed of epitaxial shell directional growth, which is predictable as the higher concentration of F^- ions will supply sufficient amount of ions to participate a faster growth.

Using very low concentration of F^- ions can enhance the crystal dissolution effect and therefore produce more interesting shapes of the nanocrystals, which has been thoroughly investigated and presented in the Chapter 3.

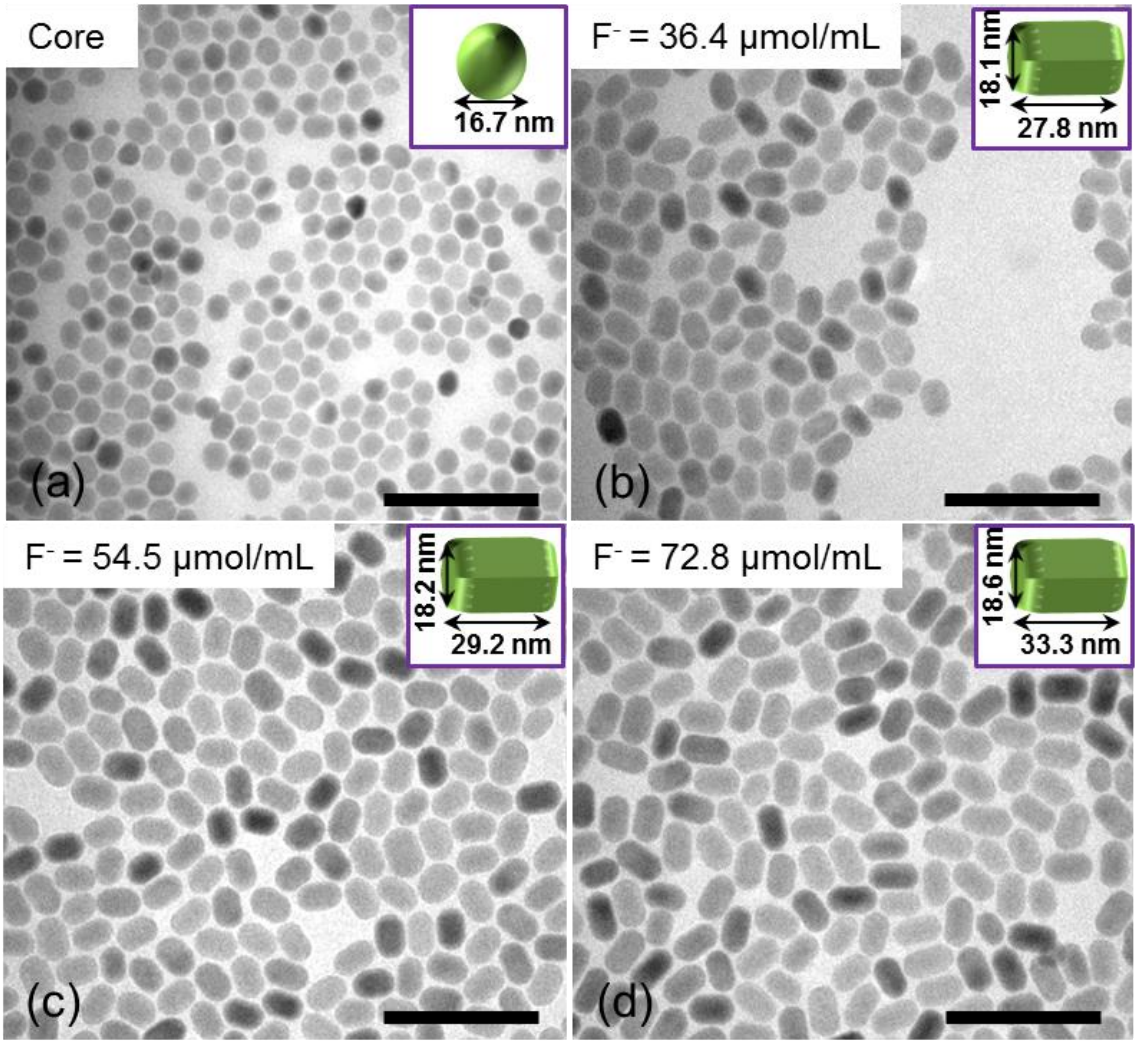

Figure 3.3.7, TEM images of $NaYF_4$ core only nanocrystals (a) and grown with $NaYF_4$ shells under varied the concentration of F^-, 36.4 μmol/mL (0.4 mmol) (b), 54.5 μmol/mL (0.6 mmol) (c) and 72.8 μmol/mL (0.8 mmol) (d) Note, other reaction conditions kept the same as these in the longitudinal growth process. (Scale bar: 100 nm)

Brief conclusion:

The F^- concentration has little influence to the epitaxial shell growth direction, though the higher concentration of F^- will result in longer nanocrystal rods.

3.3.5 The role of Na^+ concentration to shell growth

Method:

The purpose for this experiment is to assess the role of Na^+ concentration in the directional epitaxial growth of shells onto the core. We adopted the same synthesis method used in section 2.3.1, except decreasing the amount of NaOH from 0.5 mmol to 0.3 mmol, with the Na^+ concentration calculated as 45.5 μmol/mL to 27.3 μmol/mL.

Results and discussion

As shown in the Figure 3.3.8, with decreasing the Na^+ concentration from 45.5 μmol/mL to 27.3 μmol/mL, the shape of core-shell nanocrystals changed from nanorods to nanospheres.

The obvious changes in the shape of core-shell nanocrystals suggest that the epitaxial shell growth direction were highly related to the Na^+ concentration. The increase of the Na^+ concentration can cause more OAH reacted to OA^-, which leads to the increase of the ratio of OA^-/OAH. And higher ratio of OA^-/OAH will lead to longitudinal shell growth under 310 °C. This result further supports our mechanism that the ratio of OA^-/OAH is the key factor to control the epitaxial shell growth direction.

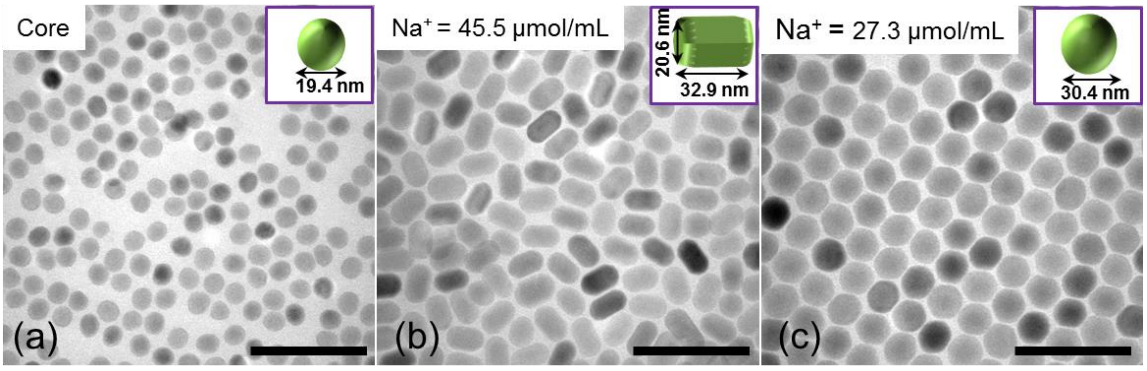

Figure 3.3.8 TEM images of $NaYF_4$ core-only nanocrystals (a) and grown with $NaYF_4$ shells under two different concentration of Na^+, 45.5 μmol/mL (NaOH=0.5 mmol) (b) and 27.3 μmol/mL (NaOH=0.3 mmol) (c). Note, other reaction conditions kept the same as these in the longitudinal growth process. (Scale bar: 100nm)

Brief conclusion:

The varied Na^+ concentration can change the epitaxial shell growth direction due to the fact that the ratio of OA^-/OAH is altered. Higher Na^+ concentration (45.5 μmol/mL) leads to more OA^- formed that results in the longitudinal shell growth.

3.3.6 Further experiment to verify OA^- ions as a determine factor in longitudinal growth of $NaYF_4$ nanorods

In this work, to generate longitudinal epitaxial growth of nanocrystals, we adopted a simple approach: Increases in the ratio of OA^- to OAH by increasing the amount of NaOH lead to the conversion of more OAH into OA^- and to changes in the morphology of the crystals. In order to rule out the interference from OH^- (from NaOH) that may play a role in directional epitaxial growth and as well to further verify if it is the oleate ion (OA^-) that do indeed play a major role in passivating the side surfaces (100), we further designed and ran an experiment that used sodium oleate (NaOA) to replace NaOH as the sodium source. As a comparison, in one control experiment we grow the $NaYF_4$ nanocrystals with $NaYF_4$ shell using NaOH as sodium source, and in the other experiment, we used the same molar amount of Na-OA (sodium oleate) as a sodium source and as a replacement for the NaOH

Method for longitudinal growth to form $NaYF_4$ nanorods using Na-OA

0.2 mmol YCl_3 in 1 ml methanol solution was magnetically mixed with OA (9.5mmol) and ODE (25mmol) in a 50 mL three-neck round-bottom flask. The mixture was degassed under an Ar flow and heated to 150 ˚C for 30 min to form a clear solution, and then cooled to room temperature. 5 mL of methanol solution containing NH_4F (0.8 mmol) and **sodium oleic acid Na-OA (0.5 mmol)** was added and stirred for 60 min. The solution was slowly heated to 110 ˚C and kept at 110 ˚C for 30 min to completely remove any methanol and any remaining water. Then, 0.2 mmol of $NaYF_4$ in cyclohexane was injected into the nanocrystals in cyclohexaneand the mixture was kept at 110 ˚C for another 10 minutes so that the cyclohexane could be evaporated. Then, the reaction mixture was quickly heated to 310 ˚C and aged before aging for 1 hour.

Results and discussion:

As shown in Figure 3.3.9 (b) and in (c), identical results were obtained with $NaYF_4$ shell grown longitudinally onto the $NaYF_4$ core no matter if OH^- was present in the reaction or not, ruling out OH^- as a key factor for longitudinal growth in the reaction system described here.

Brief conclusion:

In other reaction system for synthesis of nanorods, the ratio of OA^- to OAH was a key factor in directing longitudinal growth of the crystals.

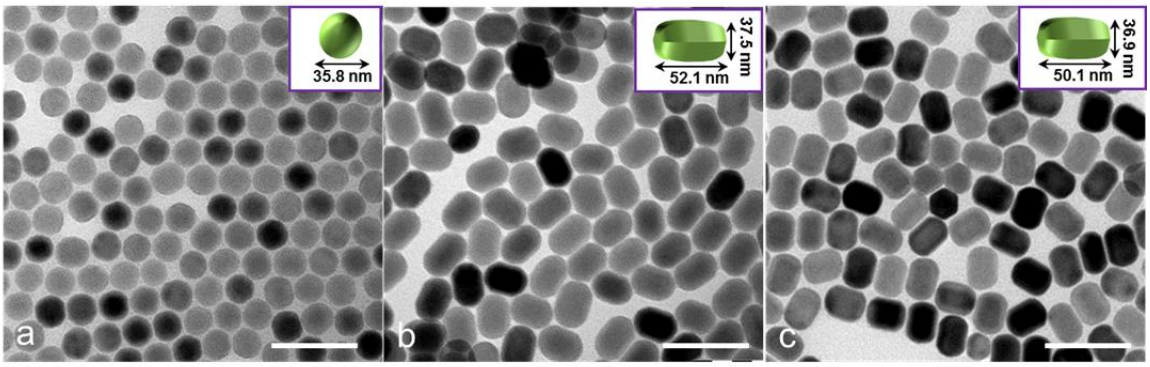

Figure 3.3.9. TEM images of $NaYF_4$ core (a) and $NaYF_4$ coated with $NaYF_4$ shell using NaOA as a sodium source (b) and $NaYF_4$ nanorods synthesized with NaOH as a sodium source (c).

3.3.7 Longitudinal epitaxial growth of heterogeneous $NaGdF_4$ shells onto $NaYF_4$ cores

Method for longitudinal growth of $NaGdF_4$ -$NaYF_4$ nanorods

0.2 mmol of $GdCl_3$ in 1 mL methanol solution was magnetically mixed with OA (9.5 mmol) and ODE (25 mmol) in a 50 mL three-neck round-bottom flask. The mixture was degassed under an Ar flow and heated to 150 ˚C for 30 min to form a clear solution, and then cooled to room temperature. 4 mL of methanol solution containing NH_4F (0.8 mmol) and NaOH (0.5 mmol) was added to the OA and the ODE solution and stirred for 60 min. The solution is slowly heated to 110 ˚C and kept at 110 ˚C for 30 minutes to remove methanol and the remaining water completely. Then, 0.2 mmol of $NaYF_4$ core nanocrystals in cyclohexane was infected into the reaction solution. After holding the reaction temperature at 110 ˚C for further 10 min to evaporate all cyclohexane, the reaction mixture was quickly heated to 310 ˚C and aged for 1 hour.

Results and Discussions:

Figure 3.3.10 shows that the process of longitudinal growth of $NaGdF_4$ shell onto the $NaYF_4$ core is similar to that seen in the$NaYF_4$ - $NaYdF_4$ nanorods structure. The contrast that can be achieved with a TEM between the $NaGdF_4$ shell and $NaYF_4$ crystal provides better resolution to record this process.

Small α phase $NaGdF_4$ nanocrystals are formed at the beginning of the reaction step. After 15 minutes of reaction the shape of $NaYF_4$ cores changes from spherical to hexagonal. At 30 minutes of reaction, thin layers of $NaGdF_4$ have formed on the bottom and top surfaces (001) of the $NaYF_4$ hexagonal prism and the $NaGdF_4$ layer has also formed along the c axis. At the completion of the reaction, $NaGdF_4$@$NaYF_4$ dumbbell-shape nanocrystals have formed which could be attributed to the selective growth of the $NaGdF_4$ shells along the longitudinal direction. The concentration of shell source reagents in the reaction mix decreases rapidly as it was consumed by the growth of the β-$NaGdF_4$ shell and the α-$NaGdF_4$ nanocrystals. With this decrease in the concentration, α-$NaGdF_4$ nanocrystals were rapidly dissolved and formed the β-$NaGdF_4$ shell.

The results of the characterization (Figure 3.3.11) of another validation experiments showed that the heterogeneous nanocrystals exhibit a dumbbell shape with $NaGdF_4$ nanocrystals at the two ends. The dissolution (etching) phenomenon from the side surfaces (100) of $NaYF_4$ core was observed, which was attributed to the strong binding of the oleate ions (OA^-) to the exposed rare earth ions on the side surfaces of the particles. Detailed investigation of this interesting phenomenon were carried out and are described in part 3 of

this supplementary. The length of the $NaYF_4$– $NaGdF_4$ nanocrystals was observe to visibly increase in the longitudinal direction from 42 nm to 62 nm, while the width of $NaYF_4$ in the middle of each nanorods decreased by 8 nm, due to the dissolution of the $NaYF_4$ crystal during growth of the $NaGdF_4$. The width of the newly formed $NaGdF_4$ crystals at each end was measured at 29 nm, which was similar to the original width of the $NaYF_4$ core nanocrystals.

The HAADF-STEM images (Figure 3.3.11 (c)) demonstrate the density contrast of the $NaGdF_4$ at the ends and the $NaYF_4$ in the middle and the elemental mapping images confirm the distribution of the elements Y and Gd. The combined elemental mapping image confirms that the two compositions are well aligned.

Brief conclusion:

At a high concentration of oleate ions (OA^-), the deposition and epitaxial growth of heterogeneous shells ($NaGdF_4$) still prefer the bottom and top surfaces (001) of $NaYF_4$ crystal core.

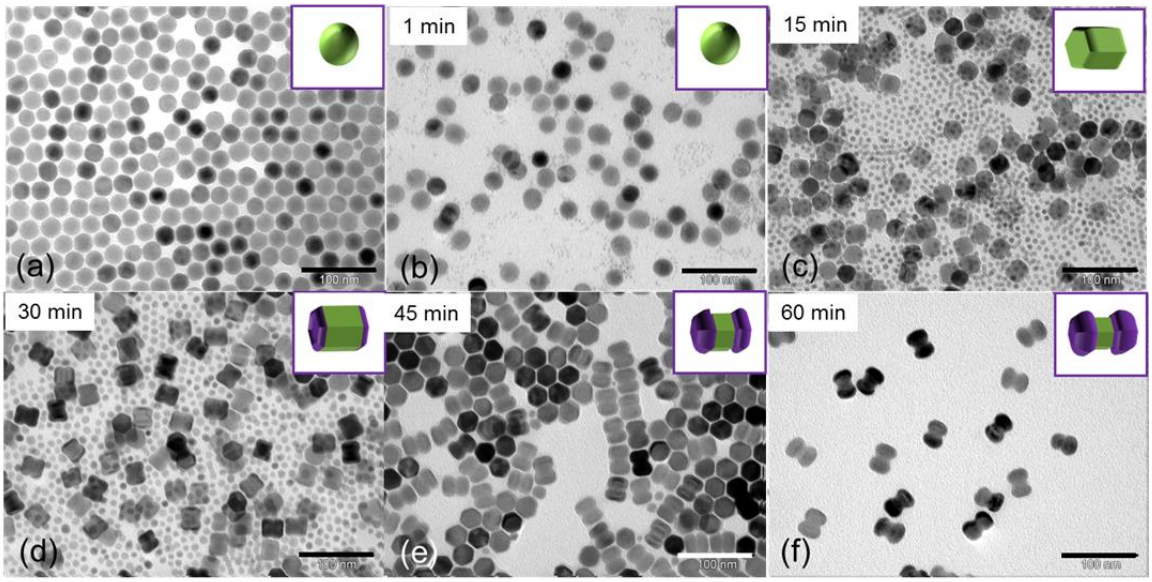

Figure 3.3.10 Real-time monitoring morphology evolution in the process of longitudinally growth of heterogeneous $NaGdF_4$ shell onto $NaYF_4$ cores is shown. The TEM images of the $NaYF_4$ cores (a) and the evolution of its heterogeneous products are shown by step-by-step sampling during the reaction at 310˚C after 1 min (b), 15 min (c), 30 min (d), 45 min (e), 60 min (f) of reaction time (scale bars: 100 nm)

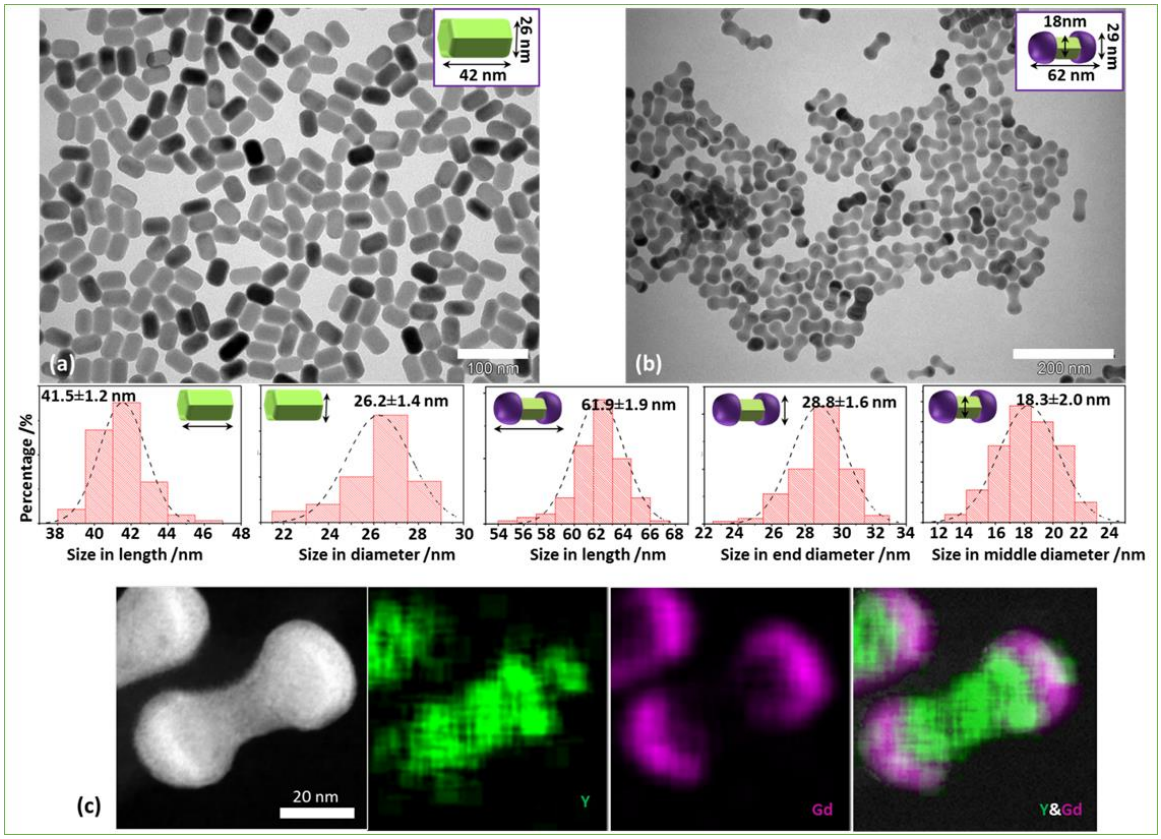

Figure 3.3.11. TEM images, size distributions and characterization of elemental compositions of heterogeneous growth of $NaGdF_4$ onto the $NaYF_4$ core nanocrystals is shown. The (a) $NaYF_4$ core nanocrystals; and (b) the $NaGdF_4$ - $NaYF_4$ nanocrystals after epitaxial growth of $NaGdF_4$ in the longitudinal direction. The (c) HAADF-STEM image of a single dumbbell shaped $NaYF_4$ – $NaGdF_4$ nanocrystal is shown with its elemental mapping images.

3.3.8 The stability of shell material in affecting crystal dissolution

In the section 3.3.7, I find that $NaYF_4$ is partially etched off while grow $NaGdF_4$ shell. To figure the mechanism behind this phenomenon, I search relevant literatures about the $NaYF_4$ nanocrystal etching in thermal decomposition reaction. According to literature[2], the size and dipole polarizability of the lanthanide ion dominate the crystal formation stability, and the nanocrystals formed with larger lanthanide ions are more stable. Yb^{3+} has been chosen because it is smaller than Y^{3+}, and Tb^{3+} is in between Y^{3+} and Gd^{3+}. This in principle will make the core $NaYF_4$ more stable than the $NaYbF_4$ as shell, but not as stable as $NaTbF_4$ and $NaGdF_4$ shells. The stability is ranked as $NaGdF_4$> $NaTbF_4$> $NaYF_4$ > $NaYbF_4$.

Method:

The purpose for this experiment is to assess the stability of shell material to crystal dissolution. We adopted the same synthesis method used in section 3.3.7, except YCl_3, $TbCl_3$ or $YbCl_3$ used as shell precursor materials instead of $GdCl_3$.

Results and Discussions:

As shown in the Figure 3.3.12 comparing to $NaGdF_4$ as shell (b), only slight dissolution was observed during the growth of $NaTbF_4$ as shell (c), but no dissolution effect was observed when using the $NaYbF_4$ as the shell (d), in which case rather than being dissolved from the core the overall size of nanorods was increased.

These results suggest that the dissolution of core is intrinsically caused by the thermal stability between core and shell materials, for example, $NaGdF_4$ shell is more stable than $NaYF_4$ core [10] so that the core was dissolved. The degree of thermal stability of the different $NaLnF_4$ nanocrystals affects the dissolution rate. Comparing the dissolution rates using $NaTbF_4$ as shell and $NaGdF_4$, the dissolution in the case of $NaGdF_4$ was more obvious. But because the $NaYbF_4$ is less stable than the core $NaYF_4$, the core was stable without dissolution observed. A similar evidence was observed when growing $NaYF_4$ onto $NaGdF_4$ there was no dissolution but slightly increase in diameter (see Figure 3.3.14).

Although it has been confirmed in Figure 3.3.7 that the concentration of F^- did not affect the direction of the epitaxial growth as long as the OA^-/OAH ratio was unchanged, the concentration of F^- can be used to kinetically control the degree in the core dissolution because of the gradient of reagent concentration. The dissolution only occurred slowly at high concentration of F^- source (usually 72 μmol/ml), but it became much more obvious and quicker when the epitaxial growth was conducted without F^- source (see the main text Figure 3, the hourglass shaped nanocrystals). When the concentration of F^- source was adjusted to

the medium level, the dissolution rate and amount from the core nanocrystals can be accordingly controlled.

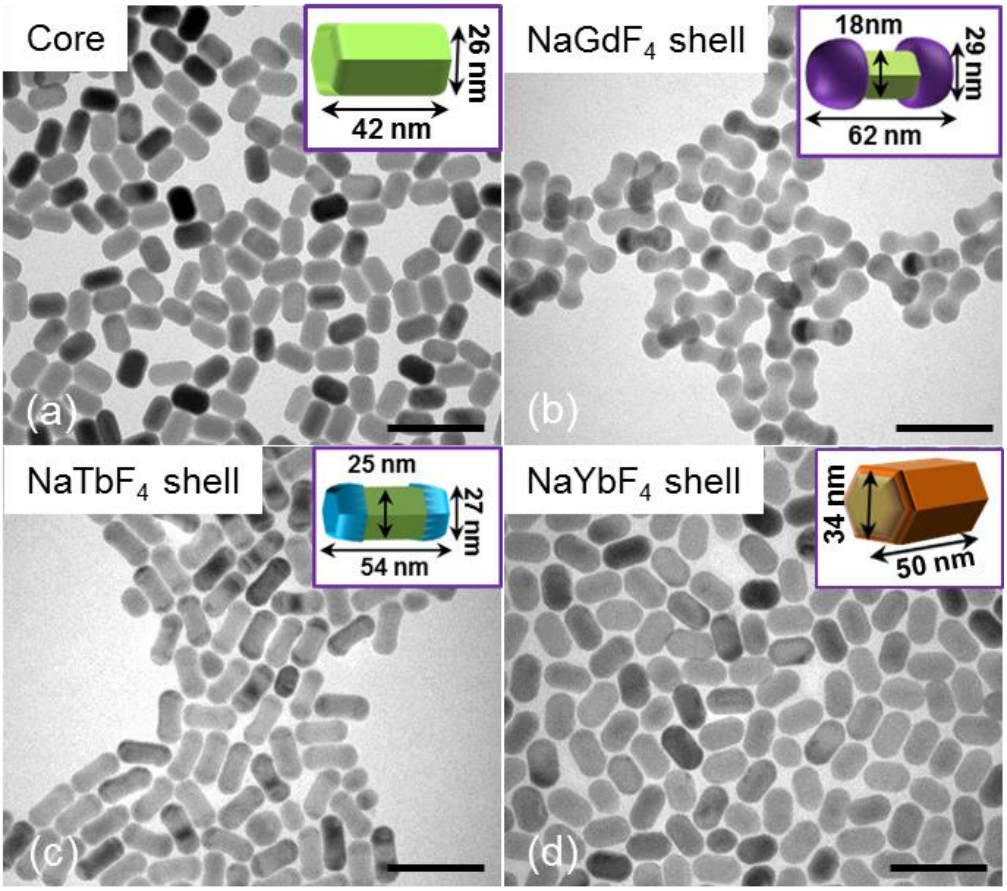

Figure 3.3.12, TEM images of $NaYF_4$ core only nanocrystals (a) and grown with different $NaLnF_4$ shells, $NaGdF_4$ (b), $NaTbF_4$ (c) and $NaYbF_4$ (d). Note, other reaction conditions kept the same as these in the longitudinal growth process. (Scale bar: 100 nm)

Brief conclusion:

The dissolution of core is caused by the thermal stability between core and shell materials. It requires that the shell materials have higher thermal stability than core material to ensure the core crystal dissolution. The bigger difference of thermal stability between core and shell will result in the higher dissolution rate.

3.3.9. Accelerated longitudinal growth of $NaGdF_4$ -$NaYF_4$ nanorods by adding KOH

Based on our hypothesis, the shell growth direction is high impacted by the ratio of OA^-/OAH, appropriately increasing the ratio of OA^-/OAH should increase the longitudinal growth speed. KOH has a higher dissociation constant than NaOH, adding additional KOH will increase the amount of OA^- dissociated from OAH and increase the passivation effect on the side surfaces of the particles. This will accelerate epitaxial growth in longitudinal direction. To verify this hypothesis, we add 0.4 mmol of KOH to the reaction mix.

Method for accelerated longitudinal growth of $NaGdF_4$ -$NaYF_4$ nanorods by adding KOH

0.2 mmol of YCl_3 (or $GdCl_3$) in 1 mL of methanol solution was magnetically mixed with OA (9.5 mmol) and ODE (25 mmol) in a 50 mL three-neck round-bottom flask. The mixture was degassed under Ar flow and heated to 150 ˚C for 30 min to form a clear solution, before cooling to room temperature. 5 mL of methanol solution containing NH_4F (0.8 mmol), **KOH (0.4 mmol)** and NaOH (0.5 mmol) was added into the OA and ODE solution and stirred for 60 min. The solution was slowly heated to 110 ˚C and kept at 110 ˚C for 30 minutes to remove the methanol and water completely. The reaction mix was then injected with 0.2 mmol of $NaYF_4$ core nanocrystals (or nanorods), both suspended in cyclohexane, into the reaction solution. After holding the reaction mix at 110 ˚C for further 10 min to evaporate all cyclohexane, the mixture was heated rapidly to 310 ˚C before aging for 1 hour at this temperature.

Results and discussions

With the aid of KOH, the longitudinal growth of the $NaYF_4$ and $NaGdF_4$/$NaYF_4$ nanocrystals became faster and the end particles were longer in contrast to the particles formed when KOH was not present in the mix. (Figure 3.3.13) The final nanorods or nanocrystal dumbbells have sharper edges compared to the ones produced without the presence of KOH. (Figure 3.3.14) This suggests that the amount of the OA^- ions available on the side surfaces during the reaction to passivate the side surfaces (100) by acting as surfactants was sufficient.

Brief conclusion:

KOH can quickly supply sufficient OA^- ions on the side surfaces and therefore it promotes the longitudinal growth of the nanocrystals. KOH reacts with Oleic Acid (OA) and forms KOA, which significantly increasing the ratio of OA^- to OAH. The higher ratio of OA^- /OAH promotes this trend in longitudinal growth.

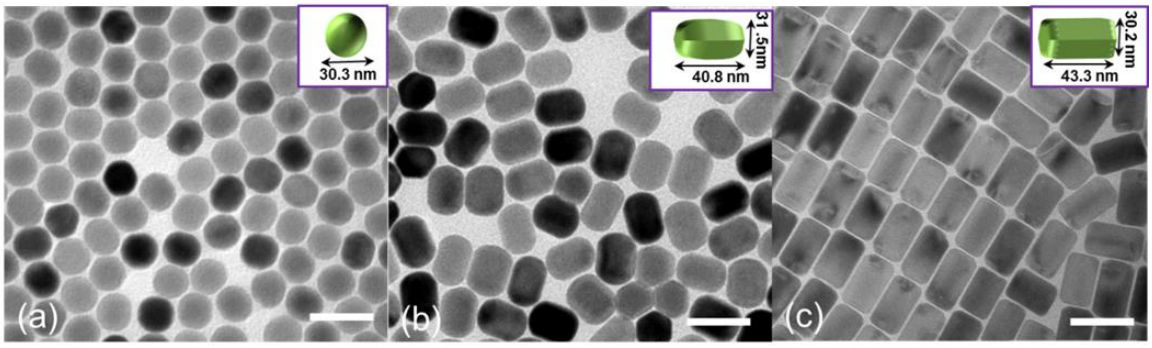

Figure 3.3.13. TEM images of the $NaYF_4$ core (a) and the $NaYF_4$ coated with a $NaYF_4$ shell without KOH present (b) and with 0.4 mmol of KOH present (c) (Scale bars: 50 nm)

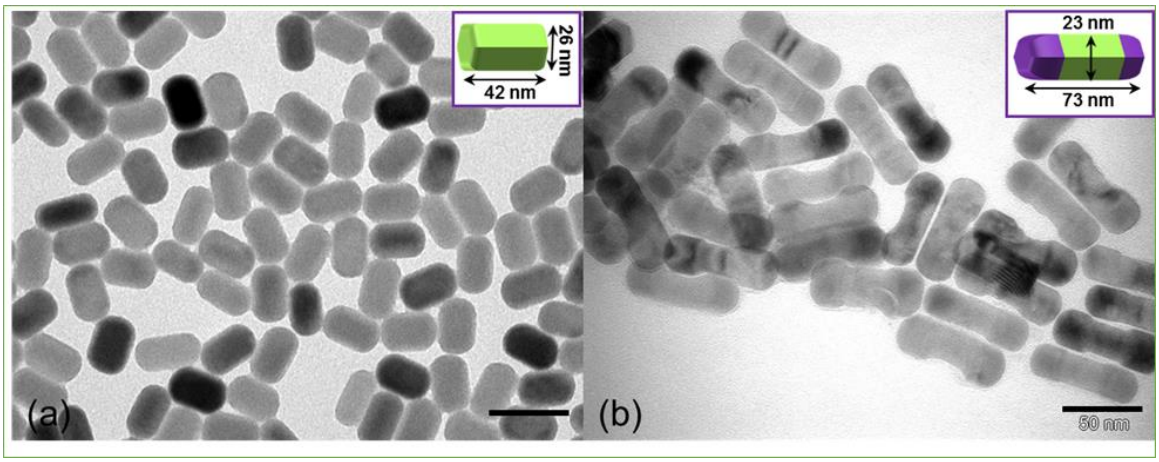

Figure 3.3.14. TEM images of the $NaYF_4$ nanorods acting as the core (a) and the longitudinal growth of the $NaGdF_4$ shell onto the $NaYF_4$ core with 0.4 mmol KOH present in the mix. (Scale bars: 50 nm)

3.3.10. Longitudinal epitaxial growth of multiple-section $NaYF_4$-$NaGdF_4$ nanorods

Method for longitudinal synthesis of five-section $NaYF_4$ - $NaGdF_4$ - $NaYF_4$ bamboo-like nanorods

0.2 mmol of YCl_3 in 1 mL of methanol solution was magnetically mixed with OA (9.5 mmol) and ODE (25 mmol) in a 50 mL three-neck round-bottom flask. The mixture was degassed under Ar flow and heated to 150 ˚C for 30 minutes to form a clear solution, and then cooled to room temperature. 5 mL of methanol solution containing NH_4F (0.8 mmol), KOH (0.4 mmol) and NaOH (0.5 mmol) was added into the OA and ODE solution and stirred for 60 minutes. The solution was slowly heated to 110 ˚C and kept at 110 ˚C for 30 minutes to remove the methanol and water completely. The reaction solution was then injected with 0.2 mmol of $NaGdF_4$ and of $NaYF_4$ nanorods in cyclohexane solution. After the reaction at 110 ˚C for a further 10 minutes to evaporate all the cyclohexane, the reaction mixture was quickly heated to 310 ˚C and held at this temperature for 1 hour.

Method for longitudinal synthesis of seven-section $NaGdF_4$ - $NaYF_4$ - $NaGdF_4$ - $NaYF_4$ bamboo-like nanorods

The same procedure was repeated, and then followed by the injection of 0.2 mmol of the five-section *$NaYF_4$ - $NaGdF_4$ - $NaYF_4$* nano-bamboos which acted as the core, all in cyclohexane solution, into the reaction solution. After holding at 110 ˚C for a further 10 minutes to evaporate all cyclohexane, the reaction mixture was quickly heated to 310 ˚C and held again for 1 hour.

Discussion and brief conclusion:

It is well known that the co-precipitation method is useful for the synthesis of sub-100 nm nanocrystals, while the hydrothermal method is suitable for synthesizing larger sized nanocrystals in the micron size range.[11, 12] Our current experiments show that with the aid of high concentration of NaOH or KOH in the reaction OA^- ions can passivate effectively the side surfaces (100) (010) of nanorods and so grow very long homogeneous or heterogamous nanocrystals with some control.

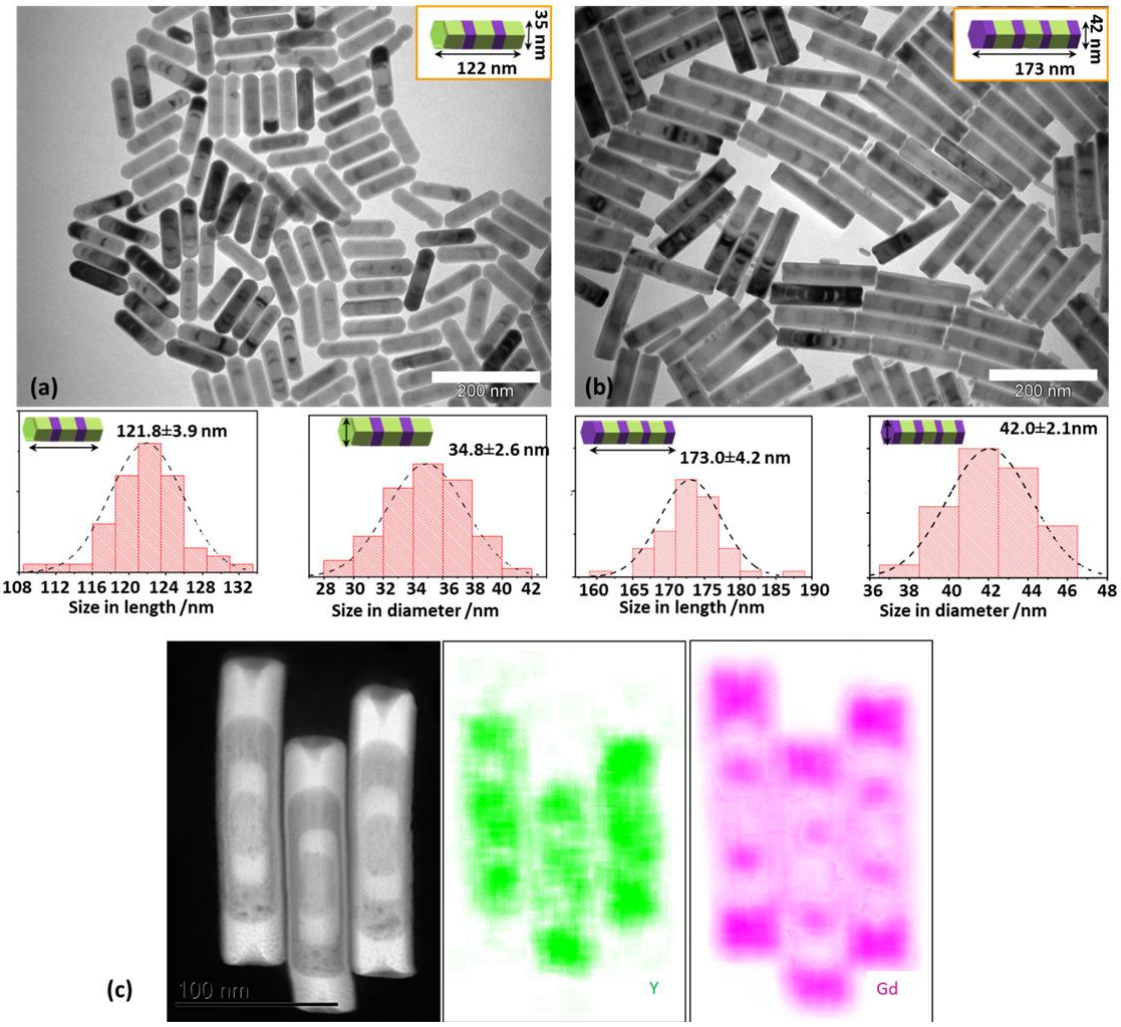

Figure 3.3.15. TEM images, size distribution and characterization of the elemental composition of periodical $NaYF_4$–$NaGdF_4$ nanocrystals which form a bamboo-like nanostructure. (a) five-section $NaYF_4$–$NaGdF_4$ nanocrystals in a bamboo shape obtained by an epitaxial growth of $NaYF_4$ and $NaGdF_4$ in a longitudinal direction; (b) seven-section $NaYF_4$–$NaGdF_4$ nanocrystals in an bamboo shape; the length of the five-section $NaYF_4$–$NaGdF_4$ nanocrystals can reach 122 nm and its width, 35 nm. With two more sections, the seven-section $NaYF_4$–$NaGdF_4$ nanocrystals grow to 173 nm and the width increases to 42 nm. (c) HAADF-STEM image of three single $NaYF_4$–$NaGdF_4$ nanocrystals and their elemental mapping images. The HAADF-STEM image demonstrates the contrast in density between the $NaGdF_4$ and the $NaYF_4$ as well as their elemental corresponding mapping images, which confirm the distribution of the elements Y and Gd. (scale bars: 200 nm in (a) and (b), 100 nm in (c))

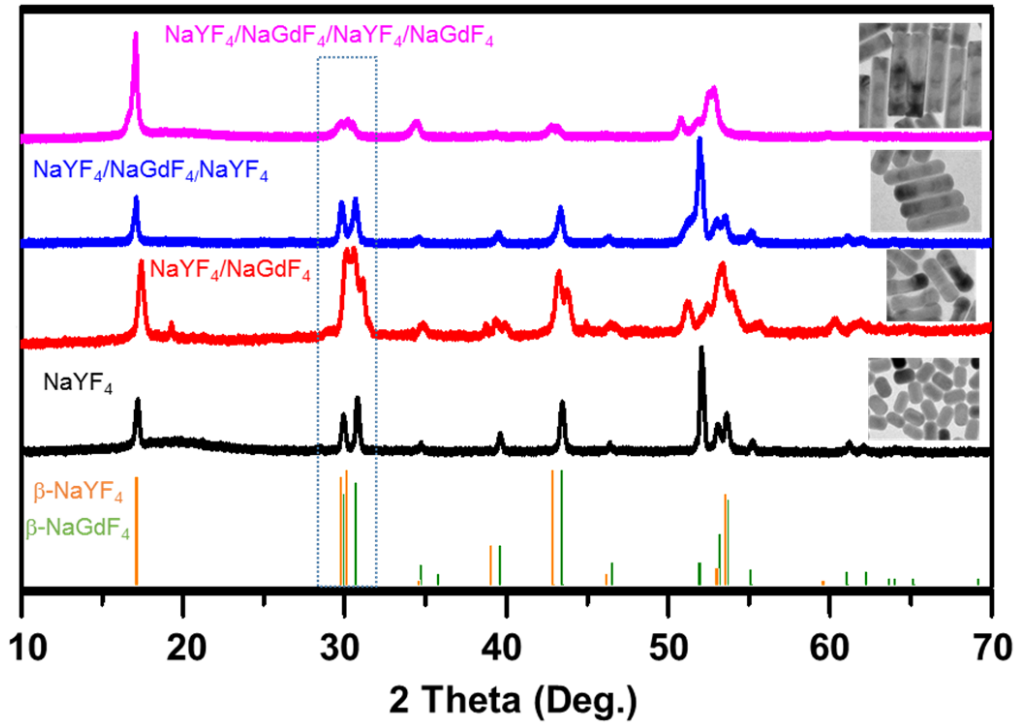

Figure 3.3.16. The X-ray powder diffraction patterns for the β-$NaYF_4$ nanorods, $NaYF_4$/$NaGdF_4$ nanorods, $NaYF_4$/$NaGdF_4$/$NaYF_4$ nanorods and the $NaYF_4$/$NaGdF_4$/$NaYF_4$/$NaGdF_4$ nano-bamboos. The figure shows that all these $NaYF_4$/$NaGdF_4$ hetero nanocrystals were identified as hexagonal phase when compared to the β-$NaYF_4$: JCPDS:16-0334 and β-$NaGdF_4$: JCPDS: 27-0699 file shown). As the marked peaks shown, the two peaks of the $NaYF_4$ and $NaGdF_4$ at approximately 30 degrees, overlap to form a broad peak, which suggests that the nanocrystals are composited by both the β-$NaYF_4$ and the β-$NaGdF_4$.

3.4 Transversal epitaxial growth of heterogeneous $NaGdF_4$ shell onto $NaYF_4$ core

To develop a set of approaches for the programmable growth of arbitrary shapes of nanocrystals, and according to the selective preference of OAH molecules and OA^- ions to different facets of nanocrystal cores, we identified the condition of the lower ratio of OA^-/OAH at slightly lower temperature (290 ºC vs. 310 º C) which better passivate the top and bottom surfaces (001) of the nanocrystal cores so that the epitaxial shell growth will be based on the side surfaces (100) along their transversal direction.

Method for transversal synthesis of $NaGdF_4$ shell onto $NaYF_4$ core

0.1mmol of $GdCl_3$ in 1 mL methanol solution was magnetically mixed with OA (19.0 mmol) and ODE (18.7 mmol) in a 50 mL three-neck round-bottom flask. The mixture was degassed under Ar flow and heated to 150 ˚C for 30 min to form a clear solution, and then cooled to room temperature. 3 mL of methanol solution containing NH_4F (0.4 mmol) and NaOH (**0.15 mmol**) was added into the OA and ODE solution and stirred for 60 min. The solution was slowly heated to 110 ˚C and kept at 110 ˚C for 30 min to remove completely the methanol and water. Then 0.1mmol of the $NaYF_4$ cores in cyclohexane solvent were injected into the reaction mix. After being kept at 110 ˚C for further 10min to evaporate all cyclohexane, the reaction mixture was quickly heated up to **290 ˚C** and held at that temperature **for 3 hours**.

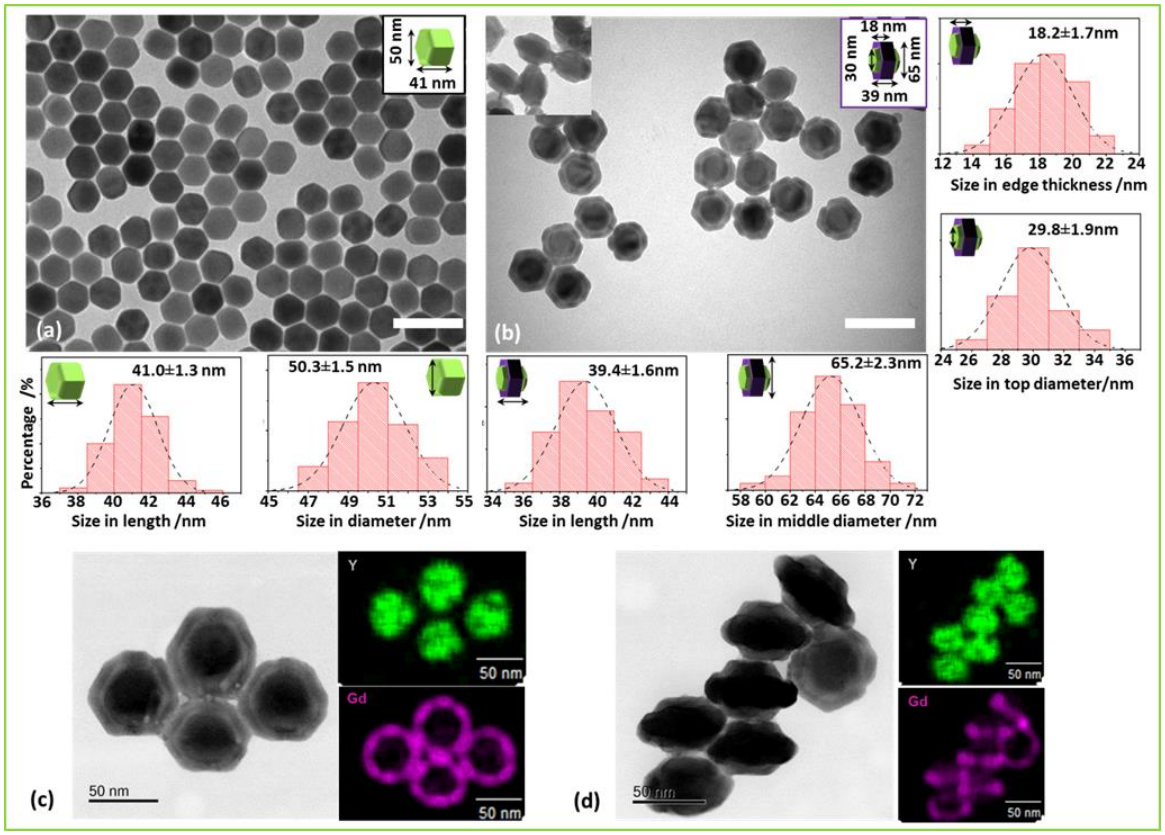

Figure 3.4.1. (a-b): TEM images and size distribution histograms. (a): the $NaYF_4$ core nanocrystals (scale bar is 100 nm). b): the $NaYF_4$-$NaGdF_4$ nanocrystals with transversal growth of $NaGdF_4$ on their side surfaces (scale bar is 100 nm). (c-d) High magnification TEM images and EDS elemental mapping images of the $NaYF_4$-$NaGdF_4$ nanocrystals (scale bar is 50 nm); from the top view (c) and the side view (d). The EDS elemental mapping images clearly show that that $NaGdF_4$ is located well outside the $NaYF_4$ core nanocrystals in the middle part of its structure.

Results and Discussion:

TEM characterization results shown in Figure 3.4.1 and in Figure 3.4.2 confirm a core-shell structure when viewed from the top of the nanocrystals, while the insert image (Figure 3.4.1 (b)) and high resolution image of (Figure 3.4.1 (d)) reveal a core-ring structure when viewed from the side, with the shell grown only around the side surfaces of the nanocrystal cores.

The length of the nanocrystal slightly reduces from 41 nm to 39 nm after transversal growth, while the size in diameter increases from 50 nm to 65 nm, indicating that the thickness of $NaGdF_4$ ring layer was 7.5 nm. The height of $NaGdF_4$ ring was measured and found to be 18.2 nm.

It is worth noting that the diameter of the $NaYF_4$ core nanocrystals at its two ends was reduced from 49 nm to 30 nm, suggesting a disillusion (etching) phenomenon occurred on the

end edges during the epitaxial growth of $NaGdF_4$ rings in the middle part of the core. The elemental mapping images in Figure 3.4.1 (c) and (d) demonstrate that the ion Gd^{3+} was deposited within the rings with the ion Y^{3+} deposited in the core.

From the high resolution TEM images in Figure 3.4.2, we can confirm that the growth direction of $NaGdF_4$ shell was vertical to the [001] direction. The (110) plane distance at the top edge area was 2.97 Å while the (110) distance at the middle area was 3.02 Å, which is consistent with the standard parameters of the β-$NaYF_4$ from pdf #16-0334 and the β-$NaGdF_4$ from pdf #27-0699.

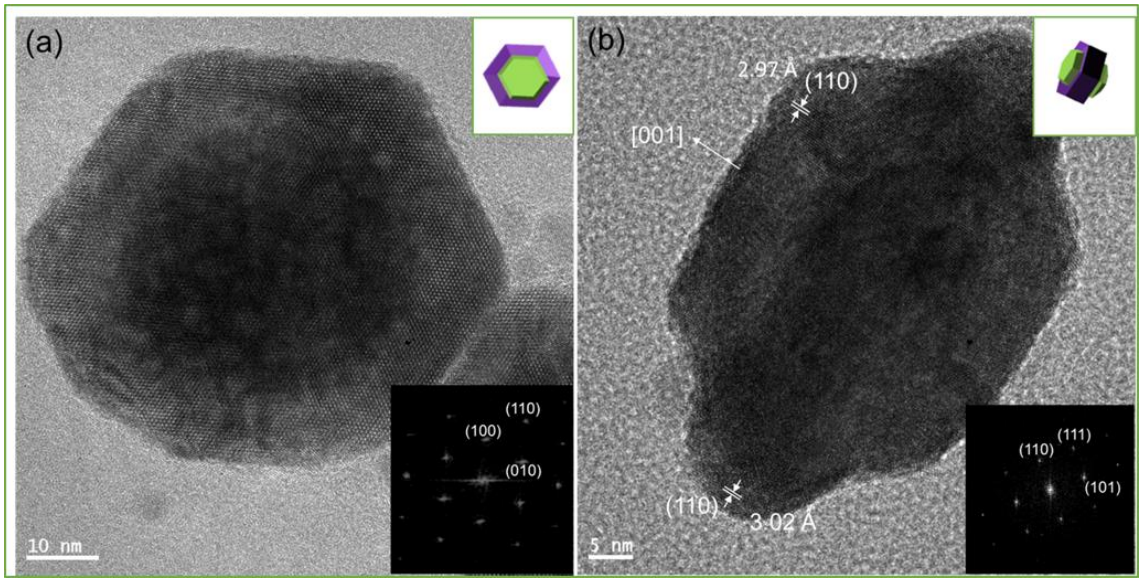

Figure 3.4.2 (a) Top view high-resolution TEM image of a single nanocrystal and its corresponding selected-area electron diffraction pattern (inset) taken in the [001] incidence and in (b) the side view high-resolution TEM image and its corresponding selected area electron diffraction pattern as an insert.

Brief conclusion:

According to the computational modeling results performed in this work, the binding energy of OAH on the (001) facet was two times stronger than that calculated on the (100) facets, and the relatively higher concentration of OAH molecules generated a stronger passivation effect to block the access for epitaxial growth of shells onto the end surfaces. Under relatively low reaction temperature that facilitates the binding of OAH molecules, the difference in binding strength of the surfactants covering on each facet caused the anisotropic

shell formation. Even though the difference was smaller than that observed in the longitudinal growth, the result was still very clear when a shorter reaction was performed.

With a lower ratio of OA^-/OAH (which equates to a relatively low OA^- concentration) and at lower reaction temperature, the OAH molecules were the main surface ligands preferably on the top and bottom surfaces of nanocrystal cores, inhibiting the end surfaces (001) and therefore promoting the epitaxial growth of $NaGdF_4$ shell in its transversal direction.

The etching phenomenon observed on the ends of the side surfaces (100) of the $NaYF_4$ was due to the strong binding of the oleate ions (OA^-) to the exposed rare earth ions on the side surfaces of the particles.

Therefore, for the longitudinal growth, 310 ˚C was selected. On the other hand, with low ratio of OA^- and OAH, OAH will become the major surfactant, which attach onto (001) planes with higher bonding energy than that on (100) planes but much lower than the bonding energy of OA^- on (100) planes in the case of high ratio of OA- and OAH. To keep the binding of OAH onto (001), 290 ˚C was used for the transversal growth.

3.5 Summary

Systemic experiment results prove that the ratio of oleate anion and oleic acid (OA^-/OAH ratios) added, the reaction temperature of the synthesis, and the concentration of the reagents as combined factors to effect the shell growth direction. Under certain temperature, the ratio of OA^-/OAH is the key factor to control the longitudinal shell growth and transversal shell growth. Under 310 ^oC, the shell growth direction can be controlled to be longitudinal by applying a high ratio of OA^-/OAH. So we generated a series of rod like nanocrystals, such as nanorods, nano-dumbbells, nano-bamboo, et al.

Under 290 ^oC, the shell growth direction can be controlled to be transversal by applying a low ratio of OA^-/OAH. Following this method, disk shaped nanocrystals were synthesized.

Also, a $NaYF_4$ etching phenomena was discovered in the synthesis of $NaYF_4$/$NaGdF_4$ nano-dumbbells. By a series of experiment, we find that the dissolution of core is caused by the thermal stability between core and shell materials. It requires that the shell materials have higher thermal stability than core material to ensure the core crystal dissolution. The bigger difference of thermal stability between core and shell will result in the higher dissolution rate. This etching effect will be studied further in the next chapter.

Reference

[1] F. Wang, R.R. Deng, X.G. Liu, Nat Protoc, 9 (2014) 1634-1644.
[2] F. Wang, R.R. Deng, J. Wang, Q.X. Wang, Y. Han, H.M. Zhu, X.Y. Chen, X.G. Liu, Nat Mater, 10 (2011) 968-973.
[3] D. Chen, P. Huang, Dalton transactions, 43 (2014) 11299-11304.
[4] G.Y. Chen, H. Agren, T.Y. Ohulchanskyy, P.N. Prasad, Chem Soc Rev, 44 (2015) 1680-1713.
[5] J. Chen, J.X. Zhao, Sensors, 12 (2012) 2414-2435.
[6] Y. Sun, Y. Chen, L. Tian, Y. Yu, X. Kong, J. Zhao, H. Zhang, Nanotechnology, 18 (2007) 275609.
[7] D. Yang, Z. Hou, Z. Cheng, C. Li, J. Lin, Chem Soc Rev, 44 (2015) 1416-1448.
[8] J. Zhuang, L. Liang, H.H. Sung, X. Yang, M. Wu, I.D. Williams, S. Feng, Q. Su, Inorganic chemistry, 46 (2007) 5404-5410.
[9] N.J.J. Johnson, F.C.J.M. van Veggel, Nano Res, 6 (2013) 547-561.
[10] F. Wang, Y. Han, C.S. Lim, Y.H. Lu, J. Wang, J. Xu, H.Y. Chen, C. Zhang, M.H. Hong, X.G. Liu, Nature, 463 (2010) 1061-1065.
[11] C. Li, Z. Quan, J. Yang, P. Yang, J. Lin, Inorg Chem, 46 (2007) 6329-6337.
[12] F. Zhang, Y. Wan, T. Yu, F. Zhang, Y. Shi, S. Xie, Y. Li, L. Xu, B. Tu, D. Zhao, Angew Chem Int Edit, 46 (2007) 7976-7979.

Chapter 4. Programmable Growth of 3D Shapes of Heterogeneous Nanocrystals

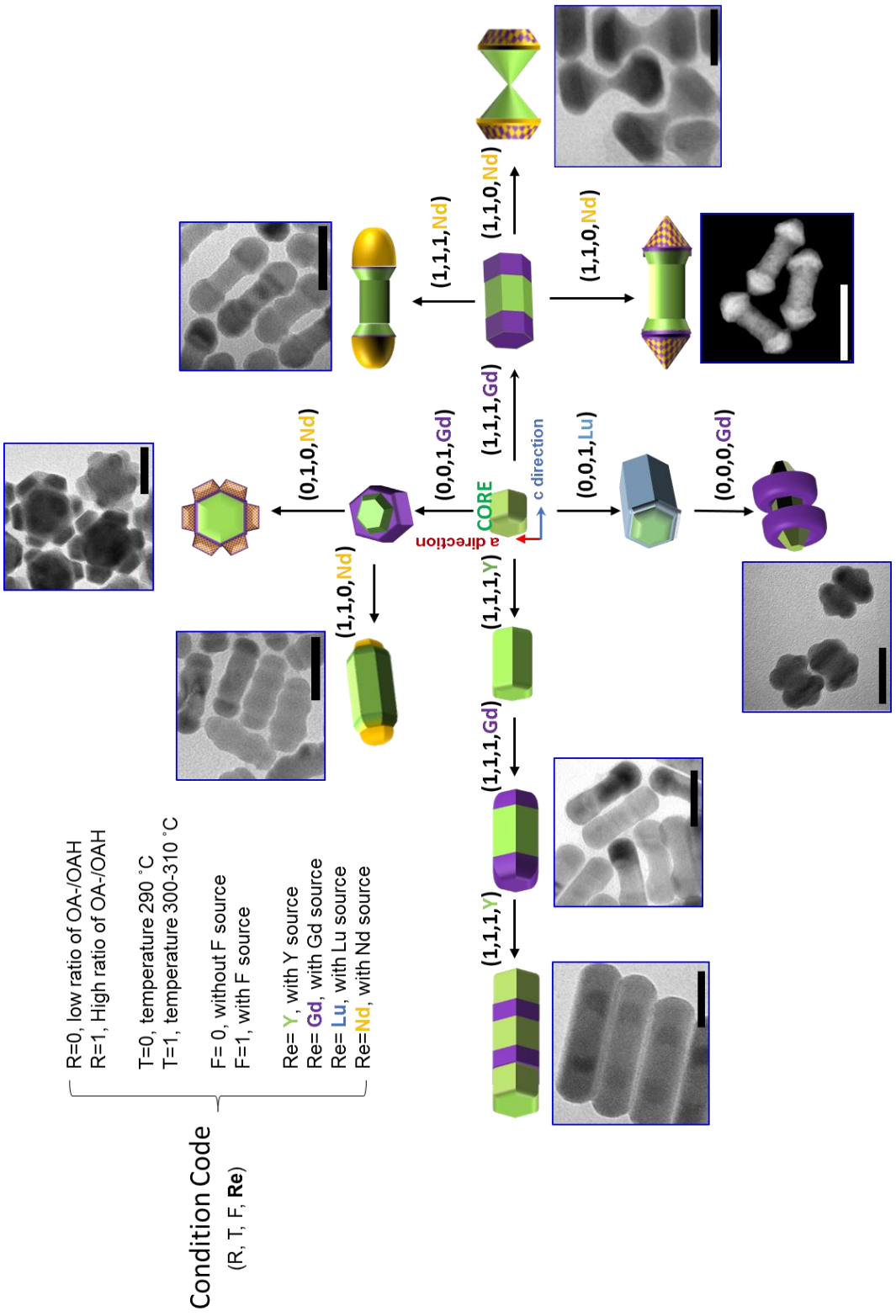

Figure 4.1 Scheme of Logically growth of heterogeneous nnaocrystals

Rare earth doped nanocrystals have emerged as a means to provide exceptional optical, magnetic and physical-chemical properties,[1-9] for photon upconversion, background-free biological assays, multimodal *in vivo* bio-imaging (fluorescence, MRI, X-ray, SPECT, etc.),[10-13] targeted drug delivery as carriers, cancer therapy, full color displays, infrared upconversion photovoltaic and photo catalysis for energy management, security inks, and photonics. As a logically extensive research on these applications, integrating multiple functions in single nanoparticles can provide more cross-linking options and new possibilities in as yet unrealized frontier areas. Multi-functionalizing heterogeneous nanoparticles present an extremely attractive research topic that is motivated by both physical-chemistry researches and biomedical life science applications. To realize the myriad of these opportunities, readily scalable, hybrid materials should be synthesized through an integrated approach so that its different structural constituents can collectively contribute to the same challenge.

We have already demonstrated the precise control in the growth of homogeneous shells, longitudinal and transversal growth of heterogeneous shells in Chapter 2 and Chapter 3. In this chapter, we introduce another shell growth process, migration shell growth, and we use these range of combinatory techniques to design and fabricate some $NaREF_4$ heterogeneous core-shell nanocrystals with interesting shapes, such as hourglass, flower, spintop, dumbbell and so on.

In the Chapter 3, an interesting phenomenon of $NaYF_4$ etched off in the reaction of $NaGdF_4$ shell growth. And we figure out that the dissolution of $NaYF_4$ core is caused by the thermal stability between core and shell materials. It requires that the shell materials have higher thermal stability than core material to ensure the core crystal dissolution. The bigger difference of thermal stability between core and shell will result in the higher dissolution rate. In this chapter, we further study the etching effect via controlling the concentration of F anion in the reaction solution.

4.1 Crystal lattice mismatch for crystallographic parameters c and a & b for hexagonal phase $NaREF_4$ crystals.

Towards developing scalable synthesis protocols for multifunctional heterogeneous nanostructures with high degree of controls in size, shape, surface and composition, we have further studied the lattice mismatch for crystallographic parameters *c* and *a* for hexagonal phase $NaREF_4$ crystals.

Table 4.1 shows the crystal lattice parameters of hexagonal phase $NaREF_4$ crystals. The difference between the two crystallographic parameters (*a* & *b*, and *c*) can affect the epitaxial growth of subsequent layers. For example, the $NaNdF_4$ crystals can be grown with no hindrance onto $NaGdF_4$ than onto $NaYF_4$ due to the close similarities in their crystallographic parameters; likewise $NaGdF_4$ crystals prefer to grow onto the $NaYF_4$ crystal lattice than onto the $NaLuF_4$ crystal lattice.

Table 4.1 The crystal lattice parameters of hexagonal phase $NaREF_4$ crystals.

Crytal Host	a & b(Å)	C(Å)
$NaLaF_4$	6.178	3.828
$NaCeF_4$	6.15	3.781
$NaNdF_4$	**6.1**	**3.711**
$NaSmF_4$	6.051	3.64
$NaEuF_4$	6.059	3.625
$NaGdF_4$	**6.02**	**3.601**
$NaTbF_4$	6.008	3.58
$NaPrF_4$	5.991	3.537
$NaDyF_4$	5.985	3.554
$NaYF_4$	**5.96**	**3.53**
$NaErF_4$	5.959	3.514
$NaTmF_4$	5.953	3.494
$NaYbF_4$	5.925	3.471
$NaLuF_4$	**5.901**	**3.453**

By calculating the mismatch rate for the difference in the crystal lattice units, we can quantify the possibility of direct epitaxial growth of different crystal types onto the core crystal when forming a heterogeneous rare-earth doped single nanocrystals. Table 4.2 summarizes the lattice mismatch for crystallographic parameter *c* for hexagonal phase $NaREF_4$ crystals. The green area shown represents the pair crystals with a lattice mismatch that is less than 3%, which suggests a close crystal lattice match, while the yellow and the red areas mark a higher lattice mismatch rate of either 3.1% to 5% or 5.1% respectively, indicating greater difficulty in the direct epitaxial growth of a heterogeneous nanocrystal from these two constituents

Table 4.2 Summary of the lattice mismatch for crystallographic parameters c for a hexagonal phase $NaREF_4$ crystals. The crystallographic potential for high quality epitaxial growth increases with a change of color from green to red.

	$NaLuF_4$	$NaYbF_4$	$NaTmF_4$	$NaErF_4$	**$NaYF_4$**	$NaDyF_4$	$NaPrF_4$	$NaTbF_4$	**$NaGdF_4$**	$NaEuF_4$	$NaSmF_4$	**$NaNdF_4$**	$NaCeF_4$	$NaLaF_4$
$NaLaF_4$	0.109	0.103	0.096	0.089	0.084	0.077	0.082	0.069	0.063	0.056	0.052	0.032	0.012	0.000
$NaCeF_4$	0.095	0.089	0.082	0.076	0.071	0.064	0.069	0.056	0.050	0.043	0.039	0.019	0.000	
$NaNdF_4$	0.075	0.069	0.062	0.056	**0.051**	0.044	0.049	0.037	**0.031**	0.024	0.020	0.000		
$NaSmF_4$	0.054	0.049	0.042	0.036	0.031	0.024	0.029	0.017	0.011	0.004	0.000			
$NaEuF_4$	0.050	0.044	0.037	0.032	0.027	0.020	0.025	0.013	0.007	0.000				
$NaGdF_4$	0.043	0.037	0.031	0.025	**0.020**	0.013	0.018	0.006	0.000					
$NaTbF_4$	0.037	0.031	0.025	0.019	0.014	0.007	0.012	0.000						
$NaPrF_4$	0.024	0.019	0.012	0.007	0.002	0.005	0.000							
$NaDyF_4$	0.029	0.024	0.017	0.011	0.007	0.000								
$NaYF_4$	0.022	0.017	0.010	0.005	0.000									
$NaErF_4$	0.018	0.012	0.006	0.000										
$NaTmF_4$	0.012	0.007	0.000											
$NaYbF_4$	0.005	0.000												
$NaLuF_4$	0.000													

4.1.1 Materials and Equipment

Chemical Materials

Reagents: $YCl_3.6H_2O$ (99.99%), $YbCl_3.6H_2O$ (99.99%), $GdCl_3.6H_2O$ (99.99%), $NdCl_3.6H_2O$ (99.99%), $TbCl_3.6H_2O$ (99.99%), $LuCl_3.6H_2O$ (99.99%), NH_4F (99%), $ErCl_3.6H_2O$ (99.99%), KOH (99%), NaOH (99%), 1-octadecene (ODE) (90%), NaF (99%), Ethanol (100%), Methanal (99%) and oleic acid (OA) (90%) were purchased from Sigma-Aldrich. Unless otherwise noted, all materials were used as starting materials and without further purification.

Equipment

Heating mental, temperature controller (working range 0 to 400 ºC), magnetic stirrer, thermometer (range to 20 to 350 ºC), ultrasonic, centrifuge, argon (scientific grade).

Transmission Electron Microscopy Characterization

Standard transmission electron microscope (TEM) measurements were performed using a Philips CM10 TEM with Olympus Sis Megaview G2 Digital Camera. The samples were prepared for TEM analysis by placing a drop of a dilute suspension of nanocrystals onto formvar-coated copper grids (300 meshes) and were allowed to dry in a desiccator at room temperature before using.

High resolution transmission electron microscope (TEM) measurements were performed with an aberration-corrected analytical transmission electron microscopy (TEM, JEOL ARM-200F) operated at 80 kV. High-angle annular dark-field (HAADF) scanning transmission electron microscope (STEM) images and their corresponding element mapping images were collected with the same TEM equipped with a Centurio SSD energy-dispersive X-ray spectroscopy (EDS) detector set at 77 K.

4.2 Design and fabrication of heterogeneous $NaYF_4/NaGdF_4/NaNdF_4$ nanocrystals in an hourglasses shape: investigation on the migration growth mechanism

Our first example is to show the design and synthesis of $NaYF_4/NaGdF_4/ NaNdF_4$ heterogeneous nanocrystals to form a heterogeneous nanoscale hourglasses. In this experiment, we observed for the first time a new epitaxial shell growth process and a migration growth pattern, which consists of the dissolution of $NaYF_4$ with the subsequent growth of the $NaNdF_4$ on the another facet.

The design logics is described as:

1. We first employed the approach of longitudinal growth of $NaGdF_4$ nanocrystal shells onto the top and bottom ends of the $NaYF_4$ nanocrystal cores;
2. then we continued to longitudinally grow $NaNdF_4$ nanocrystals, but in a condition of absence of F^- source; in such a condition, direct epitaxial shell growth of $NaNdF_4$ was stopped due to the lack of an F^- ion source;
3. In contrast, OA^- ligands were strongly anchored onto the surface of the rare earth ions on their side surfaces (100) facets which become unstable with the erosion of $NaYF_4$ being the most obvious; this causes the middle part of nanorods to be trimmed off;
4. A minimum amount of F^- ions gradually released from $NaYF_4$ into the reaction solution under the high reaction temperature of 310 ˚C helps to form $NaNdF_4$ nanocrystals longitudinally; this end-surface preference was also caused by the crystalline mismatch rate of $NaNdF_4$ vs. $NaYF_4$ was greater than that for the $NaNdF_4$ vs. $NaGdF_4$;
5. Finally, F^- ions and part of the Y^{3+} and Gd^{3+} ions are migrated from the middle part of nanorods to the $NaNdF_4$ section on each end of the heterogeneous nanocrystals.

Method for synthesis of $NaYF_4$ /$NaGdF_4$/$NaNdF_4$ nanocrystals in hourglasses shape

0.4 mmol of the $NdCl_3$ in 2 mL of methanol solution was magnetically mixed with OA (9.5 mmol) and ODE (25 mmol) in a 50 mL three-neck round-bottom flask. The mixture was degassed under Ar flow and heated to 150 ˚C for 30 min to form a clear solution, and then cooled to room temperature. 5 mL of the methanol solution containing KOH (0.8 mmol) and NaOH (0.8 mmol) was added and stirred for 60 min. The solution was slowly heated to 110 ˚C and kept at 110 ˚C for 30 minutes to completely remove the methanol and some of the water. It was then injected with 0.1 mmol 50 nm x 60 nm $NaYF_4/NaGdF_4$ nano-prisms particles, in a solution of cyclohexane, into the reaction mix. After having been kept at 110 ˚C

for another 10 minutes to evaporate all cyclohexane, the reaction mixture was quickly heated to 310 ˚C. 500 uL samples of the reaction solution were collected each time with a syringe at 5 minutes, 15 minutes, 30 minutes, 40 minutes, 50 minutes, and 60 minutes after the start of the reaction.

Results and discussion:

By real-time monitoring of the migration growth process, Figure 4.2.1 provided direct evidence that migration growth consists of a two-step reaction, (1) the dissolution of $NaYF_4$ with subsequent (2) growth of $NaNdF_4$ on the another facet. The size of nanocrystal core decreased significantly in the first 5 minutes, but without forming new component crystal on the crystal surface, indicating that the speed of dissolution of the nanocrystals was faster than crystal growth speed in this reaction step; After 15 minutes, new crystals started to form onto the top and bottom ends of the core as the width of the nanocrystal cores decreased. This result directly rules out "surface mobility" ("atom diffusion") as the possible driving force, since if this was the case the decrease of $NaYF_4$ and the increase of $NaNdF_4$ would happen at the same time, which was not the case with the sample taken after 5 minutes. The only mechanism that could explain the 5 minute sample was that the absence of the F^- ion source in the reaction mix at beginning makes $NaNdY_4$ growth impossible until the concentration of released F^- ions reaches a certain threshold.(see Figure 4.2.3)

Figure 4.2.1 shows the evolution process of the $NaYF_4/NaGdF_4$ cores as they form the $NaYF_4$-$NaGdF_4$-$NaNdF_4$ heterogeneous nanoscale hourglasses. In the modified protocol for longitudinal growth of heterogeneous nanocrystal rods, the absence of an F^- ion source with unbalanced F^- ion concentration causes the accelerated erosion of the $NaYF_4$ rods and the selective trimming off the $NaYF_4$ and the $NaGdF_4$ from the (100) facets on the side of the nanorods particles.

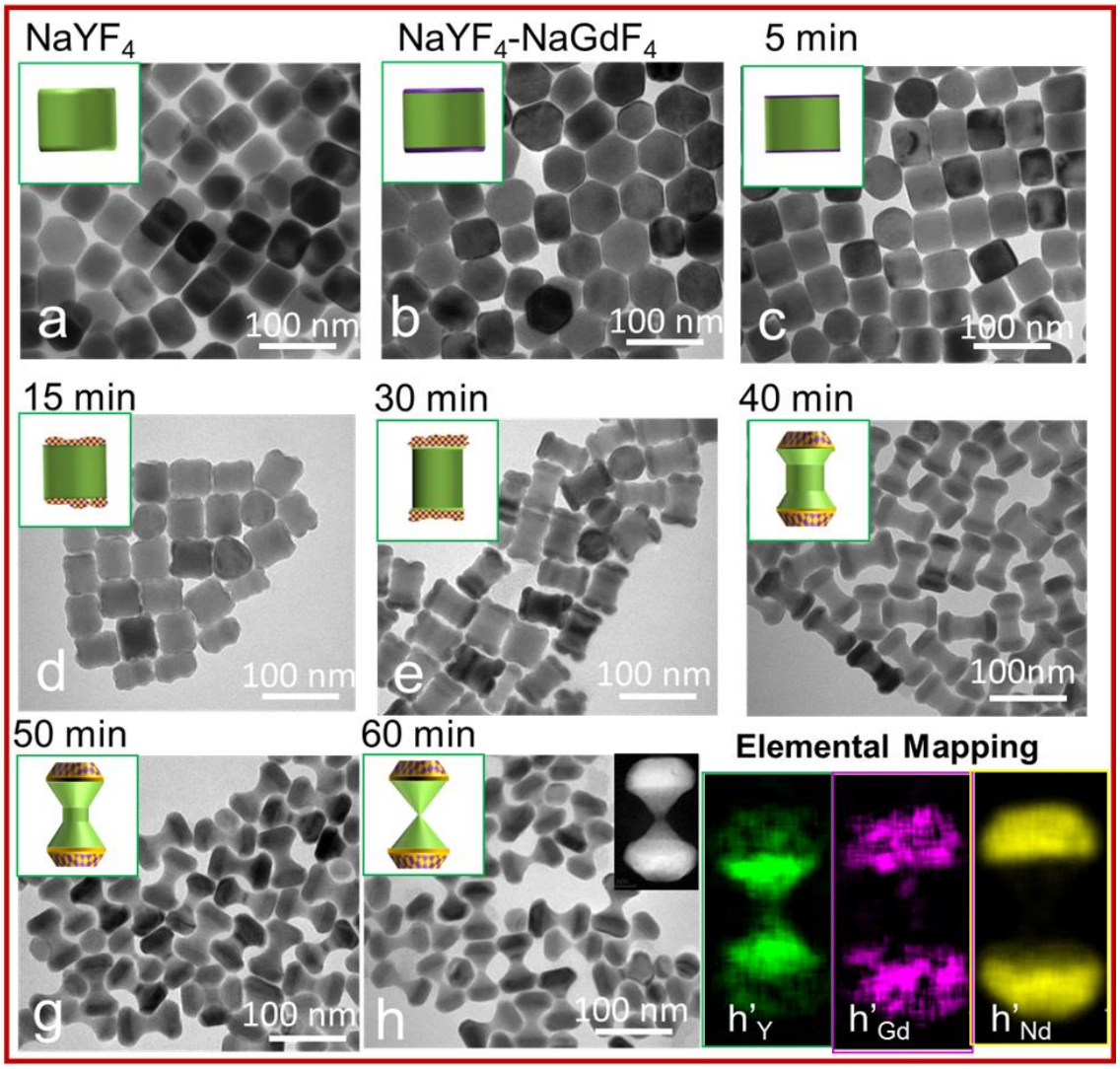

Figure 4.2.1. Real-time montitoring of the migration growth process in the formation of the $NaYF_4$-$NaGdF_4$-$NaNdF_4$ heterogeneous nanoscale hourglass particles. TEM images of $NaYF_4$ nanocrystal (a), $NaYF_4$ –$NaGdF_4$ core-shell nanocrystals (b), the migration growth after 5 minutes (c), 15 minutes (d), 30 minutes (e), 40 minutes (f), 50 minutes (g), 60 minutes (h) and the elemental mapping of Y(h'_Y), Gd (h'_{Gd}) and Nd (h'_{Nd}) elements.

The elemental mapping images in Figure 4.2.1 (h) further reveals the distributions of the three ions Y^{3+}, Gd^{3+} and Nd^{3+} within one single nanocrystal, with the majority of the Y^{3+} ions in the middle, the Gd^{3+} ions as a bridge, and the minority of the Y^{3+} and Gd^{3+} ions migrating to the end section with the Nd^{3+} ions found only on the end of each nanocrystal.

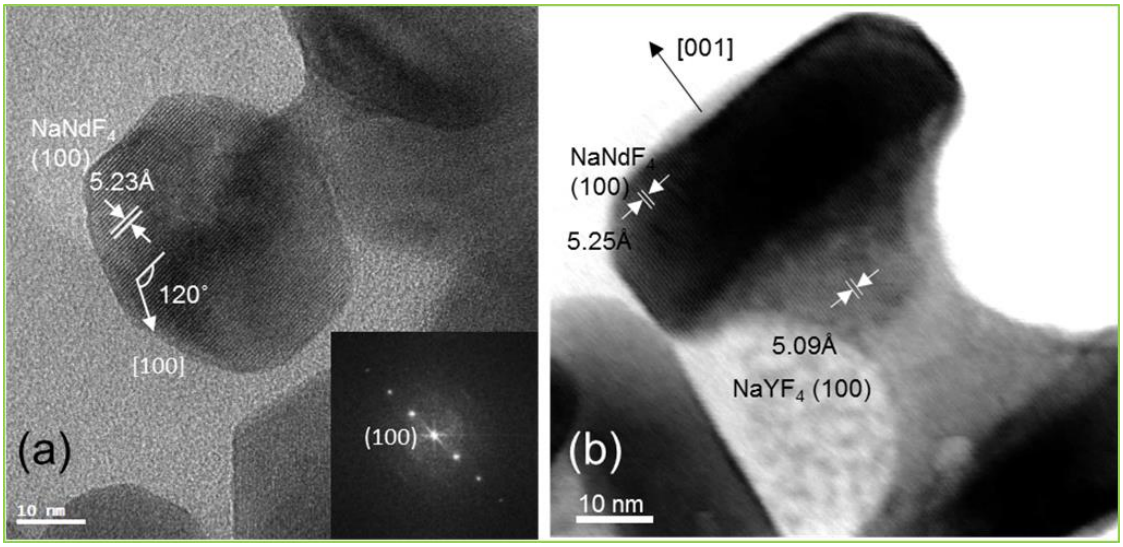

Figure 4.2.2 High-resolution TEM images of nanoscale hourglass: (a) the top view and (b) the side view of the nano-hourglass.

Figure 4.2.2 (a) shows the appeared crystal lattice, which was confirmed as a $NaNdF_4$ (100) plane by the analysis which matched the lattice distance. From the side view, the lattice of (100) planes were also presented. The small difference of lattice distance at different areas was also measured, the lattice distance in the dark area was 5.25 Å that is close to the standard value for the $NaNdF_4$ (100) plane distance, while the lattice distance in the grey area was 5.09 Å which is close to the standard value of the $NaYF_4$ (100) plane distance. This resault is consistent with the STEM data showed in the Figure 4.2.1.

Brief conclusion:

Oleate ions (OA^-) acting as surfactant ligands firmly bond to the rare earth ions on the side surfaces (100) facet planes; in the absence of an F^- source ion and at a high temperature (310 ^oC), the nanocrystal side surfaces become unstable and there is an observed accelerated site-selective erosion phenomenon. With the release of the F^- ions, the migration growth occurs when $NaYF_4$/$NaGdF_4$ nanocrystals as cores are fabricated in the condition for their longitudinal growth with $NaNdF_4$, but without a F^- ion source.

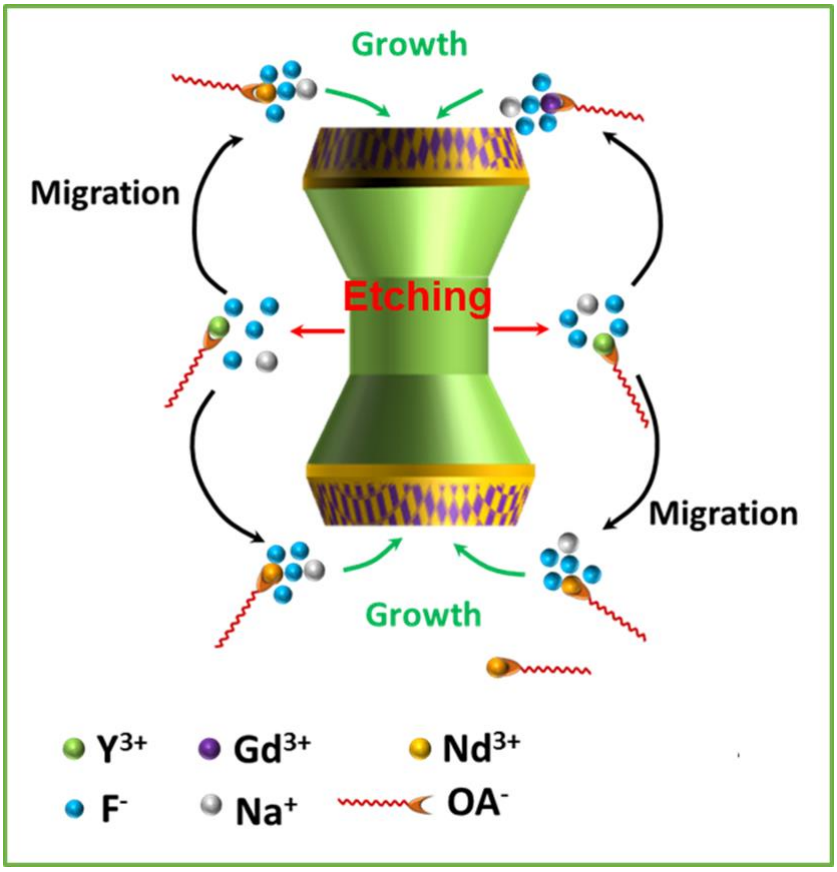

Figure 4.2.3. Detailed schematic processes of the simultaneous erosion of the $NaYF_4$-$NaGdF_4$, epitaxial growth of $NaNdF_4$ in the longitudinal direction and the migration growth of F^-, Y^{3+} and Gd^{3+} ions. The etching of $NaGdF_4$-$NaYF_4$ nanocrystals is initially triggered by the OA^- ions strongly bonding to the side surfaces at a high reaction temperature (310 ^oC). As a result, F^-, Na^+ and Y^{3+} ions are released into the solution.

4.3 Design and fabrication of "pupa-like" heterogeneous $NaYF_4/NaGdF_4/NaNdF_4$ nanocrystals: a further verification experiment to reveal that oleate ions (OA^-) on side surfaces cause dissolution

The observed dissolution (etching) phenomenon could possibly be caused by the relative crystal stability difference between $NaYF_4$ and $NaGdF_4$. To provide further insight into its formation, we designed the following experiment which selectively protected the side surface of $NaYF_4$ nanocrystal using a more stable $NaGdF_4$ nanocrystal shell. We provide experimental evidence that the surfactant oleate ions (OA^-) firmly bonds to the side-surface rare earth ions as the main factor which causes the loss of $NaYF_4$ and $NaGdF_4$ from the side surface of the particles.

The experimental approach to the design of the particles is described:

1. We first employed the approach of the transversal growth of $NaGdF_4$ nanocrystal shells onto the side surface of $NaYF_4$ nanocrystal cores. This provided a relatively stable side surface protected by the $NaGdF_4$ nanocrystal leaving the top and bottom surfaces of $NaYF_4$ exposed;
2. We then continue to longitudinally grow the $NaNdF_4$ nanocrystals, but without the F^- ion source; in such a condition, the direct epitaxial shell growth of $NaNdF_4$ was stopped because of the lack of an F^- ion source;
3. With OA^- ligands strongly anchored to the surface Gd^{3+} ions on each side surface (100) facet and under the high reaction temperature condition of 310 ˚C, if the etching was caused by relative less stable $NaYF_4$, the exposed top and bottom surfaces of $NaYF_4$ will be first etched; while if the etching was caused by the OA^- ligands, the $NaGdF_4$ shell on the side surface will be first etched;

Method to verify the driving force for the selective-surface etching

0.4 mmol of $NdCl_3$ in 2 mL methanol solution was magnetically mixed with OA (9.5 mmol) and ODE (25 mmol) in a 50 mL three-neck round-bottom flask. The mixture was degassed under Ar flow and heated to 150 ˚C for 30 minutes to form a clear solution, and then cooled to room temperature. 5 mL of methanol solution containing KOH (0.8 mmol) and NaOH (0.8 mmol) was added and stirred for 60 minutes. The solution was slowly heated to 110 ˚C and kept at 110 ˚C for 30 minutes to completely remove the methanol and someof the water. The reaction mix was then injected with 0.1 mmol of 50 nm x 60 nm $NaYF_4/NaGdF_4$ core/shell nano-prisms ($NaGdF_4$ growing on the lateral faces of $NaYF_4$ nanocrystal), suspended in cyclohexane solution, into the reaction solution. After holding at 110 ˚C for a

further 10 minutes to evaporate all the cyclohexane, the reaction mixture was quickly heated to 310 ˚C. 500 uL samples of the reaction solution was collected each time with a syringe at 5 minutes, 15 minutes, 30 minutes, 40 minutes, 50 minutes, and 60 minutes after the reaction started.

Results and discussion:

By a transversal growth approach, $NaGdF_4$ shell was first grown on the side surfaces of $NaYF_4$, as shown in Figure 4.3.1 (a). Figure 4.3.1 (b) to (f) recorded the evolution process of the epitaxial growth of the $NaNdF_4$ nanocrystals onto the $NaGdF_4/NaYF_4$ nano-prisms in the absence of the F^- ions and at a high temperature (310 ^oC). The a reduced diameter of $NaGdF_4/NaYF_4$ was observed by comparing Figures 3.3.1 (a) and (b) which clearly show that the dissolution (etching) only happens on the side surfaces for the first 10 minutes of the reaction. Figure 4.3.1 (c) shows simultaneous etching from the side surfaces and epitaxial growth of the $NaNdF_4$ onto the end surfaces of the $NaGdF_4/NaYF_4$ cores, resulting in a thinner and longer "pupa-like" crystal. This indicates that the etching of $NaYF_4$ was relatively faster than the more stable $NaGdF_4$ nanocrystals, but it should be noted that the etching still mostly occurs on the side surfaces of nanocrystals with the OA^- ligands acting as a surfactant. Once the $NaGdF_4$ removed (as seen in Figure 4.3.1 (d), the etching process appears more even on the side surface of $NaYF_4$ with a relatively smooth side surface created between the $NaNdF_4$ nanocrystal caps. Finally, the $NaYF_4$ crystals completely disappears after 60 minutes of reaction with only hexagonal-shape $NaNdF_4$ nanocrystals as the only yield.

Brief conclusion:

Although the side surface of $NaGdF_4$ was much more stable than the $NaYF_4$ and has a smaller mismatch than the $NaNdF_4$, etching still occurs on the side surface and the migration growth direction was still observed to occur from the side and the end surfaces. This suggests that in a highly unstable growth environment, such as a reaction at a high temperature, in absence of an F^- ion source, the strongly binding surfactant oleate ions (OA^-) remove the rare earth ions from the side surfaces of the particles which acts as the main factor driving behind the observed etching. .

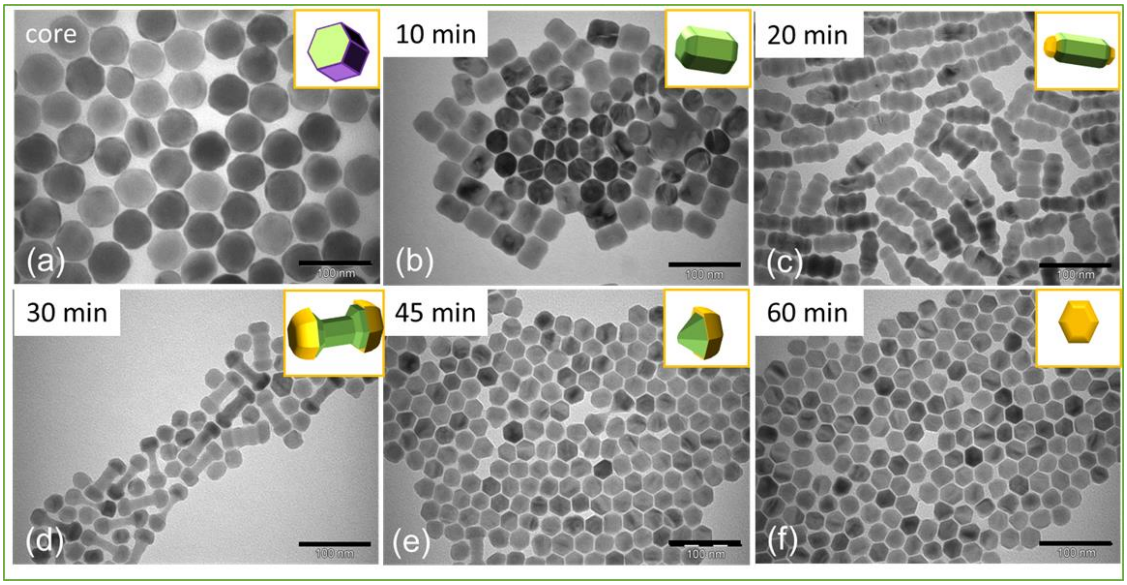

Figure 4.3.1 TEM images of $NaYF_4/NaGdF_4$ cores and their migration growth with Nd for 10 min, 20 min, 30 min, 45 min and 60 min after the start of the reaction. (Scale bars: 100 nm)

4.4 Design and fabrication of heterogeneous $NaYF_4/NaGdF_4/NaNdF_4$ nanocrystals in flower shape: the direction of migration growth is also determined by the ratio of OA^-/OAH

Our next example demonstrates the design and synthesis of $NaYF_4/NaGdF_4/NaNdF_4$ heterogeneous nanocrystals to form heterogeneous nanoscale flower-shaped particles. In this experiment, we demonstrate migration growth of the $NaNdF_4$ to the transversal structure rather than to the end surfaces. Using the principle that the direction of epitaxial shell growth can be controlled through adjustment of the ratio of OA^-/OAH, here we demonstrate that a low ratio of OA^-/OAH at relatively lower temperature can direct the migration growth instead along the transverse direction.

The design logics is described as:

1. We first transversally grow $NaGdF_4$ nanocrystal shells onto the side surface of the $NaYF_4$ nanocrystal core;
2. In absence of the F^- ion source, the direct epitaxial shell growth of $NaNdF_4$ was stopped;
3. Considering the weak erosion process due to the low ratio of OA^-/OAH, we increased the reaction temperature from 290 ˚C to 300 ˚C to promote the erosion of $NaYF_4/NaGdF_4$ nanocrystals to release F^- ions. This has the effect of trimming off part of the $NaGdF_4$ shells around the $NaYF_4$ from its side surfaces;
4. A minimum amount of F^- ions slowly released from $NaYF_4/NaGdF_4$ nanocrystals into the reaction solution will help form the $NaNdF_4$ nanocrystals transversally from $NaGdF_4$ crystalline shell on side surfaces of the hexagonal prism;
5. Finally, F^- ions and part of Y^{3+} and Gd^{3+} ions migrate from the $NaYF_4$ to the $NaNdF_4$ section on the lateral faces of heterogeneous nanocrystals, forming a flower shape nanostructure.

Method: Synthesis of $NaYF_4/NaGdF_4/NaNdF_4$ flower-shaped nanocrystals

0.1 mmol of $NdCl_3$ in 1 mL of methanol solution was magnetically mixed with OA (19 mmol) and ODE (18.7 mmol) in a 50 mL three-neck round-bottom flask. The mixture was degassed under Ar flow and heated to 150 ˚C for 30 minutes to form a clear solution, and then cooled to room temperature. 5 mL of methanol solution containing NaOH (0.6 mmol) was added and stirred for 60 minutes. The solution was slowly heated to 110 ˚C and kept at 110 ˚C for 30 minutes to completely remove the methanol and some of the water. Then, the reaction mix was injected with 0.1 mmol of 50 nm $NaYF_4/NaGdF_4$ nano-prisms prisms ($NaGdF_4$

growing on the lateral faces of $NaYF_4$ nanocrystal), suspended in a cyclohexane solution, into the reaction mix. After holding at 110 ˚C for another 10 minutes to evaporate all cyclohexane, the reaction mixture was quickly heated to 300 ˚C. 500 uL samples of the reaction solution were collected each time with a syringe after 10 minutes, 25 minutes and 45 minutes of the reaction time.

Results and Discussion:

By this transversal growth approach, $NaGdF_4$ shell was first grown on the side surfaces of $NaYF_4$, as shown in Figure 4.4.1 (a). Figure 4.4.1 (b) to (d) record the evolution process of epitaxial growth of $NaNdF_4$ nanocrystals onto $NaGdF_4/NaYF_4$ nano-prisms in absence of F^- ions and at lower ratio of OA^-/OAH. The slightly reduced diameter of $NaGdF_4/NaYF_4$ is compared in Figures 4.4.1 (a) and in (b) some parts of NaGdF4 was etched from the side surfaces after the first 10 minutes of reaction. Figure 4.4.1 (c) show the simultaneous etching of the side surfaces and the epitaxial growth of $NaNdF_4$ onto the $NaGdF_4$ area forming "island-shaped" anchors on the side surfaces of $NaGdF_4/NaYF_4$ cores. Figure 4.4.1 (d) shows that more $NaNdF_4$ was growth around the anchors which form a heterogeneous flower-shape nanocrystal.

Because there was few OA^- ligands on the side surface, OA^- mediated etching process for $NaGdF_4/NaYF_4$ nanocrystals dissolution of the side surfaces becomes very slow at this relatively lower reaction temperature. Despite high concentration of OAH on the end surfaces, no etching phenomenon was observed at the top and bottom end surface of $NaGdF_4/NaYF_4$ of the nano-prisms. This indirectly provides further evidence for the mechanism of OA^- mediated etching process from side surfaces.

Programmable longitudinal growth of heterogeneous nanocrystals was much easier and faster than programmable transversal growth in yielding mono-disperse morphology. More fine-tuning experiments, such as using lower temperature and much longer reaction time, were still required for the identification of the optimum reaction conditions for the fabrication of truly mono-disperse flower-shaped heterogeneous nanocrystals.

Brief conclusion:

The migration growth in transversal direction was made possible through the use of a low ratio of OA^-/OAH and a low reaction temperature, though the etching process was much less efficient at the side surfaces of nanocrystal due to fewer OA^- ligands bounding to rare earth ions to these side surfaces.

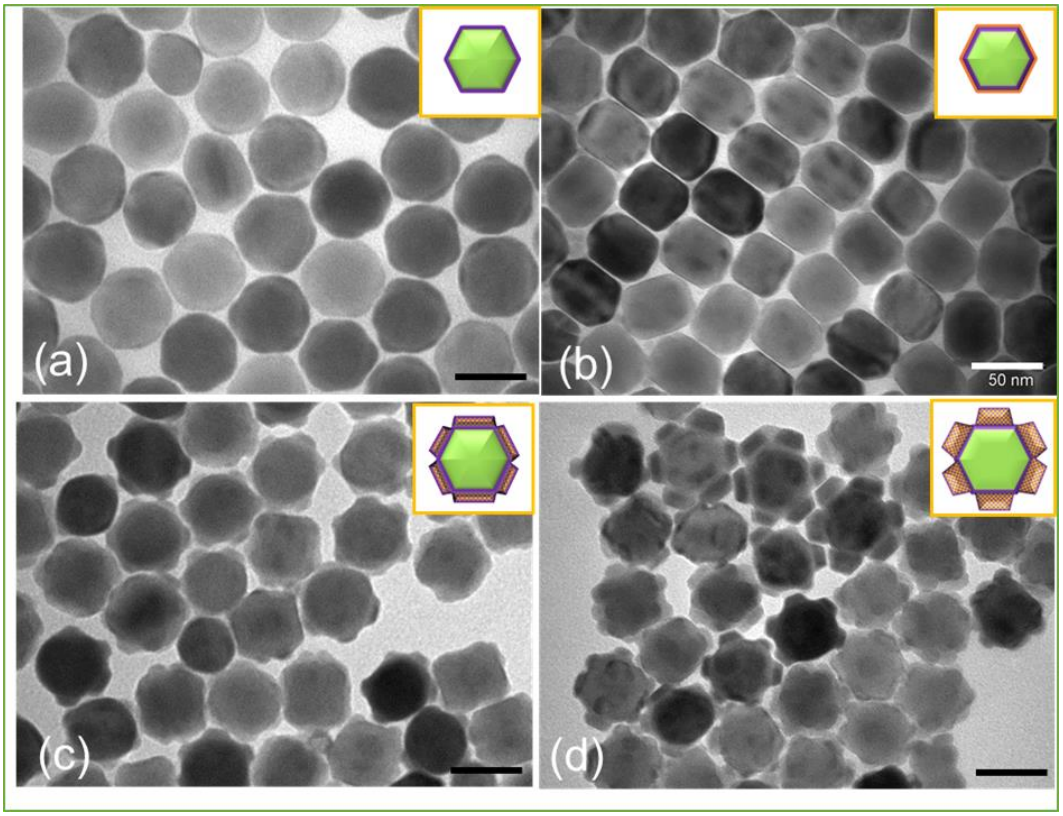

Figure 4.4.1. TEM images of $NaYF_4/NaGdF_4$ nanocrystals as cores, and migration growth with the Nd^{3+} element at 300˚C after 10 minutes, 25 minutes and 45 minutes of reaction time. (Scale bars: 50 nm)

4.5 Design and fabrication of heterogeneous $NaYF_4/NaGdF_4/NaNdF_4$ nanocrystals in dumbbell shapes: fine tuning experiments for more choice of morphology engineering

Our next two experiments were designed to demonstrate that our protocols for programmable growth of heterogeneous nanocrystals can be further refined to meet more specific needs.

The design logic of the reaction method is described as:

1. For example, during the process of forming the $NaYF_4/NaGdF_4/NaNdF_4$ heterogeneous nanoscale hourglasse particles, reduction of the amount of Nd^{3+} ion source can slow down the migration growth process which consists of dissolving $NaYF_4$ and reforming $NaNdF_4$ nanocrystals;
2. In the longitudinal growth environment (high ratio of OA^-/OAH; high temperature 310 ^oC), with a slowly released F^- ion source and a small amount of Nd^{3+} ion source, the longitudinal growth along *c* axis direction of the $NaYF_4/NaGdF_4$ nanorods will be quite limited in the formation of stable sharper tips;
3. While instead of relying on the released F^- ion source supplied by dissolved $NaYF_4$, supply of F^- the ion source in the reaction will increase the diameter of dumbbell ends, and will form round polished tips.

Method for synthesis of $NaYF_4$-$NaGdF_4$-$NaNdF_4$ nanocrystals in sharp-end dumbbell shape

0.1 mmol of $NdCl_3$ in 1 mL of methanol solution was magnetically mixed with OA (9.5 mmol) and ODE (25 mmol) in a 50 mL three-neck round-bottom flask. The mixture was degassed under Ar flow and heated to 160 ˚C for 30 minutes to form a clear solution, and then cooled to room temperature. 5 mL of the methanol solution containing KOH (0.2 mmol) and NaOH (0.2 mmol) was added and stirred for 60 minutes. Note: in this reaction **no NH_4F** was added to the solution. The solution was slowly heated to 110 ˚C and kept at 110 ˚C for 30 min to remove the methanol and the water completely. It was then injected with 0.1 mmol of $NaYF_4/NaGdF_4$ nanorod particle in suspended in cyclohexane solvent into the reaction solution. After holding at at 110 ˚C for a further 10 minutes to evaporate all cyclohexane, the reaction mixture was quickly heated to 310 ˚C and held at this temperature for a further 30 minutes.

Method for synthesis of $NaYF_4$-$NaGdF_4$-$NaNdF_4$ nanocrystals in round-end dumbbell shape

0.1 mmol of $NdCl_3$ in 1 mL of methanol solution was magnetically mixed with OA (9.5 mmol) and ODE (25 mmol) in a 50 mL three-neck round-bottom flask. The mixture was

degassed under Ar flow and heated to 160 ˚C for 30 min to form a clear solution, and then cooled to room temperature. 5 mL of methanol solution containing **NH_4F (0.3 mmol)** KOH (0.2 mmol) and NaOH (0.2 mmol) was added and the mixture was stirred for 60 min. The solution was slowly heated to 110 ˚C and kept at 110 ˚C for 30 minutes to remove the methanol and the water completely. Then, it was injected with 0.1 mmol of $NaYF_4$-$NaGdF_4$ nanorods suspended in cyclohexane into the reaction solution. After being held at 110 ˚C for further 10 minutes to evaporate all cyclohexane, the reaction mixture was quickly heated to 310 ˚C and held for 30 minutes at room temperature.

Results and Discussion:

The longitudinal growth direction was determined by adding a higher ratio of oleate (OA^-) to oleic acid (OA) ligands at a higher reaction temperature (310 ^oC), which selectively passivates the nanorods side surface (100) planes. A lower concentration of Nd^{3+} ion source will slow down the epitaxial growth on the ends and lead to a reduction in the diameter of the $NdYF_4$ nanocrystals. Moreover the absence of a F^- ion source will make the tips sharper while the presence of additional a F^- ion source leads to the formation of rounded-polished tips.

A decrease of a F^- and Nd^{3+} ion source in the reaction mix accelerates the etching of the $NaYF_4$. Since the $NaNdF_4$ is relatively more stable than $NaYF_4$, a released F^- ion source will form $NaNdF_4$ nanocrystals with $NaYF_4$ located in the rod middle area continuously becoming dissolved. This migration growth process of dissolving $NaYF_4$ and re-growing $NaNdF_4$ gradually diminishes as the Nd^{3+} ion source is consumed, which leads to the formation of sharp tips.

Figures 4.5.1 (c) and 4.6.1 (c) show highly uniform heterogeneous nanocrystals. The STEM image (Figure 4.5.1 d) illustrates two separate partitions of tips and core particles. The elemental mapping images show the distributions of the Y^{3+}, Gd^{3+} and Nd^{3+} ions The combined elemental mapping image shows three well aligned components, consistent with the formation mechanism already described.

Brief conclusion:

The oleate ions (OA^-) mediated longitudinal growth, transversal growth, etching process and migration growth in consideration of crystal lattice mismatching rates and crystal stability have jointly formed a toolbox for highly controlled nanoscale materials engineering to fabricate rare-earth doped heterogeneous nanocrystals. The switches between these growth mechanisms are externally controllable by fine-tuning the reaction temperature, concentration and ratio of surfactant ligands, and elemental concentrations and balance in the reaction environment.

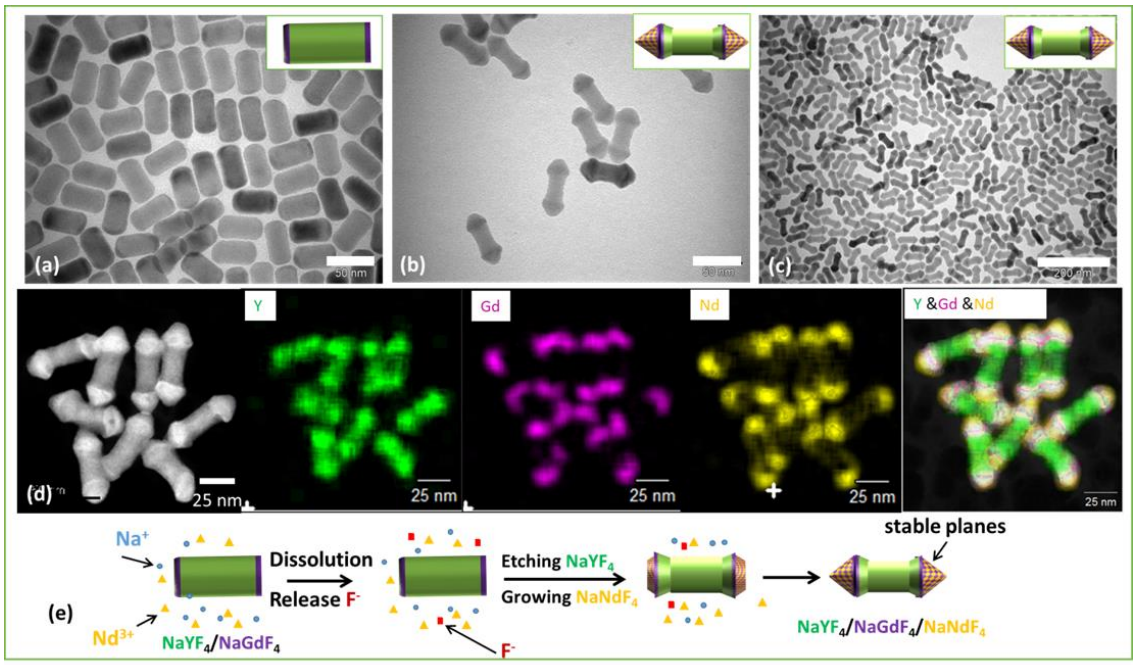

Figure 4.5.1. TEM images, elemental composition characterization and schematic illustration of the $NaYF_4$–$NaGdF_4$-$NaNdF_4$ dumbbell-shape nanocrystals with sharp tips via migration growth of $NaNdF_4$ (a) the cores of $NaYF_4$–$NaGdF_4$ nanocrystals with a thin layer of $NaGdF_4$ at the ends of $NaYF_4$ nanorods; (b) the high magnification image and (c) the overview image of the $NaYF_4$–$NaGdF_4$-$NaNdF_4$ dumbbell shape nanocrystals with sharp tips; (d) HAADF-STEM image and elemental mapping images of $NaYF_4$–$NaGdF_4$-$NaNdF_4$ nanocrystals.(e) the schematic illustration of the formation process of the $NaYF_4$-$NaGdF_4$-$NaNdF_4$ dumbbell nanocrystals with sharp tips (Scale bar: 50 nm for a and b; 200 nm for c and 25 nm for d)

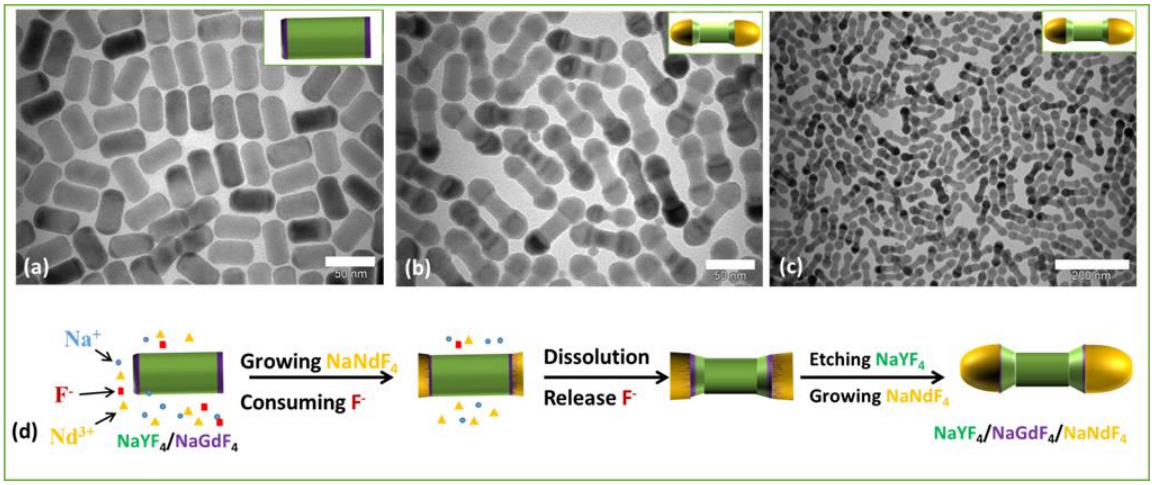

Figure 4.5.2. TEM images and schematic illustration of the $NaYF_4$–$NaGdF_4$-$NaNdF_4$ dumbbell nanocrystals with round polished tips. (a) $NaYF_4$–$NaGdF_4$ nanocrystals with a thin layer of $NaGdF_4$ at the ends of $NaYF_4$ nanorods; (b) high magnification image and (c) overview image of $NaYF_4$–$NaGdF_4$-$NaNdF_4$ nanocrystals. (d) Schematic illustration of the

formation process of the $NaYF_4$-$NaGdF_4$-$NaNdF_4$ nanocrystals with round ends. (Scale bar: 50 nm for a and b; 200 nm for c)

4.6 Design and fabrication of heterogeneous $NaYF_4$/$NaLuF_4$/$NaGdF_4$ nanocrystals: a showcase synthesis for multifunctional single heterogeneous nanocrystal

Using the combinational approaches of longitudinal growth and transversal growth as well as taking the consideration of crystallographic mismatch rates, we demonstrate here a series of examples to illustrate our rational design and programmable epitaxial growth techniques for the bottom-up fabrication of 3-dimensional heterogeneous nanostructures.

The hexagonal-phase $NaYF_4$ nanocrystal is acknowledged elsewhere as the most efficient photon upconversion host [14]. Recent pioneer works has revealed that the incorporation of other functions in these nanocrystals can enrich their hybrid applications, for example, by providing X-ray computed tomography imaging through the use of $NaLuF_4$ as a host or Magnetic Resonance Imaging using $NaGdF_4$ as a host. Our first example here is to show the design and synthesis of $NaYF_4$/$NaLuF_4$/$NaGdF_4$ heterogeneous nanocrystals with two $NaGdF_4$ rings on a $NaLuF_4$ @ $NaYF_4$ nanorod.

The design logics is described as:

1. We first employed the approach of longitudinal growth to grow $NaYF_4$ nanoparticles to $NaYF_4$ nanorods;
2. We then employed the protocol for transversally coating the side surfaces of $NaYF_4$ nanorods with a thin layer of $NaLuF_4$. This thin layer of $NaLuF_4$ functions as a mask;
3. The surface of $NaLuF_4$ @ $NaYF_4$ nanorods at the top edge areas are less stable and are easier to dissolved after the transversal epitaxial shell growth, which leaves the $NaLuF_4$ mask at the end edges also becoming removed so that $NaYF_4$ was exposed;
4. According to Table 4.2, the mismatch rate between $NaGdF_4$ and $NaLuF_4$ was about 4.3% while the mismatch rate between $NaGdF_4$ and $NaYF_4$ was about 2%, which suggests that the $NaGdF_4$ will prefer to grow on $NaYF_4$ rather than on $NaLuF_4$;
5. To facilitate the etching process, in our modified protocol towards transversal growth of $NaLuF_4$ onto the side surfaces of $NaYF_4$ nanorods, absence of F source causes a faster erosion occur at the top edge area;
6. Finally, by injecting the α-$NaGdF_4$ nanocrystals with F element source by slowing dissolving it into the solution, β-$NaGdF_4$ nanocrystal shells start to grow onto the exposed $NaYF_4$ areas, forming double rings of $NaGdF_4$ shells transversally grown around the top and bottom edges of $NaLuF_4$ @ $NaYF_4$ nanorods.

Method for synthesis of pure α-$NaGdF_4$ nanocrystals

2 mL of the methanol solution of $GdCl_3$ (1.0 mmol) was magnetically mixed with OA (19 mmol) and ODE (47 mmol) in a 100 mL three-neck round-bottom flask. The mixture was degassed under Ar flow and heated to 150 ^oC for 30 minutes to form a clear solution, and then cooled to room temperature. 10 mL of the methanol solution containing NH_4F (4 mmol) and NaOH (2.5 mmol) was added and stirred for 60 min. Then, the solution was slowly heated to 110 ^oC and kept at 110 ^oC for 30 minutes to remove the methanol and water completely. After that, the reaction mixture was quickly heated to 240 ^oC and aged for 45 minutes.

Method for synthesis of $NaLuF_4/NaYF_4$ nanorods

0.1 mmol of $LuCl_3$ in 1 ml method solution was magnetically mixed with OA (9.50 mmol) and ODE (25 mmol) in a 50 mL three-neck round-bottom flask. The mixture was degassed under Ar flow and heated to 150 ˚C for 30 min to form a clear solution, and then cooled to room temperature. 2 mL of methanol solution containing NaOH (0.15 mmol) was added and stirred for 60 min. The solution was slowly heated to 110 ˚C and kept at 110 ˚C for 30 minutes to completely remove the methanol and some of the water. It was then injected with 0.4 mmol of $NaYF_4$ seed particles in a cyclohexane solution. After holding the reaction mix at 110 ˚C for a further 10 minutes to evaporate cyclohexane, the reaction mixture was quickly heated to 290 ˚C and held at that temperature for a further 1 hour.

Method for synthesis of $NaGdF_4$ double-ring structure onto the $NaLuF_4$@$NaYF_4$ nanorods

0.1 mmol of $GdCl_3$ in 1 ml methanol solution was magnetically mixed with OA (19.0 mmol) and ODE (18.7 mmol) in a 50 mL three-neck round-bottom flask. The mixture was degassed under Ar flow and heated to 150 ˚C for 30 minutes to form a clear solution, and then cooled to room temperature. 2 mL of the methanol solution containing NaOH (at 0.15 mmol) was added and stirred for 60 minutes. The solution was slowly heated to 110 ˚C and kept at 110 ˚C for 30 minutes to completely remove the methanol and some of the water. It was then, injected with 0.1 mmol of the *$NaLuF_4/NaYF_4$* seed particles, in a cycloexane solution, into the reaction solution. After having been held the reaction mix at 110 ˚C for another 10 minutes to evaporate cyclohexane, the reaction mixture was quickly heated to 300 ˚C. It was then, injected with 0.02 mmol of α-$NaGdF_4$ nanocrystals (see Figure 4.6.3) into the reaction system. This was done every 10 minutes for 5 times at 300 C. The reaction mix was held at this temperature for another 10 minutes after the last injection.

Results and Discussion:

The elemental mapping images in Figure 4.6.1(c) further confirms that the three elements of Y^{3+} , Lu^{3+} and Gd^{3+} are separated in three partitions within one single nanocrystal, with Y^{3+} only in the inner core of the rod, Lu^{3+} only in the outer shell of the rod, and Gd^{3+}

only in the two rings. The high resolution TEM images shown in Figure 4.6.1, provides further evidence of the direct growth of crystalline structures. The two rings can be seen to grown around the [001] crystallographic direction and the select area electron diffraction pattern has a close match to theβ-$NaYF_4$, β-$NaLuF_4$ and β-$NaGdF_4$.

After a thin layer of $NaLuF_4$ shell is transversally formed onto the $NaYF_4$ core nanorods at 290˚C, the F element source was removed so that $NaLuF_4$ layer can start to dissolve slowly, particularly at the sharp end areas of nanorods where the $NaYF_4$ is firstly exposed. With the drop-wise addition of α-$NaGdF_4$ (as the F source) into the reaction system, $NaGdF_4$ prefer to grow onto the (100) (010) facets of the exposed $NaYF_4$ cores with $NaLuF_4$ shell acting as a mask because of the inherent difference in crystalline mismatch rate between $NaGdF_4$ vs. $NaYF_4$ and $NaGdF_4$ vs. $NaLuF_4$.

Brief conclusion:

We report for the first time a bottom-up programmable controlled fabrication of 3-D shaped heterogeneous nanocrystals using the combinational approaches of an oleate ion (OA^-) assisted longitudinal growth, transversal growth and selective etching which includes controlling for and using the crystallographic mismatch rates.

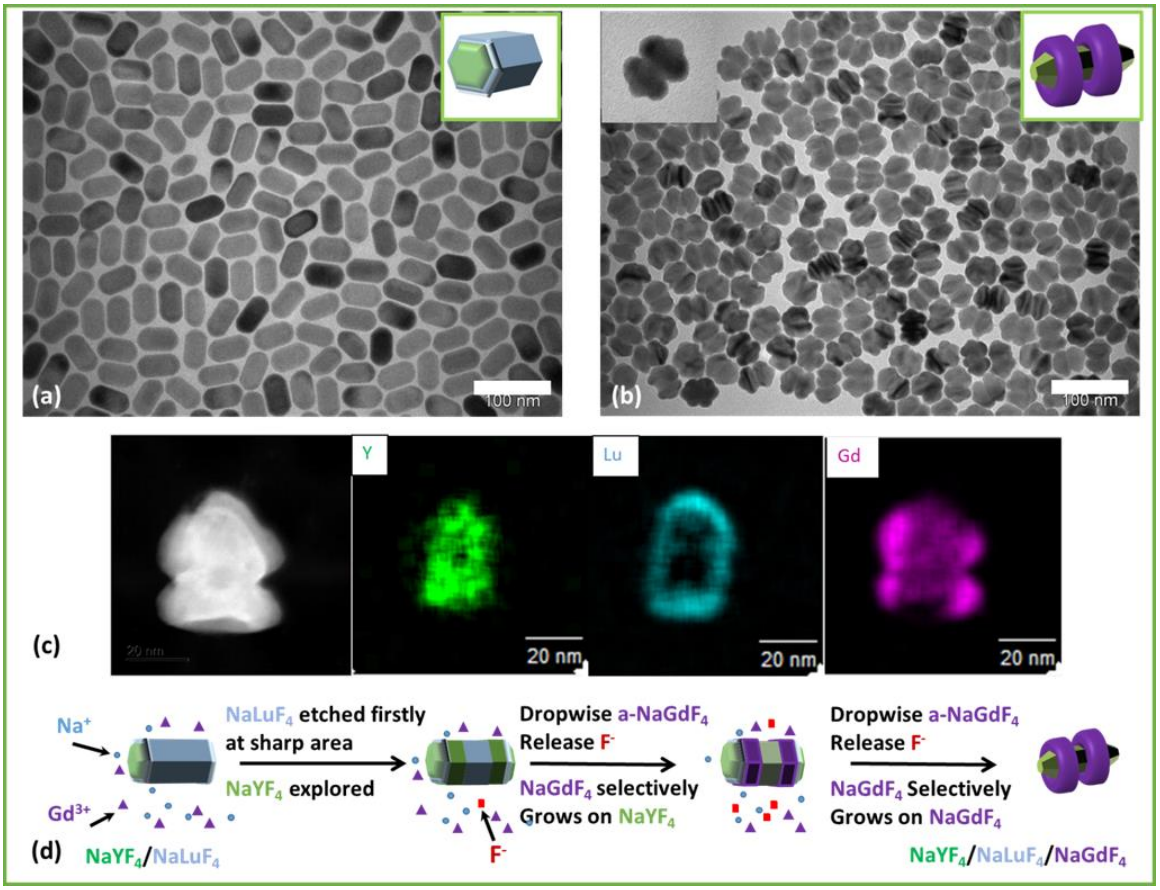

Figure 4.6.1. TEM and elemental composition characterization of the $NaYF_4$-$NaLuF_4$-$NaGdF_4$ heterogeneous nanocrystals which form a unique shape of two $NaGdF_4$ rings onto a $NaLuF_4$/$NaYF_4$ nanorod. (a) $NaLuF_4$ nanocrystal shells transversally coated onto $NaYF_4$ core nanocrystals; (b) an overview image of the $NaYF_4$-$NaLuF_4$-$NaGdF_4$ nanocrystals and a single $NaYF_4$-$NaLuF_4$-$NaGdF_4$ nanocrystal (top-left inset); (c) HAADF-STEM image of a single $NaYF_4$–$NaLuF_4$-$NaGdF_4$ nanocrystal and its elemental mapping images. The elemental mapping images confirm the distribution of the Y^{3+} ions in the middle of the rod and the Lu^{3+} ions as a thin layer coating surrounding the nanorod. The Gd^{3+} ions is present as a double ring surrounding the $NaYF_4$-$NaLuF_4$ nanorods in the transversal direction. (d) A schematic illustration of the formation process "selective mask – etching – epitaxial growth" of the $NaYF_4$-$NaLuF_4$-$NaGdF_4$ heterogeneous nanocrystals is provided.

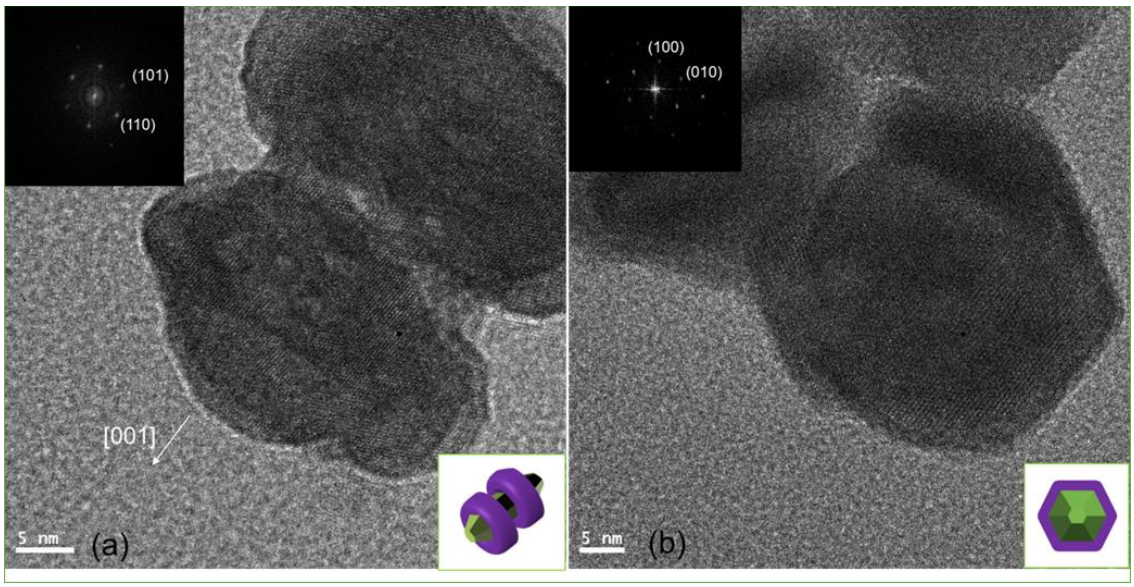

Figure 4.6.2. (a) A side view high-resolution TEM image and its corresponding selected area electron diffraction pattern (insert) and (b) a top view high-resolution TEM image of a single nanocrystal and its corresponding selected-area electron diffraction pattern (inset)

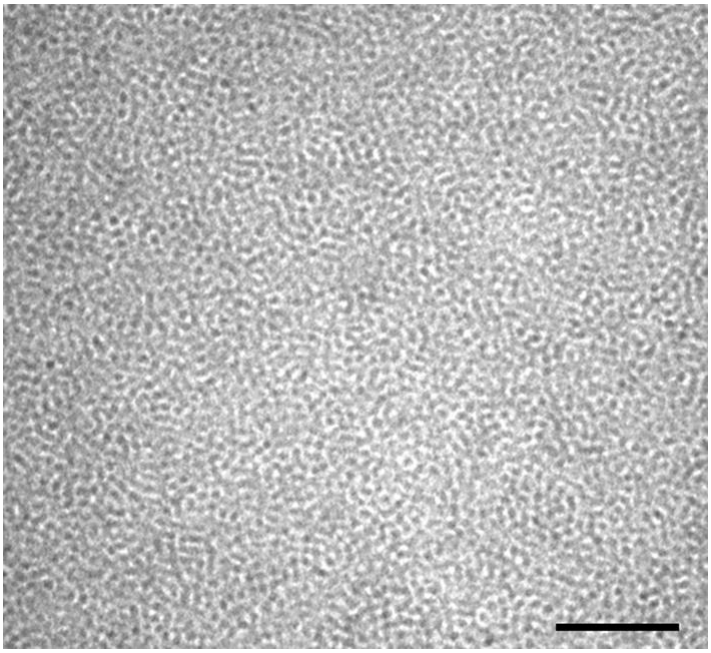

Figure 4.6.3 TEM image of α-$NaGdF_4$ nanocrystals used in this experiment. (Scale bar is 50 nm)

4.7 Summary

In this chapter, we systemically studied migration shell growth process and applied this method to synthesize a series of $NaYF_4$/$NaGdF_4$/$NaNdF_4$ heterogeneous nanocrystals. In the migration shell growth process, the etching effect of $NaYF_4$ is promoted due to the low value of the F anion concentration in the reaction solution. The migration shell growth direction cannot be tuned by the specific mismatch between core and shell, but it can be controlled by adjusting the ratio of OA^-/OAH. Under a high ratio of OA^-/OAH, the growth direction is longitudinal, in which the new formed shell will grow on the (001) plane of $NaLnF_4$. Under a low ration of OA^-/OAH, the growth direction is transversal, in which the new formed shell will grow along the lateral surface of $NaLnF_4$ nanocrystals.

Through combining the longitudinal shell growth, transversal shell growth and migration shell growth, we can design and fabricate many different structured heterogeneous nanocrystals.

References:

[1] H. Dong, L.D. Sun, Y.F. Wang, J. Ke, R. Si, J.W. Xiao, G.M. Lyu, S. Shi, C.H. Yan, J Am Chem Soc, 137 (2015) 6569-6576.
[2] X.Q. Ge, L.N. Sun, L.Y. Shi, R.Y. Wei, Biomed Spectrosc Ima, 4 (2015) 391-412.
[3] F.Y. Li, W. Feng, J. Zhou, Y. Sun, Chemistry of Molecular Imaging, (2015) 299-319.
[4] B. Liu, Y.Y. Chen, C.X. Li, F. He, Z.Y. Hou, S.S. Huang, H.M. Zhu, X.Y. Chen, J. Lin, Adv Funct Mater, 25 (2015) 4717-4729.
[5] L.D. Sun, H. Dong, P.Z. Zhang, C.H. Yan, Annu Rev Phys Chem, 66 (2015) 619-642.
[6] D.M. Yang, P.A. Ma, Z.Y. Hou, Z.Y. Cheng, C.X. Li, J. Lin, Chem Soc Rev, 44 (2015) 1416-1448.

[7] S. Ye, G.Y. Chen, W. Shao, J.L. Qu, P.N. Prasad, Nanoscale, 7 (2015) 3976-3984.
[8] Z.G. Yi, X.L. Li, Z.L. Xue, X. Liang, W. Lu, H. Peng, H.R. Liu, S.J. Zeng, J.H. Hao, Adv Funct Mater, 25 (2015) 7119-7129.
[9] X.M. Zou, Y. Liu, X.J. Zhu, M. Chen, L.M. Yao, W. Feng, F.Y. Li, Nanoscale, 7 (2015) 4105-4113.
[10] W. Feng, C.M. Han, F.Y. Li, Adv Mater, 25 (2013) 5287-5303.
[11] Q. Liu, M. Chen, Y. Sun, G.Y. Chen, T.S. Yang, Y. Gao, X.Z. Zhang, F.Y. Li, Biomaterials, 32 (2011) 8243-8253.
[12] L.D. Sun, Y.F. Wang, C.H. Yan, Accounts Chem Res, 47 (2014) 1001-1009.
[13] S.L. Zhong, B.M. Li, Y.H. Ji, C.H. Zeng, J Inorg Organomet P, 26 (2016) 527-535.
[14] S.J. Clark, M.D. Segall, C.J. Pickard, P.J. Hasnip, M.J. Probert, K. Refson, M.C. Payne, Z Kristallogr, 220 (2005) 567-570.

4.8 Contribution to Paper 2

The Chapter 3 and Chapter 4 are the results summarized from more than six hundreds of experimental synthesis and characterizations I conducted during my PhD program, as the supplementary information details to underpin a published work in the journal of *Nature Communications*.

	D.L	X.X	D.Y	Q.X	Y.Z	C.M	S.W	W.R	E.G	J.M	S.D	X.L	D.J
Experiment Design	•												•
Sample Preparation	•				•								
Data Collection	•	•	•					•			•		
Analysis	•	•	•	•									
Manuscript	•	•		•	•	•	•	•	•	•		•	•

4.9 Paper 2

Liu, Deming, Xiaoxue Xu, Yi Du, Xian Qin, Yuhai Zhang, Chenshuo Ma, Shihui Wen, Wei Ren1,5, Ewa M. Goldys, James A Piper, Shixue Dou, Xiaogang Liu, Dayong Jin, Three-dimensional controlled growth of monodisperse sub-50 nm heterogeneous nanocrystals, ***Nature Communications***.7 (2016) DOI: 10.1038/ncomms10254

nature COMMUNICATIONS

ARTICLE

Received 17 Jul 2015 | Accepted 20 Nov 2015 | Published 8 Jan 2016

DOI: 10.1038/ncomms10254 OPEN

Three-dimensional controlled growth of monodisperse sub-50 nm heterogeneous nanocrystals

Deming Liu[1], Xiaoxue Xu[1,2], Yi Du[3], Xian Qin[4], Yuhai Zhang[5], Chenshuo Ma[1], Shihui Wen[1,2], Wei Ren[1,2], Ewa M. Goldys[1], James A. Piper[1], Shixue Dou[3], Xiaogang Liu[4,5] & Dayong Jin[1,2]

The ultimate frontier in nanomaterials engineering is to realize their composition control with atomic scale precision to enable fabrication of nanoparticles with desirable size, shape and surface properties. Such control becomes even more useful when growing hybrid nanocrystals designed to integrate multiple functionalities. Here we report achieving such degree of control in a family of rare-earth-doped nanomaterials. We experimentally verify the co-existence and different roles of oleate anions (OA^-) and molecules (OAH) in the crystal formation. We identify that the control over the ratio of OA^- to OAH can be used to directionally inhibit, promote or etch the crystallographic facets of the nanoparticles. This control enables selective grafting of shells with complex morphologies grown over nanocrystal cores, thus allowing the fabrication of a diverse library of monodisperse sub-50 nm nanoparticles. With such programmable additive and subtractive engineering a variety of three-dimensional shapes can be implemented using a bottom-up scalable approach.

[1] Laboratory of Advanced Cytometry, ARC Centre of Excellence for Nanoscale BioPhotonics, Department of Physics and Astronomy, Macquarie University, Sydney, New South Wales 2109, Australia. [2] Faculty of Science, Institute for Biomedical Materials and Devices, University of Technology Sydney, New South Wales 2007, Australia. [3] Institute for Superconducting and Electronic Materials, Innovation Campus, University of Wollongong, New South Wales 2522, Australia. [4] Institute of Materials Research and Engineering, 3 Research Link, Singapore 117602, Singapore. [5] Department of Chemistry, National University of Singapore, 3 Science Drive 3, Singapore 117543, Singapore. Correspondence and requests for materials should be addressed to X.L. (email: chmlx@nus.edu.sg) or to D.J. (email: dayong.jin@uts.edu.au).

Nanocrystal engineering, design and fabrication of nanocrystals with desirable size, shape[1–6], surface properties[7] and composition[8,9] is attracting growing interest due to its essential role in fundamental research and commercial relevance. Rare-earth-doped upconversion nanocrystals have recently emerged as the new generation of functional nanomaterials, because they exhibit exceptional optical, magnetic and chemical properties underpinning their diverse applications. In particular, alkaline rare-earth fluoride ($AREF_4$) nanocrystals[10–12], including hexagonal-phase β-$NaYF_4$, β-$NaGdF_4$, β-$NaNdF_4$ or β-$NaLuF_4$ are used in full-colour displays[12,13], photovoltaics[14], security inks[15], forensic science[16], autofluorescence-free biomolecular sensing[17–19], multimodal *in vivo* bio-imaging (fluorescence, magnetic resonance imaging, X-ray, SPECT and so on.)[20] and theranostics[17,21–23]. A trial-and-error approach is frequently used to produce nanoparticles with spherical, rod-like or other shapes[24–26] by varying dopant concentrations and/or constituent materials[27], reaction time and temperature[28–31]. This random sampling of vast, multidimensional parameter space, needs to be done rationally, with proper understanding of the underpinning growth mechanisms.

Here we find that oleate anions (OA^-), the dissociated form of oleic acid molecules (OAH), have variable, dynamic roles in mediating the growth of $AREF_4$ nanocrystals. This allows us to introduce a molecular approach to tailoring the shape and composition of $AREF_4$ nanocrystals. This new method is based on a selective epitaxial core–shell growth process in the presence of oleic acid, commonly used as a surfactant during the synthesis of β-$AREF_4$ nanocrystals[32]. Drawing inspiration from the recently discovered co-existence of oleic acid molecules (OAH) and their dissociated form, oleic acid ions (OA^-) in the binary systems of PbS[33] and PbSe nanocrystals[34], we hypothesize that the change in the ratio of OA^- to OAH could influence the interaction of these ligands with the particle surface and hence the resulting morphology. Our computational modelling (Fig. 1, Supplementary Figs 1–6, Supplementary Notes 1 and 2 and Supplementary Table 1) and experimental results (Figs 2–4, Supplementary Figs 7–35, Supplementary Tables 2 and 3 and Supplementary Notes 3–18) demonstrate that the preferential affinity of OAH and OA^- to different crystalline facets dictates the formation of nanocrystals of different shape. Importantly, we demonstrate that the precise control over the shell thickness and the particle shape can be achieved by deliberately switching the passivation, additive and subtractive roles of these surfactants.

Results

Computational modelling. To quantify the surface coordination chemistry between β-$NaYF_4$ surface and OAH and OA^- ligands, we performed first-principles calculations based on density functional theory using CASTEP (CAmbridge Serial Total Energy Package)[35]. As shown in Fig. 1b and Supplementary Fig. 1, we treated the (001) and (100) planes of the *β*-$NaYF_4$ nanocrystals terminated with specific atomic arrangement as the most stable facets according to the calculated surface energies. Considering that the oxygen moiety in the ligands has a strong binding affinity to Y^{3+} ions at the particle surface[36], we modelled the interactions between the OAH and OA^- molecules and the Y^{3+} ions under a number of conditions, such as different adsorption configurations (Supplementary Figs 2 and 3 and Supplementary Note 1), ligand chain length and ligand coverage (Supplementary Figs 4 and 5 and Supplementary Note 2). The key conclusion from these simulations is that OA^- preferentially binds to RE^{3+} ions exposed on the (100) facet of the hexagonal fluoride nanocrystal, with a much higher binding energy (-35.4 eV) than on the (001) facet (-21.8 eV). It should be noted that the OAH molecule binds with a higher probability to the (001) facet than the (100) facet and has relatively small binding energies of -9.4 eV and -4.6 eV, respectively, on each of these facets (Supplementary Table 1). Our charge analysis (Supplementary Fig. 6) further indicates that such selective binding is attributed to the difference in the atomic arrangements of these two facets (Fig. 1b), giving rise to different charge transfer paths between the ligands and the surface ions.

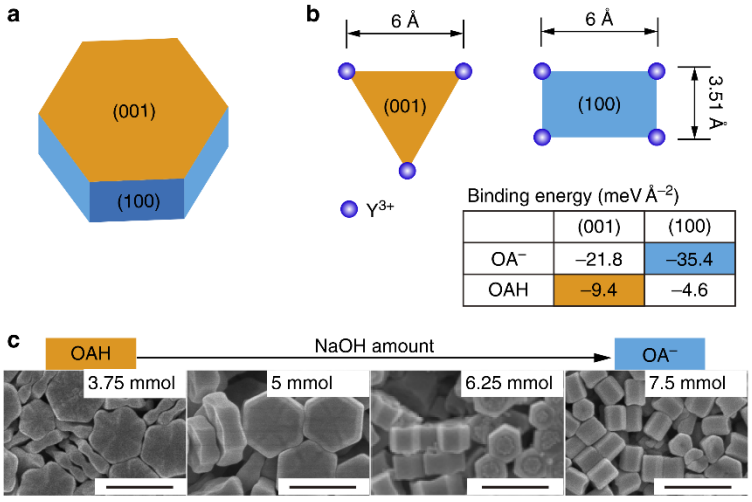

Figure 1 | Preferred molecular bonding models of OA^- and OAH. (**a**) The schematic shape of a *β*-$NaYF_4$ nanocrystal chosen as the core for directional epitaxial growth in this work. The hexagonal cylinder consists of the (001) facets at the ends and identical (100) and (010) facets around the cylinder sides. (**b**) The Y^{3+} arrangements and binding energies (see insert table) of OAH and OA^- on the most stable (001) and (100) facets. The Y^{3+} atoms form equilateral triangles with a length of 6 Å in the relaxed (001) surface, while rectangles are observed in the (100) surface with a shorter length of 3.51 or 3.69 Å; (**c**) SEM characterization of submicron-sized nanocrystals synthesized using the hydrothermal route (detailed synthesis is included in the method; scale bar, 500 nm).

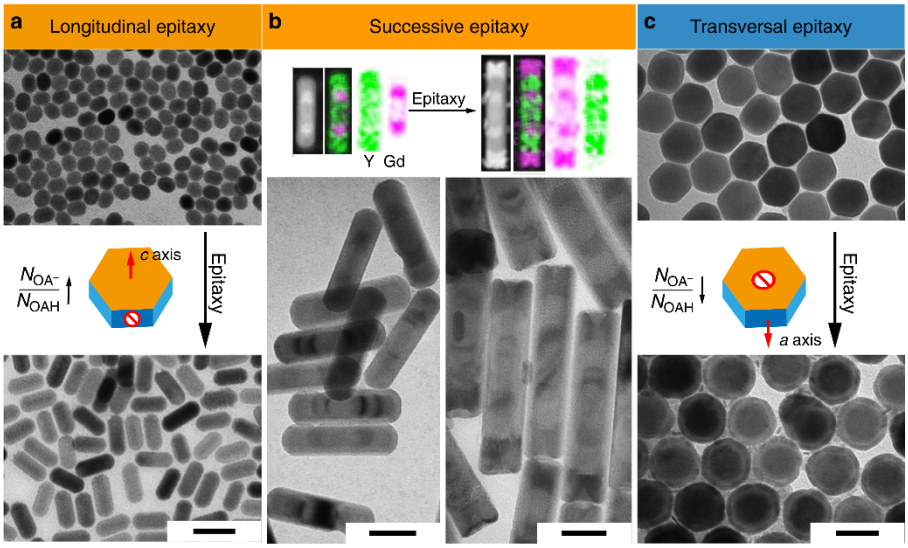

Figure 2 | Physical characterization of epitaxial growth of $NaReF_4$ NCs. (**a**) $NaYF_4$ core and homogenous $NaYF_4$ NCs after epitaxial growth of $NaYF_4$ in longitudinal direction with 0.5 mmol NaOH and 9.5 mmol OA at 310 °C for 1 h; (**b**) five-section and seven-section 'bamboo-shaped' $NaYF_4$/$NaGdF_4$ NRs formed by successive heterogeneous growth of periodical shells of $NaGdF_4$-$NaYF_4$ and $NaGdF_4$-$NaYF_4$-$NaGdF_4$ onto $NaYF_4$ core in the longitudinal direction, with 0.5 mmol NaOH and 0.4 mmol KOH and 9.5 mmol OA at 310 °C. Upper part of the panel shows elemental mapping of Y and Gd; (**c**) $NaYF_4$ core and heterogeneous $NaYF_4$/$NaGdF_4$ NCs after epitaxial growth of $NaGdF_4$ in the transversal direction with 0.15 mmol NaOH and 19 mmol OA at 290 °C for 3 h; the dimensions of individual nanocrystal were analysed statistically and included in the Supplementary Figs 10, 20–24. Scale bar, 50 nm.

Controlled epitaxial growth direction. The binding preferences of OAH and OA^- molecules to different facets were first used to induce longitudinal epitaxial growth. We demonstrated (Fig. 1c) that sub-micrometre-sized $NaYF_4$ crystals of different aspect ratios could be prepared by tuning the concentration ratio of OA^- to OAH in the hydrothermal synthesis system. As shown in Supplementary Fig. 7, higher concentrations of OA^- encourage epitaxial growth along a longitudinal direction. A similar effect was observed in the synthesis of sub-50 nm $NaYF_4$ nanoparticles prepared by a co-precipitation method. Figure 2a,b show that high concentration of NaOH leads to longitudinally grown nanoparticles because of a large concentration of passivating OA^- ions on the (100) facets (Supplementary Figs 8–10). The zeta potential of +20 mV for $NaYF_4$ nanocrystals after the removal of ligands (Supplementary Fig. 11) shows that the RE^{3+} cations are more abundant on the crystal surfaces than the F^- ions. We further systemically studied other possible factors that could influence the epitaxial shell growth (experimental details in Supplementary Methods), including the reaction temperature (Supplementary Fig. 12 and Supplementary Note 3), the oleic acid concentration (Supplementary Fig. 13 and Supplementary Note 4), the F^- ion concentration (Supplementary Fig. 14 and Supplementary Note 5) and the Na^+ concentration (Supplementary Fig. 15 and Supplementary Note 6). From these results, we confirm that the ratio of OA^-/OAH is a key factor that determines the epitaxial shell growth direction. However other parameters also have an effect on the growth speed or can change the OA^-/OAH ratio that indirectly affects the direction of growth. To rule out the effect of OH^- on longitudinal growth, we added sodium oleate as the sodium source instead of hydroxide and identical results were obtained (Supplementary Fig. 16 and Supplementary Note 7). Supplementary Figures 17 and 18 further confirm that high ratio of OA^-/OAH directs longitudinal deposition of heterogeneous shells ($NaGdF_4$) on the end surfaces of $NaYF_4$ core. Interestingly, subtractive growth (dissolution) is observed from their side (100) surfaces. This results in concurrent decrease of the core width from 26 to 18 nm, thus producing dumbbell-shaped nanocrystals (Supplementary Note 8).

Moreover, we found that the addition of KOH further accelerates longitudinal growth rate (Supplementary Fig. 19 and Supplementary Note 9) due to a higher dissociation constant of KOH than NaOH, which increases the dissociation of OAH producing more OA^-. With the aid of KOH, heterogeneous 'bamboo-shaped' nanorods (NRs) with sharp edges were formed in a stepwise manner with a length of up to 173 nm (Fig. 2b, Supplementary Fig. 21 and Supplementary Note 10). The interesting one-dimension architecture of 'bamboo-shaped' NRs suggests that integrated multiple functionalities can be built. Thus our new platform enables rational design and facile synthesis of multiple sections of rare-earth-doped heterogeneous materials and investigation of their interactions and functions within a single integrated rod. We were also able to induce transversal epitaxial growth by increasing the amount of OAH and reducing the amount of NaOH. At a reaction temperature of 290 °C, the transversal growth was observed and $NaGdF_4$ rings of 7-nm-thick around the $NaYF_4$ cores formed without a measurable change in the longitudinal direction (Fig. 2c, Supplementary Figs 23 and 24 and Supplementary Note 11). Notably, the dissolution of the (100) facets of the cores took place as well, and the width of the core was, again, reduced from 49 to 30 nm at both ends. The observed dissolution always occurred on the (100) facets in both cases of longitudinal and transversal growth. This is consistent with the strong chelating character of OA^- on the (100) facet, and with the fact that $NaYF_4$ is dissolved faster than $NaGdF_4$ because $NaYF_4$ is comparably less energetically stable[12]. To shed more light on this issue, we provided more evidence in the Supplementary Fig. 25 and Supplementary Note 12 to show that the dissolution of core is caused by the thermal stability difference

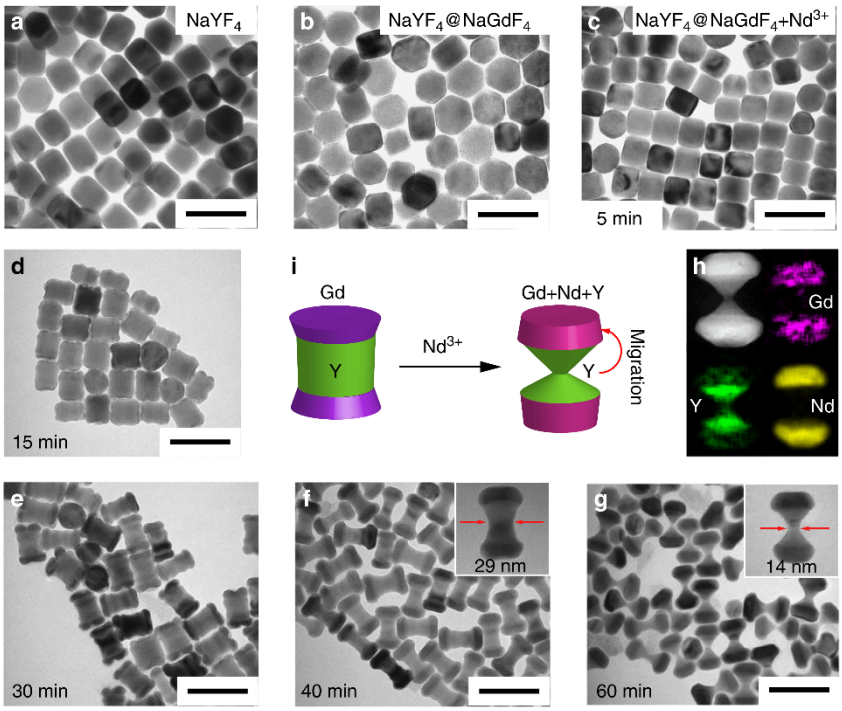

Figure 3 | Evolution of morphology and composition in migration growth. (**a**,**b**) $NaGdF_4$ growth along the longitudinal direction onto the ends of the $NaYF_4$ core; (**c**) transmission electron microscope image of the sample stopped 5 min after reacting with $NaGdF_4$/$NaYF_4$ nanocrystals in the presence of Na^+, K^+, Nd^{3+}, OA^- and in the absence of F^- at 310 °C, dissolution occurs first; (**d**–**g**) real-time monitoring of the epitaxial growth of $NaNdF_4$ along the longitudinal direction onto $NaYF_4$-$NaGdF_4$ nanocrystals, involving the dissolution of $NaYF_4$ and $NaGdF_4$ from the transversal surfaces of the crystal and their subsequent re-growth onto the $NaNdF_4$ nanocrystals in the presence of Na^+, K^+, Nd^{3+}, OA^- and absence of F^- ions at 310 °C. (**h**) HAADF-STEM image with elemental mapping results of the samples stopped after 60 min of reaction to confirm the distributions of Y^{3+}, Gd^{3+}, Nd^{3+} ions within a single $NaYF_4$/$NaGdF_4$/$NaNdF_4$ nanocrystal. (**i**) schematic processes of dissolution of $NaYF_4$/$NaGdF_4$ and the sequent epitaxial growth of $NaNdF_4$ in the longitudinal direction and the migration growth of F^-, Y^{3+} and Gd^{3+} ions (scale bar, 100 nm).

between core and shell materials in presence of OA^- which leads to higher binding strength on the side surfaces. By comparing growth of $NaTbF_4$ as shell or $NaYbF_4$ as shell on a $NaYF_4$ core (Supplementary Fig. 25), we demonstrate that the dissolution of the core requires the shell materials to have higher thermal stability than the core material. Larger difference of thermal stability between core and shell result in a higher dissolution rate.

Controlled migration growth. By combining the approaches of longitudinal and transversal growth and selective dissolution with consideration of lattice mismatch (Supplementary Tables 2 and 3), we synthesized a variety of three-dimensional (3D) hybrid nanostructures (Supplementary Figs 26–34). Figure 3 shows a typical example of real-time evolution of morphology and composition of the $NaYF_4$/$NaGdF_4$/$NaNdF_4$ NCs, including the dissolution process of the $NaYF_4$/$NaGdF_4$ nanocrystals and subsequent longitudinal growth of $NaNdF_4$. The dissolution of $NaYF_4$/$NaGdF_4$ is initiated by the OA^- adsorbed on the surface of the nanocrystals. The concomitant depletion of dissolved F^- ions used for longitudinal growth of $NaNdF_4$ in the presence of high concentration of OA^- facilitates the dissolution of $NaYF_4$/$NaGdF_4$ nanocrystals and this, in turn, promotes longitudinal growth of $NaNdF_4$. Following the dissolution of the Y^{3+} and Gd^{3+} ions from the surface of $NaYF_4$–$NaGdF_4$ nanocrystals, these ions then participate in the epitaxial growth of $NaNdF_4$ nanocrystals, as evidenced by the elemental mapping (Fig. 3h). Moreover, our real-time sampling transmission electron microscope data further confirmed the underpinning mechanism (Fig. 3a–g, Supplementary Figs 26–28). The size of nanocrystal core decreased significantly in the first 5 min, indicating that the dissolution rate of the nanocrystals is faster than their growth rate. After 15 min, new material started to form at the top and at the bottom ends of the core with simultaneous decrease of the nanocrystal core width. This observation rules out 'surface mobility' ('atom diffusion') as the possible driving force behind the formation of the final shell, otherwise it is expected that the dissolution of $NaYF_4$ and growth of $NaNdF_4$ would occur at the same time. The only mechanism which explains the shape of this nanocrystal is that the absence of F^- source in the reaction solution at its beginning prevents growth of $NaNdY_4$ until the concentration of released F^- source exceeds a certain threshold.

Our control experiments (Supplementary Fig. 29 and Supplementary Note 15) further support the mechanism of OA^--induced dissolution in which a firm bonding of the surfactant OA^- to the surface RE^{3+} cations is the main factor responsible for the removal of the surface crystalline layers (experimental details in Supplementary Methods). As shown in Supplementary Fig. 29, we applied transversal growth approach to first grow a layer of $NaGdF_4$ on the side surfaces of $NaYF_4$ core. We see that smaller mismatch of $NaGdF_4$ versus $NaNdF_4$ compared with the $NaYF_4$ versus $NaNdF_4$ fails to direct the transversal migration growth of the $NaNdF_4$ on the side surfaces of $NaGdF_4$. Instead, dissolution occurs in the first 10 min of the reaction (Supplementary Fig. 29a,b) and both dissolution from

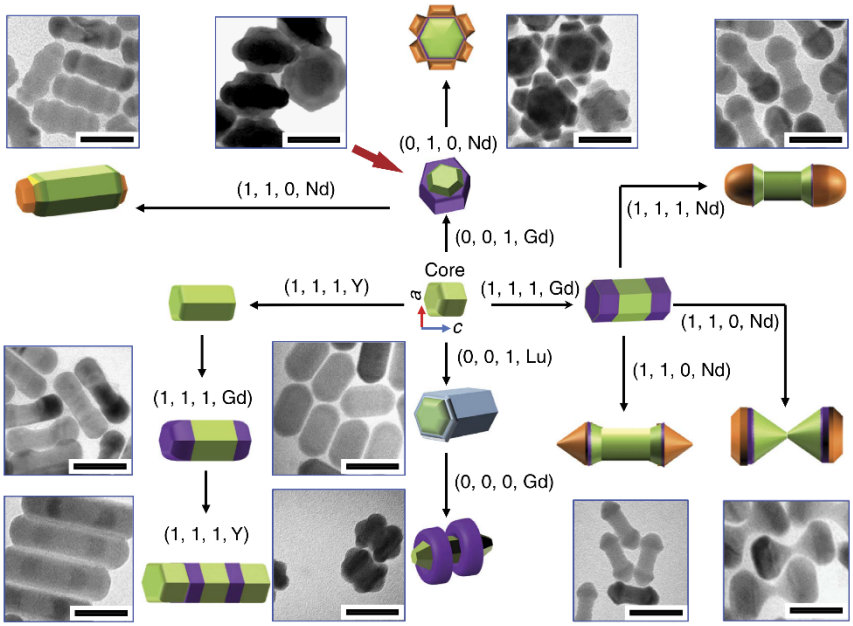

Figure 4 | Programmable routes for fabricating 3D nano-architectures. The four digital condition codes (R, T, F and RE) represent different reaction conditions where: $R=0$, represents a low ratio of OA^-/OAH; $R=1$, represents a high ratio of OA^-/OAH; $T=0$, where the temperature is at 290 °C; $T=1$, where the temperature is at 310 °C; $F=0$, which designates the absence of an F^- ion source; $F=1$, indicates the presence of an F^- ion source; RE = Y, with a rare earth Y^{3+} ion source; RE = Gd, with Gd^{3+} ion source; RE = Lu, with a Lu^{3+} source; RE = Nd, with Nd^{3+} source. By combining these different growth processes into a synthesis procedure, a variety of complex $NaREF_4$ nanostructures are fabricated as shown in the transmission electron microscope images, including hourglass shaped $NaYF_4/NaGdF_4/NaNdF_4$ nanocrystals, $NaYF_4/NaGdF_4/NaNdF_4$ nano-flowers, $NaYF_4/NaLuF_4$ co-axial nano-cylinders, $NaYF_4/NaLuF_4/NaGdF_4$ nanoscale spins with double rings, and $NaYF_4/NaGdF_4/NaNdF_4$ nano-dumbbells with smooth or sharp ends (scale bar, 50 nm).

the side surfaces and epitaxial growth of $NaNdF_4$ on the end surfaces of $NaGdF_4/NaYF_4$ cores result in a thinner and longer nanocrystal.

Guided by the principle that the ratio of OA^-/OAH controls the direction of epitaxial shell growth, we further demonstrated (as shown in Supplementary Fig. 30 and Supplementary Note 16) that a low ratio of OA^-/OAH at a lower temperature directs the migration growth along transverse direction. This enables the formation of heterogeneous $NaYF_4/NaGdF_4/NaNdF_4$ nanocrystals in the shape of a flower, although in this case the dissolution process on the side surfaces of nanocrystals is much less efficient because there are too few OA^- ligands bound to RE^{3+} cations on the (100) facet. Two additional experiments (Supplementary Note 17) demonstrate that well established parameters, such as reagent concentration, can be further applied to fine-tune our programmable protocols for other types of heterogeneous nanocrystals. During the formation of hourglass-shaped nanocrystals, the decrease in the amount of Nd^{3+} source is found to hinder the migration growth process and yield sharper tips (Supplementary Fig. 31), whereas a supply of additional F^- ions in the reaction increases the diameter of dumbbell ends with round tips (Supplementary Fig. 32). Such level of fine tuning to grow progressively sharper tips may suggest future rational methods, for example to optimize tip-sensitive physical and biochemical properties of NRs.

Figure 4 shows an array of heterogeneous $NaREF_4$ nanostructures synthesized by carrying out specific sequences of longitudinal, transversal growth, selective dissolution and directional migration growth of epitaxial shells in the presence of various OA^-/OAH ratios. To the best of our knowledge, these sub-50 nm nanoparticles are the smallest 3D objects prepared by a bottom–up additive and subtractive process. To illustrate the application of this novel method we designed and synthesized multifunctional $NaYF_4/NaLuF_4/NaGdF_4$ heterogeneous nanocrystals with two $NaGdF_4$ rings on a $NaLuF_4/NaYF_4$ NRs (Supplementary Figs 33 and 34 and Supplementary Note 18). The hexagonal-phase $NaYF_4$ nanocrystal is an efficient luminescence upconversion material[37]. The addition of $NaLuF_4$ enables X-ray computed tomography[38], whereas using $NaGdF_4$ enables magnetic resonance imaging[39]. To the best of our knowledge, this work presents the first controlled fabrication of sub-50 nm 3D shaped heterogeneous nanocrystals logically programmed by the combinational approaches of OA^--assisted longitudinal growth, transversal growth and selective crystalline facet dissolution with consideration of crystallographic mismatch rates.

Discussion

The nanoscale engineering capability presented in this work enables quantitative studies which are virtually impossible by conventional approaches. We anticipate that optical properties of these nanostructures can be designed to precisely promote or inhibit inter-particle energy transfer. Similarly, magnetic properties may be optimized to enhance magnetic resonance imaging by correlating the morphology with the surface distribution of magnetic signals. In addition, such hybrid nanomaterials may be used as a platform for transporting biologically important molecules across cell membranes. Furthermore, access to a new library of precisely controlled shapes of nanoparticles provide a novel approach for the targeted delivery in nanomedicine where optimized morphologies of these nanoscale molecular carriers will yield greater efficiencies. This

process could be further facilitated by harnessing the anisotropic properties of different types of nanoparticles that permit diverse surface functionalizations and multi-modal bio-conjugations. The concept presented in this work may further advance our current capabilities of nanoscale programmable and reproducible engineering of new classes of heterogeneous materials in scalable quantities. Our findings may lead to a new class of multi-functional nanomaterials and provide the groundwork for developing previously unforeseen applications of nanoparticles with complex programmable shapes and surface properties.

Methods

Hydrothermal synthesis of $NaYF_4$ crystal. The β-$NaYF_4$ disks were synthesized via a slightly modified hydrothermal reaction. In a typical experiment, NaOH (3.75 mmol) was first dissolved into 1.5 mL of double distilled water, followed by the addition of OA (7.5 mmol) and ethanol (2.5 mL) while undergoing vigorous stirring. Thereafter, an aqueous solution of NaF (0.5 M; 2 mL) was added to form a turbid mixture. Subsequently, a 1.2 mL aqueous solution of YCl_3 (Yb^{3+}/Tm^{3+} = 10/0.5 mol%; 0.2 M) was added and the solution was stirred for 20 min. The resulting mixture was then transferred into a 14 mL Teflon-lined autoclave and heated to 220 °C and the temperature maintained for 12 h. After cooling down to room temperature, the reaction product was isolated by centrifugation and washed with ethanol. In this work, different amounts of NaOH were added to adjust the ratio of OA^-/OAH by its reaction with OAH to form OA^-.

$NaYF_4$ nanocrystal cores. In a typical procedure, 4 ml of methanol solution of YCl_3 (2.0 mmol) was magnetically mixed with OA (38 mmol) and ODE (93 mmol) in a 100-ml three-neck round-bottom flask. The mixture was then degassed under the Ar flow and then heated to 150 °C for 30 min to form a clear solution, before cooling to room temperature. 15 ml of methanol solution containing NH_4F (8 mmol) and NaOH (5 mmol) was added to the solution of YCl_3 in OA and ODE and stirred for 60 min. The mixture solution was slowly heated to 110 °C and kept at 110 °C for 30 min to completely remove methanol and any residual water. The mixture solution was then quickly heated to the reaction temperature of 300 °C and aged for 1 h. After the solution was left to cool down to room temperature, ethanol was added to precipitate the nanocrystals. The product was washed with cyclohexane, ethanol and methanol for at least 4 times, before the final $NaYF_4$ nanocrystals were re-dispersed in 10 ml cyclohexane in preparation for their further use.

Longitudinal growth of $NaYF_4$ NRs. YCl_3 (0.2 mmol) in 1 ml methanol solution was magnetically mixed with OA (9.5 mmol) and ODE (25 mmol) in a 50-ml three-neck round-bottom flask. The mixture was degassed under Ar flow and heated to 150 °C for 30 min to form a clear solution, and then cooled to room temperature. Methanol solution (5 ml) containing NH_4F (0.8 mmol) and NaOH (0.5 mmol) was added and stirred for 60 min. The solution was slowly heated to 110 °C and kept at 110 °C for 30 min to completely remove methanol and residual water. The solution was then injected with 0.2 mmol $NaYF_4$ of nanocrystals in cyclohexane and the mixture kept at 110 °C for another 10 min to evaporate the cyclohexane. Then, the reaction mixture was quickly heated to 310 °C and aged for 1 h.

$NaGdF_4/NaYF_4$ nano-dumbbells. $GdCl_3$ (0.2 mmol) in 1 ml methanol solution was magnetically mixed with OA (9.5 mmol) and ODE (25 mmol) in a 50-ml three-neck round-bottom flask. The mixture was degassed under an Ar flow and heated to 150 °C for 30 min to form a clear solution, and then cooled to room temperature. Methanol solution (4 ml) containing NH_4F (0.8 mmol) and NaOH (0.5 mmol) was added to the OA and ODE solution and stirred for 60 min. The solution is slowly heated to 110 °C and kept at 110 °C for 30 min to remove methanol and the remaining water completely. Then, 0.2 mmol of $NaYF_4$ core nanocrystals in cyclohexane was injected into the reaction solution. After holding the reaction temperature at 110 °C for further 10 min to evaporate all cyclohexane, the reaction mixture was quickly heated to 310 °C and aged for 1 h.

$NaGdF_4/NaYF_4$ NRs by adding KOH. $GdCl_3$ (0.2 mmol) in 1 ml of methanol solution was magnetically mixed with OA (9.5 mmol) and ODE (25 mmol) in a 50-ml three-neck round-bottom flask. The mixture was degassed under Ar flow and heated to 150 °C for 30 min to form a clear solution, before cooling to room temperature. Methanol solution (5 ml) containing NH_4F (0.8 mmol), KOH (0.4 mmol) and NaOH (0.5 mmol) was added into the OA and ODE solution and stirred for 60 min. The solution was slowly heated to 110 °C and kept at 110 °C for 30 min to remove the methanol and water completely. The reaction mix was then injected with 0.2 mmol of $NaYF_4$ core nanocrystals in cyclohexane, into the reaction solution. After holding the reaction mix at 110 °C for further 10 min to evaporate all cyclohexane, the mixture was heated rapidly to 310 °C before aging for 1 h at this temperature.

$NaYF_4/NaGdF_4/NaYF_4$ NCs in a bamboo-like shape. 0.2 mmol of YCl_3 in 1 ml of methanol solution was magnetically mixed with OA (9.5 mmol) and ODE (25 mmol) in a 50-ml three-neck round-bottom flask. The mixture was degassed under Ar flow and heated to 150 °C for 30 min to form a clear solution, and then cooled to room temperature. Methanol solution (5 ml) containing NH_4F (0.8 mmol), KOH (0.4 mmol) and NaOH (0.5 mmol) was added into the OA and ODE solution and stirred for 60 minutes. The solution was slowly heated to 110 °C and kept at 110 °C for 30 min to remove the methanol and water completely. The reaction solution was then injected with 0.2 mmol of $NaYF_4/NaGdF_4$ NRs in cyclohexane solution. After the reaction at 110 °C for a further 10 min to evaporate all the cyclohexane, the reaction mixture was quickly heated to 310 °C and held at this temperature for 1 h.

$NaYF_4/NaGdF_4/NaYF_4/NaGdF_4$ NCs in a bamboo-like shape. The same procedure for synthesizing $NaYF_4/NaGdF_4/NaYF_4$ NCs in bamboo-like shape was repeated, and then followed by the injection of 0.2 mmol of the five-section $NaYF_4/NaGdF_4/NaYF_4$ nano-bamboos which acted as the core, all in cyclohexane solution, into the reaction solution. After holding at 110 °C for a further 10 min to evaporate all cyclohexane, the reaction mixture was quickly heated to 310 °C and held again for 1 h.

$NaYF_4/NaGdF_4/NaNdF_4$ NCs in an hourglass shape. $NdCl_3$ (0.4 mmol) in 2 ml of methanol solution was magnetically mixed with OA (9.5 mmol) and ODE (25 mmol) in a 50-ml three-neck round-bottom flask. The mixture was degassed under Ar flow and heated to 150 °C for 30 min to form a clear solution, and then cooled to room temperature. Methanol solution (5 ml) containing KOH (0.8 mmol) and NaOH (0.8 mmol) was added and stirred for 60 min. The solution was slowly heated to 110 °C and kept at 110 °C for 30 min to completely remove the methanol and some of the water. It was then injected with 0.1 mmol 50 nm × 60 nm $NaYF_4/NaGdF_4$ nano-prisms particles, in a solution of cyclohexane. After having been kept at 110 °C for another 10 min to evaporate all cyclohexane, the reaction mixture was quickly heated to 310 °C. Samples (500 ul) of the reaction solution were collected each time with a syringe at 5, 15, 30, 40, 50 and 60 min after the start of the reaction.

Transversal growth of $NaGdF_4$ shell onto $NaYF_4$ core. $GdCl_3$ (0.1 mmol) in 1 ml methanol solution was magnetically mixed with OA (19.0 mmol) and ODE (18.7 mmol) in a 50-ml three-neck round-bottom flask. The mixture was degassed under Ar flow and heated to 150 °C for 30 min to form a clear solution, and then cooled to room temperature. Methanol solution (3 ml) containing NH_4F (0.4 mmol) and NaOH (0.15 mmol) was added into the OA and ODE solution and stirred for 60 min. The solution was slowly heated to 110 °C and kept at 110 °C for 30 min to remove completely the methanol and water. Then 0.1 mmol of the $NaYF_4$ cores in cyclohexane solvent were injected into the reaction mix. After being kept at 110 °C for further 10 min to evaporate all cyclohexane, the reaction mixture was quickly heated up to 290 °C and held at that temperature for 3 h.

Synthesis of $NaYF_4/NaGdF_4/NaNdF_4$ NCs in flower shape. $NdCl_3$ (0.1 mmol) in 1 ml of methanol solution was magnetically mixed with OA (19 mmol) and ODE (18.7 mmol) in a 50-ml three-neck round-bottom flask. The mixture was degassed under Ar flow and heated to 150 °C for 30 min to form a clear solution, and then cooled to room temperature. Methanol solution (5 ml) containing NaOH (0.6 mmol) was added and stirred for 60 min. The solution was slowly heated to 110 °C and kept at 110 °C for 30 min to completely remove the methanol and some of the water. Then, the reaction mix was injected with 0.1 mmol of 50 nm $NaYF_4/NaGdF_4$ nano-prisms prisms ($NaGdF_4$ growing on the lateral faces of $NaYF_4$ nanocrystal), suspended in a cyclohexane solution. After holding at 110 °C for another 10 min to evaporate all cyclohexane, the reaction mixture was quickly heated to 300 °C. samples (500 ul) of the reaction solution were collected each time with a syringe after 10, 25 and 45 min of the reaction time.

Synthesis of $NaYF_4/NaGdF_4/NaNdF_4$ sharp-end dumbbell. $NdCl_3$ (0.1 mmol) in 1 ml of methanol solution was magnetically mixed with OA (9.5 mmol) and ODE (25 mmol) in a 50-ml three-neck round-bottom flask. The mixture was degassed under Ar flow and heated to 160 °C for 30 min to form a clear solution, and then cooled to room temperature. Methanol solution (5 ml) containing KOH (0.2 mmol) and NaOH (0.2 mmol) was added and stirred for 60 min. Note: in this reaction no NH_4F was added to the solution. The solution was slowly heated to 110 °C and kept at 110 °C for 30 min to remove the methanol and the water completely. It was then injected with 0.1 mmol of $NaYF_4/NaGdF_4$ NR particle in suspended in cyclohexane solvent into the reaction solution. After holding at 110 °C for a further 10 min to evaporate all cyclohexane, the reaction mixture was quickly heated to 310 °C and held at this temperature for a further 30 min.

Synthesis of $NaYF_4/NaGdF_4/NaNdF_4$ round-end dumbbell. $NdCl_3$ (0.1 mmol) in 1 ml of methanol solution was magnetically mixed with OA (9.5 mmol) and

ODE (25 mmol) in a 50-ml three-neck round-bottom flask. The mixture was degassed under Ar flow and heated to 160 °C for 30 min to form a clear solution, and then cooled to room temperature. Methanol solution (5 ml) containing NH_4F (0.3 mmol), KOH (0.2 mmol) and NaOH (0.2 mmol) was added and the mixture was stirred for 60 min. The solution was slowly heated to 110 °C and kept at 110 °C for 30 min to remove the methanol and the water completely. Then, it was injected with 0.1 mmol of $NaYF_4$/$NaGdF_4$ NRs suspended in cyclohexane into the reaction solution. After being held at 110 °C for further 10 min to evaporate all cyclohexane, the reaction mixture was quickly heated to 310 °C and held for 30 min at this temperature.

Synthesis of pure α-$NaGdF_4$ NCs. Methanol solution (2 ml) of $GdCl_3$ (1.0 mmol) was magnetically mixed with OA (19 mmol) and ODE (47 mmol) in a 100-ml three-neck round-bottom flask. The mixture was degassed under Ar flow and heated to 150 °C for 30 minutes to form a clear solution, and then cooled to room temperature. Methanol solution (10 ml) containing NH_4F (4 mmol) and NaOH (2.5 mmol) was added and stirred for 60 min. Then, the solution was slowly heated to 110 °C and kept at 110 °C for 30 min to remove the methanol and water completely. After that, the reaction mixture was quickly heated to 240 °C and aged for 45 min.

Synthesis of $NaLuF_4$/$NaYF_4$ NRs. $LuCl_3$ (0.1 mmol) in 1 ml method solution was magnetically mixed with OA (19 mmol) and ODE (25 mmol) in a 50-ml three-neck round-bottom flask. The mixture was degassed under Ar flow and heated to 150 °C for 30 min to form a clear solution, and then cooled to room temperature. Methanol solution (2 ml) containing NaOH (0.15 mmol) and 0.4 mmol NH_4F was added and stirred for 60 min. The solution was slowly heated to 110 °C and kept at 110 °C for 30 min to completely remove the methanol and some of the water. It was then injected with 0.4 mmol of $NaYF_4$ seed particles in a cyclohexane solution. After holding the reaction mix at 110 °C for a further 10 min to evaporate cyclohexane, the reaction mixture was quickly heated to 290 °C and held at that temperature for a further 1 h.

Synthesis of $NaLuF_4$/$NaYF_4$ NRs with $NaGdF_4$ double-ring. $GdCl_3$ (0.1 mmol) in 1 ml methanol solution was magnetically mixed with OA (19.0 mmol) and ODE (18.7 mmol) in a 50-ml three-neck round-bottom flask. The mixture was degassed under Ar flow and heated to 150 °C for 30 min to form a clear solution, and then cooled to room temperature. Methanol solution (2 ml) containing NaOH (at 0.15 mmol) was added and stirred for 60 min. The solution was slowly heated to 110 °C and kept at 110 °C for 30 min to completely remove the methanol and some of the water. It was then injected with 0.1 mmol of the $NaYF_4$/$NaLuF_4$ seed particles, in a cyclohexane solution, into the reaction solution. After having been held the reaction mix at 110 °C for another 10 min to evaporate cyclohexane, the reaction mixture was quickly heated to 300 °C. It was then, injected with 0.02 mmol of α-$NaGdF_4$ nanocrystals into the reaction system. This was done every 10 min for 5 times at 300 °C. The reaction mix was held at this temperature for another 10 min after the last injection.

References

1. Jia, G. H. *et al.* Couples of colloidal semiconductor nanorods formed by self-limited assembly. *Nat. Mater.* **13,** 302–308 (2014).
2. Jones, M. R., Seeman, N. C. & Mirkin, C. A. Programmable materials and the nature of the DNA bond. *Science* **347,** 1260901 (2015).
3. Ye, X. *et al.* Seeded growth of metal-doped plasmonic oxide heterodimer nanocrystals and their chemical transformation. *J. Am. Chem. Soc.* **136,** 5106–5115 (2014).
4. Yu, H. *et al.* Dumbbell-like bifunctional Au-Fe3O4 nanoparticles. *Nano Lett.* **5,** 379–382 (2005).
5. Jun, Y. W., Choi, J. S. & Cheon, J. Shape control of semiconductor and metal oxide nanocrystals through nonhydrolytic colloidal routes. *Angew. Chem. Int. Ed.* **45,** 3414–3439 (2006).
6. Hill, J. P. *et al.* Self-assembled hexa-peri-hexabenzocoronene graphitic nanotube. *Science* **304,** 1481–1483 (2004).
7. Yin, Y. & Alivisatos, A. P. Colloidal nanocrystal synthesis and the organic-inorganic interface. *Nature* **437,** 664–670 (2005).
8. Zeng, H. & Sun, S. H. Syntheses, properties and potential applications of multicomponent magnetic nanoparticles. *Adv. Funct. Mater.* **18,** 391–400 (2008).
9. Qian, H. F., Zhu, Y. & Jin, R. C. Atomically precise gold nanocrystal molecules with surface plasmon resonance. *Proc. Natl Acad. Sci. USA* **109,** 696–700 (2012).
10. Zheng, W. *et al.* Lanthanide-doped upconversion nano-bioprobes: electronic structures, optical properties, and biodetection. *Chem. Soc. Rev.* **44,** 1379–1415 (2015).
11. Wang, X., Zhuang, J., Peng, Q. & Li, Y. D. A general strategy for nanocrystal synthesis. *Nature* **437,** 121–124 (2005).
12. Wang, F. *et al.* Simultaneous phase and size control of upconversion nanocrystals through lanthanide doping. *Nature* **463,** 1061–1065 (2010).
13. Deng, R. *et al.* Temporal full-colour tuning through non-steady-state upconversion. *Nat. Nanotechnol.* **10,** 237–242 (2015).
14. Ramasamy, P. & Kim, J. Combined plasmonic and upconversion rear reflectors for efficient dye-sensitized solar cells. *Chem. Commun.* **50,** 879–881 (2014).
15. Lu, Y. Q. *et al.* Tunable lifetime multiplexing using luminescent nanocrystals. *Nat. Photon.* **8,** 33–37 (2014).
16. Wang, J. *et al.* Near-infrared-light-mediated imaging of latent fingerprints based on molecular recognition. *Angew. Chem.* **126,** 1642–1646 (2014).
17. Huang, P. *et al.* Lanthanide-doped $LiLuF_4$ upconversion nanoprobes for the detection of disease biomarkers. *Angew. Chem. Int. Ed.* **53,** 1252–1257 (2014).
18. Zhao, J. *et al.* Single-nanocrystal sensitivity achieved by enhanced upconversion luminescence. *Nat. Nanotechnol.* **8,** 729–734 (2013).
19. Gargas, D. J. *et al.* Engineering bright sub-10-nm upconverting nanocrystals for single-molecule imaging. *Nat. Nanotechnol.* **9,** 300–305 (2014).
20. Liu, Q. *et al.* F-18-labeled magnetic-upconversion nanophosphors via rare-earth cation-assisted ligand assembly. *ACS Nano* **5,** 3146–3157 (2011).
21. Idris, N. M. *et al.* In vivo photodynamic therapy using upconversion nanoparticles as remote-controlled nanotransducers. *Nat. Med.* **18,** 1580–1585 (2012).
22. Wang, C., Cheng, L. & Liu, Z. Upconversion nanoparticles for photodynamic therapy and other cancer therapeutics. *Theranostics* **3,** 317–330 (2013).
23. Kang, X. J. *et al.* Lanthanide-doped hollow nanomaterials as theranostic agents. *Wiley Interdiscip. Rev. Nanomed. Nanobiotechnol.* **6,** 80–101 (2014).
24. Mai, H. X., Zhang, Y. W., Sun, L. D. & Yan, C. H. Highly efficient multicolor up-conversion emissions and their mechanisms of monodisperse $NaYF_4$: Yb,Er core and core/shell-structured nanocrystals. *J. Phys. Chem. C* **111,** 13721–13729 (2007).
25. Shen, J. *et al.* Tunable near infrared to ultraviolet upconversion luminescence enhancement in (alpha-NaYF4:Yb,Tm)/CaF2 core/shell nanoparticles for in situ real-time recorded biocompatible photoactivation. *Small* **9,** 3213–3217 (2013).
26. Wen, H. *et al.* Upconverting near-infrared light through energy management in core-shell-shell nanoparticles. *Angew. Chem. Int. Ed.* **52,** 13419–13423 (2013).
27. Johnson, N. J. & van Veggel, F. C. Lanthanide-based hetero-epitaxial core-shell nanostructures: the compressive vs. tensile strain asymmetry. *ACS Nano* **8,** 10517–10527 (2014).
28. Zhang, C. & Lee, J. Y. Prevalence of anisotropic shell growth in rare earth core-shell upconversion nanocrystals. *ACS Nano* **7,** 4393–4402 (2013).
29. Johnson, N. J. J. & van Veggel, F. C. J. M. Sodium lanthanide fluoride core-shell nanocrystals: a general perspective on epitaxial shell growth. *Nano Res.* **6,** 547–561 (2013).
30. Xia, Y., Xiong, Y., Lim, B. & Skrabalak, S. E. Shape-controlled synthesis of metal nanocrystals: simple chemistry meets complex physics? *Angew. Chem. Int. Ed.* **48,** 60–103 (2009).
31. Zhuang, Z., Peng, Q. & Li, Y. Controlled synthesis of semiconductor nanostructures in the liquid phase. *Chem. Soc. Rev.* **40,** 5492–5513 (2011).
32. Wang, F., Deng, R. R. & Liu, X. G. Preparation of core-shell $NaGdF_4$ nanoparticles doped with luminescent lanthanide ions to be used as upconversion-based probes. *Nat. Protoc.* **9,** 1634–1644 (2014).
33. Zherebetskyy, D. *et al.* Hydroxylation of the surface of PbS nanocrystals passivated with oleic acid. *Science* **344,** 1380–1384 (2014).
34. Bealing, C. R., Baumgardner, W. J., Choi, J. J., Hanrath, T. & Hennig, R. G. Predicting nanocrystal shape through consideration of surface-ligand interactions. *ACS Nano* **6,** 2118–2127 (2012).
35. Clark, S. J. *et al.* First principles methods using CASTEP. *Z. Kristallogr.* **220,** 567–570 (2005).
36. Sui, Y. Q., Tao, K., Tian, Q. & Sun, K. Interaction between Y^{3+} and oleate ions for the cubic-to-hexagonal phase transformation of NaYF4 nanocrystals. *J. Phys. Chem. C* **116,** 1732–1739 (2012).
37. Yi, G. *et al.* Synthesis, characterization, and biological application of size-controlled nanocrystalline $NaYF_4$: Yb, Er infrared-to-visible up-conversion phosphors. *Nano Lett.* **4,** 2191–2196 (2004).
38. Xia, A. *et al.* Gd^{3+} complex-modified $NaLuF_4$-based upconversion nanophosphors for trimodality imaging of NIR-to-NIR upconversion luminescence, X-Ray computed tomography and magnetic resonance. *Biomaterials* **33,** 5394–5405 (2012).
39. Hou, Y. *et al.* $NaGdF_4$ nanoparticle-based molecular probes for magnetic resonance imaging of intraperitoneal tumor xenografts in vivo. *ACS Nano* **7,** 330–338 (2012).

Acknowledgements

We thank D. Birch in Microscope Unit at Macquarie University and D.R.G. Mitchell in Electron Microscopy Centre at the University of Wollongong for their help and valuable discussion on transmission electron microscope characterizations. This project is primarily supported by the Australian Research Council (ARC) Future Fellowship Scheme (FT 130100517; D.J.), ARC Centre of Excellence Scheme through Centre for Nanoscale BioPhotonics, Macquarie University Research Fellowship Scheme (X.X.), ARC LIEF grant (LE120100104, Y.D.), ARC Discovery Project (DP140102581, Y.D.), China

Scholarship Council CSC scholarships (no.201206170136, D.I., C.M.) and the Agency for Science, Technology and Research (A*STAR; grant no. 1231AFG028, X.L.).

Author contributions

D.J. and X.L. conceived the project and supervised the research; X.X., D.L., D.J. and X.L. designed the experiments; D.L., C.M., Y.Z. and S.W. conducted synthesis; X.Q. and X.X. conducted crystallography analysis and computational modelling; D.L., Y.D., S.D., W.R. and X.X. conducted characterizations and analysis; D.L., X.X., X.Q. and Y.Z. prepared figures and supplementary information sections; D.J., D.L., X.X., E.M.G., X.Qin. and X. Liu wrote the manuscript. All authors contributed to data analysis, discussions and manuscript preparation.

Additional information

Supplementary Information accompanies this paper at http://www.nature.com/naturecommunications

Competing financial interests: The authors declare no competing financial interests.

Reprints and permission information is available online at http://npg.nature.com/reprintsandpermissions/

How to cite this article: Liu, D. *et al.* Three-dimensional controlled growth of monodisperse sub-50 nm heterogeneous nanocrystals. *Nat. Commun.* 7:10254 doi: 10.1038/ncomms10254 (2016).

Chapter 5 Conclusion and Future Scope

5.1 Conclusion

In this thesis, we focus on the core-shell structure engineering of rare-earth doped $NaReF_4$ nanocrystals. Core-shell structured nanocrystals provide an opportunity in integrating multiple functional materials into one structure for tailored applications including the ultra-sensitive bio assays, multi-modality biomedical imaging, targeted delivery and controlled release of drugs, high efficiency of green energy harvesting and other advanced applications by building novel devices with new optical, magnetic, catalytic and chemical properties. This thesis explores the roles of surfactants and study the interplays between different growth mechanisms in forming anisotropic shapes of nanocrystals. To this end, we introduce the anisotropic bonding feature of different surfactants on the different crystal facets, to direct either unidirectional growth of homogeneous shells by tuning the ratio of oleylamine (OM)/oleic acid (OA) or directional growth of heterogeneous shells by adjusting the ratio of oleic acid ions (OA^-)/ oleic acid (OAH). Based on these discoveries, we demonstrate our new ability of rationale design and programmable fabrication of 3D structured heterogeneous $NaReF_4$ nanocrystals.

The key results of this PhD work can be summarized below:

1) We systematically prepared a series of homogeneous core-shell UCNPs by epitaxial growth of the $NaYF_4$:Yb^{3+}, Er^{3+} nanocrystals with different thickness (1.5 to 8 nm) of inert shells by controlling the volume ratio of OM/OA. This level of controlled synthesis allowed us to systemically investigate and compare the luminescence responses to different pH and temperature in aqueous solution for both core-only and core-shell UCNPs. We found the inert shells efficiently prevented the luminescence quenching, but failed in avoiding the irreversible quenching by the acid environment. The inert shell also reduced the sensitivity and liner response resolution of the ratio-metric (524 nm/ 545 nm) green emissions of Er^{3+} doped UCNPs for temperature sensing below 60 ºC. This work adds the new knowledge that underpins the rapid development of upconversion nanotechnology towards emerging biomedical applications and further suggests new careful designs are necessary according to the temperature and pH environments for the specific applications.

2) We demonstrated that the bonding strength for the surfactants of OA- and OAH on the (100) and (001) faces of β-$NaYF_4$ nanocrystals are different. OA- has stronger bonding on (100) facets than (001) facets, while OAH has stronger bonding affinity on (001) facet

compared with (100) facets. Based on this knowledge, we demonstrated that the shell growth direction can be controlled via tuning the ratio of surfactant molecules.

3) Through further systematically designed experiments to study the impact of different ratio of OA^-/OAH on the shell growth directions, we confirmed that longitudinal shell growth occurred in the condition of high ratio of OA^-/OAH, while transversal shell growth occurred in the condition of low ratio of OA^-/OAH. Other reaction factors, Na^+ concentration, OA concentration, Re^{3+} concentration may indirectly influence the shell growth by changing the ratio of OA^-/OAH. These results directly supported our hypothesis that the shell growth direction can be precisely controlled by simply adjusting the ratio of surfactants.

4) Etching effect of $NaYF_4$ nanocrystals in OA-ODE system was observed for the first time and systemically studied. We found the etching effect was caused by the thermal stability between core and shell materials. It required that the shell materials had higher thermal stability than core material to induce the core crystal dissolution. These results suggest that subtractive growth can be used for the controlled growth of heterogeneous nanocrystals with different shapes.

5) Controlled migration shell growth was observed and studied when growth $NaNdF_4$ shell for $NaYF_4$/$NaGdF_4$ nanocrystals under the condition of absence of F^- source, in which $NaYF_4$ core nanocrystal were gradually dissolving into the reaction solution, while the $NaNdF_4$ shell were grown on the $NaYF_4$/$NaGdF_4$ cores by consuming the shell sources released by dissolved $NaYF_4$. The migration shell growth direction was also controllable by adjusting the ratio of OA-/OAH. These results suggest a new route for fabricating more complex structured heterogeneous nanocrystals.

6) By combining the approaches of longitudinal and transversal growth and selective dissolution with consideration of lattice mismatch, we designed and fabricated a variety of 3D hybrid nanostructures, including $NaYF_4$/$NaLuF_4$/$NaNdF_4$ topspin shape, $NaYF_4$/$NaGdF_4$/$NaNdF_4$ dumbbell shape and $NaYF_4$/$NaGdF_4$/$NaNdF_4$ flower shape, and $NaYF_4$/$NaGdF_4$ bamboo shape. These results suggest the possibility for programmable synthesis of 3D structured heterogeneous nanocrystal.

7) The highly controlled shell growth technique is reproducible, which is helpful to scale up production of multifunctional heterogeneous nanocrystals. 20 mg heterogeneous nanocrystals can be synthesized from one bench reaction via the current protocol. In high scale synthesis, the cost per mg heterogeneous will be greatly decreased.

The controlled heterogeneous nanocrystal growth is the first step towards real excellent applications of nano-device fabrication, which is as significant as the silicon wafer production

for electronic products. Under the base of this work, more specific application related research projects are ready to start.

5.2 Future Scope

My PhD thesis, by exploring new mechanisms and methods for highly controlled core-shell engineering of $NaReF_4$ nanocrystals, suggests a new field in controlled growth of other heterogeneous nanocrystals. Three possible directions of research in nanomaterials engineering may become possible.

2D heterogeneous nanocrystals synthesis via transversal shell growth in wet chemical synthesis

Two dimensional (2D) structured nanocrystals and nanomaterials, such as graphene and metal chalcogenide nanostructures, are attracting a lot of research interests by many unique optical, electronic, catalytic and mechanical properties recently discovered. Heterogeneous structured 2D nanocrystals may be synthesized by epitaxial growth of semiconductor and metal materials as shells onto the core of 2D nanocrystal to form hetero-2D-structure. Engineering of the core-shell 2D heterogeneous nanocrystals will bring new opportunity for fabricating nanoscale electronics-device (nanodevice).

Current high quality 2D heterogeneous nanocrystals (e.g. $MoS_2/MoSe_2$, and WS_2/WSe_2) are mainly obtained by vapour-phase deposition, chemical vapour deposition (CVD) or MOCVD. These methods require high temperature, high vacuum and specific substrates, which is hard for the field to achieve controlled fabrications of new 2-D materials. The wet chemistry synthesis route is a better alternative method towards the high-yield, low-cost and mass production of all types of ultrathin 2D nanosheets. In the chapter 3 of this thesis, we successfully demonstrate the controlled lateral shell growth of $NaReF_4$ nanocrystals in wet chemical synthesis route by decreasing the ratio of OA^-/OAH, which suggests that the 2D heterogeneous nanocrystal may be synthesized in wet chemistry route. The thickness of 2D heterogeneous nanocrystal may be controlled by adjusting the size of core nanocrystals. The lateral shell growth mechanism via tuning the ratio of different surfactants may be suitable to direct the synthesis of semiconductor materials, due to their anisotropic crystal structure and similar synthesis conditions with $NaReF_4$ nanocrystals.

Hybrid materials

We may further design and fabricate a range of hybrid nanostructures by bringing together the rare earth fluorides, semiconductor nanocrystals, and noble metal structures. Several advanced properties are attractive: for example, the upconversion luminescence enhancement may be achieved by using semiconductor as photon antenna for increasing absorption of infrared light; the plasmonic enhancement effect may be achieved by using noble metal nanostructures; photo catalysis capability may be enhanced by the hybrid structure of UCNPs and N-type and P-type semiconductor nanomaterials to increase photovoltaic efficiency in harvesting the solar lights and rational designed structures to control the free carriers to be enriched on the metal material's surfaces.

The key challenge in synthesizing these hybrid materials via epitaxial growth approach lies in the selection of the matched crystalline facets between $NaReF_4$, semiconductor, and metal nanocrystals, and considerations of the etching effect due to the different stability of in reaction environment.

When the mismatch between the two nanomaterials is too big to allow direct epitaxial growth, tailoring the out-layer composition of core nanocrystals to bridge the core and the shell crystal lattice structures may be a solution. The methods for changing the out-layer's composition includes transition layer growth, surface cation exchange, surface redox reaction, etc.

Controlled surface engineering of nanocrystals

The surface structure is an important attribute of nanocrystals that influences many aspects of the nanocrystals, such as surface–volume-ratio, surface charge and surface activity, and affect their physical and chemical properties and practical performance in their applications. The highly controlled epitaxial shell growth techniques introduced in this thesis suggest new opportunities in engineering the surface structure of nanocrystals to selectively expose a desirable crystal facet of the heterogeneous nanocrystals, which will optimize the nanocrystals' performance, such as catalysis performance. The exposed crystal facets are generally formed by the facets with lowest surface energy in certain environment. The surface energy of facets will be different according to their surround conditions, such as surface charges, the selective bonding of surface ligand, and relative stability difference comparing to other crystal facets.

Appendix A---Computational Modeling

6.1 Surface and absorption models

In order to unravel the underlying mechanism of ligand directed growth of nanocrystals, the density functional theory (DFT) based first principles calculations were performed using CASTP[1] in Material Studio. We simulated the interactions between the surface of β-$NaYF_4$ and selected ligands. Throughout the entire DFT calculations we have implemented a generalized gradient approximation (GGA) using a kinetic energy cut-off of 500 eV for the plane wave. The calculated lattice constants used for the bulk β-$NaYF_4$ were a = 6.001 Å and c = 3.603 Å, which were similar to the experimental values observed (a = 5.96 Å, c = 3.53 Å for β-$NaYF_4$).[2] The surface structure was modeled using a super-cell which consisted of a 10-layer slab separated by a vacuum of 15 Å. In the case of un-passivated surfaces, a more general expression of surface energy, applicable to both stoichiometry and non-stoichiometry surface models, was used:

$$\sigma = \frac{1}{2A}[E_{tot}(Slab) - n_{Na}\mu_{Na} - n_Y\mu_Y - n_F\mu_F] \qquad [1]$$

Where $E_{tot}(Slab)$ is the total energy of the slab, n_{Na}, n_Y and n_F are the number of Na, Y and F atoms in the slab, and μ_{Na}, μ_Y and μ_F are their corresponding chemical potentials. The (001) and (100) facets of β-$NaYF_4$ with differently terminated atomic configurations were also investigated, and the most stable (001) and (100) surfaces calculated, with the surface energies of 44.58 meV/Å^2 and 57.43 meV/Å^2, are shown in Figure 1. The surface relaxation was also considered inside the top two layers which are free to relax without constraint, and our simulations were unable to show a significant change in the location of the atoms after relaxation. We calculated the capping of (001) and (100) facets by OAH and OA^- ligands presented in the solution using the adsorption model of ligands onto these two stable surfaces. The spurious interaction between ligands caused by the periodic boundary condition in our case can be ignored since the distance between the ligands is about 10 angstrom, which is a sufficient distance for the quantum simulation. In particular, the long carbon chain is a sufficient distance from the active functional group of OAH and OA^- ligands to make the surface binding energy negligible. Hence, we used two simplified molecules, namely $C_2H_3O_2$ and $C_2H_4O_2$ to mimic the adsorption characters of the OA^- and OAH ligands to the β-$NaYF_4$ facets, respectively. Note that in our simulation, atoms in the top two layers were allowed to relax until the force on each atom was less than 0.02 eV/Å while the other atoms were fixed (shadow areas shown in Fig. S2 and S3). Since the oxygen atoms of the ligands prefer to bind with Y^{3+} ions in cubic $NaYF_4$, [3] we only considered the interaction of molecule with Y^{3+} ions when testing different initial configurations. The initial adsorption configurations of ligands onto the (001) and (100)

surfaces were considered, and are illustrated in Fig. S2 and S3, respectively. The binding energy was determined by

$$E_b = E(Combined) - [E(Surf) + E(Mol)] \qquad [2]$$

where $E(Combined)$, $E(Surf)$ and $E(Mol)$ were the energies of the binding complex, the $NaYF_4$ slab and the isolated molecule, respectively. The binding energies of these molecules (first row in Table 1) follow the sequence of $E_b(OA^-) > E_b(OAH)$ both for (001) and (100) surfaces as a result of the chemical activity of the molecules. Furthermore, we also found that the adsorption of OA^- ligands onto (100) facet was stronger than that of (001), whereas the OAH ligands prefer to be adsorbed onto the (001) compared to (100). The different binding strength can be ascribed to the different atomic arrangement of Y^{3+} ions on these two facets as seen in Figure 1c, which give rise to different charge transfer paths between ligands and surfaces (Figure 4).

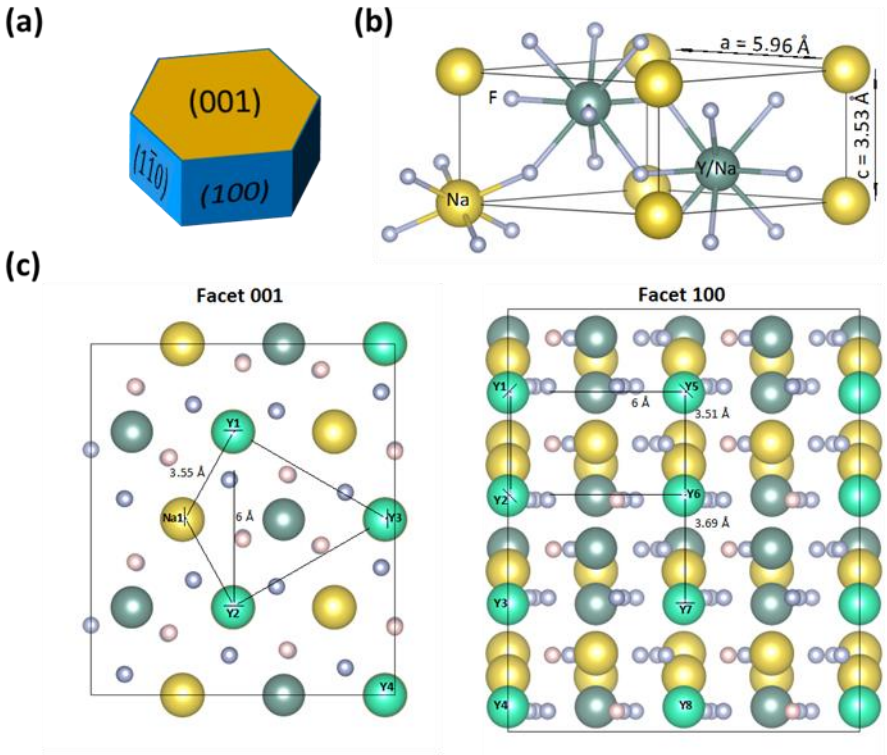

Figure 1. Computational models of the crystalline structure of β-$NaYF_4$ facets. a), The schematic shape of a β-$NaYF_4$ nanocrystal chosen as the core for directional epitaxial growth in this work is illustrated. The hexagonal cylinder consists of the (001) facets at the ends and identical (100) and $(1\bar{1}0)$ facets around the cylinder sides. b), A unit cell of β-$NaYF_4$ structure with detailed atomic arrangement and the lattice parameters; c), The relaxed atomic configurations of the most stable (001) and (100) facets. The Y^{3+} atoms form equilateral triangles with a length of 6 Å in the relaxed (001) surface, and rectangles are

observed in the (100) surface with a shorter length of 3.51 or 3.69 Å; The light green and pink balls represent surface Y^{3+} and F^{-} atoms, respectively.

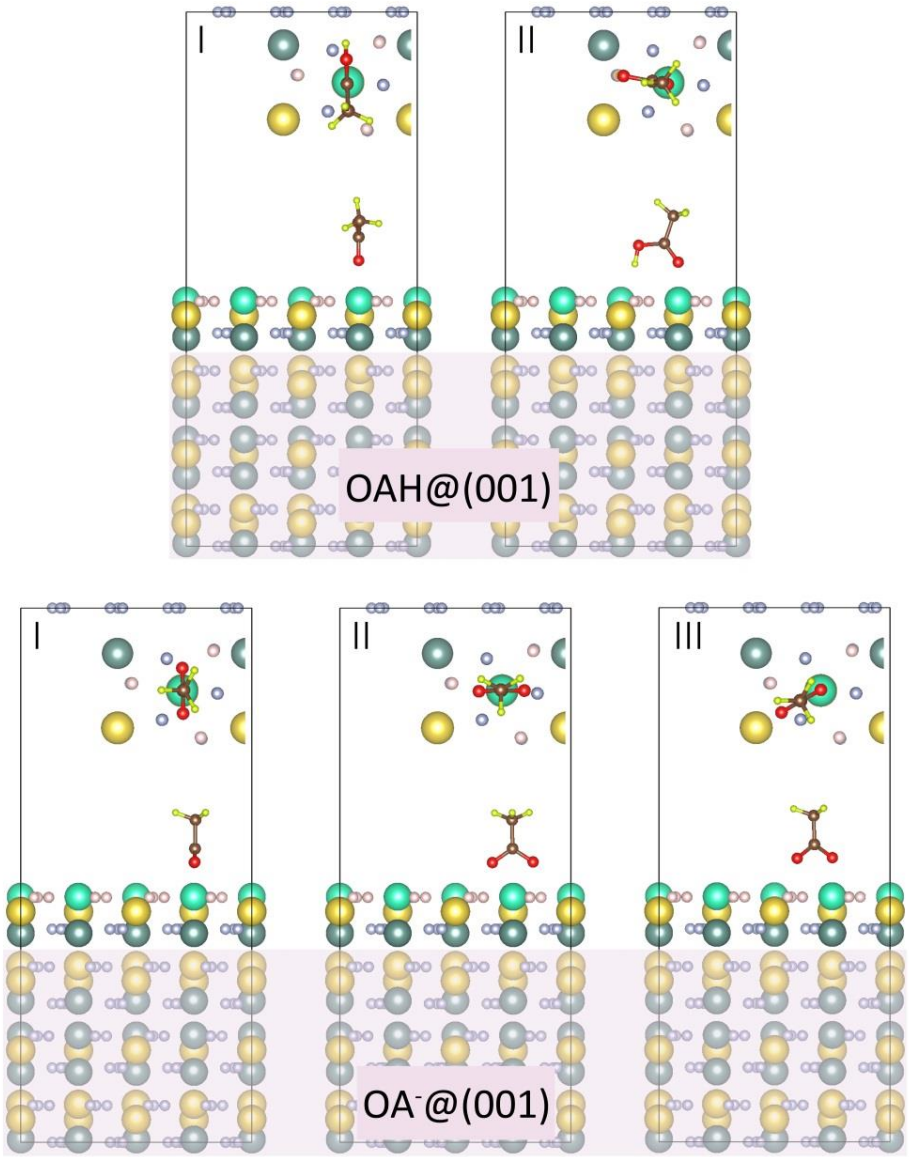

Figure 2. The adsorption models of OAH and OA^{-} ligands on the (001) surface with different initial configurations. Top-view configuration is shown as an inset. The shadowed area represents the fixed atomic layers. The colour of the atoms are: Na atoms: yellow, Y atoms: cyan, F atoms: white, C atoms: brown, O atoms: red and H atoms: light yellow. The light green and pink spheres represent the surface Y and F atoms, respectively.

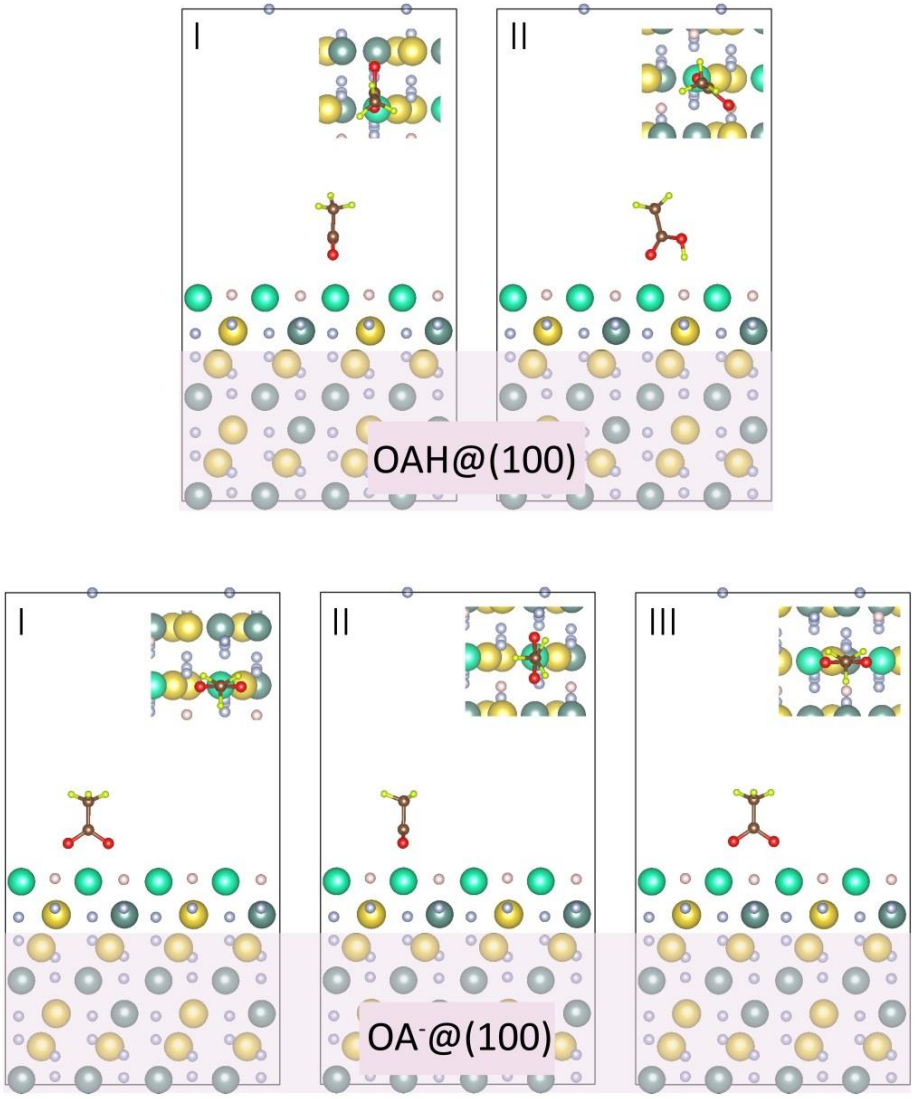

Figure 3. The adsorption models of OAH and OA^- ligands on the (100) surface with different initial configurations. Top-view configuration is shown as an inset. The shadowed area represents fixed atomic layers. The colour of the atoms are: Na atoms: yellow, Y atoms: cyan, F atoms: white, C atoms: brown, O atoms: red and H atoms: light yellow. The light green and pink spheres represent surface Y and F atoms, respectively.

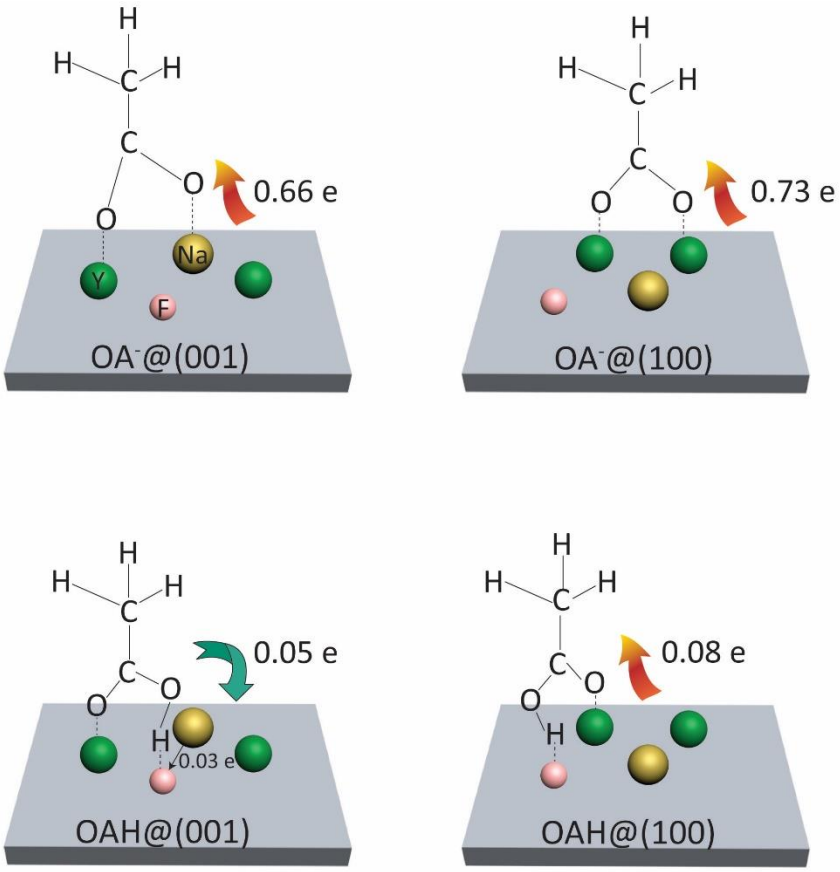

Figure 4 Schematic description of the charge transfer between ligands and surfaces. The details of respective mechanisms are as follows. When the OA^- ions approach the exposed Y^{3+} ions they bind to the Y-Y and Y-Na pairs on the (100) and (001) surfaces, respectively. The charge analysis calculated that the Y atoms located on the (100) surface have about 0.35 electrons/atom less saturated than the same atoms located on the (001) surface, although Y ions on both surfaces have the same 6-fold coordination. Therefore, the charge can be easily transferred from the (100) surface to OA^- through a pair of Y-O bonds, giving rise to higher binding strength on that surface compared to (001). In the case of OAH molecule the binding mechanism is less straightforward since the OAH molecules bind to Y-F pairs at both (001) and (100) surfaces. However, our charge analysis reveals that the OAH molecules donate electrons to fluorine atoms located on the (001) surface, but not to the same atoms on the (100) surface. Moreover, adsorption of OAH onto the (001) surface induces a charge transfer from the surface Na atoms to F atoms, resulting in a self-saturation. These two separate modes of charge transfer enhance the stability of the capped system for the (001) orientation. On the other hand, when the OAH approaches the (100) surface, the

charge is transferred from the surface F/Y atoms to OAH. In this case, the stability of the capped system deteriorates because of the fact that the F atoms accept rather than donate electrons.

6.2 Effect of coverage and steric carbon chain of ligand on binding energy

The aforementioned proposed (001) and (100) adsorption models correspond to the ligand surface coverage of 0.8 and 0.58 ligand/nm^2, respectively. In order to clarify the effect of the coverage on the binding energies, we minimized the slab models, giving rise to enhanced coverage of 1.6 and 1.15 ligand/nm^2 for (001) and (100) facets, respectively. Here the adsorption model of OA^- on (001) with low and high coverage is shown in Fig. S5. According to the calculated binding energies (row two in Table 1), we found that the increased coverage that was applied in this example did not affect the binding trend of the original calculation, which was based on a low ligand coverage.

To mimic the experimental situation, we also calculated the interaction between the slabs and the real oleic acid molecules containing 18 carbon atoms (Fig. 6). The corresponding binding energies (the last row of Table 1) indicate that the binding trend of the original calculation based on a simplified molecule model is still accurate when the real oleic acid molecules are taken into consideration. It should be noted that a decrease of the absolute values of the binding energy was observed, indicating that the long alkyl tail can weaken the interaction between molecules and the surfaces that were tested.

In summary, the validity of our simplified computational model was confirmed since it displayed the same trend in binding strength observed in the three calculation sets. Since the binding energy of OA^- is much higher than that of OAH in both of (001) and (100) planes, OA^- has a lot stronger passivating effect at the crystal facets. For example, the binding energy of OA^- at (100) planes is about 13.6 eV higher than its binding energy at the (001) planes. This suggests that OA^- has a stronger bond at (100) planes (lateral faces of hexagonal nanocrystals) than at the (001) planes (top and bottom faces of hexagonal nanocrystals) In contrast, OAH has a higher binding energy at the (001) planes than that at the (100) planes, which suggests that OAH has a stronger bond at the (001) planes (top and bottom faces) than that at the (100) planes (lateral faces). Therefore, in the condition where there is a high ratio of OA^-/OAH, OA^- will become the major surfactant that passivates the (100) planes (lateral faces) and promotes crystal growth along the [001] crystallographic direction. On the other hand, where there is a low ratio of OA^-/OAH, OAH will become the major surfactant, which makes the top and bottom faces relatively more passive in comparison to the lateral faces. Therefore the growth direction of nanocrystals can be controlled from longitudinal to transverse by adjusting the ratio of OA^- to OAH.

Table 1. Binding energy of OA^- and OAH to (001) and (100) planes

	OA^-+001 (meV)	OAH+001 (meV)	OA^- +100(meV)	OAH+100 (meV)
Simplified model	-30.05	-12.23	-37	-6.05
Enhanced coverage	-34.5	-24.5	-73.2	-10.6
Real oleic acid	-21.8	-9.4	-35.4	-4.6

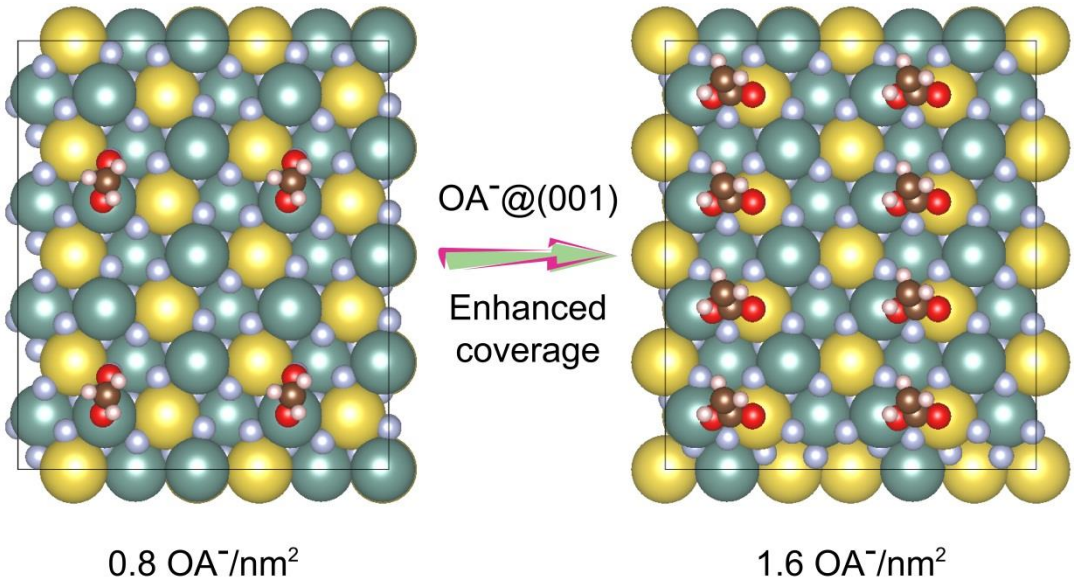

Figure 5. The adsorption model of OA^- ligands on the (001) surface with different ligand coverage. The color of the atoms are: Na atoms: yellow, Y atoms: cyan, F atoms: white, C atoms: brown, O atoms: red and H atoms: pink.

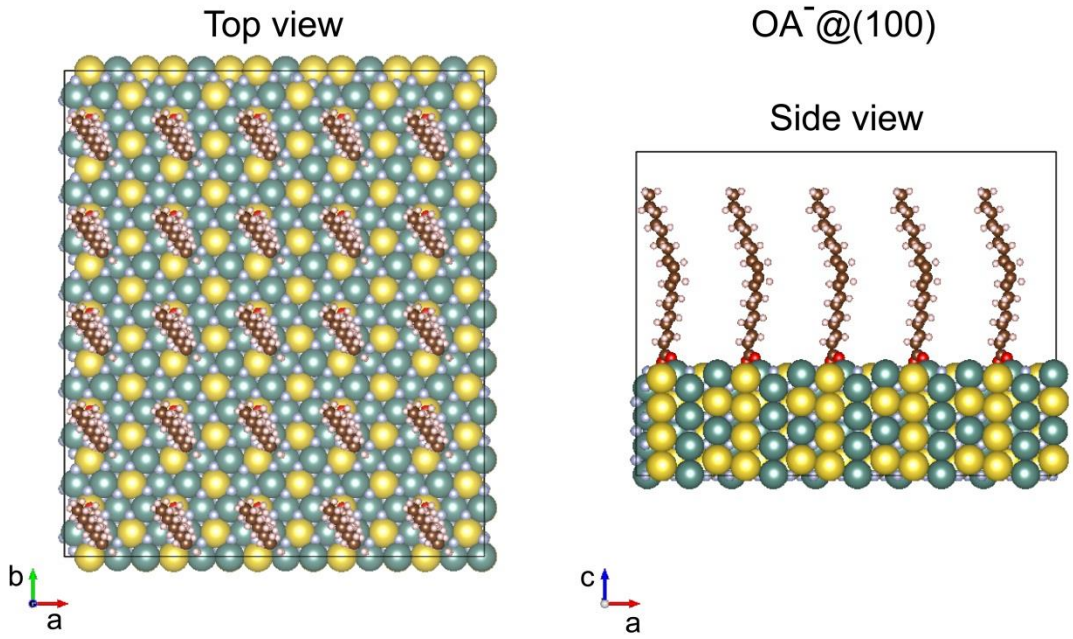

Figure 6. The adsorption model of real OA^- ligands (18 C atoms) on the (100) surface. The colour of the atoms are: Na atoms: yellow, Y atoms: cyan, F atoms: white, C atoms: brown, O atoms: red and H atoms: pink.

Reference

[1] S.J. Clark, M.D. Segall, C.J. Pickard, P.J. Hasnip, M.J. Probert, K. Refson, M.C. Payne, Z Kristallogr, 220 (2005) 567-570.

[2] F. Wang, Y. Han, C.S. Lim, Y.H. Lu, J. Wang, J. Xu, H.Y. Chen, C. Zhang, M.H. Hong, X.G. Liu, Nature, 463 (2010) 1061-1065.

[3] Y.Q. Sui, K. Tao, Q. Tian, K. Sun, J Phys Chem C, 116 (2012) 1732-1739.